

**UNIVERSITY OF SOUTHAMPTON**

**The Efficiency of Photovoltaic Systems**

by

Athanasios Gousiopoulos

A thesis for the degree of Doctor of Philosophy

in

Electrical and Electronic Engineering

Faculty of Physical Sciences and Engineering

Department of Electronics and Computer Science

November 2016



# UNIVERSITY OF SOUTHAMPTON

## ABSTRACT

FACULTY OF PHYSICAL SCIENCES AND ENGINEERING

DEPARTMENT OF ELECTRONICS & COMPUTER SCIENCE

Doctor of Philosophy

### **The Efficiency of Photovoltaic Systems**

by Athanasios Gousiopoulos

At this work the principle aim is to create new low cost hardware test circuitry that can emulate the behavior of solar cells under different insolation and temperature conditions. Another goal is to propose a new MPPT algorithm that could accurately and reliably estimate the maximum power operating point.

The transcendental equation describing a solar cell IV characteristic contains current on both sides in a function of the form  $I = f(V, I)$ . In this work, a current-independent voltage expression is derived for the maximum power point as a function of a new variable which is mathematically well defined. Validation is performed on four different photovoltaic modules. The best case scenario has shown a divergence in  $P_{mpp}$  of 0.08% while the worst 0.84%. The new method is examined for sensitivity, up to  $\pm 5\%$  on values of five fitting parameters ( $R_s$ ,  $R_{sh}$ ,  $n$ ,  $I_o$ ,  $I_{ph}$ ), with  $I_{ph}$  to have the higher impact effect (up to 5% error).

Two topologies, of  $V_{BE}$  multiplier, have been proposed that can reliably emulate solar cell operation. Analysis shows that both circuits have the potential to deliver good quality characteristic IV curves with small  $RMSE$  ( $10^{-3}$ ). The second improved  $V_{BE}$  multiplier has the ability to operate over wider range of illumination and temperature conditions. Through this model it was possible to build a low cost (£230) fully functional prototype digital controlled emulator solar system “*DiceSol*”.

A MPPT device has been implemented based on a powerful mathematical modeling tool. The proposed method “*Goose Waddle (GW)*” was employed on a boost DC/DC converter configuration. Excellent static and dynamic performances were exhibited. At all cases considered convergence is higher than 98.53% while convergence time is on average 220 msec.



# Table of Contents

<b>Table of Contents</b> .....	<b>i</b>
<b>List of Tables</b> .....	<b>vii</b>
<b>List of Figures</b> .....	<b>xi</b>
<b>Declaration of Authorship</b> .....	<b>xxi</b>
<b>Acknowledgements</b> .....	<b>xxiii</b>
<b>1 Introduction</b> .....	<b>1</b>
1.1 Background and Motivation .....	1
1.2 Aims of this Work.....	7
1.3 Structure of Report.....	8
<b>2 Literature Review</b> .....	<b>11</b>
2.1 Device Physics .....	11
2.2 <i>P-N</i> Junction.....	14
2.3 Solar Cell Characteristics.....	17
2.4 Fundamentals of Silicon Solar Cell Design.....	19
2.5 Efficiency Limits .....	20
2.6 Equivalent Circuits.....	22
2.6.1 Comparison of single diode model and two diode model of photovoltaic module. ....	25
2.7 Dependencies on insolation and temperature .....	28
2.7.1 Insolation .....	28
2.7.2 Temperature .....	29
2.8 Software Simulator Program - PC1D .....	31
2.8.1 PC1D modelling .....	32
2.9 DC to DC Converters.....	34
2.9.1 Buck, Boost, Buck-Boost converter .....	34
2.9.2 Buck Converter.....	35
2.9.2.2 Continuous – Conduction Mode.....	37
2.9.3 Boost Converter .....	39
2.9.3.4 Inductor Current Ripple – Inductor Choice.....	48
2.9.3.5 Output Capacitor Choice .....	50

2.9.4	Buck-Boost Converter.....	53
2.9.5	Measuring Regulator Efficiency of DC-DC Converters.....	57
2.10	MPPT Methodologies -Techniques.....	58
2.10.1	Introduction.....	58
2.10.2	Perturb and Observe.....	58
2.10.3	Hill-Climbing.....	60
2.10.4	The incremental conductance method.....	61
2.10.5	Constant Voltage (CV).....	63
2.10.6	Fractional open-circuit voltage control.....	64
2.10.7	Fractional short-circuit current control.....	65
2.10.8	Other “hill climbing” maximum power point tracking methods.....	66
2.10.9	Temperature Gradient Method.....	69
2.10.10	Current and Temperature Method (I&T).....	70
2.10.11	Look Up Table (LUT).....	70
2.10.12	Simulation Results Evaluating MPPT Methods.....	71
2.10.13	Discussion.....	76
2.11	Review on current solar simulators.....	79
2.11.1	Solar simulator based on PV Sandia Database.....	79
2.11.2	Solar simulator light sources.....	80
2.11.3	SunaPlayer: Emulation Platform of Solar Cells.....	83
2.12	Conclusions.....	85
<b>3</b>	<b>Derivation of maximum power point.....</b>	<b>89</b>
3.1	Introduction.....	89
3.2	The current - voltage relationship for a photovoltaic device.....	89
3.3	Theoretical Analysis - Equations for Determining $I_{mpp}$ , $V_{mpp}$ , $P_{mpp}$ and A90.....	
3.4	Experimental Validation.....	96
3.5	Resistor Sensitivity to MPP.....	97
3.6	Sensitivity of parameters $I_o$ , $I_{ph}$ , $n$ to MPP.....	102
3.7	Conclusion.....	110
<b>4</b>	<b>Modeling of Photovoltaic Cell Operation and Behavior Using and Improved <math>V_{BE}</math> Multiplier.....</b>	<b>111</b>
4.1	Introduction.....	111

4.2	Schematic overview of the experimental setup. ....	112
4.2.1	Electronic load - Principle of operation.....	113
4.3	Analytical Model of a PV Cell.....	115
4.4	Basic $V_{BE}$ Multiplier.....	118
4.4.1	Parameter extraction from PC1D.....	120
4.4.2	Parameter extraction for the Transistor .....	123
4.4.3	Error Calculation .....	126
4.4.4	Series Resistance Compensation .....	126
4.4.5	Experimental Results – Discussion .....	129
4.5	Improved $V_{BE}$ Multiplier .....	136
4.5.1	Extracting PV Cell Parameters from PC1D.....	138
4.5.2	Improved $V_{BE}$ Multiplier – Application to Modelling Photovoltaic Cell Behavior.....	139
4.5.3	Parameter Extraction for the Transistor.....	143
4.5.4	Series Resistance Compensation .....	145
4.5.5	Temperature Compensation.....	146
4.5.6	Distribution of Data Points .....	149
4.5.7	Discussion.....	152
4.6	Conclusion .....	158
<b>5</b>	<b>Programmable Solar Cell Emulator .....</b>	<b>161</b>
5.1	Introduction.....	161
5.2	Aims – Experimental System.....	161
5.3	Design and construction of artificial solar cell board .....	163
5.3.1	Current Source .....	164
5.3.2	Proposed Transistor Topology.....	165
5.3.3	Digital Potentiometer.....	166
5.3.4	Digital Switch .....	167
5.3.5	Difference Amplifier .....	168
5.3.6	Analog to Digital Converter (ADC) .....	169
5.3.7	Temperature Sensor .....	169
5.3.8	Connection Socket.....	170
5.3.9	Decoupling Capacitors.....	171

5.4	Motherboard Circuit Design.....	172
5.4.1	Electronic load circuit .....	173
5.4.2	Triangular Waveform.....	175
5.4.3	I/O I-squared-C Expander .....	176
5.4.4	Voltage Regulators .....	177
5.4.5	Other Components .....	178
5.5	Measurement System Recording Current – Voltage Data .....	179
5.6	Graphical User Interface (GUI).....	181
5.7	Microcontroller Board.....	184
5.8	Experimental Results.....	186
5.9	Discussion .....	193
5.10	Conclusion.....	195
<b>6</b>	<b>Maximum Power Point Tracking Implementation.....</b>	<b>197</b>
6.1	Introduction .....	197
6.2	Portable Devices Self Charging .....	197
6.3	Experimental System.....	198
6.4	Pilot Artificial Solar Cell.....	200
6.4.1	Pilot Artificial Solar Cell Electronic Circuit Configuration....	200
6.5	DC to DC Boost Converter .....	203
6.5.1	DC to DC Boost Converter Electronic Circuit Configuration	203
6.6	System Operation .....	205
6.7	Microcontroller.....	206
6.8	Evaluation, Experimental Results - Discussion .....	207
6.8.1	Comparison against FOCV and FSCC.....	210
6.9	Oscilloscope Characteristic Waveforms .....	216
6.9.1	Transient Response .....	219
6.10	Estimating Inductance and Capacitance Values.....	222
6.11	Calculating Converter Losses.....	223
6.12	More Efficient MPPT Platform.....	225
6.13	Conclusion.....	227
<b>7</b>	<b>Conclusions and Future Works .....</b>	<b>229</b>



7.1	Conclusions.....	229
7.2	Future Work.....	232
<b>Appendix A .....</b>		<b>235</b>
<b>A.1 Mathematical Derivation – Matlab scripts .....</b>		<b>235</b>
A.1.1	Mathematical Derivation.....	235
A.1.2	Matlab scripts .....	240
<b>Appendix B .....</b>		<b>243</b>
<b>B. Series Resistance Modelling .....</b>		<b>243</b>
<b>Appendix C .....</b>		<b>247</b>
Table 5.2	Summarizing experimental values at different irradiances and temperatures.....	247
Table 5.3	Summarizing theoretical values for different irradiances and temperatures.....	248
<b>Appendix D.....</b>		<b>249</b>
D.	MPP Software Code in Matlab.....	249
<b>8</b>	<b>Bibliography.....</b>	<b>255</b>



# List of Tables

Table 2.1. Nominal characteristic of the panel. Adapted from [48].	26
Table 2.2. Input data. Adapted from [48].	26
Table 2.3. Error in approximated curves with single diode model. Adapted from [48].	27
Table 2.4. Error in approximated curves with double diode model. Adapted from [48].	27
Table 2.5. Simulation parameters for PC1D.	33
Table 2.6. Equations for switch status “close”.	46
Table 2.7. Equations for switch status “open”.	46
Table 2.8. Summary of P&O Algorithm. Adapted from [66].	59
Table 2.9. Fractional open circuit voltage, relationship between $V_{oc}$ and $V_{mpp}$ . Adapted from [100].	64
Table 2.10. Major Characteristics of MPPT Techniques.	77
Table 3.1. Data from catalogues (STC) and estimated loss resistances (for $n=1$ ). Reproduced from [140].	96
Table 3.2. Summarize theoretical data provided by manufacturers and experimental data derived by the proposed method, along with errors for each photovoltaic module.	97
Table 3.3. Percentage relative errors to MPP for series resistance variation from -5% to +5% of nominal value.	98
Table 3.4. Percentage relative errors to MPP for shunt resistance variation from -5% to +5% of nominal value.	98
Table 3.5. Percentage relative errors in respect to nominal value of series resistor.	101
Table 3.6. Percentage relative errors in respect to nominal value of shunt resistor.	101

Table 3.7. Percentage relative errors to MPP for saturation current variation from -5% to +5% of nominal value. ....	103
Table 3.8. Percentage relative errors to MPP for photocurrent variation from -5% to +5% of nominal value.....	103
Table 3.9. Percentage relative errors to MPP for ideality factor variation from 0% to +5% of nominal value.....	104
Table 3.10. Percentage relative errors to MPP for ideality factor variation from 1 to 2. Nominal value $n=1$ .....	104
Table 4.1. Parameters set and values obtained from PC1D software.....	121
Table 4.2. Curve fitting algorithm calculated values.....	123
Table 4.3. Data required for theoretical calculation of series resistance value. Also, experimental resistor utilised along with percentage difference. ...	128
Table 4.4. Parameters related to PC1D simulation.....	129
Table 4.5. Parameters related to Artificial Solar Cell proposed electronic circuit...	130
Table 4.6. Summarizing experimental setup values for experiment conducted, at 1000 W/m <sup>2</sup> irradiance and different temperature conditions.....	131
Table 4.7. Summarizing theoretical setup values for experiment conducted, at 1000 W/m <sup>2</sup> irradiance and different temperature conditions.....	131
Table 4.8. Series resistance experimentally placed and theoretically calculated along with relevant data. ....	131
Table 4.9. <i>Basic <math>V_{BE}</math> multiplier</i> biasing arrangement for all cases considered.....	131
Table 4.10. Parameters set and values obtained from PC1D software.....	138
Table 4.11. Extracted values.....	138
Table 4.12. Data required for theoretical calculation of series resistance value. Also, experimental resistor utilised along with percentage difference. ...	146
Table 4.13. Parameters for simulated version of solar cell. ....	153
Table 4.14. Parameters for artificial solar cell.....	153

Table 4.15. Summary of values for experiment conducted at 1000 W/m <sup>2</sup> irradiance and different temperatures.....	154
Table 4.16. Summary of theoretical values for the experiment conducted at 1000 W/m <sup>2</sup> irradiance and different temperatures.....	154
Table 4.17. Series resistance experimentally placed and theoretically calculated, along with relevant data.....	154
Table 5.1. Digital switch truth table. Adapted from [153].....	167
Table 6.1. Experiments performed testing the proposed MPP methodology, varying insolation and temperature conditions.....	209
Table 6.2. Energy generated as function of MPPT technique and irradiance input.	212
Table 6.3. Percentage efficiencies of FOCV, FSCC and GW. ....	213
Table 6.4. Time to reach steady state condition in each algorithm studied. ....	213
Table 6.5. Percentage efficiencies of FOCV and FSCC. Adapted from [88, 90]....	214
Table 6.6. Main features of MPPT techniques presented. ....	216



# List of Figures

Figure 1.1. Global solar photovoltaic cumulative installed capacity at the end of 2014 and annual installed capacity since 2008. Adapted from [9].....	2
Figure 1.2. Reduction in total PV system costs. Data pre-2012 is historical; post-2012 are projected from industry estimates. [13, 14]. Reproduced from [11]. .....	3
Figure 1.3. Usage and energy consumed by portable devices. ....	4
Figure 1.4. i) Solar radiation, ii) Array temperature, iii) Theoretical maximum power and iv) Experimental performance with direct load connection. Adapted from [22]. .....	6
Figure 2.1. Graph showing I-V characteristics of a diode and a solar cell under illumination. Adapted from [31].....	16
Figure 2.2. Test circuit to produce the output characteristics. ....	17
Figure 2.3. Typical silicon solar cell characteristics (I-V, P-V). ....	17
Figure 2.4. Spectral power density of sunlight. The different spectra refer to the black body radiation at 6000K, the extraterrestrial AM0 and the AM1.5 radiation. Reproduced from [36]. .....	19
Figure 2.5. Cross section of <i>p-n</i> junction cell. Adapted from [30]. ....	20
Figure 2.6. Equivalent circuit for an ‘ideal’ solar cell. Adapted from [41]. ....	22
Figure 2.7. Single diode equivalent circuit model with parasitic resistances. Adapted from [43]. .....	23
Figure 2.8. Two diode equivalent circuit model. Adapted from [45]. .....	24
Figure 2.9. I-V characteristics of a photovoltaic cell array for a range of irradiance <i>S</i> at 25 °C. Adapted from [50]. .....	28
Figure 2.10. P-V characteristics of a photovoltaic module for a range of irradiance <i>S</i> at 25°C. Adapted from [50]. .....	29

Figure 2.11. I-V characteristics of a photovoltaic array for a range of temperatures at an irradiance of 1000 W/m <sup>2</sup> . Adapted from [50].	30
Figure 2.12. P-V characteristics of a photovoltaic cell array for various values of temperature T at an irradiance of 1000 W/m <sup>2</sup> . Adapted from [50].	30
Figure 2.13. Ideal switch voltage $v_s(t)$ , duty ratio $D$ , and switching period $T_S$ . Adapted from [50].	35
Figure 2.14. Ideal buck converter circuit. Adapted from [50].	35
Figure 2.15. Equivalent circuit of a buck converter at closed switch time $DT_S$ . Adapted from [50].	36
Figure 2.16. Equivalent circuit of a buck converter at open switch time $D'T_S$ . Adapted from [50].	36
Figure 2.17. Buck regulator inductor current. Adapted from [58].	37
Figure 2.18. Step-down converter circuit states (a) inductor voltage and current waveforms, (b) switch on (c) switch off. Adapted from [59].	38
Figure 2.19. Ideal boost converter circuit. Adapted from [50].	39
Figure 2.20. Equivalent circuit of a boost converter at closed switch time $DT_S$ . Adapted from [50].	39
Figure 2.21. Equivalent circuit of a boost converter at open switch time $D'T_S$ . Adapted from [50].	40
Figure 2.22. Continuous Conduction mode: (a) inductor voltage and current waveforms (b) switched on; (c) switched off. Adapted from [59].	41
Figure 2.23. Waveforms at the boundary of continuous discontinuous conduction. Adapted from [59].	42
Figure 2.24. Average Output Current at the Boundary of continuous – discontinuous. Reproduced from [59].	43
Figure 2.25. Step up converter waveforms at Discontinuous Conduction. Adapted from [59].	44
Figure 2.26. Circuit of boost up converter.	47



Figure 2.27. Voltage waveforms in the boost up converter (inductor, switch and diode).....	48
Figure 2.28. Current waveforms in the boost up converter (inductor, switch and diode).....	48
Figure 2.29. Ripple Inductor current. Adapted from [59].....	49
Figure 2.30. Effect of parasitic elements on voltage conversion ratio. Reproduced from [59].....	51
Figure 2.31. Ideal buck-boost converter circuit. Adapted from [50]. .....	54
Figure 2.32. Equivalent circuit of a buck-boost converter at closed switch time $DT_s$ . Adapted from [50].....	54
Figure 2.33. Equivalent circuit of a buck-boost converter at open switch time $D'T_s$ . Adapted from [50]. .....	55
Figure 2.34. Buck-boost (inverting) converter when the switch is opened. Adapted from [58].....	55
Figure 2.35. Continuous conduction mode: a) inductor voltage and current waveforms b) switch on; c) switch off. Adapted from [59]. .....	56
Figure 2.36. Characteristic PV array power curve versus voltage or current. Reproduced from [66]. .....	59
Figure 2.37. Deviation from the MPP with the P&O algorithm under rapidly changing insolation levels $S$ . Reproduced from [50]. .....	60
Figure 2.38. Block diagram representation of MPPT methods a) constant voltage; b) temperature gradient; c) open circuit voltage; d) short circuit current; e) P&O; f) I&T. Reproduced from [91]. .....	71
Figure 2.39. Efficiency of MPPT techniques considering irradiance variation. Reproduced from [91]. .....	72
Figure 2.40. Steady-state behavior of MPPT techniques ( $1000 \text{ W/m}^2$ , $45^\circ\text{C}$ ): (a) constant voltage; (b) temperature gradient; (c) open-circuit voltage; (d) short-circuit current; (e) P&O; (f) I&T. Reproduced from [91].....	73

Figure 2.41. Efficiency of MPPT techniques considering both irradiance and temperature variation. Reproduced from [91].....	74
Figure 2.42. Tracking efficiency of MPPT techniques (1000 W/m <sup>2</sup> to 500 W/m <sup>2</sup> and 65°C to 25°C): (a) constant voltage; (b) temperature gradient; (c) open-circuit voltage; (d) short-circuit current; (e) P&O; (f ) I&T. Reproduced from [91].....	75
Figure 2.43. Efficiency of MPPT methods at changing insolation condition. Adapted from [111].....	76
Figure 2.44. Schematic diagram of an LED-based solar simulator. Reproduced from [130]. ....	81
Figure 2.45. Simplified schematic overview of an LED based solar simulator. Reproduced from [130].....	82
Figure 2.46. LED based solar simulator prototype with parts description. Reproduced from [131].....	82
Figure 2.47. SunaPlayer emulation platform of solar cells. Reproduced from [133].....	83
Figure 2.48. The multi-scale circuit to drive the base voltage of the PNP darlington. Reproduced from [133]. ....	84
Figure 2.49. The multi-scale circuit for measuring the output voltage and the output current. Reproduced from [133]. ....	85
Figure 3.1. “Solar array equivalent circuit” (N <sub>s</sub> – series, N <sub>p</sub> – parallel). Adapted from [139]. ....	90
Figure 3.2. Percentage relative errors against series resistance deviation limits for all four modules. ....	99
Figure 3.3. Percentage relative errors against shunt resistance deviation limits for all four modules. ....	100
Figure 3.4. Percentage relative errors against saturation current deviation limits for all four modules.....	105

Figure 3.5. Percentage relative errors against photocurrent deviation limits for all four modules. ....	106
Figure 3.6. Percentage relative errors against ideality factor deviation limits for all four modules. ....	107
Figure 3.7. Percentage relative errors against ideality factor deviation limits for all four modules ( $n \in [1, 2]$ ). ....	108
Figure 4.1. Schematic overview of the experimental set up. ....	112
Figure 4.2. Basic test circuit for PV modules using a MOSFET as an electronic load. Reproduced from [142]. ....	113
Figure 4.3. Characteristics of a PV module at STC and characteristics of a MOSFET. Reproduced from [142]. ....	114
Figure 4.4. Proposed transistor equivalent circuit model. ....	115
Figure 4.5. Current sources – diode and transistor with gain $G$ circuits. ....	116
Figure 4.6. $V_{BE}$ multiplier for biasing. Adapted from [144]. ....	118
Figure 4.7. Proposed transistor model, biased with two potentiometers. ....	119
Figure 4.8. Current voltage characteristics, obtained from simulation and fitting algorithm. ....	123
Figure 4.9. I-V characteristic curve plots for PC1D software simulation program, Artificial Solar Cell circuit proposed and Error. ....	124
Figure 4.10. Plot of current flowing through the transistor in logarithmic scale against base emitter voltage. ....	125
Figure 4.11. Deviation between I-V characteristic curves for standard series resistance. ....	127
Figure 4.12. Experimental values versus Temperature for irradiance $1000 \text{ W/m}^2$ . ....	132
Figure 4.13. Theoretical values versus Temperature for irradiance $1000 \text{ W/m}^2$ . ....	133
Figure 4.14. I-V characteristic curve plots for all cases considered. ....	134
Figure 4.15. Ideal transistor with amplifier block diagram circuit. ....	136

Figure 4.16. Circuit with amplifier $G_2$ and attenuator $B$ .....	136
Figure 4.17. Circuit with non-inverting operational amplifier and resistive divider.	137
Figure 4.18. Current versus voltage characteristics, simulated version (PC1D) and fitting algorithm (FIT).....	139
Figure 4.19. Oscillations observed in uncompensated circuit. ....	139
Figure 4.20. <i>In-loop compensation</i> circuit.....	140
Figure 4.21. Simplified, low-frequency hybrid-pi bjt model. Adapted from[144]. .	141
Figure 4.22. Bipolar hybrid-pi model with parasitic capacitances to model frequency dependence. Adapted from [144].....	141
Figure 4.23. Applying the <i>in-loop compensation</i> technique to the proposed electronic circuit.....	142
Figure 4.24. I-V characteristic curves observed in compensated circuit.....	142
Figure 4.25. Circuit with non-inverting operational amplifier, resistive divider, in loop compensation and transistor biased. <i>Improved <math>V_{BE}</math> multiplier</i> topology. ....	143
Figure 4.26. I-V characteristic curve related to <i>Improved <math>V_{BE}</math> multiplier</i> topology.	143
Figure 4.27. Plot of current flowing through the transistor in logarithmic scale against base emitter voltage. ....	144
Figure 4.28. Series resistance uncompensated I-V characteristic curves.....	145
Figure 4.29. I-V characteristic curves for PC1D (blue line), EXP1 “cold start” (red), EXP2 (green) after 15 minutes of continuous operation, EXP3 (brown) after compensation technique is applied. ....	147
Figure 4.30. Error and temperature variation versus voltage for cases considered..	147
Figure 4.31. Distribution of simulation data points.....	149
Figure 4.32. Distribution of experimental data points.....	150
Figure 4.33. Distribution of expanded simulation data. ....	151

Figure 4.34. Final theoretical distribution data points. ....	152
Figure 4.35. Experimental values versus Temperature for irradiance 1000 W/m <sup>2</sup> ..	155
Figure 4.36. Theoretical values versus Temperature for irradiance 1000 W/m <sup>2</sup> . ....	156
Figure 4.37. I-V characteristic for all cases considered. ....	157
Figure 5.1. Prototype Digitally Controlled Emulation Solar System (“DiceSol”)..	162
Figure 5.2. Schematic overview of artificial solar cell board. ....	163
Figure 5.3. Artificial solar cell board. ....	164
Figure 5.4. Current Source for control of the optically generated current. Adapted from [151]. ....	165
Figure 5.5. Proposed artificial solar cell topology. ....	166
Figure 5.6. Digital potentiometer configuration. W wiper of potentiometer, moving from terminal A to terminal B. Adapted from [152]. ....	167
Figure 5.7. Digital Switch schematic configuration. Adapted from [153]. ....	168
Figure 5.8. Instrumentation amplifier configured as a difference amplifier. Adapted from [154]. ....	168
Figure 5.9. Analog to digital converter MAX1132 pin configuration and typical application circuit. Adapted from [155]. ....	169
Figure 5.10. Digital thermometer configuration. Adapted from [150]. ....	170
Figure 5.11. Pin Header layout. ....	171
Figure 5.12. Decoupling Capacitors. ....	172
Figure 5.13. Schematic overview of motherboard. ....	172
Figure 5.14. Motherboard. ....	173
Figure 5.15. Electronic load configuration. ....	174
Figure 5.16. DAC provides triangular waveform. Adapted from [159]. ....	176
Figure 5.17. I-squared-C Expander configuration circuit. Adapted from [160]. ....	177

Figure 5.18. Voltage regulator at +5V. Adapted from [162].....	178
Figure 5.19. Voltage regulator at +12V. Adapted from [163].....	178
Figure 5.20. a) Signals to the microcontroller, b) Measuring current and voltage, c) power supply connector d) Digital to analog ground connection through 0 Ohm resistor. ....	179
Figure 5.21. Schematic overview of the measurement system board. ....	180
Figure 5.22. Measurement System board. ....	180
Figure 5.23. Measuring output voltage and current circuit design.....	181
Figure 5.24. GUI Solar panel control unit. ....	182
Figure 5.25. Microcontroller board. ....	184
Figure 5.26. Flowchart of the process. ....	185
Figure 5.27. Experimental values versus temperature for different irradiances.....	187
Figure 5.28. Theoretical values versus temperature for different irradiances. ....	188
Figure 5.29. Experimental values versus irradiance for different temperatures.....	189
Figure 5.30. Theoretical values versus irradiance for different temperatures. ....	190
Figure 5.31. I-V characteristics for all cases considered.....	191
Figure 5.32. Non-linear interpolation for estimating $G$ value. ....	193
Figure 6.1. Experimental System. ....	199
Figure 6.2. Basic Circuit for measuring $I_{sc}$ and $V_{oc}$ , using a MOSFET.....	201
Figure 6.3. Voltage divider configuration. ....	201
Figure 6.4. Pilot cell circuit configuration.....	202
Figure 6.5. In detail circuit schematic. ....	205
Figure 6.6. Arduino Uno microcontroller.....	206
Figure 6.7. Maximum power point against temperature, for three insolation levels.	210

Figure 6.8. Maximum power point against insolation, for five temperature values.	210
Figure 6.9. Irradiation diagrams of cases 1, 2 and 3.	211
Figure 6.10. Power generated in all cases by different MPPT methods (red line) and ideal MPPT method (blue line).	212
Figure 6.11. Power generated by the PV array by different MPPT methods (solid line) and ideal (dot-dashed line). a) FOCV and b) FSCC. Reproduced from [90].	215
Figure 6.12. Square wave gate signal in the MOSFET of dc-dc converter.	216
Figure 6.13. Input voltage, voltage across coil and voltage across drain source.	217
Figure 6.14. Drain-Source voltage, voltage across the diode and output voltage.	218
Figure 6.15. Transition from $1000\text{W/m}^2$ to $800\text{W/m}^2$ at $40^\circ\text{C}$ . Time response 246.5 msec. Characteristics of input current, voltage and power produced.	219
Figure 6.16. Characteristic PV array power curve.	220
Figure 6.17. GW flow chart.	222





# Declaration of Authorship

I, Athanasios Gousiopoulos, declare that this thesis titled, 'The Efficiency of Photovoltaic Systems' and the work presented in it are my own and has been generated by me as the result of my own original research.

I confirm that:

- This work was done wholly or mainly while in candidature for a research degree at this University;
- Where any part of this thesis has previously been submitted for a degree or any other qualification at this University or any other institution, this has been clearly stated;
- Where I have consulted the published work of others, this is always clearly attributed;
- Where I have quoted from the work of others, the source is always given. With the exception of such quotations, this thesis is entirely my own work.
- I have acknowledged all main sources of help;
- Where the thesis is based on work done by myself jointly with others, I have made clear exactly what was done by others and what I have contributed myself;
- None of this work has been published before submission;

Signed:

---

Date:

---



## **Acknowledgements**

I would like to express my sincere and deepest gratitude to my supervisor, Professor Darren Bagnall, for offering me this opportunity and providing invaluable guidance throughout the project. His kind and expert supervision, friendly approach and continuous support helped me through the difficult times encountered in the project.

I am also grateful to Professor William Redman-White for valuable advices and theoretical discussions on electronic circuits. I would also like to thank Dr Gregory Telemachos Stamkopoulos for his support and discussion on aspects of this research.

Working in Nano Research Group of the University of Southampton was a great and memorable experience for me. I would like to thank Darren's group, particularly Dr Stuart Boden, Dr Adel Ghiass and Dr Mehdi Banakar. Thanks also to the rest of students, academic and secretaries in Nano Group.

Finally, I will like to thank my parents Asimakis and Eugenia, my dear sister Polyxeni for their unconditional love, support and encouragement all these years of my studies.



# 1 Introduction

## 1.1 Background and Motivation

Recently, there has been significant environmental and political motivation to shift power generation to renewable sources such as wind and solar. Factors such as the rising rate of energy consumption, energy security, the increasing cost of fossil fuels and the local and global environmental problems caused by the conventional power generation are increasingly motivating attention to renewable energy technologies. The main advantage of renewable energy over fossil fuels and nuclear power is the absence of harmful emissions, renewable energy systems are low-carbon and pollution free at point of use, they are user friendly and good for society [1, 2].

A rapid rise in global temperature has occurred in the 21<sup>st</sup> century due to the increase in the concentration of greenhouse gases in the atmosphere. In 2011, global carbon dioxide (CO<sub>2</sub>) emission reached more than 31.6 gigatonnes with an increase of 3.2% on 2010 levels and coal-fired power plants accounted for about 43% of this emission [3]. CO<sub>2</sub> contributes the highest proportion of the greenhouse effect mainly due to its higher concentration in the atmosphere. The upper safe limit of CO<sub>2</sub> concentration is suggested to be 350 ppm (parts per million) so as not to harm the environment and CO<sub>2</sub> level exceeding 450 ppm is expected to cause severe damage to the environment [4]. In October 2015, the global CO<sub>2</sub> concentration reached almost 400ppm and its current growth rate is more than 2 ppm/year [5]. According to the Intergovernmental Panel on Climate Change report 2011, this continued emission from fossil fuels will result in an increase in the environmental temperature from 1.4°C to 5.8°C from 1990 to 2100 [6]. Rapid depletion of fossil fuel reserve, awareness on carbon footprint and effect of global warming have thus forced a policy of accelerated utilization of renewable energy sources for electricity production [7].

Photovoltaics is one of the fastest growing technologies in the world with a growth rate of 35–40% per year [8]. Solar power is at the forefront of clean, renewable energy, and is gaining momentum due to advances in solar panel manufacturing and module efficiency, and the commensurate reduction in \$/W cost, as well as increasingly volatile fossil fuel costs. Solar power is an attractive

option because of the large energy resource available in incident sunlight, particularly in large industrial parks, in urban and suburban homes, for grid connected or stand-alone applications. Solar energy system can be particularly valuable at remote locations where utility power is unavailable, as well as on space satellites.

New solar capacity installed worldwide by the end of 2014 was 40 GW, compared to 38.4 GW in 2013 and 30 GW in 2012 [9]. World cumulative solar plants installed capacity in 2012 was reached the mark of 100 GW and by the end of 2014 had been installed globally 178 GW. Europe remains the world’s leading region in terms of PV cumulative installed capacity, with 89 GW as of 2014.

China became the top PV market in the world in 2013 and achieved the world’s largest PV installation figure in one year with 11.8 GW [10]. China is currently the fastest growing market, installing 10.6 GW in 2014, followed by Japan with 9.7 GW and the US with just over 6.5 GW [9] (figure 1.1). The Chinese government decided to raise the official PV installation target to 17.8 GW in 2015 [9]. These additions will allow the country to retain its world-leading status for annual solar PV additions.

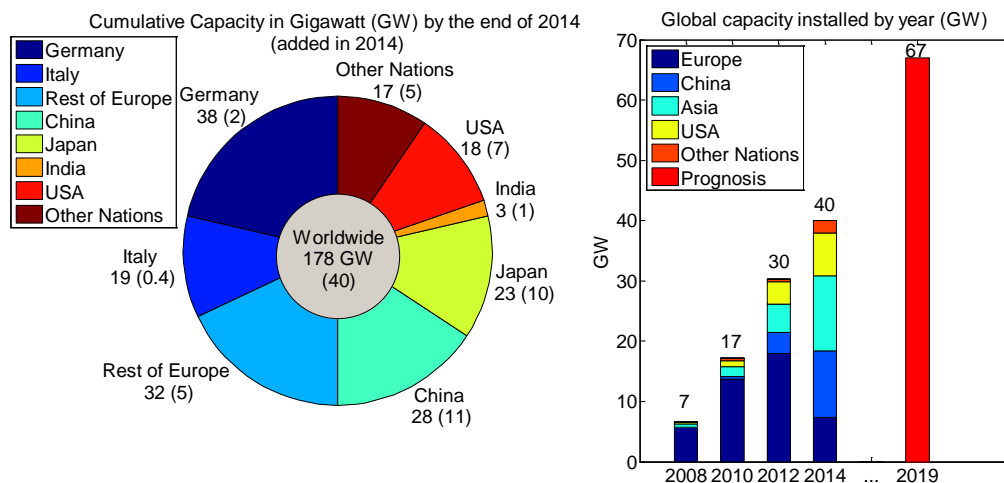


Figure 1.1. Global solar photovoltaic cumulative installed capacity at the end of 2014 and annual installed capacity since 2008. Adapted from [9].

The PV system usually consists of a set of PV modules, electronics to control the output, mounting structures, electrical cables, and commonly, an inverter to convert the direct current (DC) generated by the panels into alternating current (AC). The modules are made from a semiconductor, most often silicon, and the

remaining components are grouped as the ‘Balance of Systems’ (*BoS*). In a system which is not connected to the grid, batteries are also needed but the AC/DC converter may not be [11].

The trend in PV module prices mainly reflect c-Si module prices and have fallen with the growth of installed capacity through economies of scale in manufacture, reduced silicon usage, and innovations in device design and processing. As a result, the price has fallen with a ‘learning ratio’ of around 20%, [12] that is, prices have fallen by 20% for every doubling of capacity. Silicon module prices have descended from around  $\$6/W_p$  in 1989 to below  $\$1/W_p$  [11] (figure 1.2). In the mid-2000, the silicon demand for PV module manufacture outstripped that for microelectronic components and caused a temporary shortage in silicon feedstock [11] (as reflected in module prices in figure 1.2).

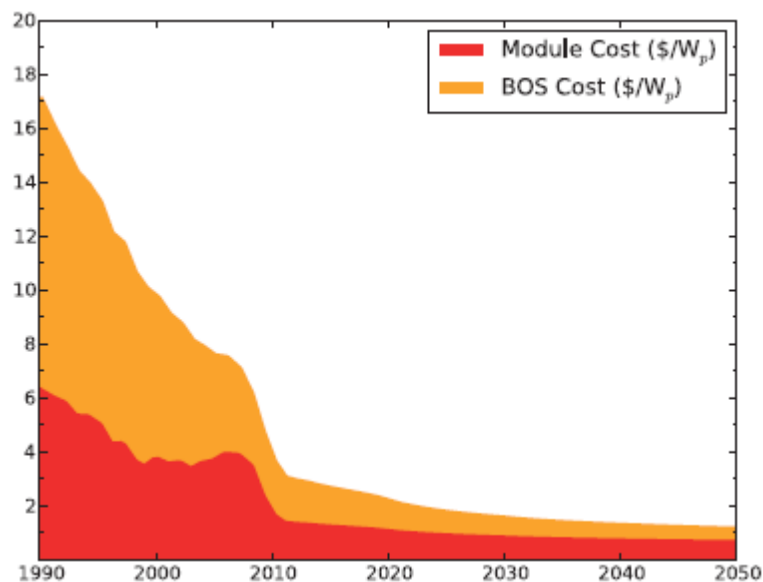


Figure 1.2. Reduction in total PV system costs. Data pre-2012 is historical; post-2012 are projected from industry estimates. [13, 14]. Reproduced from [11].

Solar energy is an attractive energy source for powering portable electronic devices. For some time, it has been widely used in applications like calculators. In recent years, a number of portable electronic devices like cell phones, laptops, PDA, mp3 and mp4 players, digital camera, have come to our lives. It would be very beneficial if a circuit “could scavenge” energy from a solar cell and power modern portable electronic devices providing continuous operation and maximum end-user flexibility when mains electric power supply is not available.

Mobile communication is one of the most rapidly expanding technologies and has influenced every facet of human life since its inception. Thanks to the economic viability and decreasing prices of micro-electronic components, more people are able to own a mobile devices than ever before. When it comes to electricity consumption, we have reached a stage where portable electronic devices can no longer be ignored anymore because of their sheer volume.

At the end of 2010, an important milestone was achieved with over 5 billion mobile cellular subscriptions worldwide [15], 460 million laptops [15] and 19 million tablets [16]. The latest figures suggest that at the end of 2015, 7.2 billion mobile phones are in circulation, 1.4 billion laptops and 1 billion tablets [17, 18]. Ericsson forecast indicates that by 2020 there will be 9.2 billion mobile phone devices [17], 2.3 billion laptops and 2.6 billion tablets [18]. Annual electricity consumption for a mobile phone as cited by Nokia study is around 11 kWh per year [15]. The energy consumption of a single laptop for a year is 97.34 kWh [19]. Annual electricity consumption for a tablet as cited by Electric Power Research Institute is 11.9 kWh [20]. Hence, at the end of 2015 overall consumption in the world due to usage of all the above portable devices is 227 TWh as illustrated in figure 1.3.

According to the latest information provided at the end of 2015 by the Central Intelligence Agency (CIA) World Factbook, the amount of electricity consumed world-wide in 2012 was 19.71 PWh [21]. Hence, electricity consumed by the above portable devices is about 1.15% of the global electricity consumption.

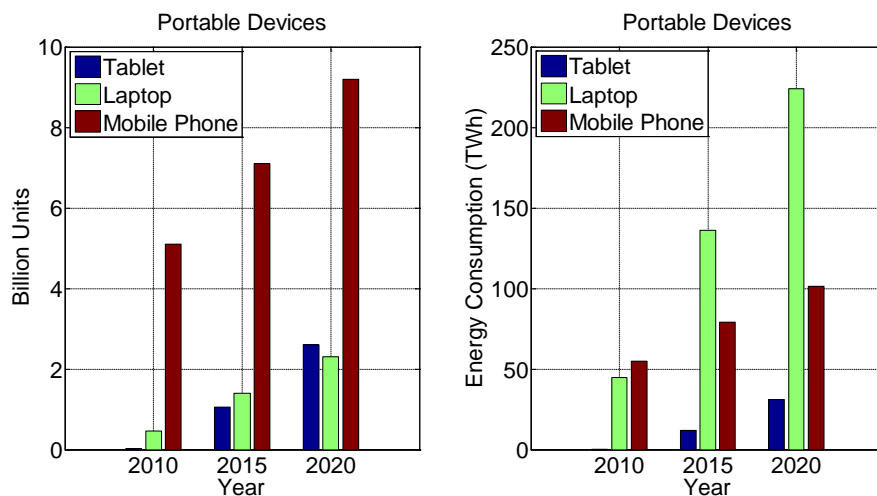


Figure 1.3. Usage and energy consumed by portable devices.



A solar panel is heavily dependent on operating environment conditions that change during the day, therefore batteries are typically used as an energy storage element. They can be charged when extra power is available from the solar panel, as well as to power the system when the available power from the solar panel is insufficient.

Despite of the advantages, the main restriction for solar PV uptake is the relatively high investment required. In order to amortize the investment, in most applications, it is desirable to get as much power as possible out of the solar module. Since, output power is the product of output voltage ( $V$ ) and current ( $I$ ), it is therefore necessary to determine which point of the cell's operating characteristic yields the maximum value of  $VI$ . This is known as the maximum power point (MPP). It can easily be proved (or experimentally observed) that in any application, the MPP occurs somewhere on the knee of the solar cell's output characteristic. Maximum power point trackers (MPPT's) find and maintain operation at the maximum power point for a given set of conditions, using an MPPT algorithm, in order to maximize module or array efficiency.

Experimental data was recorded by Hussein et al [22] for different atmospheric conditions. The experimental setup consists of an array made of six 70 W PV modules arranged in a 3 (series) x 2 (parallel) configuration. Figure 1.4 presents the effect of changing atmospheric conditions solar radiation (i) and array temperature (ii), the theoretical maximum array power (iii) and the significant power loss (iv) when the load is directly connected to the PV array, giving an efficiency of 31.3%.

When the PV array is connected directly to the load without any MPPT algorithm a significant power loss is noticeable. The efficiency  $n$  was calculated using equation (1.1).

$$n = \frac{\int_{t_1}^{t_2} P dt}{\int_{t_1}^{t_2} P_{\max} dt} \quad (1.1)$$

where  $t_1$  and  $t_2$  are the start-up (sunrise) and shut-down (sunset) times of the system, respectively,  $P$  is the array output power, and  $P_{\max}$  is the theoretical maximum array power.

The efficiency of 31.3% refers to average daily efficiency when the load is directly connected to the array. The poor PV utilization in the case of direct load connection is due to mismatch between load and optimum load which can be greatly improved by using a MPPT algorithm. The system can be almost three times more effective with a MPPT algorithm. That means less time is required for the same size of photovoltaic module to charge a given battery.

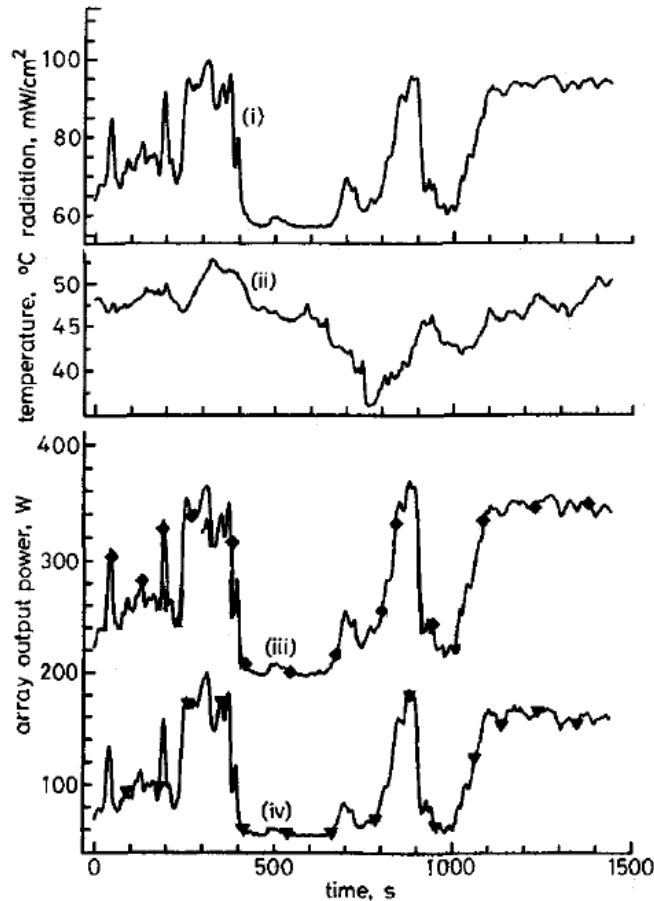


Figure 1.4. i) Solar radiation, ii) Array temperature, iii) Theoretical maximum power and iv) Experimental performance with direct load connection. Adapted from [22].

The problem in practice is that the exact location of the MPP varies with incident light and ambient temperature. Systems designed to maximize solar power generation must therefore dynamically scale the current drawn from the solar cell so that it operates at or near the MPP under the actual operating conditions. There are various ways to implement a MPP tracker but these can often become quite complex and expensive devices particularly since the use of integrated circuits (IC) or microprocessors is often required. Many complex algorithms have been proposed and implemented for microprocessor controlled schemes, each algorithm

has strengths and weaknesses and represents a compromise between efficiency, speed and cost.

In many applications, a simple, low-cost solution able to harness 90% to 95% of the available energy is all that is required. The digitally controlled MPPT systems have the advantage that a power point tracking algorithm will always be very reliable.

## 1.2 Aims of this Work

At the outset of this work the principle aim was to explore and develop understanding of small photovoltaic systems suitable for charging mobile devices. This would include study and potential development of small scale controllers and maximum power point trackers and algorithms.

While understanding that the primary efficiency limit to the efficiency of mobile charging systems is the placement of the photovoltaic array with respect to a light source, the object of this work was to develop understanding of the most efficient systems.

Many types of PV cell technologies exist and thus different diode characteristics. This work is focused on silicon solar cells and their characteristics, since they are currently 95% of solar cell market [23].

In this context this project has set-out to achieve the following objectives:

- Develop a practical laboratory method for testing and evaluation PV cells with a flexible programmable source with characteristics matching an arbitrary PV cell at any practical chosen illumination and temperature condition. The new type of solar emulator should be able to realistically mimic outdoor conditions.
- The emulator system should be constructed from simple electronic components while its operation should be based on a programmable microcontroller. Study available MPPT algorithms in the literature to identify alternative approaches, so that the maximum power point can be maintained with a high degree of reliability and small deviation error.
- Build a MPPT platform that would allow MPPT algorithms to be tested and systematically compared for a variety cell technologies.

- Implement the proposed MPPT algorithm on a boost DC/DC converter using a dedicated microcontroller. Compare its efficiency on tracking maximum power point with existing algorithms.

At the end of this project the aim was to have developed a prototype system that can accurately emulate solar cell behavior along with the development of a MPPT platform able to operate with different MPPT algorithms. These should be helpful tools for any laboratory involved in photovoltaics and can assist in a variety of photovoltaic applications.

### 1.3 Structure of Report

In Chapter 2 a review of the literature and background theory is presented. It is divided into four main parts. The first part concentrates on solar cell fundamental theory, equivalent circuits and software for modeling a solar cell and characteristic curves. The rest of the chapter describes DC to DC converters, operation and circuit models, maximum power point tracking (MPPT) methodologies and techniques. Finally, solar emulator systems are reviewed.

Chapter 3 describes the development of a mathematical derivation of maximum power point. Four different photovoltaic modules were examined to validate the accuracy of the model.

In Chapter 4 two artificial solar cell topologies are proposed to mimic solar cell behavior. Two novel equivalent circuits are analytically described and experimental evaluation is performed.

A system that allows emulation of a solar cell under different conditions in a controllable environment is designed and analysed in Chapter 5. The Chapter describes how the hardware is implemented in stages, from first synthesis to the final experimental study.

Chapter 6 describes an implementation that ensures optimum operation at the MPP by employing the proposed algorithm. The validation has performed on a DC to DC boost converter. The experimental results also confirmed good tracking efficiency and the ability to follow rapid parameter changes based on the parameters used.

Finally, conclusions are drawn and areas for further work are highlighted in Chapter 7.



## 2 Literature Review

### 2.1 Device Physics

The direct conversion of solar radiation into electricity is often described as *photovoltaic* (PV) energy conversion because it is based on the *photovoltaic effect* discovered by Becquerel in 1839 [24]. In general, the photovoltaic effect is the generation of a potential difference at the junction of two different materials in response to visible or other radiation. The field of solar energy conversion often denoted as “*photovoltaics*”.

The fundamental process behind the photovoltaic effect, is the generation of electron-hole pairs due to absorption of visible or other electromagnetic radiation by a semiconductor material. Electromagnetic radiation can be described in terms of waves, which are characterized by wavelength ( $\lambda$ ) and frequency ( $\nu$ ), or in terms of discrete particles, *photons*, which are characterized by energy ( $h\nu$ ) expressed in electron volts [25]. The following formulas show the relations between these quantities:

$$\nu = \frac{c}{\lambda} \quad (2.1)$$

$$E_{\text{photon}} = h \cdot \nu = \frac{hc}{\lambda} \quad (2.2)$$

In Equations 2.1 and 2.2,  $c$  is the speed of light in vacuum ( $2.998 \times 10^8$  m/s) and  $h$  is Planck’s constant ( $6.625 \times 10^{-34}$  Js). Equation (2.2) is known as the Planck-Einstein relation [25]. The higher the photon frequency, the higher its energy. Equally, the longer the photon's wavelength, the lower its energy [26].

Within a crystalline material an electronic band-structure is formed consisting of allowed energy bands and forbidden energy gaps, electrons can not exist within the *forbidden energy gaps*. Two very important energy bands emerge. The highest energy band filled with electrons is called the *Valence Band*, and the lowest unfilled energy band is the *Conduction Band*. The band gap is the energy difference between the highest energy level in the valence band and the lowest energy level in the conduction band. [27]

Electrons are forbidden from having energy outside these bands. An electron can only move ('be promoted') from the valence band to the conduction band if it gains energy greater than band gap energy [27]. This can happen if, for example, the electron were to absorb a photon of sufficiently high energy.

Once the electron (negative charge) is excited into the conduction band, it is free to move about the semiconductor and participate in conduction. However, the excitation of an electron to the conduction band will also allow an additional conduction process to take place. The excitation of an electron to the conduction band leaves behind an empty space for an electron. Consequently, the excitation of an electron into the conduction band results in not only an electron in the conduction band but also a *hole* (positive charge) in the valence band. Thus, both the electron and hole can participate in conduction and are called "carriers". [27]

The opposite to the generation of an electron hole pair is when an electron falls back from the conduction band to the valence band, it will recombine with a hole and thereby emit energy. This process is known as the *recombination* of an electron-hole pair [28].

Most electronic devices require techniques that control the densities of electrons and holes in regions of semiconductor, to achieve this in silicon low concentrations of *extrinsic* atoms are added. *Doping* is the intentional introduction of extrinsic atoms, in order to provide a surplus of either positive charge carriers (*p*-type conducting semiconductor layer) or negative charge carriers (*n*-type conducting semiconductor layer) in the semiconductor material [29].

In the simplest forms of doping suitable for silicon, the *dopant* will have either: three or five valence electrons, one less or one more than silicon's four valence electrons. In the case of silicon boron and phosphorous are commonly used as *p*-type and *n*-type dopants, respectively. Boron atoms become electron *acceptors* and phosphorous atoms become electron *donors*. [29]

The holes in *p*-doped silicon and the electrons in *n*-doped silicon are the *majority carriers*, because they are the most prevalent carriers in their respective silicon. However, according to the Law of Mass Action there will always be a small concentration of free electrons in *p*-doped silicon or free holes in *n*-doped silicon, these are called *minority carriers* [27].



$$n \cdot p = n_i^2 \quad (2.3)$$

Where,  $n$  is the free electron concentration ( $\text{cm}^{-3}$ ),  $p$  is the free hole concentration ( $\text{cm}^{-3}$ ) and  $n_i$  is the intrinsic carrier concentration ( $\text{cm}^{-3}$ ).

Typically  $n_i$  for silicon at room temperature will be of the order of  $10^{10} \text{ cm}^{-3}$  and since doping concentrations is in the range  $10^{16} \text{ cm}^{-3}$  to  $10^{20} \text{ cm}^{-3}$  can be readily accommodated, the ratio of majority to minority carrier concentrations in a doped region of silicon can be readily made as high as  $10^{20} \text{ cm}^{-3}$  [30]. As a consequence of this it is possible to precisely engineer the transport properties of silicon and, as we shall see, the properties of junctions formed between  $n$  and  $p$  type silicon.

To a first approximation doping levels can provide a good estimate of majority carrier concentrations and (if the intrinsic carrier concentration is known) the Law of Mass Action can provide the minority carrier concentration. However, it is important to be able to relate both minority and majority carrier concentrations to temperature and energy differences, this can be achieved by understanding the energy distribution of electrons as a function of temperature and in consideration of the density of available states in the semiconductor. Integration of the Fermi-Dirac distribution and Density-of-States functions provides two useful equations that links carrier concentrations to energy levels and temperature. [29, 31]

$$n = n_i \exp\left(\frac{E_f - E_i}{kT}\right) \quad (2.4)$$

$$p = n_i \exp\left(\frac{E_i - E_f}{kT}\right) \quad (2.5)$$

Where  $E_f$  is the Fermi Energy and  $E_i$  is the intrinsic energy.

Analytically, the probability that a level with energy  $E$  will be filled by an electron is given by a function called Fermi-Dirac distribution:

$$P(E) = \frac{1}{1 + \exp\left(\frac{E - E_f}{kT}\right)} \quad (2.6)$$

Where  $k$  is the Boltzmann's constant ( $1.3806 \times 10^{-23} \text{ JK}^{-1}$ ) and  $T$  is the temperature in degrees Kelvin.  $E_f$  is called the Fermi energy or Fermi level. It is determined as

the energy point where the probability of occupancy by an electron is exactly 50%.

In an intrinsic semiconductor the intrinsic energy ( $E_i$ ) is the same as the Fermi energy and is found mid-way between the conduction and valence bands (plus a small correction that depends linearly on the temperature). [29, 31]

For an  $n$ -type semiconductor, there are more electrons in the conduction band than there are holes in the valence band. This also implies that the probability of finding an electron near the conduction band edge is larger than the probability of finding a hole at the valence band edge. Therefore, the Fermi level is closer to the conduction band in an  $n$ -type semiconductor. [29, 31]

For a  $p$ -type semiconductor, there are more holes in the valence band than there are electrons in the conduction band. This also implies that the probability of finding an electron near the conduction band edge is smaller than the probability of finding a hole at the valence band edge. Therefore, the Fermi level is closer to the valence band in an  $p$ -type semiconductor. [29, 31]

A  $p$ - $n$  junction is formed when  $n$  and  $p$ -type semiconductors are in intimate contact. At this junction, an internal electric field is formed. In a solar cell, the field can be used to separate photogenerated charge carriers and provide a mechanism for generating useful electricity.

## 2.2 $P$ - $N$ Junction

A  $pn$ -junction is a complex system in equilibrium, in order to understand this equilibrium it is helpful to picture the formation of a junction as  $n$  and  $p$ -type layers being brought together in a conceptual experiment that in reality can not be performed. When the  $n$  and  $p$ -type regions are initially joined together there is a significant concentration gradient of both electrons and holes across the junction, as a result of this gradient, electrons will flow from the  $n$ -type semiconductor into the  $p$ -type semiconductor, and holes will flow from the  $p$ -type semiconductor into the  $n$ -type semiconductor. [32]

As the electrons *diffuse* from  $n$  to  $p$  and holes *diffuse* from  $p$  to  $n$ , they leave behind volumes of fixed charge (ionised impurities) forming *depletion regions* adjacent to the junction. These regions of fixed charge produce a built-in electric

field that changes the energy alignment between the  $n$  and  $p$  region, creating a *built-in potential*. [32]

The potential gradients then drive drift currents that cause electrons to *drift* from  $p$  to  $n$  and holes to *drift* from  $n$  to  $p$ , eventually the diffusion and drift currents cancel each other out and an equilibrium is reached. [32]

When all the currents cancel out the *chemical potentials* of the two semiconductors come to an equilibrium, and the band structure of the  $pn$ -junction is formed with a depletion region at the interface between the two types of doped semiconductor. [32]

If the  $n$ -type region is now connected to the positive terminal of a d.c. source and the  $p$ -type to the negative side a new equilibrium will be found in which the widths of the depletion regions are increased, the electric field at the junction is increased and the potential drop across the junction is increased [33, 31]. In this situation of reverse bias, the diffusion of minority carriers is reduced as the concentration gradient is reduced. At the same time, although the potential difference that drives the drift currents is increased, the actual drift currents will remain constant because they are determined by the availability of minority carriers on both sides of the junction [30].

When the  $n$ -type region is connected to the negative terminal of a d.c. source and the  $p$ -type to the positive terminal, the depletion layer becomes narrower and the potential barriers are decreased [33]. In this forward bias condition, the concentration gradients for the majority carriers are increased and there will be a large net flow of electrons from the  $n$ -type semiconductor into the  $p$ -type semiconductor, a large net flow of holes in the opposite direction [30]. The current – voltage characteristic of the  $p$ - $n$  junction is shown in Figure 2.1.

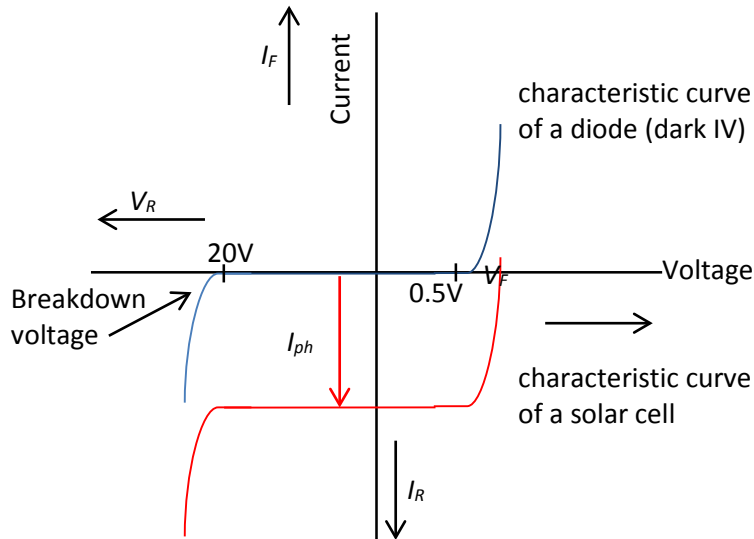


Figure 2.1. Graph showing I-V characteristics of a diode and a solar cell under illumination. Adapted from [31].

If light with photon energy greater than the semiconductor bandgap is incident on a  $pn$ -junction the process of absorption occurs, and electron-hole pair (EHP) generation will increase the number of free carriers on either side of the junction, this will in turn increase the electron and hole drift currents across the junction. The effect is to lower the IV characteristic by what is known as the *photogenerated current* ( $I_{ph}$ ) [33]. Under the right circumstances this photogenerated current creates a region in the fourth quadrant of the IV characteristic where a positive voltage is accompanied by a negative current. In this region an external circuit can gain useful power from the  $pn$ -junction [30].

Current  $I_D$  is voltage dependent in accordance with the diode equation:

$$I_D = I_o \left( \exp\left(\frac{qV}{nkT}\right) - 1 \right) \quad (2.7)$$

Where,  $I_o$  is the reverse saturation current,  $q$  is the electron charge ( $1.6 \times 10^{-19}$  C),  $k$  is the Boltzman constant,  $T$  is the Cell temperature in Kelvin and  $n$  is the diode ideality factor (ideal  $n=1$ ; real  $n>1$ ).

Physically, the reverse saturation current is a measure of the "leakage" of carriers across the  $p$ - $n$  junction in reverse bias. The reverse saturation current is given by [34]:

$$I_o = \frac{qD_n n_i^2}{L_n N_A} + \frac{qD_p n_i^2}{L_p N_D} \quad (2.8)$$

Where,  $L_n$  and  $L_p$  are minority carrier diffusion lengths,  $D_n$  and  $D_p$  are the diffusion coefficients of holes and electrons respectively, and  $N_D$  and  $N_A$  are the donor and acceptor concentrations at the  $n$  side and  $p$  side respectively.

### 2.3 Solar Cell Characteristics

The output characteristics of a solar cell are described by the current – voltage (I – V) curve. The test circuit used in order to produce the output characteristics is shown in Figure 2.2. The IV curve is produced by varying  $R_L$  (load resistance) from a small to a large value and measuring the current and voltage. Typical current-voltage (I-V) and power-voltage (P-V) characteristics of a photovoltaic device are shown in Figure 2.3.

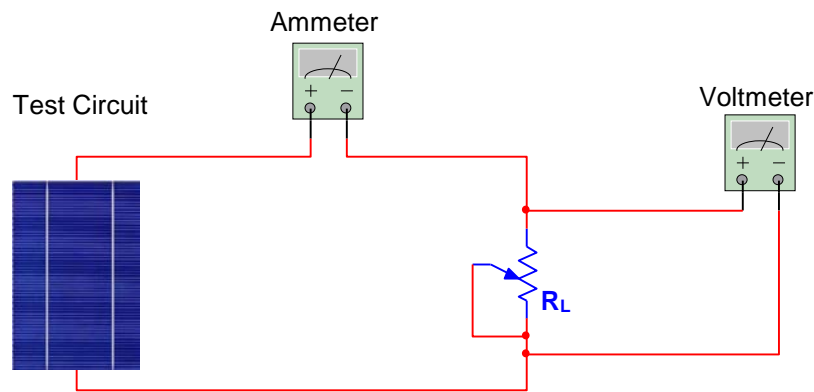


Figure 2.2. Test circuit to produce the output characteristics.

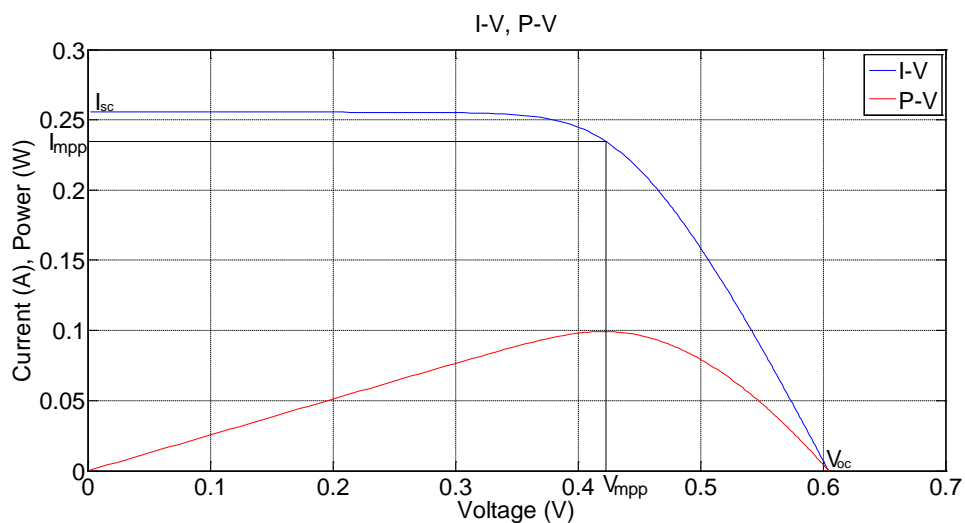


Figure 2.3. Typical silicon solar cell characteristics (I-V, P-V).

The maximum power rectangle is defined by the voltage and current values ( $V_{mpp}$  and  $I_{mpp}$ ) at the maximum power point, which is reached by optimizing the resistance of the load to draw the maximum power from the circuit. The ratio of the area of the maximum power rectangle to the area of the  $V_{oc}I_{sc}$  rectangle is termed the *fill factor* ( $ff$ ) and the closer this value is to unity, the better the quality of the solar cell [35].

$$ff = \frac{V_{mpp} I_{mpp}}{V_{oc} I_{sc}} \quad (2.9)$$

The energy conversion *efficiency*,  $\eta$ , is the ratio of the maximum electrical power obtained from the cell,  $P_p$ , to the incident light power,  $P_i$  i.e.:

$$\eta = \frac{P_p}{P_i} = \frac{V_{mpp} I_{mpp}}{P_i} = \frac{ff \cdot I_{sc} \cdot V_{oc}}{P_i} \quad (2.10)$$

The power of the incident light can be defined for any particular application but is most commonly determined by well defined and widely accepted international solar radiation standards.

Solar radiation covers a wide range of the electromagnetic spectrum; the most useful part of the spectrum in the range 200nm (ultraviolet) to 2500nm wavelengths (infrared) is similar to that of a black body at 6000K. It is no coincidence that irradiance is highest in the visible wavelengths 400nm to 700nm, life on Earth has adapted to make use of the most irradiant part of the spectrum. Absorption processes inside the Sun are responsible for the differences between black body and actual emission spectra as observed from space, the spectrum when light has travelled through no *air mass* (outside the earth's atmosphere) is known as *AM0* [36].

Solar radiation is attenuated, when it passes through the earth's atmosphere. Some light is absorbed or scattered by the different atmospheric layers and there are significant absorption lines due to water and carbon dioxide in the atmosphere. The greater the distance that sunlight has to travel through the atmosphere the greater the absorption. The path for sunlight travelling through the atmosphere is shortest at the equator and when the sun is at the zenith at this point the optical air mass is unity and the radiation is described as *air mass one (AMI)* radiation. When the sun is at an angle  $\theta$  to the zenith, the air mass is given by [36]:

$$\text{Air mass} = (\cos \theta)^{-1} \quad (2.11)$$

*AM1.5* radiation serves at present as the most widely used standard spectral distribution. It corresponds to an angle of 48.2 degrees between the sun's position and the zenith. The value of  $1000 \text{ W/m}^2$  was arbitrarily incorporated to become the standard power density for *AM1.5*. The peak power of a photovoltaic system is the power generated under this standard *AM1.5* ( $1000 \text{ W/m}^2$ ) radiation and is expressed in peak watts. [36]

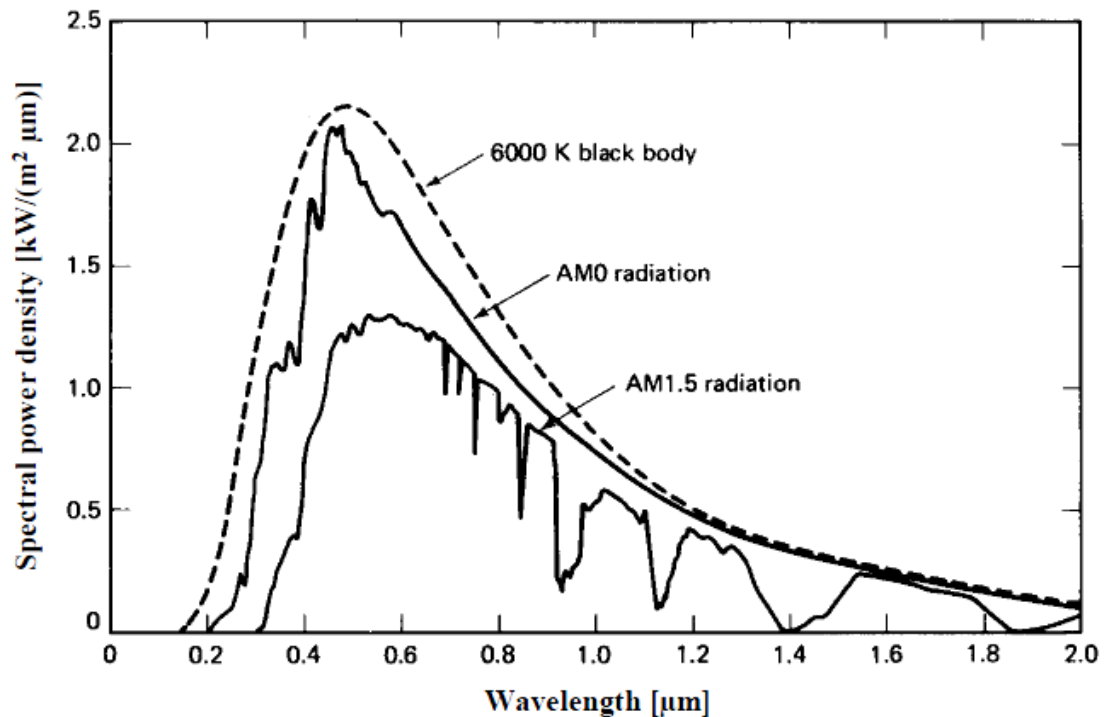


Figure 2.4. Spectral power density of sunlight. The different spectra refer to the black body radiation at 6000K, the extraterrestrial AM0 and the AM1.5 radiation.

Reproduced from [36].

## 2.4 Fundamentals of Silicon Solar Cell Design

A schematic diagram of a silicon wafer solar cell is provided in Figure 2.5. The device is divided into three *active* regions, the *n*-type emitter, the depletion region and *p*-type base. The passive components of the device include front and rear metallic contacts that provide access to an external circuit and passivation and antireflection layers. In the case of the *n*-region, which is facing the solar irradiance, the contact design must be optimized to find the best compromise

between contact resistance and shadowing by the metal; typically thin silver fingers and bus bars are used. [28]

Light is incident on the front surface of the device where it must pass through the metal contacting and any antireflection layers or textures. Ideally all photons are absorbed within the *active* thickness of the device, where they can generate electron-hole pairs. If the EHP is generated in the emitter the hole is an additional minority carrier in the *n*-type region that can, on average, diffuse a finite diffusion length ( $L_p$ ) before being swept away by the electric field in the depletion region, and increasing the hole drift current in the device. A photon absorbed in the depletion region will generate EHPs within the electric field and both electron and hole will contribute to increased drift currents. If the EHP is generated in the *p*-type base then the electron will, on average, diffuse a finite diffusion length ( $L_n$ ) before being swept away by the electric field in the depletion region. In every case the excess electron and hole concentrations cancel out (at the emitter contact) only after the electrons have travelled through an external circuit.

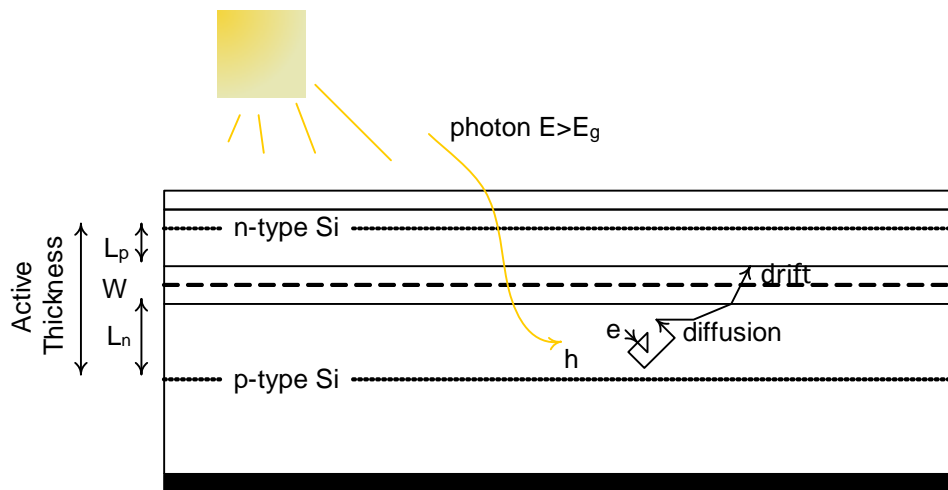


Figure 2.5. Cross section of *p-n* junction cell. Adapted from [30].

## 2.5 Efficiency Limits

Originally, Schokley and Queissar (SQ) [37] established the limit for photovoltaic conversion efficiency to be 30%, for a device illuminated by black body radiation at 6000K. The maximum theoretical efficiency that could be obtained from a single-junction silicon solar cell is 33.3% using the AM. 1.5 solar spectrum [26]. So, no matter how good a technology and design 66.7% of energy incident on a silicon solar cell will be unavoidably lost. In simple terms, most energy is lost



because of the wide spectral and angular distribution of light incident on the surface of a solar cell. Photons with energy much greater than the bandgap energy of silicon will create an electron hole pair but it will provide much more energy than is required by the electron. The electron will be excited into high-energy states and lose energy as heat before settling into the conduction band, this energy is not recovered by a conventional cell and are known as thermalisation losses. Photons with energy less than the bandgap can not generate an electron hole pair, so all photons with energy less than the bandgap are transmitted by the solar cell and also count as a loss [38]. If bandgap energy was a tunable quality then there would always be a trade-off between thermalisation and transmission losses, so materials with a relatively wide range of bandgaps (1eV through to 1.6eV) have reasonable SQ limits [32].

The very best silicon solar cells are in fact 7.7% below the SQ limit, (the current world record is 25.6% [39]), and typical commercial solar cells are typically 13% below the SQ limit. The differences between real device efficiencies and SQ efficiencies comprise a range of scientifically *avoidable losses*, that technology as yet has no way to avoid. A real device has to accommodate a range of material and process realities and design compromises.

Avoidable losses include, *optical losses* such as reflection, contact shadowing, transmission and absorption in passive layers or components. *Recombination losses* including bulk, front surface and rear surface. *Electrical losses* include series resistance (with several intrinsic and extrinsic components), shunt resistance and non-ideal fill-factor. [40]

The \$/W cost of a solar energy system is of paramount importance and dictates much about the uptake of the technology, for many years the growth of the industry has been driven by subsidy, however, over the last 3 to 5 years the \$/W has reduced to the point that the cost of solar energy is competitive with grid electricity costs faced by consumers. Over these years the cost of cell fabrication has declined, so that now the cell is only around 30% of the total cost. The remaining *balance of systems* costs is descending similarly as depicted in figure 1.2. In this dynamic, system efficiency and device efficiency become increasingly important as the efficient devices and systems produce more power and more readily reduce the \$/W.

## 2.6 Equivalent Circuits

An ideal solar cell can be represented by a current source connected in parallel with a rectifying diode [41], (Figure 2.6). The current source generates the photocurrent  $I_{ph}$ .

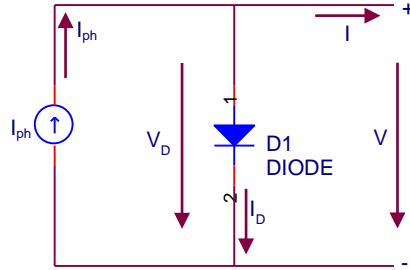


Figure 2.6. Equivalent circuit for an ‘ideal’ solar cell. Adapted from [41].

In the case of an ideal solar cell, where  $V$  is the output voltage:

$$V = V_D \quad (2.12)$$

Where the  $V_D$  is the voltage across the diode in the equivalent circuit.

The photocurrent ( $I_{ph}$ ) is proportional to the photogeneration rate ( $G$ )

$$I_{ph} = c_o G \quad (2.13)$$

Where  $c_o$  is a constant [42] and the photogeneration rate is the rate per unit volume ( $s^{-1}cm^{-3}$ ) at which light creates pairs of electron and holes [32].

The output current ( $I$ ) is simply:

$$I = I_{ph} - I_D \quad (2.14)$$

Considering the diode equation (2.7) it is:

$$I = I_{ph} - I_o \left( \exp\left(\frac{qV}{nkT}\right) - 1 \right) \quad (2.15)$$

The photogenerated current  $I_{ph}$  is related to the photon flux incident on the cell ( $\Phi$ ).

$$\Phi = \frac{\text{number of photons}}{\text{sec } m^2} \quad (2.16)$$

In practice a solar cell has parasitic series and shunt resistances. Figure 2.7 depicts a more realistic equivalent circuit known as the “single diode model” [43].

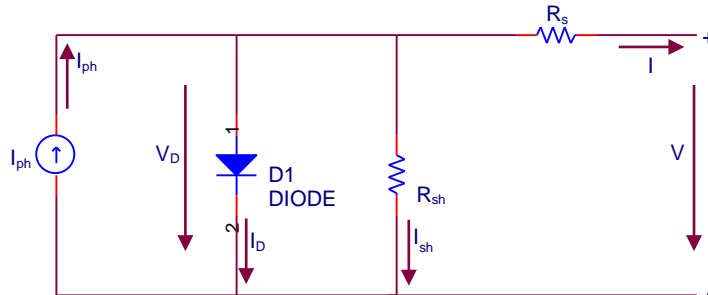


Figure 2.7. Single diode equivalent circuit model with parasitic resistances.

Adapted from [43].

The series resistance  $R_s$ , is usually just a few Ohms and represents a voltage loss. The shunt resistance, usually of the order of  $M\Omega$  represents current loss.

The shunt resistance,  $R_{sh}$ , is usually a result of leakage across the  $p$ - $n$  junction or around the edge of a cell [36]. The series resistance,  $R_s$ , is typically due to bulk resistances of the semiconductor and metallic contacts as well as the contact resistance [36].

In this non-ideal equivalent circuit the output current  $I$ , is given by:

$$I_{ph} - I_D - I_{sh} = I \quad (2.17)$$

and the output voltage is given by:

$$V = V_D - IR_s \quad (2.18)$$

and therefore,

$$V_D = V + IR_s \quad (2.19)$$

The characteristic equation of a solar cell, which relates solar cell parameters to the output current and voltage becomes:

$$I = I_{ph} - I_o \left( \exp \left( \frac{q(V + IR_s)}{nkT} \right) - 1 \right) - \frac{V + IR_s}{R_{sh}} \quad (2.20)$$

The current – voltage relationship at a fixed cell temperature and solar radiation can be expressed as:

$$I = I_{ph} - I_o \left( \exp \left( \frac{V + IR_s}{V_t} \right) - 1 \right) - \frac{V + IR_s}{R_{sh}} \quad (2.21)$$

where, the thermal voltage is:

$$V_t = nV_{th} = \frac{nKT}{q} \quad (2.22)$$

When the cell is operated at open circuit,  $I = 0$ , the voltage across the output terminals is the open-circuit voltage ( $V_{oc}$ ). Assuming the shunt resistance is high, the open-circuit voltage can be approximated [44]:

$$V_{oc} \approx \frac{kT}{q} \ln \left( \frac{I_{ph}}{I_o} + 1 \right) \quad (2.23)$$

Similarly, when the cell is operated at short circuit,  $V = 0$  and the current  $I$  is the short-circuit current. It can be shown that for a high-quality solar cell (with low  $R_s$  and  $I_o$ , and high  $R_{sh}$ ) the short-circuit current  $I_{sc}$  can be approximated [44]:

$$I_{sc} \approx I_{ph} \quad (2.24)$$

Actual measurements on real cells under diverse operating conditions, however, show the need for a more sophisticated model. This leads to the widely used “two-diode model” [45], as shown in Figure 2.8.

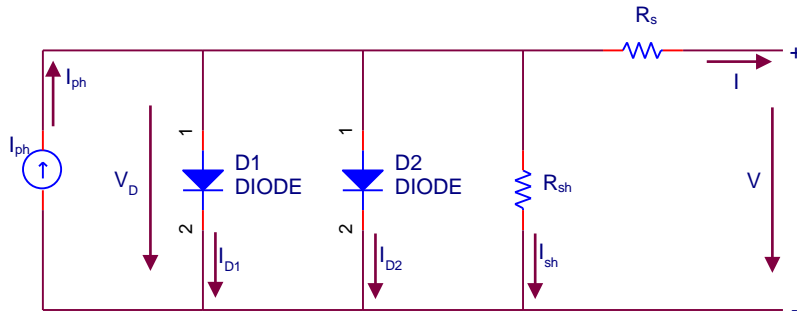


Figure 2.8. Two diode equivalent circuit model. Adapted from [45].

The second diode represents the *non-ideality* of solar cells brought about by carrier generation and carrier recombination in the depletion region.

The current is given by,

$$I = I_{ph} - I_{o1} \left( \exp \left( \frac{q(V + IR_s)}{n_1 kT} \right) - 1 \right) - I_{o2} \left( \exp \left( \frac{q(V + IR_s)}{n_2 kT} \right) - 1 \right) - \frac{V + IR_s}{R_{sh}} \quad (2.25)$$

where,  $I_{o1}$  and  $I_{o2}$  are the reverse saturation currents for the diodes, and  $n_1$  and  $n_2$  are the diode ideality factors.

### 2.6.1 Comparison of single diode model and two diode model of photovoltaic module.

In the single diode model there are five variables to be determined photocurrent ( $I_{ph}$ ), reverse saturation current ( $I_o$ ), diode ideality factor ( $n$ ), series resistance ( $R_s$ ) and shunt resistance ( $R_{sh}$ ).

In the two diode model, there are two reverse saturation currents ( $I_{o1}$  and  $I_{o2}$ ) and two ideality factors ( $n_1$  and  $n_2$ ), plus the other parameters that are the same as in the first model.

Thus, the first model has five parameters, while the second model has seven parameters to be computed. The increased number of unknown parameters implies an increased complexity in the computation. Most of the research is directed to the single diode model due to its simplicity and reduced number of unknown parameters, which makes it easier to analyse and extract the unknown parameters [46,47].

In this section a comparison of the two models is performed, in order to decide which model to select in our study. In this work a methodology has been used for the extraction of parameters of photovoltaic module applying the *Trust Region Method*. The *Trust Region Method* is an optimization method widely used in solving systems of nonlinear equations with a high rate of convergence. The procedure followed with the particular methodology in this work is described in Chapter 4. The method is analysed and validated in [48] providing statistical analysis of errors from the I-V curves obtained in a way to assess the feasibility of the method. The characteristic of the panel tested is stated in Table 2.1.

Table 2.1. Nominal characteristic of the panel. Adapted from [48].

Features	Value
Power	40 W
Voltage at MPP ( $V_{mpp}$ )	16.6 V
Current at MPP ( $I_{mpp}$ )	2.45 A
Open circuit voltage ( $V_{oc}$ )	20.5 V
Short circuit current ( $I_{sc}$ )	2.80 A
Type of material	Monocrystalline silicon
Numbers of cells connected in series	36

Tests were carried out in different cases using the two models. Table 2.2 shows data related to the cases studied.

Table 2.2. Input data. Adapted from [48].

Case	Light Intensity ( $\text{W/m}^2$ )	Temperature ( $^{\circ}\text{C}$ )
1	225.00	25
2	596.80	35
3	698.00	54
4	860.20	52

Validation has been performed comparing experimentally obtained curves from the particular panel against simulated data values established, such as to enable convergence for the applied optimization method. Extracted unknown parameters, five or seven in each case, are stated in [48].

In order to test the accuracy of the data, a statistical analysis was performed. Root mean square error has been computed for each case according to the equation (2.26).

$$RMSE = \sqrt{\frac{1}{N} \sum_{i=1}^N \left( \frac{V_{i(meas)}}{V_{i(calc)}} - 1 \right)^2} \quad (2.26)$$

where  $V_{i(meas)}$  is the measured voltage,  $V_{i(calc)}$  is the calculated voltage and  $N$  the number of variables.

For the single diode model the error obtained was less than 1% (Table 2.3), indicating a good approximation to the desired parameters.

Table 2.3. Error in approximated curves with single diode model. Adapted from [48].

Case	<i>RMSE</i> (%)
1	0.20
2	0.11
3	0.13
4	0.31

Table 2.4 presents the error calculated for the approximated curves using the two diode model.

Table 2.4. Error in approximated curves with double diode model. Adapted from [48].

Case	<i>RMSE</i> (%)
1	0.19
2	0.11
3	0.13
4	0.13

Errors obtained at the two diode model are very close to those calculated in the first case. However, for case 4 which shows the highest rate for the *RMSE*, the model with two diodes was more appropriate.

Concluding this section, it can be said that the two diode model represent more closely the observable effects on the device under consideration, in various lighting and temperature conditions. On the other hand, the single diode model has the same ability to extract the unknown parameters, describe accurately the I-V characteristic curves and in total results show a small discrepancy between the two models. The single diode model has less computation effort since less number of unknown parameters has to be computed. Thus, the main advantage is the simplified electric circuit and consequently the equation that describes the device

operation. For these reasons we decided to base our study in the single diode model.

## 2.7 Dependencies on insolation and temperature

As one might expect, the shape of the I-V curve, and hence the location of the maximum power point, changes greatly with temperature and insolation. These changes will have important consequences for the design and control of the power system.

The I-V characteristics of a photovoltaic cell strongly depend on insolation and temperature (equation 2.20). This becomes very apparent when evaluating equation (2.20) for selected values of temperature and irradiance and plotting the IV characteristics.

### 2.7.1 Insolation

Figure 2.9 shows how the output current  $I$  of an array is greatly influenced by the change in insolation  $S$ , whereas the output voltage  $V$  stays approximately constant.

The photocurrent generated by a photovoltaic device is proportional to the photon flux, so the short circuit current ( $I_{sc}$ ) increases as the isolation level increases [49]. The open circuit voltage ( $V_{oc}$ ) is less affected, as it only varies with the  $\ln$  of intensity (equation (2.23)).

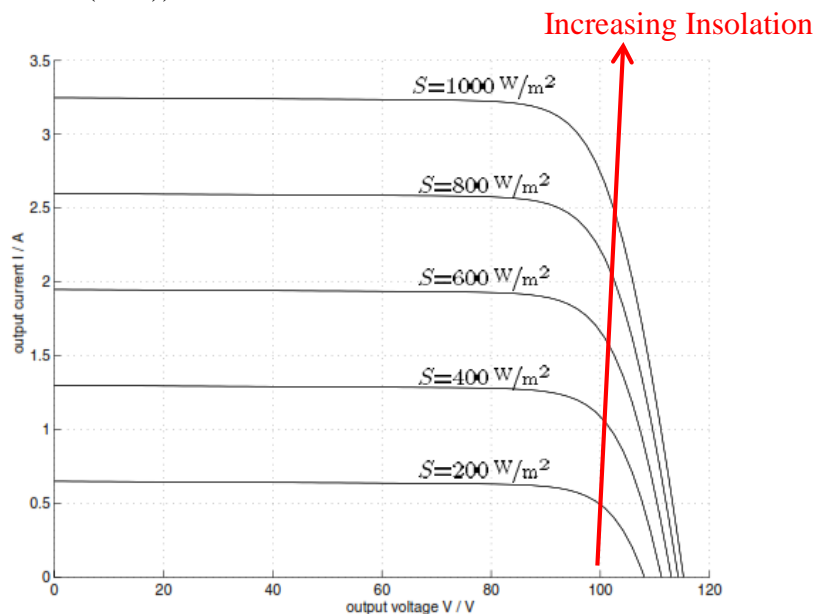


Figure 2.9. I-V characteristics of a photovoltaic cell array for a range of irradiance  $S$  at 25 °C. Adapted from [50].



The output power of a panel also increases with increasing insolation. In fact, both the current and power output of a solar panel are approximately proportional to illumination intensity (irradiance).

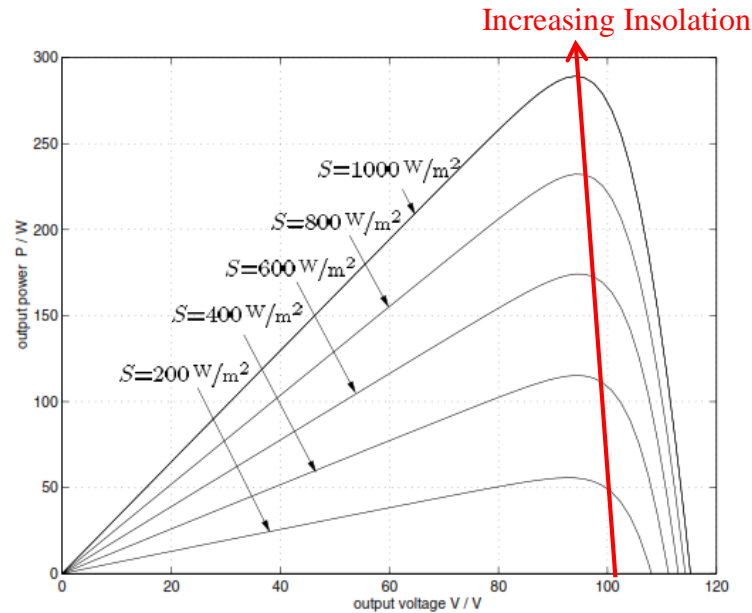


Figure 2.10. P-V characteristics of a photovoltaic module for a range of irradiance  $S$  at  $25^{\circ}\text{C}$ . Adapted from [50].

### 2.7.2 Temperature

Like all other semiconductor devices, solar cells are sensitive to temperature. Increases in temperature reduce the effective band gap of a semiconductor [51] and increases the electron energy, thereby effecting most of the semiconductor parameters relating to carrier concentrations and transport [32]. In a solar cell, the parameter most affected by an increase in temperature is the open-circuit voltage [36]. The open-circuit voltage decreases with temperature because of the temperature dependence of  $I_o$ .

Increasing temperature increases the intrinsic carrier concentration and this in turn increases the reverse saturation current  $I_o$  as a consequence of this (equation 2.23)  $V_{oc}$  will decrease. [32]

The dependence of short-circuit current with temperature can not be readily determined analytically, material properties such as carrier lifetime, the intrinsic carrier concentration and mobility are strong functions of temperature. Although intrinsic carrier concentration is likely to increase with temperature [51], lifetimes and diffusion lengths are likely to decrease.

In the case of silicon devices the short-circuit current,  $I_{sc}$ , is often observed to increase slightly with temperature [36].

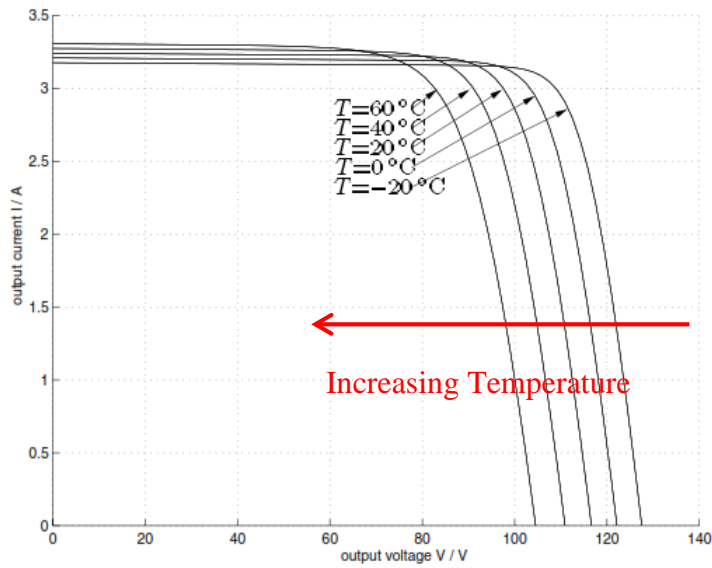


Figure 2.11. I-V characteristics of a photovoltaic array for a range of temperatures at an irradiance of  $1000 \text{ W/m}^2$ . Adapted from [50].

Output power is reduced by an increase in panel temperature. This can be explained by the significant temperature dependency of the open circuit voltage  $V_{oc}$  [52].

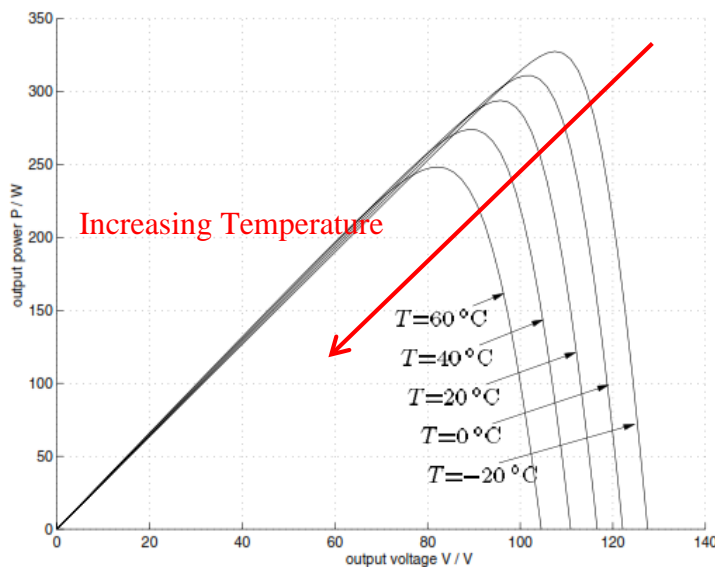


Figure 2.12. P-V characteristics of a photovoltaic cell array for various values of temperature  $T$  at an irradiance of  $1000 \text{ W/m}^2$ . Adapted from [50].

## 2.8 Software Simulator Program - PC1D

So far, solar cell operation has been described by analytical models and by equivalent circuit models. A range of experimental results have also been examined. The final approach to gaining detailed understanding of device operation is that of computer simulation. Computer simulations take complex physical models and detailed information regarding device structure, material parameters and operating conditions in order to provide accurate modeling of device behavior. In general these models can be used to help understand or predict experimental results or to help in the optimization of device designs.

A computer program that uses material parameters and detailed device designs to model the operation of devices. PC1D was developed by P. A. Basore and colleagues at the University of New South Wales [28], it is commonly used, available free of charge, and widely regarded as a valuable and reliable tool for solar cell modeling.

PC1D uses finite–element analysis to solve the fully coupled two carrier semiconductor transport equations in one dimension. The non–linear electron and hole transport equations are solved using Newton's method, which iteratively solves a sequence of linearized approximations of the equations. [53, 54]

PC1D is a quasi-one-dimensional model, so the device is spatially divided into a finite set of  $M$  elements along a solution dimension “ $x$ ”, which approximately follows the direction of current flow in the device and is not necessarily a straight line [53].

Variation of critical process parameters give the ability to investigate emitter doping, bulk doping, minority carrier lifetime, wafer thickness, and front and rear surface recombination. The program includes built-in models for calculating the photogeneration profile resulting from a textured front surface. Optimized process parameters are also provided as default values. PC1D has been used extensively in this work.

### **2.8.1 PC1D modelling**

The primary task when using PC1D is to describe and define the device, its material parameters and the operating conditions. This is achieved through a well constructed user interface that deals with suitable parameter sets for a range of different device designs and processes. The default values are listed in Table 2.5.

Excitation in PC1D includes several capabilities such as two independent illumination sources (front/rear) and common illumination standards can be selected, typically AM 1.5.

Changing excitation mode between steady state and transient, a single point or the full I-V characteristic curve can be obtained. Setting the final transient value different from the initial transient value causes the voltage to sweep linearly from the initial to the final value during the course of the transient solution [53]. The default number of points (time steps) along the I-V curve is 16, with maximum available 200 points. In order to describe the I-V curve with the best possible mean, the maximum available option was selected in order to have as many as possible data points along the I-V characteristic curve.

PC1D gives access to the voltage, current and power for the base contact. The values displayed are steady state values (for steady state excitation mode) or the final transient time step (for transient excitation).

Default PC1D parameters are summarized in Table 2.5.

Table 2.5. Simulation parameters for PC1D.

<b>Simulation Parameter</b>	<b>Value and unit</b>
Device area	100 cm <sup>2</sup>
Front surface texture depth	3μm
Exterior Front Reflectance	10%
Emitter contact	Enabled
Base contact	0.015 Ω
Internal conductor	0.3 S
Thickness	300 μm
Material	Silicon (Si)
Carrier mobilities	Internal model
Dielectric constant	11.9
Band gap	1.124 eV
Intrinsic conc. at 300 K	1E10 cm <sup>-3</sup>
Absorption coeff.	Silicon
Free carrier	Enabled
P type background doping	1.513E16 cm <sup>-3</sup>
1 <sup>st</sup> front diff. n-type	2.87E20 cm <sup>-3</sup>
Bulk recombination	7.208 μs
Front surface recombination	1E6 cm/s
Rear surface recombination	1E5 cm/s
Excitation mode	Transient, 16 time steps
Temperature	25 °C
Base circuit sweep	-0.8 to 0.8 V
Collector circuit	Zero
Primary light source	Enabled
Constant intensity	0.1 W/cm <sup>2</sup>
Spectrum	AM 1.5

## 2.9 DC to DC Converters

### 2.9.1 Buck, Boost, Buck-Boost converter

DC to DC converters are electronic devices used to change DC electrical power efficiently from one voltage level to another. DC to DC converters are used for power management in low-power applications for charging batteries, such as cellular phones, smart phones and other portable electronic products. They essentially change the input to a different impedance level, so whatever the output voltage level, the output power comes from the finite input. Of course, there is no energy manufactured inside the converter but some is inevitably used by the converter circuitry and components. The basic power flow in a converter can be represented with the following equation:

$$P_{in} = P_{out} + P_{losses} \quad (2.27)$$

where,  $P_{in}$  is the power fed into the converter,  $P_{out}$  is the output power and  $P_{losses}$  is the power wasted inside the converter.

Most modern converters achieve an efficiency of over 90%, using the latest components and circuit techniques [55], most others achieve at least 80-85% [56, 57]. There are many different types of DC-DC converter, each of which tends to be more suitable for some types of application than for others. Some converters are only suitable for stepping down the voltage, while others are only suitable for stepping it up; a third group can be used for either. The buck converter is used for voltage step-down/reduction, while the boost converter is used for voltage step-up. The buck-boost converters can be used for either step-down or step-up, but are essentially voltage polarity reversers or *inverters*. [57]

During the operation of the converter, the switch will be switched at a constant frequency ( $f_s$ ) with an on-time of  $DT_s$ , and an off-time of  $D'T_s = (1-D)T_s$ ,

where,  $T_s$  is the switching period  $\frac{1}{f_s}$  and  $D$  is the duty ratio of the switch ( $D \in$

$[0; 1]$ ) (see Figure 2.13).

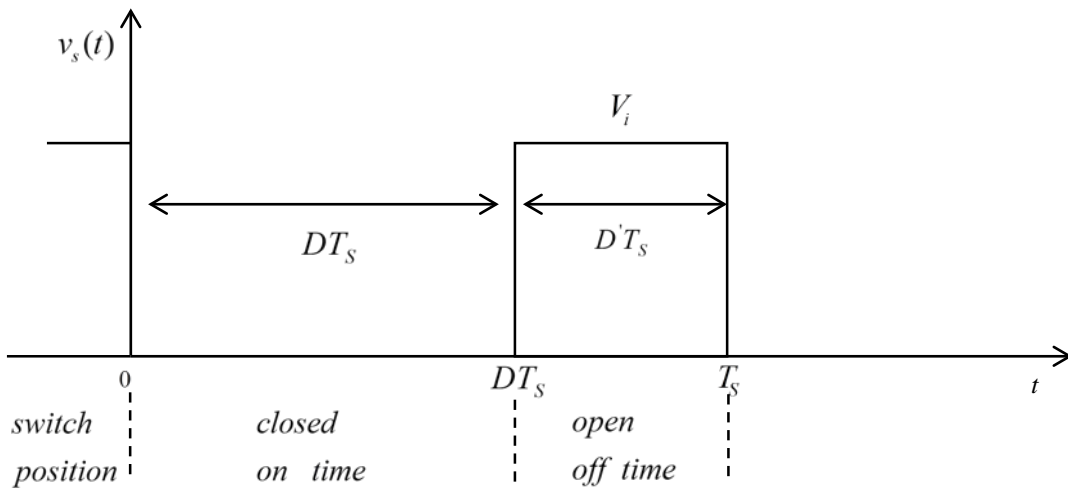


Figure 2.13. Ideal switch voltage  $v_s(t)$ , duty ratio  $D$ , and switching period  $T_s$ .

Adapted from [50].

## 2.9.2 Buck Converter

The buck switching converter is a well known step-down converter. It converts the input voltage into a lower output voltage of the same polarity with very little power loss. The basic circuit configuration used in the buck converter is shown in Figure 2.14. There are only five main components: switching power input capacitor  $C1$ , a switch (usually a MOSFET), a flywheel diode, an inductor  $L$  and output filter capacitor  $C2$ . A control circuit monitors the output voltage, and maintains it at the desired level by switching the switch on and off at a fixed rate (the converter's *operating frequency*), but with a varying duty cycle.

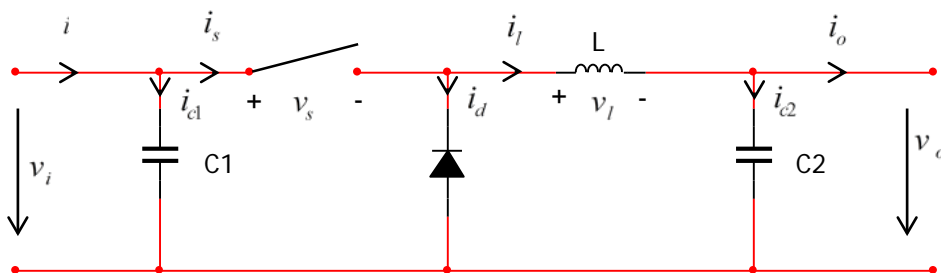


Figure 2.14. Ideal buck converter circuit. Adapted from [50].

### 2.9.2.1 The Equivalent Circuit Model

To further investigate the buck converter and to derive its mathematical model, the equivalent circuit representation for the two different switch states (open and closed switch) is analyzed [50]. Figure 2.15 shows the equivalent circuit diagram

of a buck converter with the switch closed. Figure 2.16 represents the buck converter with the switch open during the time interval  $D'T_S$ , where  $D'$  denotes the complement of the duty ratio  $D$ , defined as:

$$D' = 1 - D \quad (2.28)$$

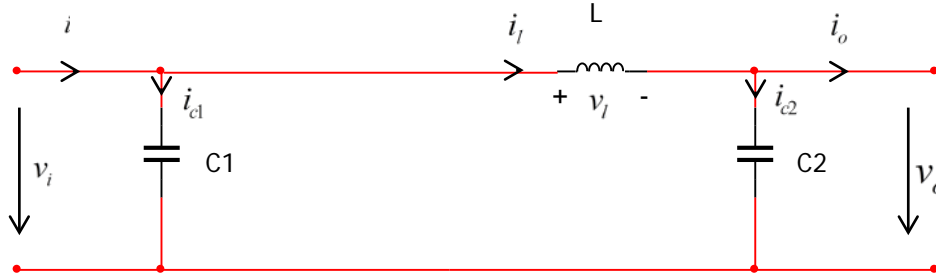


Figure 2.15. Equivalent circuit of a buck converter at closed switch time  $DT_S$ .  
Adapted from [50].

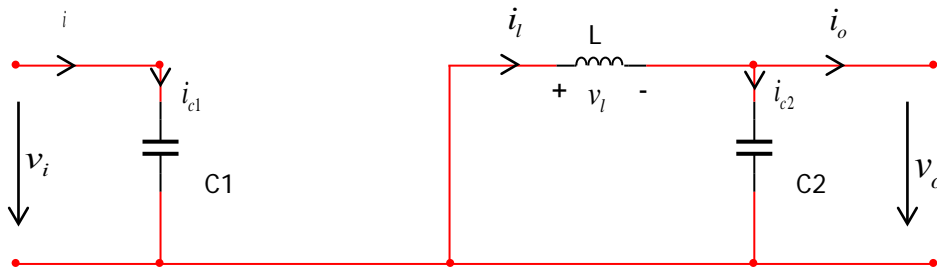


Figure 2.16. Equivalent circuit of a buck converter at open switch time  $D'T_S$ .  
Adapted from [50].

When the switch in Figure 2.14 is closed  $t \in [0, DT_S)$ , the diode will be reverse biased and current flows through the inductor into the load (Figure 2.15). The magnetic field in  $L$  increases, thereby, storing energy in the inductor, with the increasing voltage drop across  $L$  opposing or ‘bucking’ part of the input voltage.

As soon as the switch is open  $t \in [DT_S, T_S)$  the input voltage is removed, the inductor will maintain the current flow to the load, but the loop now closes through the forward biased diode (Figure 2.16). The capacitor  $C2$  discharges into the load during the off time, contributing to the total current being supplied to the load (the total load current during the switch off time is the sum of the inductor and capacitor current).

The shape of the current flowing in the inductor is similar to Figure 2.17.



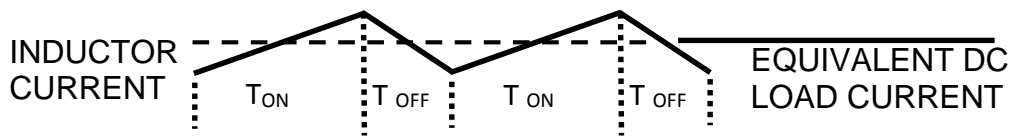


Figure 2.17. Buck regulator inductor current. Adapted from [58].

The current through the inductor ramps up when the switch is on (closed), and ramps down when the switch is off (opened). The DC load current from the regulated output is the average value of the inductor current.

The peak-to-peak difference in the inductor current waveform is referred to as the *inductor ripple current*, and the inductor is typically selected large enough to keep this ripple current less than 20% to 30% of the rated DC current [58].

The DC output voltage which appears across the load is a fraction of the input voltage, and this fraction turns out to be equal to the duty cycle. So, it can be written:

$$\frac{V_{out}}{V_{in}} = D \Rightarrow V_{out} = V_{in} D \quad (2.29)$$

where,  $D$  is the duty cycle, and equal to  $\frac{DT_s}{T_s}$ , and  $T_s$  is the switching period  $\frac{1}{f_s}$ .

So, by varying the switching duty cycle, the buck converter's output voltage can be varied as a fraction of the input voltage. A duty cycle of 50% gives a step-down ratio of 2:1, for example, as needed for a 24/12V step-down converter.

### 2.9.2.2 Continuous – Conduction Mode

Figure 2.18a shows the waveforms for the continuous-conduction mode of operation where the inductor current flows continuously [ $i_L(t) > 0$ ]. When the switch is on for a time duration  $t_{on}$ , the switch conducts the inductor current and the diode becomes reverse biased. This results in a positive voltage  $v_L = V_d - V_o$  across the inductor in Figure 2.18b. This voltage causes a linear increase in the inductor current  $i_L$ . When the switch is turned off, because of the inductive energy storage,  $i_L$  continues to flow. This current now flows through the diode, and  $v_L = -V_o$  in Figure 2.18c [59].

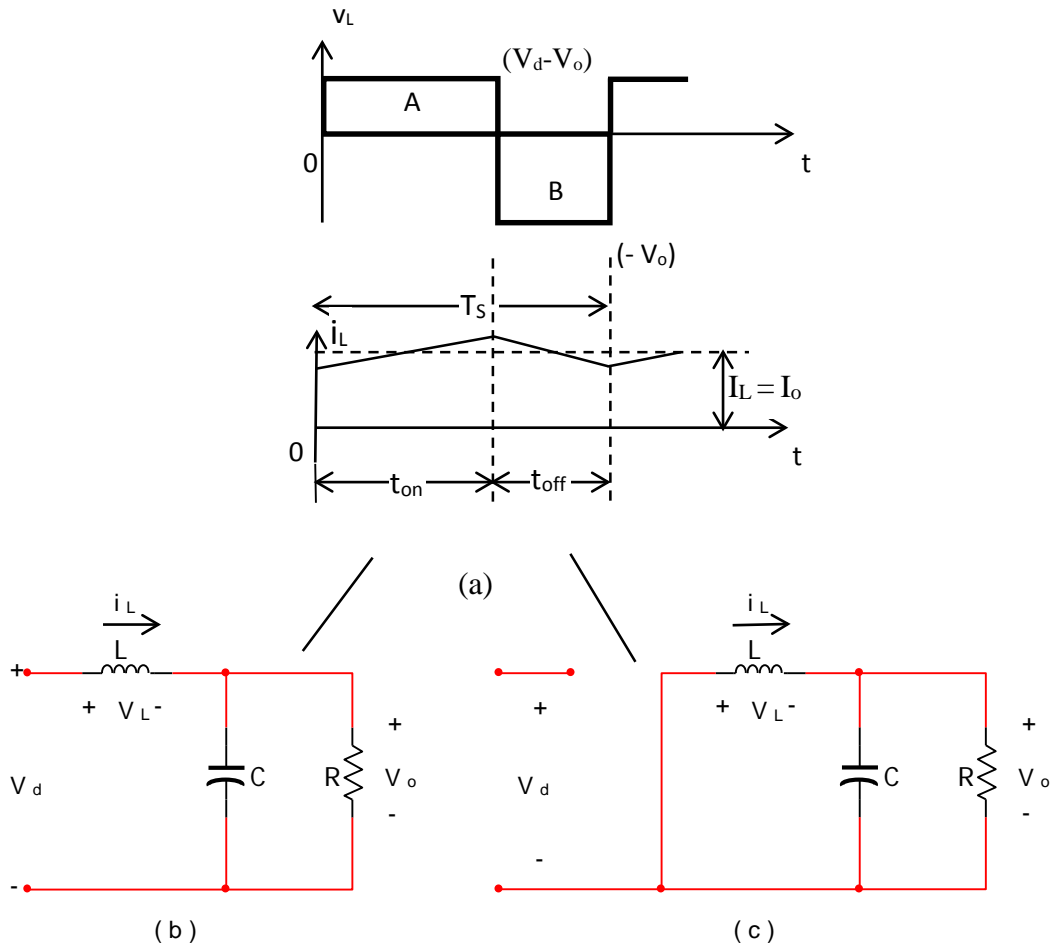


Figure 2.18. Step-down converter circuit states (a) inductor voltage and current waveforms, (b) switch on (c) switch off. Adapted from [59].

Since in steady-state operation the waveform must repeat from one time period to the next, the integral voltage  $v_L$  over one time period must be zero, where  $T_S = t_{on} + t_{off}$ :

$$\int_0^{T_S} v_L dt = \int_0^{t_{on}} v_L dt + \int_{t_{on}}^{T_S} v_L dt = 0 \quad (2.30)$$

In figure 2.18a, equation (2.30) implies that the areas A and B must be equal. Therefore,

$$(V_d - V_o)t_{on} = V_o(T_S - t_{on}) \quad (2.31)$$

$$\frac{V_o}{V_d} = \frac{t_{on}}{T_S} = D \text{ (duty ratio)} \quad (2.32)$$

Therefore, the voltage output varies linearly with the duty ratio of the switch for a given input voltage. It does not depend on any other circuit parameter.

### 2.9.3 Boost Converter

The boost converter, as shown in Figure 2.19, is also known as the step-up converter. It's typical application is to convert a low input-voltage to a high output-voltage of the same polarity, essentially functioning like a reversed buck converter [50]. Again the operation consists of a high speed switch, with output voltage control, by varying the switching duty cycle.

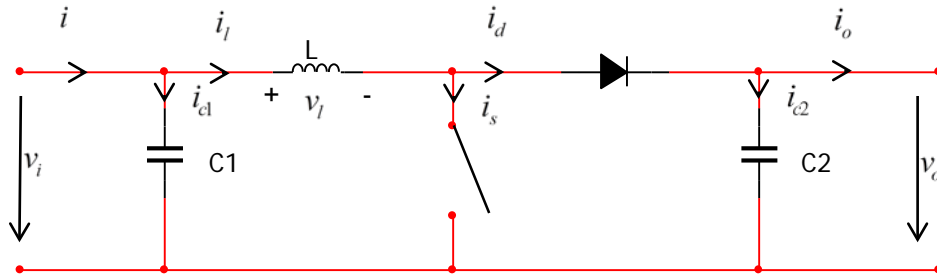


Figure 2.19. Ideal boost converter circuit. Adapted from [50].

#### 2.9.3.1 The Equivalent Circuit Model

During the first time interval  $DT_S$ , of the switching period  $T_S$ , the closed switch connects the input through the inductor to ground and a high current starts to flow. The input voltage is forced across the inductor which causes the current through it to increase (ramp up) and energy is stored in the inductor's magnetic field. The diode is reverse biased so, no inductor current flows through the load and the load current is supplied by the charge in  $C2$  (Figure 2.20).

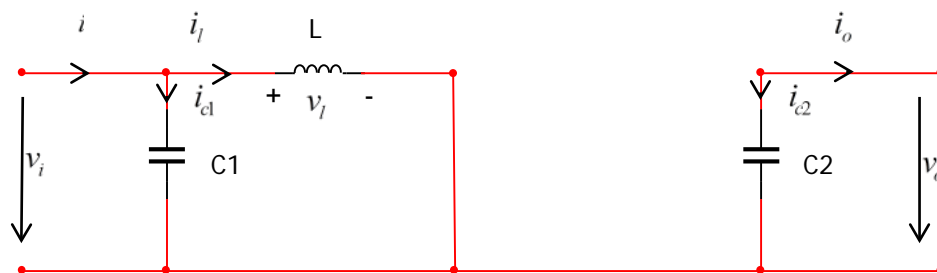


Figure 2.20. Equivalent circuit of a boost converter at closed switch time  $DT_S$ .

Adapted from [50].

After the switch is opened in the second time interval  $D'T_S$  of the switching period (Figure 2.21), the nature of the inductor objects to the discontinuity in the current flow,  $L$  opposes any drop in current by immediately reversing its EMF - so that the inductor voltage adds to (i.e., 'boosts') the source voltage, and the high current

through the now forward biased diode leads to a high voltage rise which is applied across the load, recharging  $C2$ .

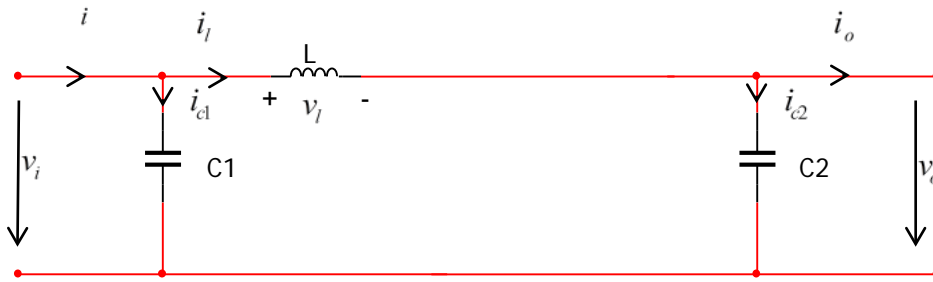


Figure 2.21. Equivalent circuit of a boost converter at open switch time  $D'T_S$ .

Adapted from [50].

The output voltage is therefore higher than the input voltage, and it turns out that the voltage step-up ratio is equal to:

$$\frac{V_{out}}{V_{in}} = \frac{1}{1-D} \quad (2.33)$$

Where  $1-D$  is the proportion of the switching cycle that the switch is off, rather than on.

So, the step-up ratio is also equal to:

$$\frac{V_{out}}{V_{in}} = \frac{T_S}{D'T_S} \quad (2.34)$$

Thus, a 2:1 step-up ratio is achieved with a duty cycle of 50% ( $D'T_S = D'T_S$ ), for example as needed for a 2/4V step up converter.

### 2.9.3.2 Continuous vs Discontinuous Operation

The DC-DC converters can have two distinct modes of operation [58] continuous conduction mode and discontinuous conduction mode. In most regulator applications, the inductor current never drops to zero during full-load operation or at least when the switch or diode is conducting (this is defined as *continuous mode operation*). Whereas in discontinuous conduction mode, the inductor current falls to zero before completing one switching cycle,  $T_S$ .

## 2.9.3.2.1 Continuous Operation

Figure 2.22a [59] shows the operation of the boost converter in the continuous conduction mode where the inductor current  $i_L(t) > 0$ . When the switch is closed the source voltage  $V_d$  is applied across the inductor and the rate of rise of inductor current is dependent on the source voltage  $V_d$  and inductance  $L$ . This results in a positive voltage across the inductor [Figure 2.22b].

$$v_L = V_d \quad (2.35)$$

When the switch is opened in Figure 2.22c, the inductor voltage becomes:

$$v_L = V_d - V_o \quad (2.36)$$

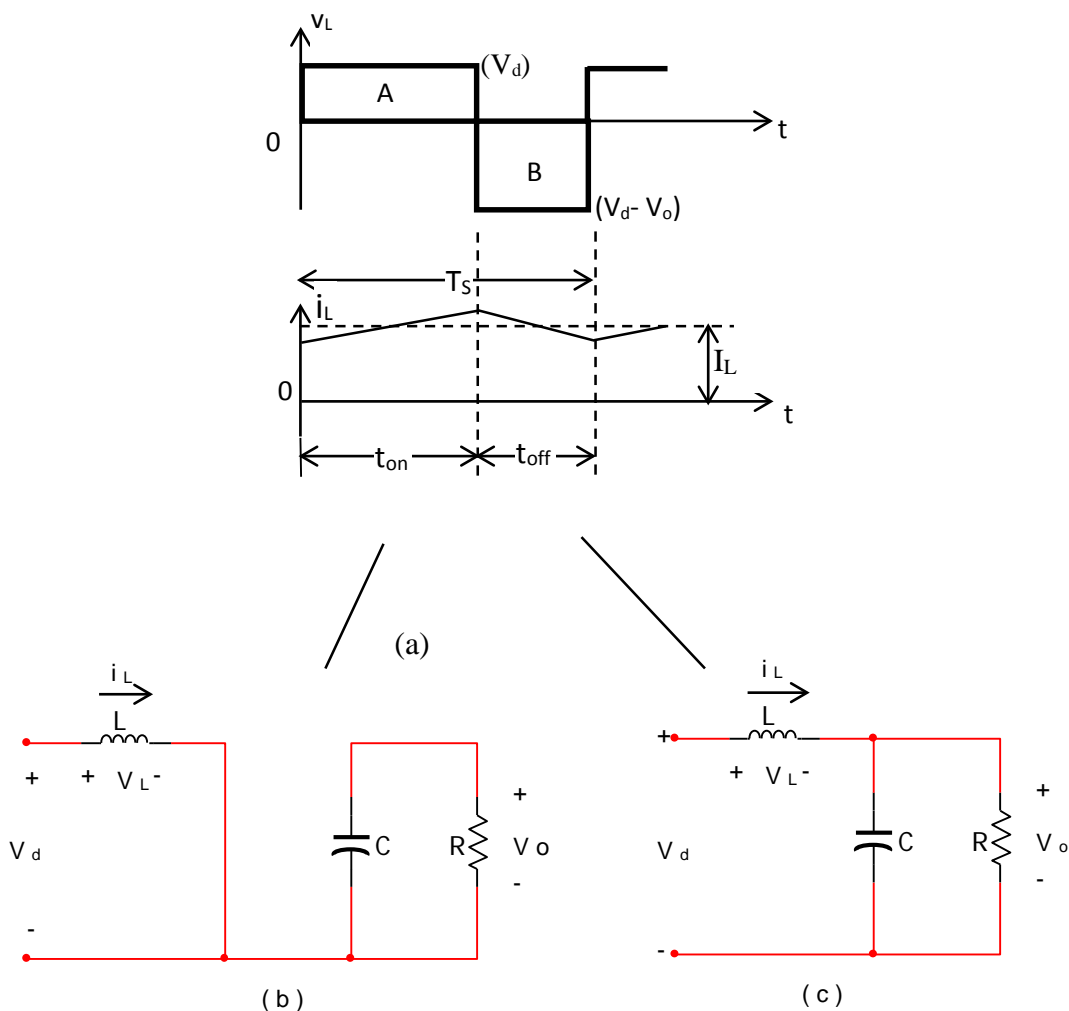


Figure 2.22. Continuous Conduction mode: (a) inductor voltage and current waveforms (b) switched on; (c) switched off. Adapted from [59].

Since in steady state operation the waveform must repeat from one time period,  $T_s$ , to the next, the time integral of the inductor voltage  $v_L$  over one time period

must be zero, where  $T_S = t_{on} + t_{off}$ . This implies that the areas A and B in Figure 2.22a must be equal. Therefore,

$$V_d t_{on} + (V_d - V_o) t_{off} = 0 \quad (2.37)$$

Dividing both sides by  $T_S$ , and rearranging all terms yields

$$\frac{V_o}{V_d} = \frac{T_S}{t_{off}} = \frac{1}{1-D} \quad (2.38)$$

Assuming the circuit is 100% efficient, i.e. the input power ( $P_d$ ) and output power ( $P_o$ ) are the same,

$$P_d = P_o \Leftrightarrow V_d I_d = V_o I_o \quad (2.39)$$

Hence,

$$\frac{I_o}{I_d} = 1 - D \quad (2.40)$$

### 2.9.3.2.2 Boundary between Continuous and Discontinuous Operation

Figure 2.23 [59] shows the waveforms for  $v_L$  and  $i_L$  at the edge of continuous conduction. Being at the boundary between the continuous and the discontinuous mode, by definition, the inductor current  $i_L$  goes to zero at the end of the off period.

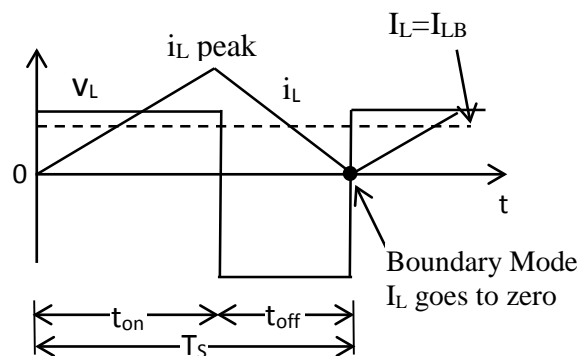


Figure 2.23. Waveforms at the boundary of continuous discontinuous conduction.

Adapted from [59].

The *average inductor current* at the boundary is:

$$\begin{aligned}
 i_{LB} &= \frac{1}{2} i_{L\ peak} \text{ (figure 2.23)} \\
 &= \frac{1}{2} \frac{V_d}{L} t_{on} \\
 &= \frac{T_s V_o}{2L} D(1-D) \text{ (using equation 2.38)} \tag{2.41}
 \end{aligned}$$

Recognizing that in a step up converter the inductor current and the input current are the same ( $i_d = i_L$ ), using equation (2.40) and (2.41) the *average output current* at the edge of continuous conduction is:

$$I_{oB} = \frac{T_s V_o}{2L} D(1-D)^2 \tag{2.42}$$

Most applications in which a step up converter is used require that  $V_o$  be kept constant. Therefore, with  $V_o$  constant,  $I_{oB}$  are plotted in figure 2.24 as a function of duty ratio  $D$ . Keeping  $V_o$  constant and varying the duty ratio imply that the input voltage is varying.

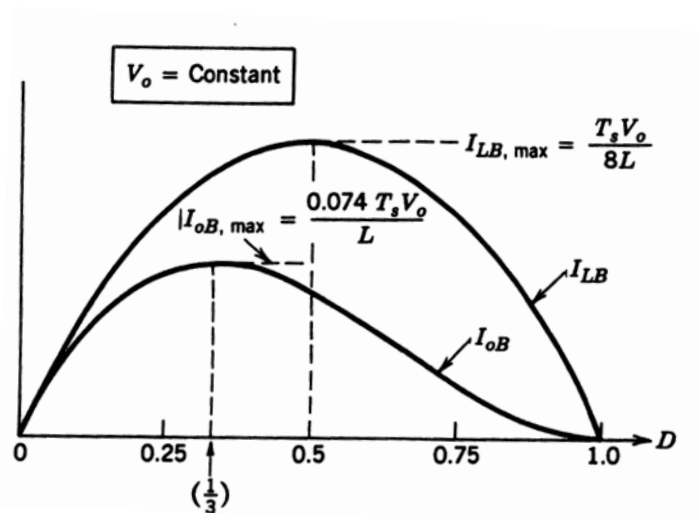


Figure 2.24. Average Output Current at the Boundary of continuous – discontinuous. Reproduced from [59].

Figure 2.24 shows that  $I_{LB}$  reaches a maximum value at  $D=0.5$ :

$$I_{LB, \max} = \frac{T_s V_o}{8L} \tag{2.43}$$

Also,  $I_{oB}$  has its maximum values at  $D = \frac{1}{3} = 0.333$  :

$$I_{oB,\max} = \frac{2}{27} \frac{T_s V_o}{L} = 0.074 \frac{T_s V_o}{L} \quad (2.44)$$

In terms of their maximum values,  $I_{LB}$  and  $I_{oB}$  can be expressed using equations (2.43) and (2.41) as:

$$I_{LB} = 4D(1 - D)I_{LB,\max} \quad (2.45)$$

and using equations (2.44) and (2.42) it is:

$$I_{oB} = \frac{27}{4} D(1 - D)^2 I_{oB,\max} \quad (2.46)$$

Figure 2.24 shows that for a given duty cycle value,  $D$ , with constant  $V_o$ , if the average load current drops below  $I_{oB}$  (and hence, the average inductor current below  $I_{LB}$ ), the current conduction will become discontinuous.

### 2.9.3.2.3 Discontinuous Operation

To understand the discontinuous current conduction mode, it is assumed that as the output load power decreases,  $V_d$  and duty ratio  $D$ , remain constant (although, in practice, this is not the case, since  $D$  would vary in order to keep the output voltage,  $V_o$ , constant). [59]

Figure 2.25 shows the discontinuous conduction assuming that  $V_d$  and duty ratio  $D$ , remain constant.

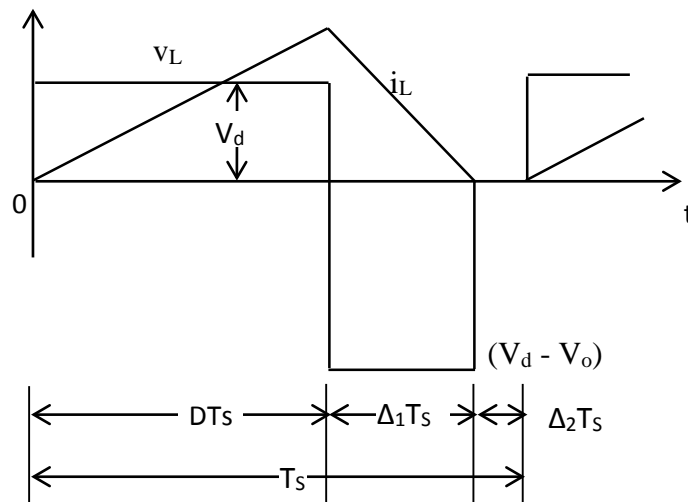


Figure 2.25. Step up converter waveforms at Discontinuous Conduction. Adapted from [59].



In figure 2.25, the discontinuous current conduction due to decreased  $P_o$  ( $=P_d$ ) and, hence, a lower  $I_L$  ( $=I_d$ ), since  $V_d$  is constant. If the integral of the inductor voltage over one time period is equate to zero,

$$V_d DT_s + (V_d - V_o) \Delta_1 T_s = 0$$

$$\frac{V_o}{V_d} = \frac{\Delta_1 + D}{\Delta_1} \quad (2.47)$$

Assuming that the circuit is 100% efficient, i.e. the input power,  $P_d$ , is equal to the output power,  $P_o$ ,

$$\frac{I_o}{I_d} = \frac{\Delta_1}{\Delta_1 + D} \quad (2.48)$$

From Figure 2.25, the average input current, which is also equal to the inductor current is:

$$I_d = \frac{V_d}{2L} DT_s (D + \Delta_1) \quad (2.49)$$

Using equation (2.48) in equation (2.49) yields:

$$I_o = \left( \frac{T_s V_d}{2L} \right) D \Delta_1 \quad (2.50)$$

In practice, since  $V_o$  is held constant and  $D$  varies in response to the variation in  $V_d$ , it is more useful to obtain the required duty ratio  $D$  as a function of load current for various values of  $V_o/V_d$ . By using equations (2.47), (2.50) and (2.44) it is determined that:

$$D = \left[ \frac{4}{27} \frac{V_o}{V_d} \left( \frac{V_o}{V_d} - 1 \right) \frac{I_o}{I_{oB,\max}} \right]^{\frac{1}{2}} \quad (2.51)$$

### 2.9.3.3 Voltage and Current Waveforms

In figure 2.26 a typical boost-up circuit is shown and is analyzed in the two distinct switch statuses, in figure 2.26a the switch is closed, and in figure 2.26b the switch is opened.

When switch is closed, the diode is reversed and the output is isolated. The input supplies energy to the inductor (Table 2.6)

Table 2.6. Equations for switch status “close”.

	Inductor	Switch	Diode
Voltage	$V_L=V_{in}$	$V_{SW}=0$	$V_d=V_o$
Current	$I_L=I_{SW}$	$I_{SW}=I_L$	$I_d=0$

When switch is opened, the output stage receives energy from the input as well as from the inductor, hence the output is large.

Table 2.7. Equations for switch status “open”.

	Inductor	Switch	Diode
Voltage	$V_L=V_{in}-V_o$	$V_{SW}=V_o$	$V_d=0$
Current	$I_L=I_{Lmin}$	$I_{SW}=0$	$I_d=I_L$

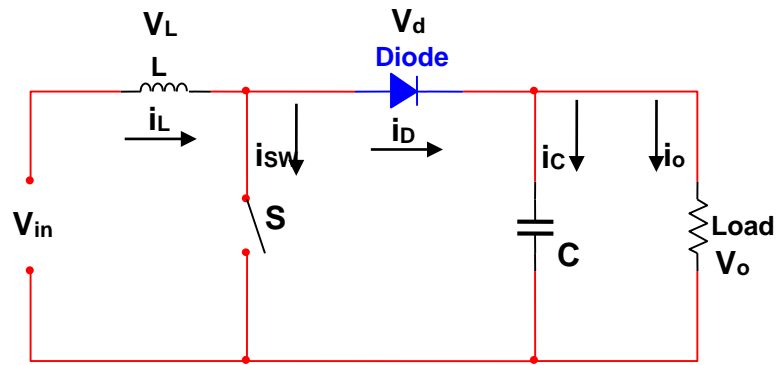


Figure 2.26. Circuit of boost up converter.

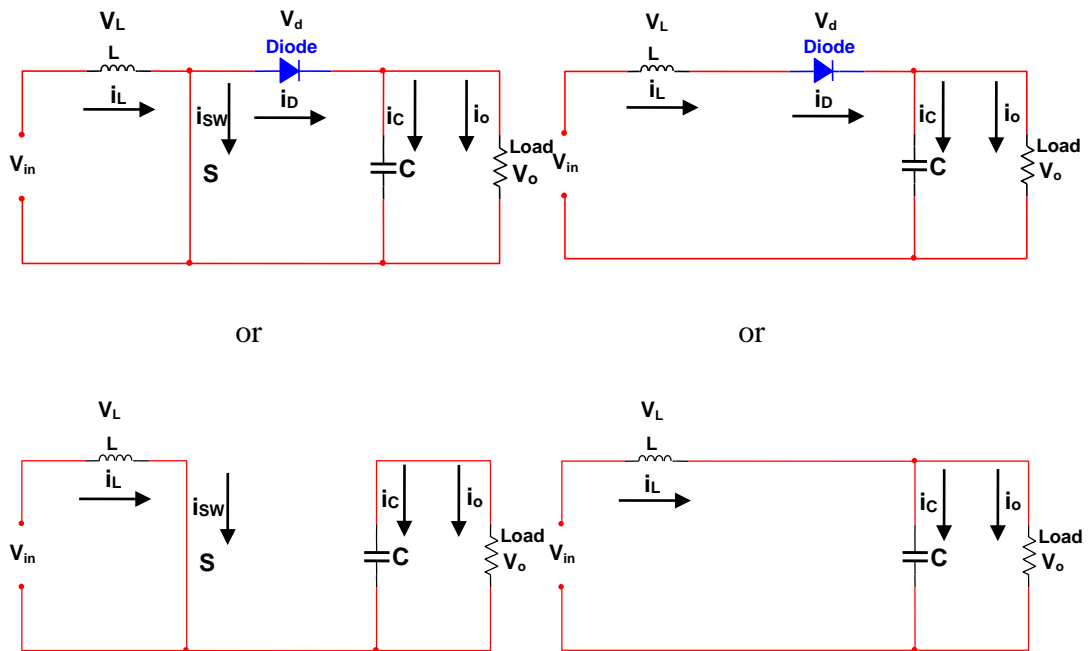


Figure 2.26 a) Circuit when switch is closed.

2.26 b) Circuit when switch is opened.

Analyzing the equations presented for the dc to dc converter the following characteristic voltage (figure 2.27) and current (figure 2.28) waveforms are obtained in the inductor, switch and diode.

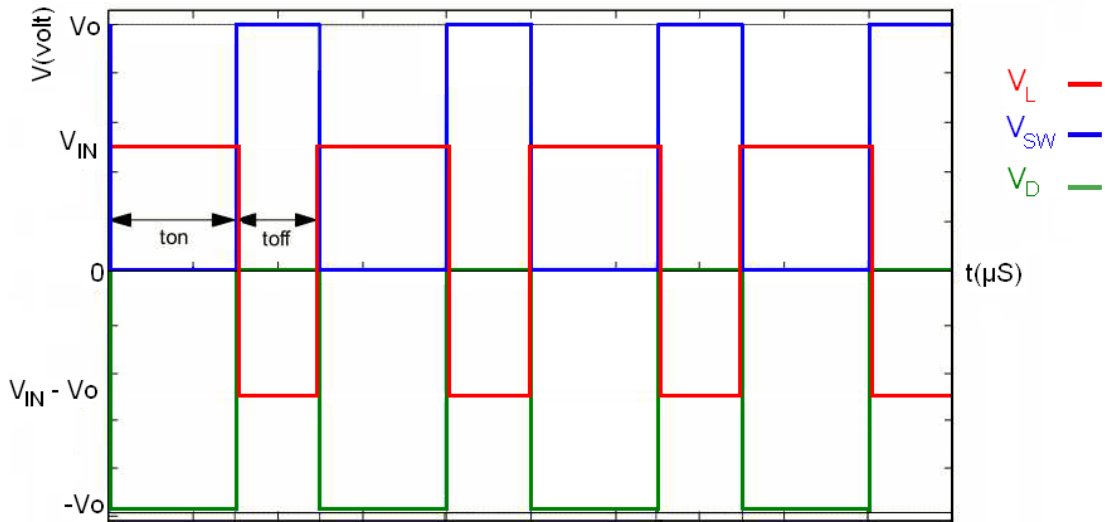


Figure 2.27. Voltage waveforms in the boost up converter (inductor, switch and diode).

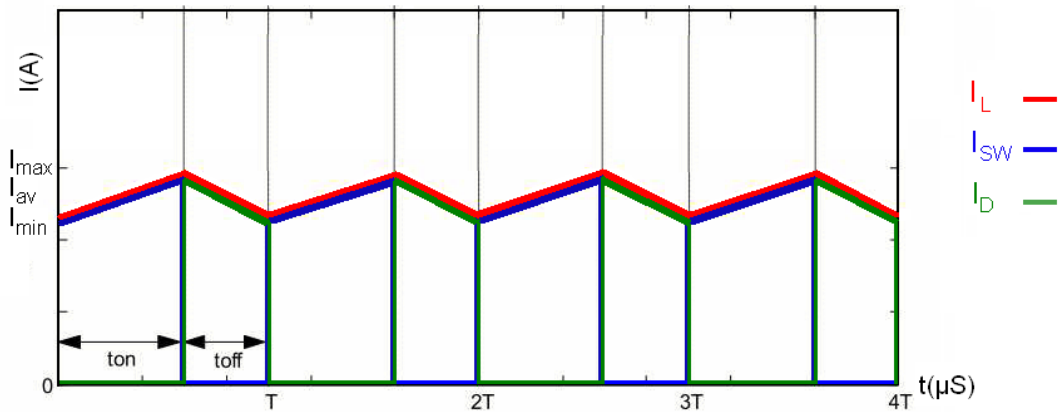


Figure 2.28. Current waveforms in the boost up converter (inductor, switch and diode).

### 2.9.3.4 Inductor Current Ripple – Inductor Choice

By definition, the voltage drop across the inductor is:

$$v_L = L \frac{di_L}{dt} \quad (2.52)$$

By using  $v_L = V_d$ , equation (2.52), becomes:

$$\frac{di_L}{dt} = \frac{v_L}{L} = \frac{V_d}{L} \quad (2.53)$$

where  $\frac{di_L}{dt}$  represent the slope of the inductor current during the first time interval  $DT_S$  of a switching period.

For the second time interval,  $D'T_S$  with equation ( $v_L = V_d - V_{out}$ ), the following expression is obtained:

$$\frac{di_L}{dt} = \frac{v_L}{L} = \frac{V_d - V_{out}}{L} \quad (2.54)$$

The slopes  $\frac{di_L}{dt}$  are shown in Figure 2.29 [59].

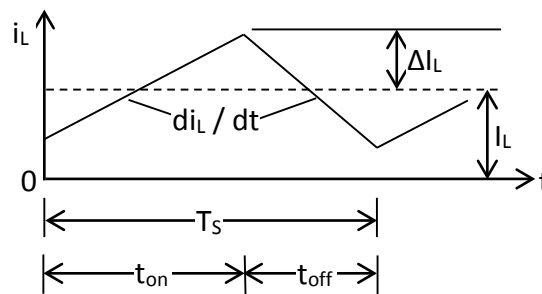


Figure 2.29. Ripple Inductor current. Adapted from [59].

Since the converter is assumed to be in steady state and 100% efficient, it does not make a difference if  $DT_S$  or  $D'T_S$  is chosen to determine the current ripple amplitude.

With the linear expression for  $\frac{di_L}{dt}$  (2.53), the equation for the peak to peak ripple can be derived:

$$I_{LP-P} = 2\Delta i_L = \frac{V_d DT_S}{L} \quad (2.55)$$

Equation (2.55) now can be solved for the inductance  $L$  so that desired current ripple amplitude can be achieved:

$$L = \frac{V_d DT_S}{2\Delta i_L} \quad (2.56)$$

### 2.9.3.5 Output Capacitor Choice

The boost converter output capacitor has to keep the output voltage when the inductor is being charged and is hence disconnected from the output. Therefore there will be a component of the output ripple due to the discharge of the output capacitor.

In addition, when the inductor is discharging, the output capacitor will experience an inrush of current and any ESR (effective series resistance) in the capacitor will also result in ripple.

Therefore the output ripple is made up of 2 components. The ripple caused by the output capacitor discharging when the inductor is being charged and the ripple caused by the inrush current from the inductor into the ESR of the output capacitor.

The ripple caused by the discharge of the output capacitor while the inductor is charging is dictated by:

$$i = C \frac{dV}{dt} \quad (2.57)$$

where,  $i$  is the load current in Amps,  $C$  is the output capacitance in Farads and  $\frac{dV}{dt}$  is the change in output voltage with time.

Solving for  $dV$  it is:

$$dV = \frac{idt}{C} = \frac{I_o DT_s}{C_{out}} \quad (2.58)$$

Finally, taking ESR into account the overall output ripple voltage [19] can be determined by equation (2.59)

$$\Delta V_{out} = I_{in} ESR + \frac{I_o DT_s}{C_{out}} \quad (2.59)$$

Solving for  $C_{out}$ , output capacitance can be calculated accordingly:

$$C_{out} = \frac{I_o DT_s}{\Delta V_{out} - I_{in} ESR} \quad (2.60)$$

### 2.9.3.6 Effect of parasitic Elements

The parasitic elements in a step-up converter are due to the losses associated with the *diode*, the *inductor* and the *switch*. Figure 2.30 [59] qualitatively shows the effect of these parasitics on the voltage transfer ratio. As  $D$  approaches unity the ratio between input and output voltage increases towards infinity. In practice,  $V_o/V_d$  declines as the duty ratio approaches unity as a result of the parasitic elements.

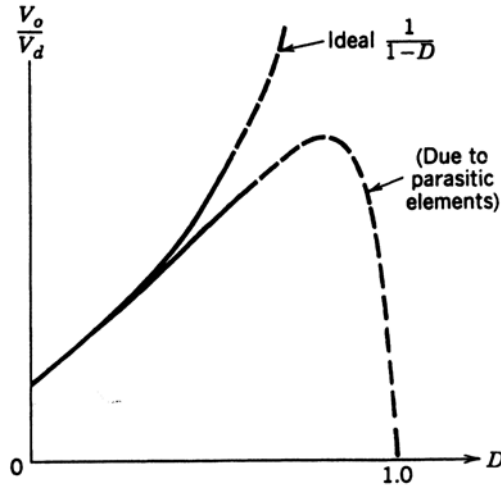


Figure 2.30. Effect of parasitic elements on voltage conversion ratio. Reproduced from [59].

### 2.9.3.7 Power Losses and Efficiency of Boost Converter for CCM

To calculate power losses in boost converter [60] parasitic resistances are considered, where MOSFET on-resistance is  $r_{DS}$ , diode forward resistance is  $R_F$ , diode threshold voltage is  $V_F$ , and ESR of the inductor  $L$  is  $r_L$ . The conduction losses will be evaluated assuming that the inductor current  $i_L$  is ripple-free and equals the dc input current  $I_I$ .

Hence, the *switch* current can be approximated by:

$$i_s = \begin{cases} I_I = \frac{I_o}{1-D}, & \text{for } 0 < t \leq DT \\ 0, & \text{for } DT < t \leq T \end{cases} \quad (2.61)$$

resulting in its rms value:

$$I_{Srms} = \sqrt{\frac{1}{T} \int_0^T i_s^2 dt} = \frac{I_o}{1-D} \sqrt{\frac{1}{T} \int_0^{DT} dt} = \frac{I_o \sqrt{D}}{1-D} \quad (2.62)$$

and the MOSFET conduction loss:

$$P_{rDS} = r_{DS} I_{Srms}^2 \quad (2.63)$$

The switching loss is expressed,

$$P_{sw} = f_s C_o V_{SM}^2 = f_s C_o V_o^2 \quad (2.64)$$

where  $C_o$  is the transistor output capacitance.

Hence, one obtains the total power dissipation in the MOSFET,

$$P_{FET} = P_{rDS} + P_{sw} = r_{DS} I_{Srms}^2 + f_s C_o V_o^2 \quad (2.65)$$

Likewise, the *diode* current can be approximated by:

$$i_D = \begin{cases} 0, & \text{for } 0 < t \leq DT \\ I_I = \frac{I_o}{1-D}, & \text{for } DT < t \leq T \end{cases} \quad (2.66)$$

yielding its rms value:

$$I_{Drms} = \sqrt{\frac{1}{T} \int_0^T i_D^2 dt} = \frac{I_o}{1-D} \sqrt{\frac{1}{T} \int_{DT}^T dt} = \frac{I_o}{\sqrt{1-D}} \quad (2.67)$$

and the power loss in  $R_F$ ,

$$P_{RF} = R_F I_{Drms}^2 \quad (2.68)$$

The diode power loss due to  $R_F$  increases rapidly with increasing duty cycle  $D$  at fixed load current  $I_o$ .

The average value of the diode current is:

$$I_D = \frac{1}{T} \int_0^T i_D dt = \frac{I_o}{T(1-D)} \int_{DT}^T dt = I_o \quad (2.69)$$

which gives the power loss associated with the voltage forward bias voltage  $V_F$ ,



$$P_{VF} = V_F I_D = V_F I_o \quad (2.70)$$

Thus, the overall diode conduction loss is:

$$P_D = P_{RF} + P_{VF} = R_F I_{Drms}^2 + V_F I_o \quad (2.71)$$

The *inductor* current is:

$$i_L \approx I_I = \frac{I_o}{1-D} \quad (2.72)$$

leading to its rms value:

$$I_{Lrms} = I_I = \frac{I_o}{1-D} \quad (2.73)$$

and the inductor loss:

$$P_{rL} = r_L I_{Lrms}^2 \quad (2.74)$$

The inductor loss increases rapidly with increasing duty cycle  $D$  at fixed load current  $I_o$ .

The overall power loss of the boost converter is:

$$P_{LS} = P_{FET} + P_D + P_{rL} \quad (2.75)$$

yielding the converter efficiency.

#### 2.9.4 Buck-Boost Converter

The buck-boost converter combines the properties of the buck and boost configurations. It can be used to ideally transform any dc input voltage into any desired dc output voltage. In practical usage the ideality is of course limited by component losses. The main components in a buck-boost converter are again much the same as in the buck and boost types, but they are to allow the voltage to be stepped either up or down, depending on the duty cycle. Figure 2.31 shows the ideal equivalent circuit diagram of the buck-boost converter.

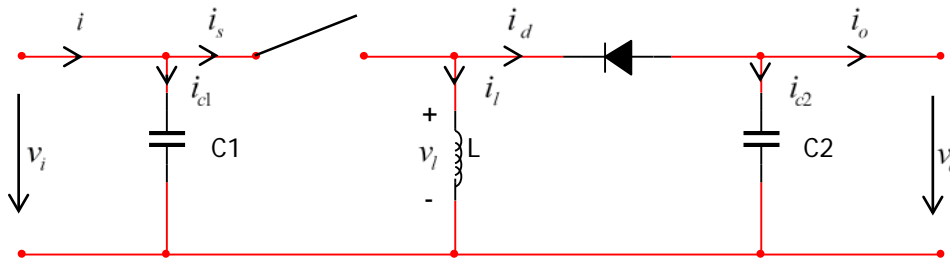


Figure 2.31. Ideal buck-boost converter circuit. Adapted from [50].

### 2.9.4.1 The Equivalent Circuit Model

If the switch is closed during the first time interval  $DT_S$  of the switching period  $T_S$ , a current starts flowing from the input source through the inductor to ground (Figure 2.32). The inductor  $L$  is again connected directly across the source voltage and current flows through it, storing energy in the magnetic field. No current can flow through the diode to the load, because the diode is reverse biased. Capacitor  $C_2$  must supply the load current in this ' $DT_S$ ' phase.

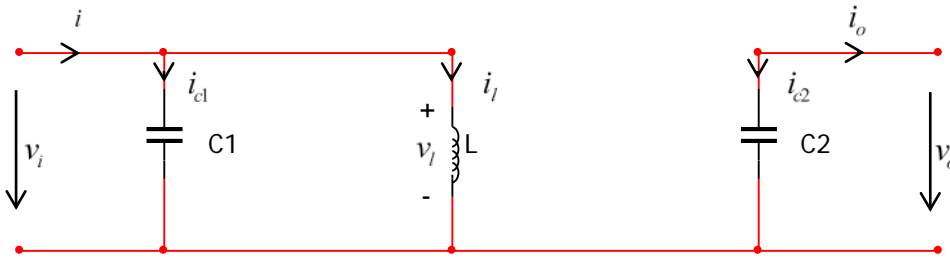


Figure 2.32. Equivalent circuit of a buck-boost converter at closed switch time  $DT_S$ . Adapted from [50].

After the switch opens at the beginning of the second time interval  $D'T_S$ ,  $L$  is disconnected from the source, but current flow is maintained by the nature of the inductor. Inductor  $L$  opposes any tendency for the current to drop, and instantly reverses its EMF. This generates a voltage which forward biases the diode, and current flows into the load and to recharge  $C_2$  (Figure 2.33). Since the current is forced to flow "backwards" through the load, the output voltage  $V_o$  of the buck-boost converter is negative.

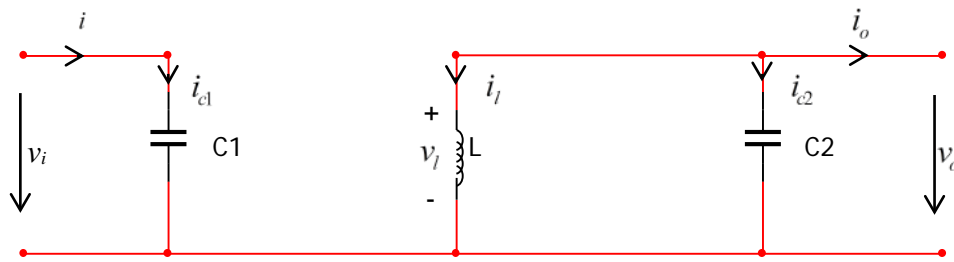


Figure 2.33. Equivalent circuit of a buck-boost converter at open switch time  $D'T_S$ . Adapted from [50].

Figure 2.34 show the current flow paths when the switch opens in order to understand better the negative output voltage.

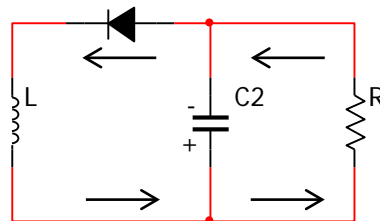


Figure 2.34. Buck-boost (inverting) converter when the switch is opened. Adapted from [58].

Figure 2.35a shows the waveforms for the continuous conduction mode where the inductor current flows continuously. [59]

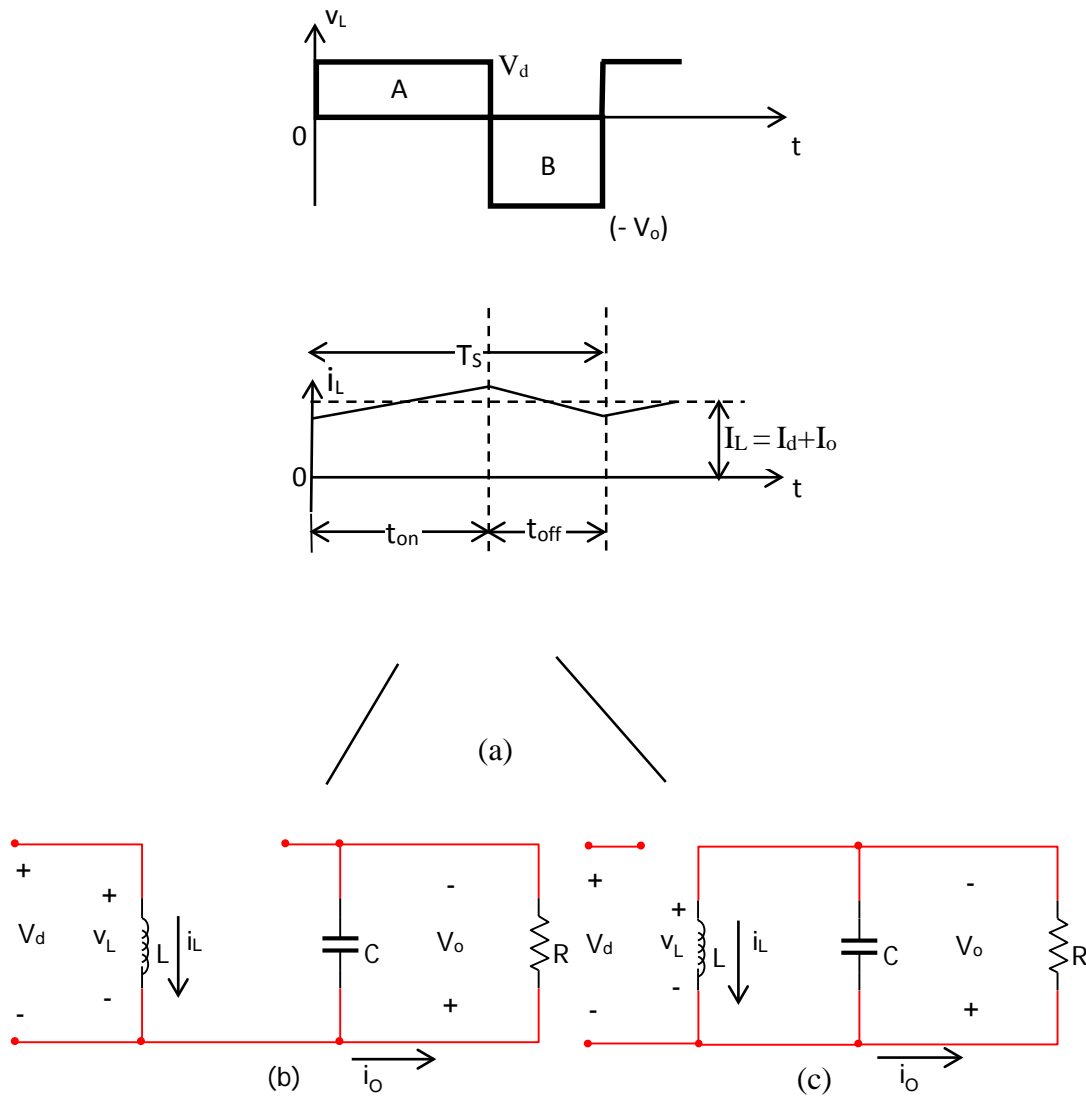


Figure 2.35. Continuous conduction mode: a) inductor voltage and current waveforms b) switch on; c) switch off. Adapted from [59].

Equating the integral of the inductor voltage over the time period to zero:

$$V_d DT_s + (-V_o)(1-D)T_s = 0 \quad (2.76)$$

$$\frac{V_o}{V_d} = \frac{D}{1-D} \quad (2.77)$$

So the buck-boost converter steps the voltage down when the duty cycle is less than 50% (i.e.,  $DT_s < D'T_s$ ), and steps it up when the duty cycle is greater than 50% ( $DT_s > D'T_s$ ).

The ratio between output and input currents is simply the reciprocal of the voltage ratio, if losses are ignored.

$$P_d = P_o \Leftrightarrow V_d I_d = V_o I_o \Leftrightarrow$$

$$\frac{I_o}{I_d} = \frac{V_d}{V_o} \quad (2.78)$$

### 2.9.5 Measuring Regulator Efficiency of DC-DC Converters

The efficiency ( $\eta$ ) of a switching regulator is defined as:

$$\eta = \frac{P_{in}}{P_{total}} = \frac{P_{load}}{P_{load} + P_{losses}} \quad (2.79)$$

In determining converter efficiency, the first thing that must be measured is the total consumed power ( $P_{total}$ ). Assuming a DC input voltage,  $P_{total}$  is defined as the total power drawn from the source, which is equal to:

$$P_{total} = V_{in} I_{in(AVE)} \quad (2.80)$$

The input current value used in the calculation must be the average value of the waveform (the input current will not be DC or sinusoidal). Since the total power dissipated must be constant from input to output,  $P_{total}$  is also equal to the load power plus the internal regulator power losses:

$$P_{total} = P_{load} + P_{losses} \quad (2.81)$$

Measuring (or calculating) the power to the load is very simple, since the output voltage and current are both DC. The load power is found by:

$$P_{load} = V_{out} I_{load} \quad (2.82)$$

Equation (2.79) is referred to the output of the converter. Another way to calculate the efficiency ( $\eta$ ) of a switching regulator considering the input power and the losses is:

$$\eta = \frac{P_{in} - P_{losses}}{P_{in}} \quad (2.83)$$

Either equation can be used in order to calculate the efficiency.

## 2.10 MPPT Methodologies -Techniques

### 2.10.1 Introduction

Many maximum power point tracking (MPPT) techniques for photovoltaic (PV) systems are well established in the literature. The most commonly known are perturb and observe (P&O) [61], hill-climbing [62], incremental conductance (IncCond) [63], fractional open-circuit voltage (FOCV) control [64] and fractional short-circuit current (FSCC) control [65] there are many others. Many techniques are reviewed and compared in [66]. The techniques vary in many aspects, including simplicity, speed of convergence, digital versus analog implementation, sensors required, and need for parameterization.

### 2.10.2 Perturb and Observe

In the Perturb and Observe (P&O) method the MPP is tracked by repeatedly increasing or decreasing the output voltage of the PV array at the MPP. This method not only has relatively simple control algorithm but also tracks the MPP well. However, in normal weather conditions, the operating point of the PV array oscillates around the MPP giving rise to some wastage of the available energy [67]. In rapidly changing atmospheric conditions, this method also takes time to track the MPP and during this time there is a significant power loss [68].

As the name of the P&O method suggests, the process works by perturbing the system by increasing or decreasing the array operating voltage and observing the impact on the array output power. Voltage ( $V$ ) and current ( $I$ ) are measured to calculate the current array output power  $P(k)$ . This value for  $P(k)$  is compared to the value obtained from the last measurement  $P(k - 1)$ . If the output power has increased since the last measurement, the perturbation of the output voltage will continue in the same direction as in the last cycle. If the output power has decreased since the last measurement, the perturbation of the output voltage will be reversed to the opposite direction of the last cycle.

From Figure 2.36, it can be seen that incrementing (or decrementing) the voltage increases (or decreases) the power when operating on the left of the MPP and decreases (or increases) the power when operating on the right of the MPP [66].

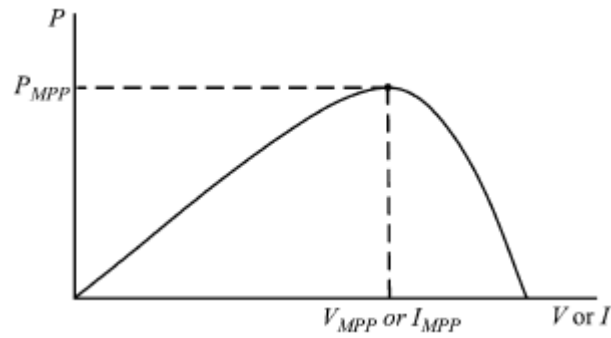


Figure 2.36. Characteristic PV array power curve versus voltage or current.

Reproduced from [66].

This algorithm is summarized in Table 2.8.

Table 2.8. Summary of P&O Algorithm. Adapted from [66].

Perturbation	Change in Power	Next Perturbation
Positive	Positive	Positive
Positive	Negative	Negative
Negative	Positive	Negative
Negative	Negative	Positive

With this algorithm the operating voltage  $V$  is perturbed with every MPPT cycle. As soon as the MPP is reached,  $V$  will oscillate around the ideal operating voltage  $V_{mpp}$ . This causes a power loss which depends on the step width of a single perturbation. If the step width is large, the MPPT algorithm will be responding quickly to sudden changes in operating conditions with the tradeoff of increased losses under stable or slowly changing conditions. If the step width is very small the losses under stable or slowly changing conditions will be reduced, but the system will be only able to respond very slowly to rapid changes in temperature or insolation. The value for the ideal step width is system dependent and needs to be determined experimentally [50].

A solution to this conflicting situation (small or large step width) is to have a variable perturbation size that gets smaller towards the MPP as shown in [69 – 71]. In [72], a two-stage algorithm is proposed that offers faster tracking in the first stage and finer tracking in the second stage.

Another drawback of the P&O method is described by Hussein and others [22]. In the case of a sudden increase in insolation  $S$ , the P&O algorithm reacts as if the increase occurred as a result of the previous perturbation of the array operating voltage. The next perturbation, therefore, will be in the same direction as the previous one. Assuming that the system has been oscillating around the MPP, it can be seen in Figure 2.37 that a continuous perturbation in one direction will lead to an operating point far away from the actual MPP. This process continues until the increase in insolation slows down or ends. [50]

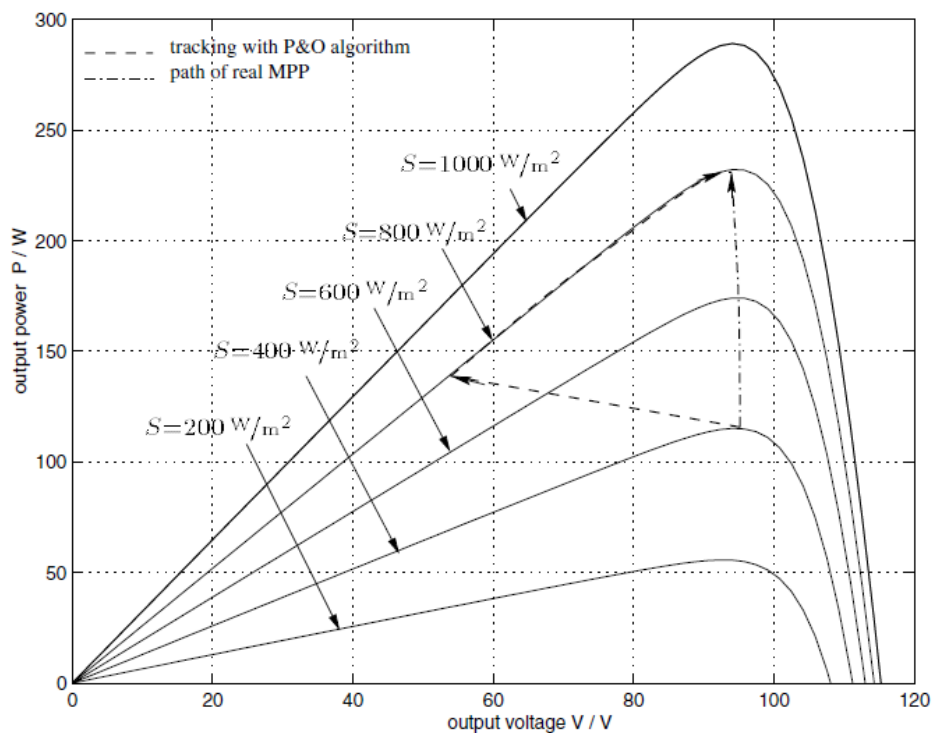


Figure 2.37. Deviation from the MPP with the P&O algorithm under rapidly changing insolation levels  $S$ . Reproduced from [50].

In an environment of rapidly changing atmospheric conditions and frequently changing insolation levels this deviation from the MPP can cause significant power loss. Experimental results [22] show an efficiency of 81.5% when using the P&O algorithm.

### 2.10.3 Hill-Climbing

Much focus has been on hill-climbing [73 – 76] which involves a perturbation in the duty ratio of the power converter, while P&O has an effect on the perturbation in the operating voltage of the PV array. In the case of a PV array connected to a power converter, perturbing the duty ratio of power converter perturbs the PV



array current and consequently perturbs the PV array voltage. Hill-climbing and P&O methods are different ways to envision the same fundamental method.

DSP or microcontroller control [74, 77, 78] is more suitable for hill-climbing and P&O, even though discrete analog and digital circuitry can be used as in [75].

#### 2.10.4 The incremental conductance method

The Incremental Conductance (IncCond) [22], [79 – 84] method is developed to remove the drawbacks of the P&O method. The IncCond method tracks the MPP of the PV array by comparing incremental conductance with the instantaneous conductance. As a result, under rapidly changing atmospheric conditions, the IncCond method tracks the MPP well. But this method has a disadvantage, that it requires a complex control circuit. IncCond method lends itself well to DSP and microcontroller control, which can easily keep track of previous values of voltage and current.

It is based on the fact that the derivative of the output power  $P$  with respect to the panel voltage  $V$  is equal to zero at the maximum power point (MPP). The solar panel's P-V characteristics in Figure 2.36 show further that the derivative is greater than zero to the left of the MPP and less than zero to the right of the MPP. This leads to the following set of equations:

$$\frac{dP}{dV} = 0, \quad \text{for } V = V_{mpp} \quad (2.84)$$

$$\frac{dP}{dV} > 0, \quad \text{for } V < V_{mpp} \quad (2.85)$$

$$\frac{dP}{dV} < 0, \quad \text{for } V > V_{mpp} \quad (2.86)$$

The fact that  $P = VI$  and the chain rule for the derivative of products yields:

$$\frac{dP}{dV} = \frac{d(VI)}{dV} = I \frac{dV}{dV} + V \frac{dI}{dV} = I + V \frac{dI}{dV} \quad (2.87)$$

Combining equations (2.84) and (2.87) leads to the MPP condition ( $V = V_{mpp}$ ) in terms of array voltage  $V$  and array current  $I$ :

$$\frac{dI}{dV} = -\frac{I}{V} \quad (2.88)$$

This shows that with equations (2.84) - (2.87) enough information is gathered to determine the relative location of the MPP by measuring only the incremental and instantaneous array conductance's  $\frac{dI}{dV}$  and  $\frac{I}{V}$ , respectively. These relations were used to develop the IncCond algorithm.

$$\frac{\Delta I}{\Delta V} = -\frac{I}{V}, \quad \text{at MPP} \quad (2.89)$$

$$\frac{\Delta I}{\Delta V} > -\frac{I}{V}, \quad \text{left of MPP} \quad (2.90)$$

$$\frac{\Delta I}{\Delta V} < -\frac{I}{V}, \quad \text{right of MPP} \quad (2.91)$$

The main idea is to compare the incremental conductance  $\left(\frac{dI}{dV}\right)$  to the instantaneous conductance  $\left(\frac{I}{V}\right)$ . Depending on the result, the panel operating voltage is either increased, or decreased until the MPP is reached. Unlike the P&O algorithm, which naturally oscillates around the MPP, incremental conductance stops modifying the operating voltage when the correct value is reached. A change in the panel current will restart the MPP tracking.

Theoretically this procedure tracks the MPP and maintains it constant without oscillation until the current changes. However, constant MPP can never be obtained in practice and therefore, oscillation is still present near the MPP [85] as in P&O technique. The voltage and current are not constantly at the MPP but oscillating around it. Therefore, in literature [86] is proposed a small value of permitted error,  $e = dP/dV = 0.002$  instead of  $e = 0$  to improve the sensitivity and eliminate the steady state error.

The basic incremental conductance algorithm uses a fixed step size for the panel operating voltage updates. Using a bigger step size will speed up tracking, but may also cause the algorithm to oscillate around the MPP instead of locking on.

Implementing the incremental conductance algorithm requires the voltage and the current output values from the panel (two sensors) and it needs to keep track of previous voltage and current values, as a result the algorithm is usually implemented using a microcontroller or a DSP. [87]

In addition, computation needs to be carried out in IncCond and this will consequently slow down the convergence speed [85]. Experimental results [22] showed for the IncCond method an efficiency of 89.9 % with tracking time of 1.5 sec. The same experimental configuration with the P&O MPPT algorithm resulted in only 81.5% efficiency with tracking time of 7.5 sec.

### 2.10.5 Constant Voltage (CV)

The Constant Voltage (CV) algorithm is the simplest MPPT control method. The operating point of the PV array is kept near the MPP by regulating the array voltage and matching it to a fixed reference voltage  $V_{ref}$ . The  $V_{ref}$  value is set equal to the  $V_{mpp}$  of the characteristic PV module or to another pre-validated best voltage value [88 – 90].

The CV method assumes that insolation and temperature variations on the array are insignificant on the  $V_{mpp}$ , and that the constant reference voltage  $V_{ref}$  is an adequate approximation of the real MPP. Therefore, the operating point is never exactly at the MPP and different data have to be adopted for different geographical regions. [90]

In the constant voltage method the voltage at the MPP is established to the STC ( $V_{mpp(STC)}$ ) and the voltage across the PV module ( $V_{pv}$ ) is compared to this value [91], through:

$$V_{pv} = V_{mpp(STC)} \quad (2.92)$$

The CV method does not require any input. It needs the measurement of the PV array voltage  $V_{pv}$  in order to set up the duty-cycle of the DC/DC converter. [88].

In [90] the CV technique is optimized for a single radiance value; the performance of this technique is strongly related with the voltage set point. It provides satisfying experimental results at low – medium insolation levels, with performance up to 94%. Simulation results presented in [88] for different insolation levels show that the efficiency of the method is on average around 80%, being more effective at low irradiance levels reaching efficiency up to 85%.

To summarize Constant Voltage algorithm is the simplest way to impose the voltage across the photovoltaic terminals; however the voltage value is clamped in

a fixed value and the MPP is not always achieved. The main aspects related to this algorithm are a single sensor (voltage sensor) and its ease of implementation.

### 2.10.6 Fractional open-circuit voltage control

Among the simplest methods for MPP tracking, fractional open-circuit voltage control is most used. It is the most cost effective methodology for small scale PV systems. This method exploits the nearly linear proportional relationship between the operating voltage at MPP ( $V_{mpp}$ ) of a PV module and the open circuit voltage ( $V_{oc}$ ), under varying irradiance and temperature levels [64, 92 – 98].

$$V_{mpp} \approx K_{FOCV} V_{oc} \quad (2.93)$$

where, the proportional constant  $K_{FOCV}$  (fractional open circuit voltage) belongs to the interval (0.70, 0.80) [99]. Table 2.9 shows the behavior of the constant  $K_{FOCV}$  of a solar cell [100], during different irradiance conditions.

Table 2.9. Fractional open circuit voltage, relationship between  $V_{oc}$  and  $V_{mpp}$ .

Adapted from [100].

$V_{oc}$ (V)	$V_{mpp}$ (V)	$K_{FOCV}$
3.24	2.50	0.77
3.40	2.52	0.74
3.40	2.44	0.72
3.60	2.80	0.78
3.60	2.60	0.72
3.96	2.92	0.74
4.50	3.50	0.78
4.50	3.30	0.73

The MPP can be approximated by periodically measuring  $V_{oc}$  by a temporary disconnection of the PV module from the circuit. Of course it is a disadvantage because of the temporarily drop of power. It is important to note that during open circuit the PV array current is zero ( $I_{pv} = 0$ ), no current thus no power is supplied by the PV system and consequently the total energy generated by the PV system is reduced.

To overcome this problem [92] uses a pilot cell from which  $V_{oc}$  can be obtained. A solar cell of only  $0.1 \text{ cm}^2$  it can be used to provide feedback information for the tracker. The pilot cell characteristic should follow almost linearly the behavior of the main PV module during light variations. Reference [97] claims that the voltage generated by pn-junction diodes is approximately 75% of  $V_{oc}$ . This eliminates the need for measuring  $V_{oc}$  and computing  $V_{mpp}$ .

Since equation (2.87) is only an approximation, the PV array technically never operates at the MPP. Depending on the application of the PV system, this can sometimes be adequate. Even if fractional  $V_{oc}$  is not a true MPPT technique, it is very easy and cheap to implement as it does not necessarily require DSP or microcontroller. The interruptions reduce array efficiency and although algorithm does not ensure finding the actual MPP, in [101] the efficiency of the MPPT circuit is stated to be above 95%.

### 2.10.7 Fractional short-circuit current control

Similar to fractional open-circuit voltage control technique is the fractional short-circuit current control. In this case the operating current at the maximum power point is linearly proportional to its short circuit current [67], [102].

$$I_{mpp} \approx K_{FSCC} I_{sc} \quad (2.94)$$

where,  $K_{FSCC}$  is a proportionality constant (fractional short-circuit current) and has to be determined according to the PV array in use. The constant  $K_{FSCC}$  is generally found to be between 0.9 and 0.98 [99].

Measuring  $I_{sc}$  during operation is problematic. An additional switch usually has to be added to the power converter to periodically short the PV array so that  $I_{sc}$  can be measured using a current sensor. This increases the number of components and cost. Power output is not only reduced when finding  $I_{sc}$  but also because the MPP is never perfectly matched as suggested by equation (2.94).

It is important to note that during the short circuit, the PV array voltage is zero ( $V_{pv} = 0$ ), consequently no power is supplied by the PV system and no energy is generated.

Medium convergence speed characterizes this approach [66]. In [103] the response speed was measured 680 msec to illuminance change while the efficiency was 90%.

The proportionality constants ( $K_{FOCV}$ ,  $K_{FSCC}$ ) are dependent on the characteristic of the PV array being used and they usually have to be computed beforehand by determining  $V_{mpp}$  and  $V_{oc}$  or  $I_{sc}$  for the specific PV array at different irradiance and temperature levels.

#### **2.10.8 Other “hill climbing” maximum power point tracking methods**

Both P&O and IncCond algorithms are based on the “hill-climbing” principle, which consists of moving the operation point of the PV array in the direction in which power increases. There are other techniques that can be grouped with the “hill climbing” algorithms such as three point weight comparison P&O method, a modified adaptive hill climbing method, ripple correlation control (RCC) and  $dP/dV$  or  $dP/dI$  feedback control.

##### **2.10.8.1 Three point weight P&O method**

The P&O algorithm compares only two points which are the current operation point and the subsequent perturbation point to observe their changes in power and thus decide whether to increase or decrease the solar array voltage.

Hsiao and Chen [104] use a three point-point weight comparison P&O method. The algorithm compares output power on three points of the P-V curve. The three points are the current operation point (A), a point (B) perturbed from point A and a point (C) with doubly perturbed in the opposite direction from point (B). Efficiency is improved compared to the classical P&O technique and the MPP is better tracked. An efficiency from 86.71% to 95.73% is stated in [88] with changing irradiance condition.

##### **2.10.8.2 Modified adaptive hill climbing method**

Xiao and Dunford [69] proposed a modified adaptive hill-climbing mechanism to prevent deviation from the MPP. The proposed MPPT control can avoid tracking deviation and result in improved performance.

A modified adaptive hill-climbing MPPT control method is introduced including an automatic parameter tuning. When the power changes in a large range primarily due to environmental variation, this tuner (duty cycle) will change to a large value to satisfy the fast response requirement during the transient stage. When the power change is small, the controller assumes that the system enters the steady-state stage and the duty cycle becomes small to keep control signal change smooth. With this tuning mechanism, both dynamic and steady-state requirements can be considered in the controller design, because the critical parameter is updated and adjusted adaptively.

An experiment is presented [69] to test system step response switching on artificial lights and keeping insolation level constant. A period of 23.5 sec was required to track the MPP with an efficiency of 98.45% from the peak power. There is a continuous oscillation of the operating point around the maximum operating point. This continuous oscillation is fundamental to this kind of tracking algorithm.

### 2.10.8.3 Ripple Correlation Control

Ripple Correlation (RCC) correlates the time derivative of the time-varying PV array power  $\frac{dp}{dt}$  with the time derivative of the time-varying PV array current  $\frac{di}{dt}$  or voltage  $\frac{dv}{dt}$  to drive the power gradient to zero, thus reaching the MPP.

Referring to Figure 2.36, if  $v$  or  $i$  is increasing ( $\frac{dv}{dt} > 0$  or  $\frac{di}{dt} > 0$ ) and  $p$  is increasing ( $\frac{dp}{dt} > 0$ ), then the operating point is below the MPP ( $V < V_{mpp}$  or  $I < I_{mpp}$ ). On the other hand, if  $v$  or  $i$  is increasing and  $p$  is decreasing ( $\frac{dp}{dt} < 0$ ), then the operating point is above the MPP ( $V > V_{mpp}$  or  $I > I_{mpp}$ ). Combining these observations, it is  $\frac{dp}{dt} \frac{dv}{dt}$  or  $\frac{dp}{dt} \frac{di}{dt}$  positive to the left of the MPP, negative to right of the MPP, and zero at the MPP [105].

These observations in a form of equations can be written as:

$$\frac{dp}{dt} \frac{di}{dt} > 0 \Rightarrow I < I_{mpp} \quad (2.95)$$

$$\frac{dp}{dt} \frac{di}{dt} = 0 \Rightarrow I = I_{mpp} \quad (2.96)$$

$$\frac{dp}{dt} \frac{di}{dt} < 0 \Rightarrow I > I_{mpp} \quad (2.97)$$

Similar equations apply in terms of voltage. Actually the same criteria is used by the IncCond algorithm but expressed in a different form. Tracking effectiveness varying the irradiance level was in the range of 94.01% to 97.18% in 20msec on experiments performed based in the proposed methodology [105]. The percentage error increases as the power decreases (i.e. irradiance level decreases). Simple and inexpensive analog circuits can be used to implement RCC. Another advantage of RCC is that it does not require any prior information about the PV array characteristics, making its adaption to different PV systems straightforward.

#### 2.10.8.4 $dP/dV$ or $dP/dI$ feedback control

Another control technique is based on  $dP/dV$  or  $dP/dI$  feedback control which computes the slope of the P-V or P-I characteristic curve and feed it back to the controller in order to drive it to zero. The MPP is located where  $dP/dV = 0$  (or  $dP/dI = 0$ ) and equations apply are:

$$\frac{dp}{dv} = \begin{cases} > 0 & \text{if } v < V_{mpp} \\ = 0 & \text{if } v = V_{mpp} \\ < 0 & \text{if } v > V_{mpp} \end{cases} \quad (2.98)$$

Similar equations apply in terms of current. Again this is another implementation of the IncCond algorithm expressed in different form, requiring two sensors for measuring voltage and current values. It is claimed in [106] that over most experimental range, tracking effectiveness was better than 98% with reacquisition time to be less than 10 msec.

However, it is impossible to reach the MPP exactly, because if  $v = V_{mpp}$ , the switch in the DC to DC converter opens, making  $v$  to increase. But this subsequently leads to the switch closing, making  $v$  to decrease. Thus, the voltage wanders around  $V_{mpp}$  following disadvantage accommodated with the IncCond algorithm.



### 2.10.9 Temperature Gradient Method

Another very good option is to use a Temperature technique for tracking MPP. This algorithm employs temperature sensor fixed on the back surface of the PV array and a voltage sensor. It starts by simultaneously measuring the temperature  $T$  and the photovoltaic voltage ( $V_{pv}$ ). The equation that guides the temperature method is:

$$V_{mpp}(T) = V_{mpp}(T_{ref}) + u_{mpp}(T - T_{ref}) \quad (2.99)$$

where  $u_{mpp}$  is the temperature coefficient of  $V_{mpp}$ ,  $T_{ref}$  is the reference temperature [107, 108]. Since,  $V_{mpp}(T_{ref})$ ,  $u_{mpp}$  and  $T_{ref}$  are datasheet information it is clear that the maximum power point voltage  $V_{mpp}$  depend only on the temperature surface  $T$  [109].

However, temperature sensing in practical implementations can be a problematic since due to irregular distribution of PV array (PV array temperature is not uniform throughout) [108, 110]. This can be avoided in small PV converters [108].

Since the temperature on the photovoltaic module surface varies slowly, due to the thermal inertia, the voltage across the PV terminals (strongly dependent on the temperature) will also varies softly. On the other hand, the short circuit current is directly proportional to the irradiation level, thus, its dynamics is faster than temperature one.

This way, it is clear that the PV output power contains two decoupled dynamics, caused by the slow variation of the temperature and the fast oscillations of the irradiation. [109].

The use of the Hill Climbing methods requires a tracking in high speed, to ensure the operation at the MPP even when the radiation varies. However, it causes more oscillations on the output voltage, and trends to become the tracking unstable. In contrast, when the MPP-temp algorithm is employed, only the temperature measurement is taken into account, thus the fast dynamic is taken out of the algorithm and the tracking trends to become more stable, i.e., the MPP is softly tracked. [109]

From simulation results in Matlab/Simulink presented in [91] it is possible to notice that the use of particular sensors in temperature method has direct impact on the MPP efficiency especially at low irradiance levels. Although at 1000 W/m<sup>2</sup> the efficiency is 99.03%, at 500 W/m<sup>2</sup> efficiency drops to 89.63% while tracking speed is 22.5 msec when the algorithm is initialized (from 0 to 1000 W/m<sup>2</sup>).

#### **2.10.10 Current and Temperature Method (I&T)**

A methodology is presented in [91] that incorporates two variables, short circuit current and temperature gradient, in order to directly relate the influence of the irradiance and temperature on the PV module characteristics. This method requires an extra sensor compared to Temperature Gradient methodology in order to measure current.

Performance and tracking speed have improved compared to Temperature algorithm. Efficiency above 99% in all cases (low or high irradiance levels) has been noticed and tracking speed is almost 18msec (from 0 to 1000 W/m<sup>2</sup>) [91]. Moreover, it presents low ripple in steady state condition, around the MPP. Finally, it has to be stated that results refer to simulations performed in Matlab/Simulink program.

#### **2.10.11 Look Up Table (LUT)**

In this method prior knowledge of PV panel material, technical data, panel characteristics at different environmental conditions are required and are stored. Then the PV panel output current  $I_{pv}$  and output voltage  $V_{pv}$  are sensed, power is calculated and compared with those of stored values to track MPP and operating point is shifted to new maximum power point. Thus, large amount of data required to be stored before actually tracking MPP and system requires a large memory capacity to store prior data. Also, system becomes complex for varying atmospheric conditions [110].

A lookup table for varying light requires a 2-D array for each possible voltage and current. Adding the ability to compensate for temperature makes the array 3 dimensions, and adding system aging requires 4 dimensions.

In [111] tracking efficiency of the proposed algorithm is around 95% and tracking time required is 15 msec.

### 2.10.12 Simulation Results Evaluating MPPT Methods

Simulations in Matlab/Simulink have performed in [91] in order to evaluate six MPPT methods, concerning irradiance and temperature variations. Figure 2.38 shows the block diagram utilized in the particular study.

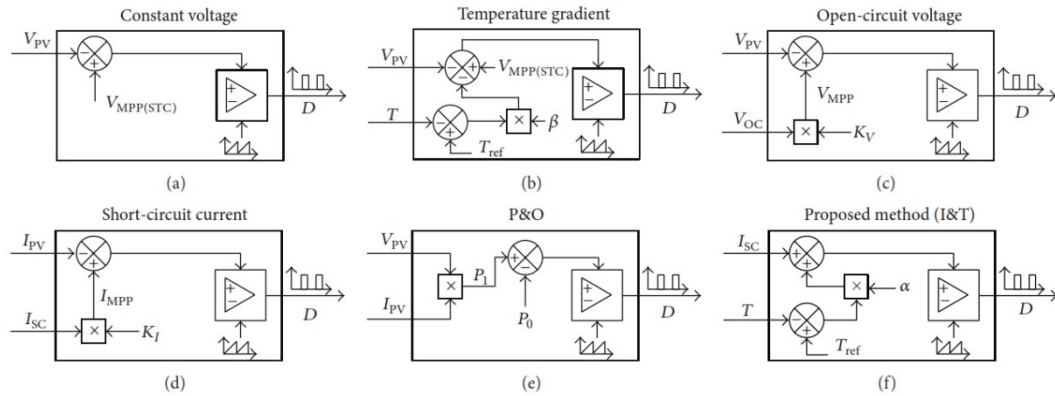


Figure 2.38. Block diagram representation of MPPT methods a) constant voltage; b) temperature gradient; c) open circuit voltage; d) short circuit current; e) P&O; f) I&T. Reproduced from [91].

Analytically, in the constant voltage method, the voltage at the MPP is established to the STC ( $V_{MPP(STC)}$ ) and the voltage across the PV module ( $V_{PV}$ ) is compared to this value, through equation (2.92). The duty cycle output ( $D$ ) is the result of the voltage error ( $V_{error} = V_{MPP(STC)} - V_{PV}$ ) and the reference signal (sawtooth wave) comparison.

The temperature gradient technique uses the PV module temperature ( $T$ ) to modify operating point of the PV module according to the voltage/temperature coefficient ( $\beta$ ), (in equation (2.99) temperature coefficient is denoted as  $u_{mpp}$ ).

Another widespread method is the fractional open circuit voltage described by equation (2.93) and a similar technique the fractional short circuit current described by equation (2.94). The MPP is determined by means of a constant of proportionality  $K_V$  and  $K_I$  in the block diagrams.

The P&O operates by periodically changing the duty cycle of the dc-dc converter, comparing the previous ( $P_0$ ) and the present ( $P_I$ ) output power, according to Table 2.8.

The final block diagram is the I&T method that uses the short circuit current and temperature variables to determine MPP. Variable  $\alpha$  is the sensitivity of current with respect to temperature and  $T_{ref}$  is the temperature under STC (25°C).

Based on the described block diagrams in Matlab/Simulink, simulation results are going to be presented. For the first test, temperature is kept constant at 45°C and irradiance varies from 100 W/m<sup>2</sup> to 1000 W/m<sup>2</sup>, in order to evaluate the steady-state behavior of the system [112]. The results are shown in Figure 2.39. The highest efficiency methods are the I&T and P&O with good approximation of MPPT at steady state.

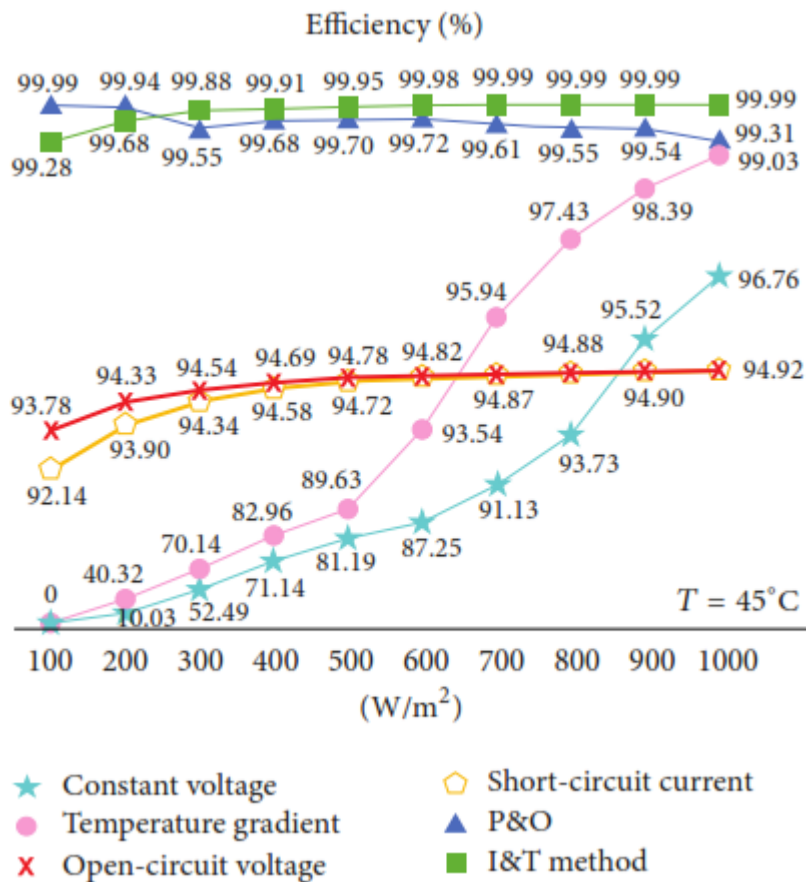


Figure 2.39. Efficiency of MPPT techniques considering irradiance variation.

Reproduced from [91].

Simulation results regarding PV power output with respect to time, for the six MPPT methods in the situation of 1000 W/m<sup>2</sup> and 45°C, are illustrated in Figure 2.40.

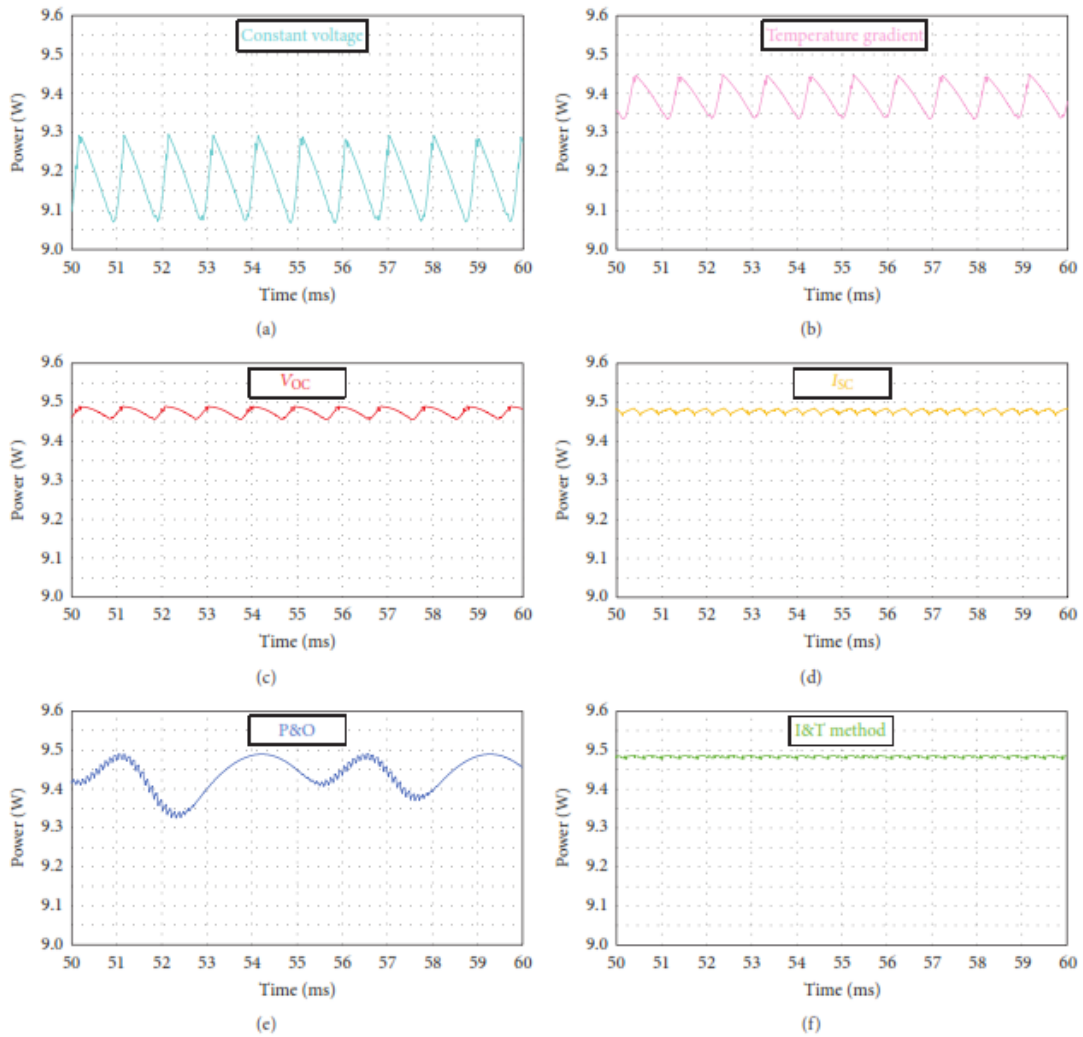


Figure 2.40. Steady-state behavior of MPPT techniques ( $1000 \text{ W/m}^2$ ,  $45^\circ\text{C}$ ): (a) constant voltage; (b) temperature gradient; (c) open-circuit voltage; (d) short-circuit current; (e) P&O; (f) I&T. Reproduced from [91]

It is possible to observe that the system oscillates around the MPP. The I&T, short-circuit and open-circuit voltage methods have the smaller oscillation magnitude. Despite having low oscillation in the MPP the average efficiency of short circuit current and open circuit voltage methods is below other methods mainly due to the need for periodic sampling and disconnection of the circuit for parameters measurements.

Other four situations have also been evaluated in [91]: standard test condition ( $STC - 1000 \text{ W/m}^2$ ,  $25^\circ\text{C}$ ); step change in irradiance ( $S - 1000 \text{ W/m}^2$  to  $500 \text{ W/m}^2$ ); step change in temperature ( $T - \text{from } 65^\circ\text{C} \text{ to } 25^\circ\text{C}$ ); and, finally, both step changes in irradiance and temperature ( $S+T$ ). The results are presented in Figure 2.41. The most efficient methods are P&O and I&T in all situations examined, compared to other available methodologies.

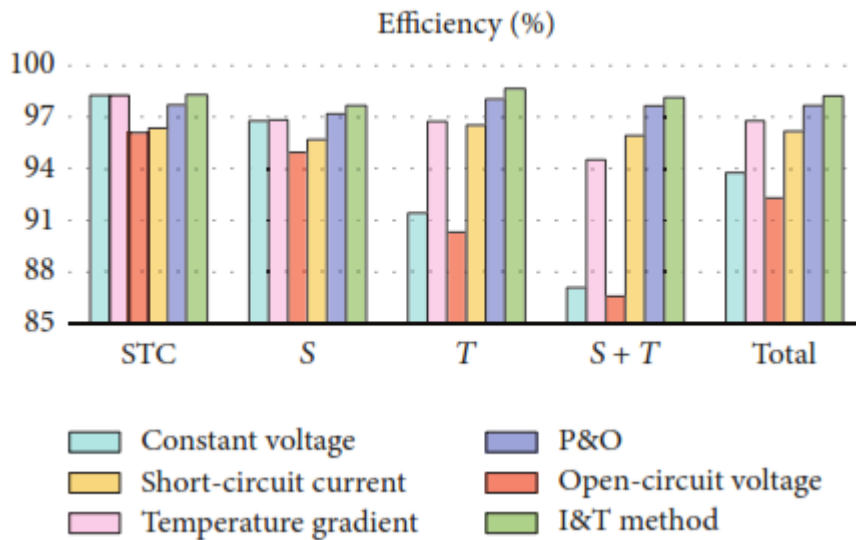


Figure 2.41. Efficiency of MPPT techniques considering both irradiance and temperature variation. Reproduced from [91].

The tracking efficiency of MPPT techniques is analyzed in Figure 2.42, for the situation where both step changes in irradiance and temperature occur ( $1000 \text{ W/m}^2$  to  $500 \text{ W/m}^2$  and  $65^\circ\text{C}$  to  $25^\circ\text{C}$ ). The output power of each method is graphically compared with the maximum power (dashed line - gray color, almost  $9 \text{ W}$  up to  $300 \text{ msec}$  and just below  $5 \text{ W}$  from  $300 \text{ msec}$  to  $600 \text{ msec}$ ).

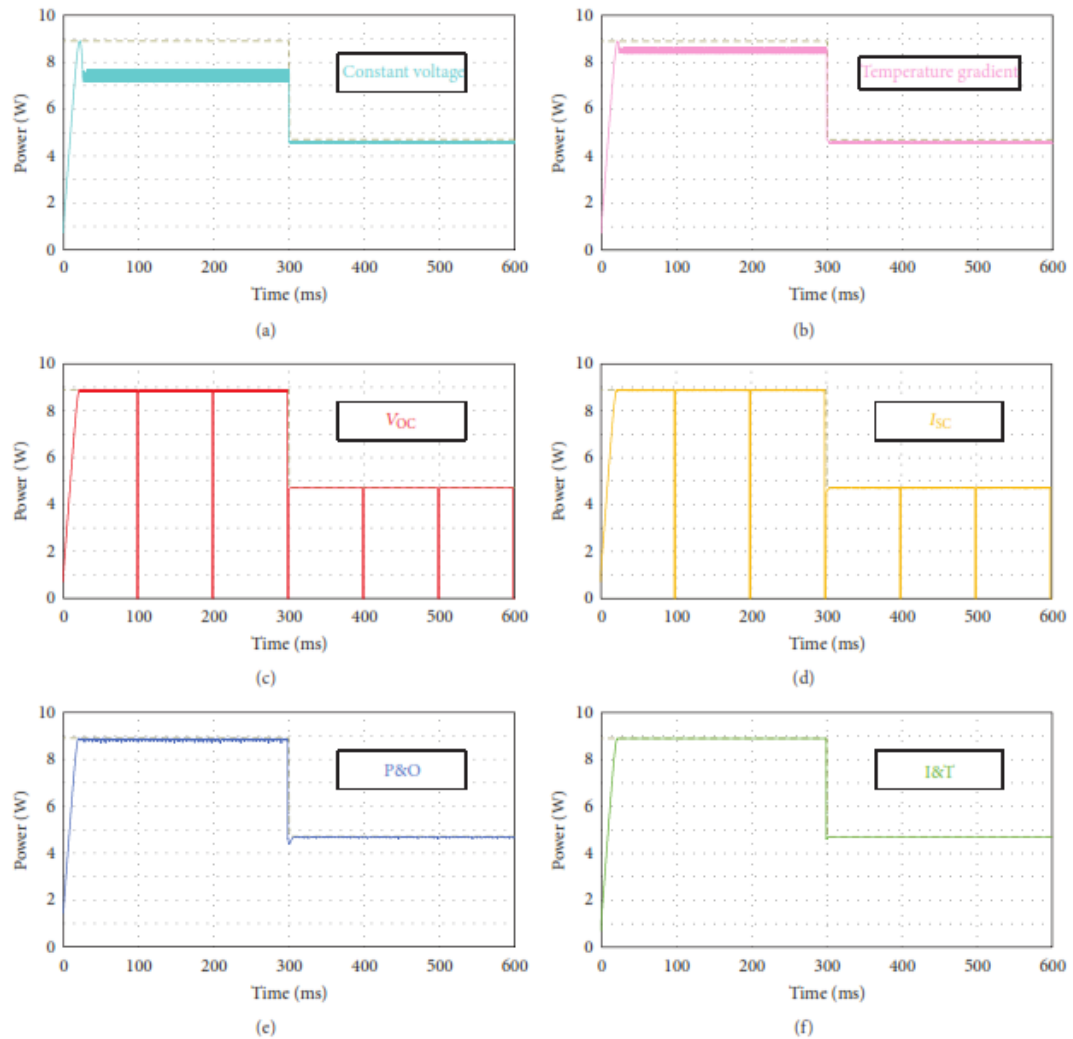


Figure 2.42. Tracking efficiency of MPPT techniques ( $1000 \text{ W/m}^2$  to  $500 \text{ W/m}^2$  and  $65^\circ\text{C}$  to  $25^\circ\text{C}$ ): (a) constant voltage; (b) temperature gradient; (c) open-circuit voltage; (d) short-circuit current; (e) P&O; (f) I&T. Reproduced from [91].

From results, presented in Figures 2.39 to 2.42, it is possible to notice that the use of a reduced number of sensors in methods, such as constant voltage and temperature gradient, has direct impact on the MPPT efficiency, especially at low irradiance levels. The open-circuit voltage and short circuit current methods perform periodic sampling of the PV module parameters. These methods present considerable power losses due to the need of disconnecting the circuit for measurement, as well as operating at lower power points between samples [88, 113]. P&O method has high efficiency. However, the output power oscillates around the MPP in steady-state condition and the technique is not adequate when there are abrupt variations of solar irradiance [88, 79]. Additionally, it requires greater computational effort due to calculation continuously required. I&T method has high efficiency with low ripple in steady-state condition. Calibration of

temperature sensor is a problem for precision measurements which may cause wrong tracking also [110]. Furthermore, the temperature algorithms require datasheet information regarding the PV array and the algorithms has to be updated to ensure accurate operation of the PV system and compensate for parameters changes caused by system aging [109].

In [111] comparison of Look up Table method against conventional methods is performed. The conventional MPPT algorithms like P&O and INC based on fix step algorithm are also simulated in Matlab/Simulink and tested for changing illumination conditions. The performance is illustrated in Figure 2.43.

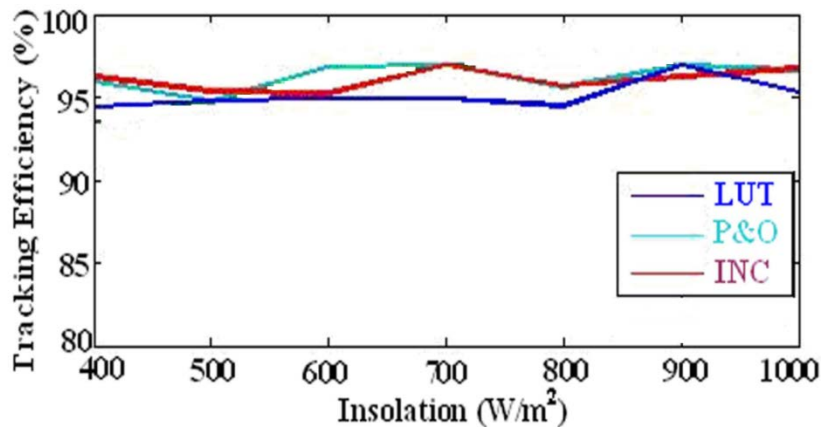


Figure 2.43. Efficiency of MPPT methods at changing insolation condition.

Adapted from [111].

All the methods examined are almost equally efficient. The Incremental Conductance method has slightly higher efficiency than the other methods. The LUT based method has very slight decrease in efficiency. [111]

Comparison of different MPPT techniques has performed in this section presenting simulation results and graphs in Matlab/Simulink available in the literature. A Table summarizing commonly used techniques examining major characteristics of MPPT methodologies will presented in the next section.

### 2.10.13 Discussion

Different MPPT techniques have been reviewed and compared in this Chapter. Advantages and disadvantages of these methods have been addressed to give better understanding, on the basis of array dependency, true MPPT, implementation complexity, sensors used, hardware requirement, cost, tracking speed and performance.



Table 2.10. Major Characteristics of MPPT Techniques.

<b>MPPT Technique</b>	<b>PV Array Dependent</b>	<b>True MPPT</b>	<b>Implementation Complexity</b>	<b>Sensed Parameters</b>	<b>Digital or Analog</b>	<b>Cost</b>	<b>Transient Speed</b>	<b>Tracking Accuracy</b>
CV	Yes	No	Simple	$V$	Digital	Low	Slow	Low (80%)
FOCV	Yes	No	Simple	$V$	Both	Low	Medium	Medium (90-94%)
FSCC	Yes	No	Simple	$I$	Both	Medium	Medium	Medium (90-94%)
P&O/Hill Climbing (Fixed Perturb. Size)	No	Yes	Simple	$V, I$	Both	Medium	Slow	Low (81.5%)
InC	No	Yes	Medium	$V, I$	Digital	High	Varies	Medium (90%)
Three Point MPPT	No	Yes	Complex	$V, I$	Digital	High	Varies	Medium (86-96%)
Mod. Adaptive Hill Climbing	No	Yes	Complex	$V, I$	Digital	High	Fast	High (98.5%)
RCC	No	Yes	Complex	$V, I$	Analog	High	Fast	High (94-97%)
dP/dV or dP/dI Feedback Control	No	Yes	Medium	$V, I$	Both	High	Fast	High (98%)
Look Up Table	Yes	No	Complex	$V, I$	Digital	Medium	Fast	High (95%)
Temperature Gradient	Yes	Yes	Medium	$V, T$	Both	High	Medium	Medium (90%)
I&T	Yes	Yes	Complex	$I, T$	Digital	High	Fast	High (99%)

The Constant Voltage is the worst of the available techniques because it fixes the reference voltage to a best voltage value and holds it constant under any operating condition instead of following the MPP [88]. However, the CV technique is more effective than P&O and INC techniques when the PV array is operated at low insolation levels and it has low implementation cost compared to the other MPPT techniques [114].

The FOCV and FSCC have better performance with moderate complexity. An additional static switch is required to perform the open-circuit or short circuit condition that increases the losses and performance is reduced. Both of them are approximation methods and the power output is not only reduced when finding  $V_{oc}$  or  $I_{sc}$  but also the MPP is never perfectly matched.

In the literature [88, 115] it has been highlighted that the P&O and INC techniques are the most efficient compared to other available MPPT methods. The P&O is the most widely applied method because of its ease of implementation. In this algorithm when atmospheric condition changes slowly or constant, the P&O algorithm oscillates around the MPP and when these change rapidly this method has incorrect or slow power tracking. As described oscillation is due to fixed step size [116, 117, 118]. There are several improvements that have been made to the conventional P&O method to reduce the oscillation around the MPP in the steady state condition. Each of these improved algorithms have reduced the oscillation to different extend but they increase the complexity and algorithm efficiency degrades in cloudy days [116].

The main advantage of INC algorithm is that it offers an effective solution under rapidly changing atmospheric conditions. It exhibits less oscillatory behavior around the MPP compared to P&O even when the P&O method is optimized [119]. The main drawback is that it requires complex control circuitry [120]. Also under low levels of insolation the differentiation process difficult and prone to measurement noise; and results can be unsatisfactory [121].

In the case of Look Up Table method, the measured values of the PV generator's voltage and current are compared with those stored in the controlling system, which correspond to the operation at the maximum point, under predetermined climatologically conditions [122]. This algorithm has the disadvantage that a large capacity of memory is required for storage of the data. Moreover, the

implementation must be adjusted for a specific PV panel. It is difficult to record and store all possible system conditions. But it has also some advantages. The system is able to perform fast tracking, as all the data regarding maximum point are available [123].

Temperature based MPPT algorithms are also available. Performance is improved in the I&T technique compared to the simpler Temperature Gradient method. Certain disadvantages are that PV array temperature is not uniform throughout and also calibration of temperature sensor is a problem for precision measurements which may cause wrong tracking [110].

## **2.11 Review on current solar simulators**

### **2.11.1 Solar simulator based on PV Sandia Database**

Work presented in [124] uses an existing power supply which is manipulated via Labview to emulate a photovoltaic panel. The emulator calculates a current-voltage (I-V) curve based on the user specified parameters of panel model, irradiance and temperature.

This system consists of a computer with control software and a power supply. The software uses user specified parameters such as solar panel type, irradiance, and temperature and will calculate the I-V curve for the power supply to follow.

To test that the power supply is able to follow the I-V curve correctly, a decade resistor box is connected to the power supply. The resistance is varied from a large resistance to a small resistance to have the PV emulator sweep through the I-V curve. A supply such as a 'BK Precision 9153' power supply [124] allows for uncomplicated communication between the computer and power supply and using a Sandia PV database, 284 different panels can be emulated.

The basic algorithm to model any given photovoltaic module is obtained from existing models developed in Matlab [125] based on the single diode equivalent circuit model. The algorithm obtained from the Matlab code was then modified to allow the emulation of solar panels from the Sandia PV database in Labview. The Labview environment can change the I-V characteristic based on the simulated irradiance and temperature as well as the specific PV model type.

### 2.11.2 Solar simulator light sources

Outdoor environmental variability leads to the need of artificial illumination systems for PV module characterization. The second approach is to use a light source solar emulator consisting of one or several lamps illuminating a PV test device. Typically, the I–V characteristics are measured by 1 sun ( $100 \text{ mW/cm}^2$ , 1.5 AM) solar simulator using the Xenon lamp. However, employment of the Xenon lamp has several drawbacks such as high cost, large space, and the high power consumption. Additionally, a Xenon light has a spectral mismatch with the sun light especially in the infrared, so typically a Xenon lamp combined with a tungsten lamp is required. However, there still remains the disadvantages of short life time and high power consumption of the Xenon lamps in the simulators [126]. A detailed review of light sources (tungsten halogen and Xenon) used in conventional solar simulators can be found in [127, 128].

Increasingly solar simulators employ a range of LEDs as a light source with lower cost and lower power consumption than Xenon lamp [126, 129, 130] are being deployed. LEDs as the main light source have a much longer lifetime than conventional high-intensity simulator bulbs (up to 100,000 h), which reduces maintenance costs, these new system also allow much better tuning of intensity and spectral matching.

One such LED-based solar simulator has been developed by researchers at Loughborough University [131, 132]. The principle construction of an LED-based solar simulator is not too dissimilar from that of conventional multi-lamp solar simulators. As depicted in Figure 2.44, the main difference is to have arrays of narrow-wavelength LEDs instead of lamps covering the whole spectral range of interest as the main illuminating source in order to provide a quasi-continuous-wavelength light output on the solar cell test area.

The simulator developed at Loughbororough used an array of 378 LEDs in 8 different colors, to provide spectral coverage from the ultraviolet at 375 nm to the red end of the spectrum at 680 nm. In the prototype, halogen lights covered the infra-red part of the spectrum, while developments are ongoing to replace this with LEDs in the final product. The area of the light sources is 380 x 380 mm and the distance to the illuminated test area is 650 mm. The control system, shown in a simplified schematic overview in Figure 2.45, allows independent control and

adjustment of the intensities of all light sources. This makes it possible to find an adequate match to the AM1.5 standard. A temperature control system is also embedded in the simulator, capable of regulating the test device temperature from 10°C to 80°C. The simulator is controlled by a PC with in - LabVIEW software. Routines for long and short time measurements can be easily configured and are carried out fully automated.

Figure 2.46 illustrates solar simulator with pointers to the positions of each of the main parts. The system works automatically and combines the functionality of several different types of costly equipment. [131]

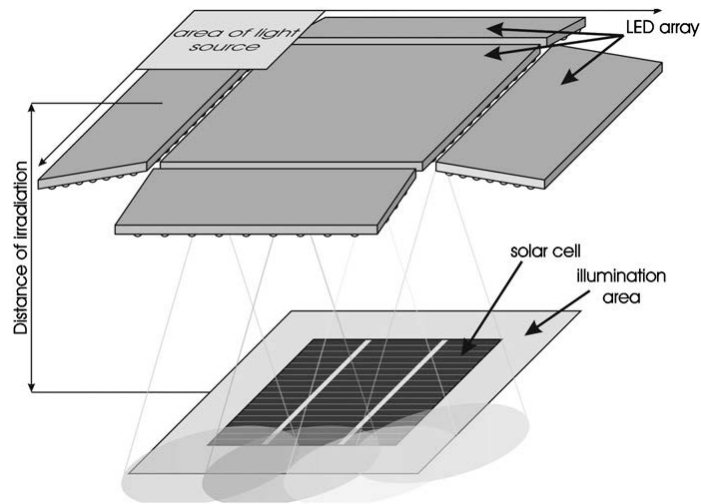


Figure 2.44. Schematic diagram of an LED-based solar simulator. Reproduced from [130].

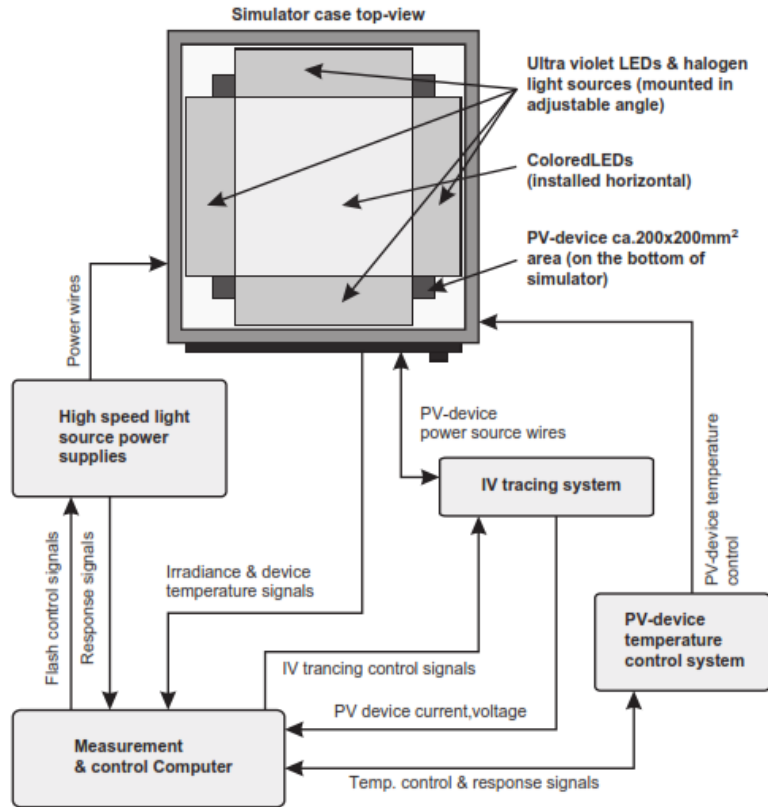


Figure 2.45. Simplified schematic overview of an LED based solar simulator.

Reproduced from [130].

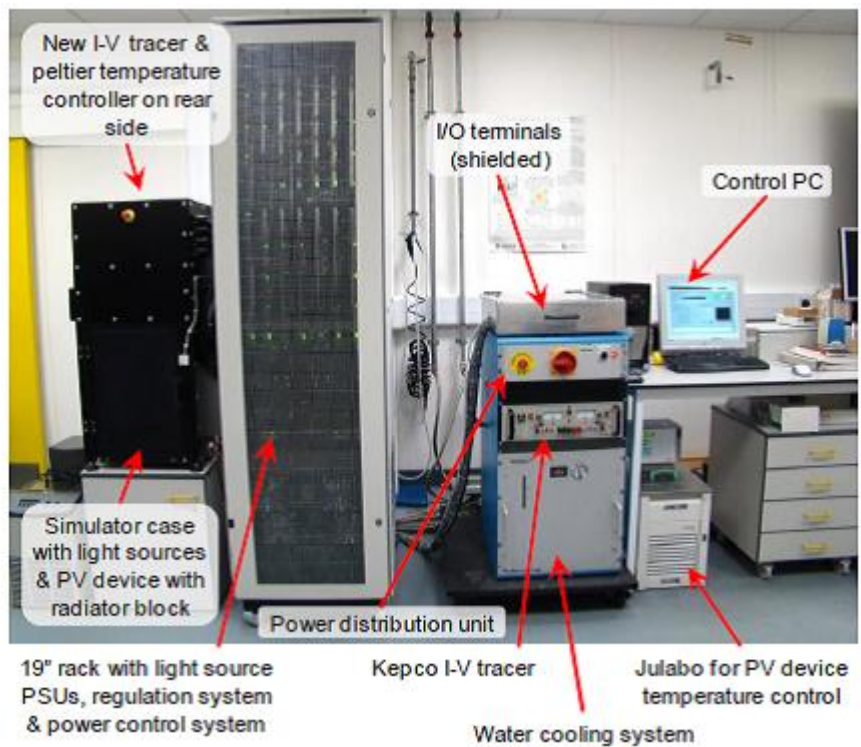


Figure 2.46. LED based solar simulator prototype with parts description.

Reproduced from [131].

It is clear that a standard PV device placed within an LED-based solar simulator, could provide a platform for any PV system optimization, with suitable software able to control the device heater and the LED array in order to repeatably mimic outdoor conditions, however this and similar schemes based around devices and light sources are large and expensive to implement.

### 2.11.3 SunaPlayer: Emulation Platform of Solar Cells

A medium range emulation platform SunaPlayer [133] uses a high gain analog device, a PNP darlington transistor, a multi-scale driving and measurement circuit and a novel proportional integral differential controller to build an accurate non-linear model of the solar panel presented in Figure 2.47. The emulator takes IV curves as input and emulates the solar cell for a given load.

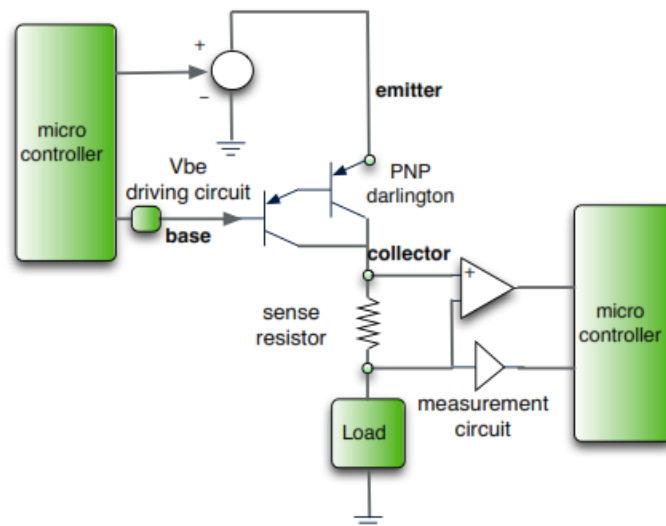


Figure 2.47. SunaPlayer emulation platform of solar cells. Reproduced from [133].

It operates in two modes - offline mode; and online mode. In the offline mode, the system is programmed with a set of solar panel IV traces. The SunaPlayer chooses an IV trace to emulate and automatically finds the correct operating voltage and current on the IV trace for a given load. The IV traces could correspond to solar panel profiles for different lighting and temperature conditions. They could also correspond to IV curves for solar panels of different sizes and compositions. If the solar panel data is not collected experimentally, the system can also use IV data from datasheets. In the online mode, the SunaPlayer senses the ambient light intensity and selects the appropriate IV curve to emulate. The online mode is

useful for testing a system on a set of solar panel data for real deployed system. The SunaPlayer measures the ambient light intensity using the onboard light sensor and selects the appropriate IV curve. It switches from one IV curve to the other when the light intensity changes, and automatically converges to a new operating point.

In the SunaPlayer design, the darlington's emitter voltage,  $V_e$ , is controlled by a  $V_+$  programmable power supply ( $V_e = V_+$ ). The value of  $V_+$  depends on the solar cell being emulated and it helps limit the output voltage of the emulator, similar to the voltage limiting characteristic of a solar cell.

The multi-scale circuit to drive the base voltage of the PNP darlington is illustrated in figure 2.48. The circuit uses a combination of fine adjustment that provides the SunaPlayer with the ability to fine-grain control the changes in  $V_{be}$  and a coarse adjustment that helps generate base voltages close to  $V_e$  ( $V_+$ ) for small output currents. The fine-grained control line is combined with the coarse grained adjustment using an amplifier and a set of resistors that create a summing amplifier.

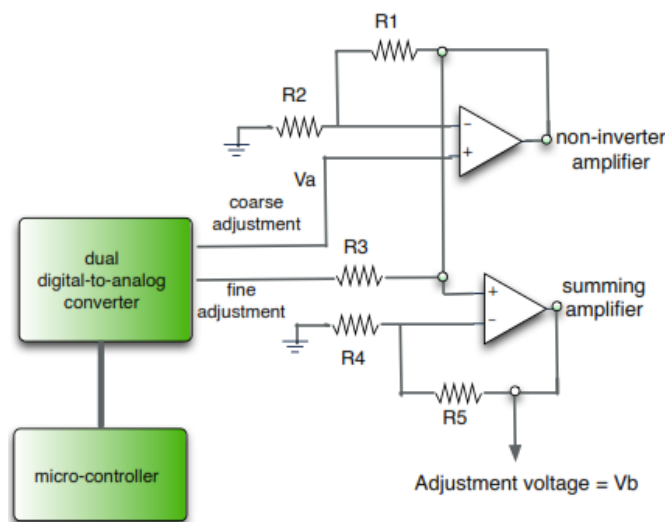


Figure 2.48. The multi-scale circuit to drive the base voltage of the PNP darlington. Reproduced from [133].

Measurements of load current and voltage are performed according to electronic circuit presented in Figure 2.49. Analytically, the load current is measured by the voltage induced across a low tolerance  $1 \Omega$  sense resistor, attached to the collector. An instrumentation amplifier, with programmable gains of 1, 10, 100, and 1000, amplifies the voltage across the sense resistor. The use of multiple gain



levels allow accurate current measurements for low and high currents. For accurate measurements, the voltage output from the amplifier is clamped using diodes, so that the output voltages do not fall below -0.3V or is above 3.0V. To measure the load voltage, a high input impedance voltage follower amplifier is used.

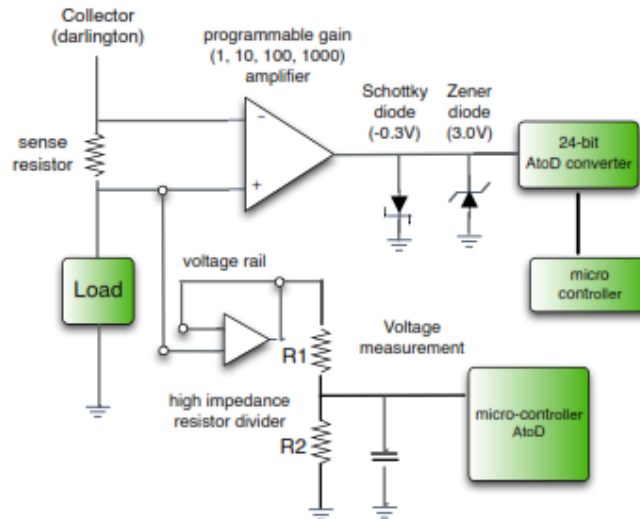


Figure 2.49. The multi-scale circuit for measuring the output voltage and the output current. Reproduced from [133].

The SunaPlayer caches  $V_{be}$ , the output current, and the output voltage in a lookup table (LUT). The SunaPlayer can then use these cached values to improve convergence when the desired output voltage and current is close to a cached value. When the SunaPlayer controller determines the predicted operating point on the IV curve, it searches the entries in the look up table to find the output voltage and output current that has the smaller error to the predicted value. The system then sets the bias voltage,  $V_{be}$  in the LUT entry. Caching operating points reduce the number of iterations required by the controller to converge.

SunaPlayer is a solar panel emulation platform that supports medium range systems with output currents up to 1.89A and voltage up to 9.8V. The primary objective is to replay continuously IV curve logging to enable repeatable design-time experimental results by emulating energy sources [134].

## 2.12 Conclusions

In this Chapter a literature review on aspects related to the thesis were presented. Fundamentals of silicon solar cell design were discussed. This work is focused on

silicon solar cells and their characteristics, since they are currently 95% of solar cell market [23]. PC1D software simulator program will be extensively used in this work to provide accurate modeling of device behavior.

The efficiency of a PV system is affected by the efficiency of the panel as well as by the efficiency of the MPPT algorithm. People work hard on cell efficiencies with innovations in the device design, however system and MPPT efficiencies are just as important. The MPPT techniques vary between them in many aspects, including simplicity, convergence speed, digital or analog implementation, sensors required, cost, range of effectiveness and need for parameterization.

Among these techniques, the P&O and the IncCond algorithms are the most common. These techniques have advantages but they also have drawbacks. The advantages of both methods are the easy implementation, simplicity, low computational power and good performance when the irradiation is constant [135, 136]. The shortcomings are oscillations around the MPP, slow transient response and they can get lost and track the MPP in the wrong direction during changing atmospheric conditions [22, 135, 136, 137]. Modified versions of “hill climbing” principle based on the fundamental theory of P&O or IncCond algorithms have shown to improve performance.

Other techniques based on different principles fractional open circuit voltage or short circuit current. Most of these methods give an approximated MPP, not the exact one. They have the particular feature of not obtaining but rather estimating the MPP for either irradiance or temperature [138]. A strategy has developed measuring only one variable (current or voltage) in contrast to previous methods requiring measurements of both variables (voltage and current).

It is clear that, there has been a lot of research in the P&O and IncCond algorithms, for this reason the project research has focused in a different methodology for determining the MPP using the equivalent electrical circuit model of solar cell and the 5 model parameters characteristic equation. A mathematical analysis of MPP is presented in the next Chapter deriving mathematical formulas that determine maximum current and maximum voltage.

The analysis will be based upon single diode electrical equivalent model of a solar cell. Single diode model requires less computation effort compared to the two diode model, it has a simplified electrical circuit and mathematical equation that

describe device operation. In the same time it describes accurately the I-V characteristic curve and results show a small discrepancy between the two models [48].

There exist a range of different solar emulator systems. Power supplies are available in the market that can perform solar panel emulation. System operation in [124] is based on a simplified version of a single diode model (shunt resistor is not considered) and the power supply is manipulated accordingly.

Another category are the solar simulators based on light sources. The spectral output is manipulated by optics and filters to achieve a good match to the AM 1.5 standard spectrum. Such systems are very expensive since they are based on functionality of several costly pieces of equipment. These simulators have in general very high operational costs, because of the high energy consumption of the light sources and limited lamp lifetime, dependent on the type of light source. Maintenance (replacement of light source) and homogeneity adjustments, checking upon specifications of uniformity over illumination area, spectral symmetry and intensity, increases costs as the recalibration is a slow and elaborate procedure.

SunaPlayer [133] uses a host of physical electronic devices to build a model of solar panel. Its architecture is based on a pair of bipolar junction transistors (BJT), a PNP darlington transistor. It takes IV curve as an input and emulates a solar cell. It selects an IV curve, stored in a card reader, from solar panel curves collected either experimentally or from datasheets. Generation of IV curves for solar cells is out of the scope of the SunaPlayer.

Solar panel emulating platforms are intended to aid the design of PV systems. In this work we designed and built a fully functional prototype emulation platform and it will be demonstrated that it can accurately mimic solar cell operation over a wide range of environmental conditions. The development of the platform is based upon a single bipolar junction transistor model which will be illustrated that is electrically equivalent to a solar cell.

The combination of a prototype system which emulates accurately the solar cell behavior – operation along with the development of a MPPT platform able to operate with different MPPT algorithms available in the literature are two helpful

tools for any laboratory involved in photovoltaics and can assist on a variety of photovoltaic applications.

## 3 Derivation of maximum power point

### 3.1 Introduction

In this chapter a mathematical expression of maximum voltage, current and power is derived based on the single diode equivalent electrical circuit of a solar cell. The model contains 5 fitting parameters including: the photocurrent  $I_{ph}$ , the saturation current  $I_o$ , the ideality factor  $n$ , the series resistance  $R_s$  and the shunt resistance  $R_{sh}$ . The behavior of the photovoltaic module is described by a current – voltage characteristic in which can be described by these parameters, that, in turn are dependent on solar irradiance and temperature. The maximum experimentally predicted voltage, current and power are compared to theoretical data provided by four different photovoltaic modules, in order to confirm the validity of the model.

### 3.2 The current - voltage relationship for a photovoltaic device

Equivalent circuit models have long been used to provide an analytical description of solar cell behavior. The most common model used is the “single diode model” [43], described in Chapter 2, shown in Figure 2.7. This equivalent circuit is composed of an optically generated current source, a diode, and series and shunt resistances. The current – voltage relationship at a fixed cell temperature and solar radiation is described by equation (2.21).

This circuit can be used either for an individual cell, for a module consisting of several cells or for an array consisting of several modules. When the solar cells are arranged in  $N_p$  – parallel and  $N_s$  – series to form a module (figure 3.1), the current – voltage equation becomes as following [139]:

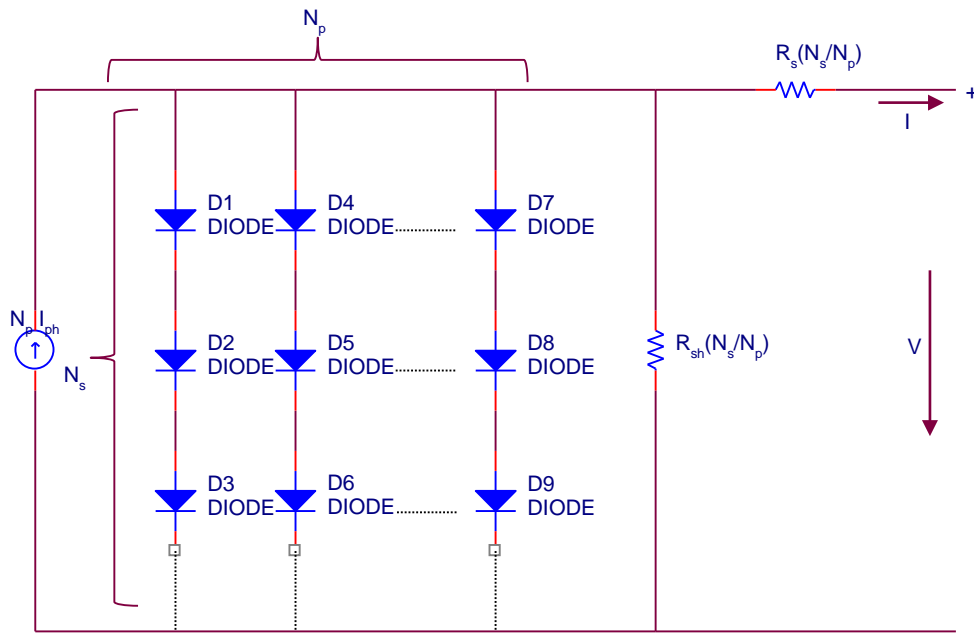


Figure 3.1. “Solar array equivalent circuit” ( $N_s$  – series,  $N_p$  – parallel). Adapted from [139].

$$I = N_p I_{ph} - N_p I_o \left( \exp \left( \frac{V}{N_s V_t} + \frac{I R_s}{N_p \cdot V_t} \right) - 1 \right) - \frac{1}{R_{sh}} \left( \frac{V}{N_s} + \frac{I R_s}{N_p} \right) \quad (3.1)$$

In principle, given a particular operating voltage  $V$  the equation (3.1) may be solved to determine the operating current at that voltage. However, the equation involves  $I$  - current on both sides in a transcendental function  $I=f(V, I)$ .

In this work maximum current  $I_{mpp}$  and maximum voltage  $V_{mpp}$  are both expressed as function of a new variable  $A$  i.e.  $I_{mpp}=f(A)$  and  $V_{mpp}=f(A)$ . In this way  $I_{mpp}$  and  $V_{mpp}$  are determined in terms of the five parameters described above. A current-independent voltage expression is derived for the maximum operating point.

### 3.3 Theoretical Analysis - Equations for Determining $I_{mpp}$ , $V_{mpp}$ , $P_{mpp}$ and $A$

The following derivations can be performed to determine both voltage and current at the maximum power point.

Working with equation (3.1):

$$I = N_p I_{ph} - N_p I_o \left( \exp \left( \frac{VN_p + IN_s R_s}{N_s N_p V_t} \right) - 1 \right) - \frac{1}{R_{sh}} \left( \frac{VN_p + IN_s R_s}{N_s N_p} \right) \quad (3.2)$$

a new term  $A$  can be defined:

$$A = \frac{VN_p + IN_s R_s}{N_s N_p} \quad (3.3)$$

So, equation (3.2) becomes:

$$I = N_p I_{ph} - N_p I_o \left( \exp \left( \frac{A}{V_t} \right) - 1 \right) - \frac{A}{R_{sh}} \quad (3.4)$$

Power is voltage times current:

$$P = VI \quad (3.5)$$

Thus:

$$P = VN_p I_{ph} - VN_p I_o \left( \exp \left( \frac{A}{V_t} \right) - 1 \right) - \frac{VA}{R_{sh}} \quad (3.6)$$

$$P = VN_p I_{ph} - VN_p I_o \exp \left( \frac{A}{V_t} \right) + VN_p I_o - \frac{VA}{R_{sh}} \quad (3.7)$$

Recognizing that the derivative of power at maximum power point is zero.

$$\frac{dP}{dV} = 0 \quad (3.8)$$

and according to the properties of derivatives:

$$df = \frac{\partial f}{\partial x} dx + \frac{\partial f}{\partial y} dy \quad (3.9)$$

So,

$$dP = \frac{\partial P}{\partial V} dV + \frac{\partial P}{\partial A} dA \Rightarrow \frac{dP}{dV} = \frac{\partial P}{\partial V} + \frac{\partial P}{\partial A} \frac{dA}{dV} \quad (3.10)$$

calculating the terms  $\frac{\partial P}{\partial V}$  and  $\frac{\partial P}{\partial A}$  separately using equation (3.7) gives:

$$\frac{\partial P}{\partial V} = \frac{\partial \left( VN_p I_{ph} - VN_p I_o \exp\left(\frac{A}{V_t}\right) + VN_p I_o - \frac{VA}{R_{sh}} \right)}{\partial V} \Leftrightarrow$$

$$\frac{\partial P}{\partial V} = N_p I_{ph} - N_p I_o \exp\left(\frac{A}{V_t}\right) + N_p I_o - \frac{A}{R_{sh}} \quad (3.11)$$

Also,

$$\frac{\partial P}{\partial A} = \frac{\partial \left( VN_p I_{ph} - VN_p I_o \exp\left(\frac{A}{V_t}\right) + VN_p I_o - \frac{VA}{R_{sh}} \right)}{\partial A} \Leftrightarrow$$

$$\frac{\partial P}{\partial A} = -\frac{VN_p I_o \exp\left(\frac{A}{V_t}\right)}{V_t} - \frac{V}{R_{sh}} \quad (3.12)$$

Thus, equation (3.10) due to (3.11) and (3.12) becomes:

$$\frac{dP}{dV} = \frac{\partial P}{\partial V} + \frac{\partial P}{\partial A} \frac{dA}{dV} \Leftrightarrow$$

$$\frac{dP}{dV} = N_p I_{ph} - N_p I_o \exp\left(\frac{A}{V_t}\right) + N_p I_o - \frac{A}{R_{sh}} - \left( \frac{VN_p I_o \exp\left(\frac{A}{V_t}\right)}{V_t} + \frac{V}{R_{sh}} \right) \frac{dA}{dV} \quad (3.13)$$

Considering equation (3.8) for maximum power point, equation (3.13) becomes

$$N_p I_{ph} - N_p I_o \exp\left(\frac{A}{V_t}\right) + N_p I_o - \frac{A}{R_{sh}} - \left( \frac{VN_p I_o \exp\left(\frac{A}{V_t}\right)}{V_t} + \frac{V}{R_{sh}} \right) \frac{dA}{dV} = 0 \quad (3.14)$$

Rearranging terms:

$$\frac{N_p I_{ph} - N_p I_o \exp\left(\frac{A}{V_t}\right) + N_p I_o - \frac{A}{R_{sh}}}{\left( \frac{VN_p I_o \exp\left(\frac{A}{V_t}\right)}{V_t} + \frac{V}{R_{sh}} \right)} = \frac{dA}{dV} \quad (3.15)$$



Substituting equation (3.4), in numerator of equation (3.15) it is:

$$\frac{dA}{dV} = \frac{I}{V \left( \frac{N_p I_o \exp\left(\frac{A}{V_t}\right)}{V_t} + \frac{1}{R_{sh}} \right)} \quad (3.16)$$

$$\text{Set, } K = \frac{N_p I_o \exp\left(\frac{A}{V_t}\right)}{V_t} + \frac{1}{R_{sh}} \quad (3.17)$$

Equation (3.16) becomes:

$$\frac{dA}{dV} = \frac{I}{VK} \quad (3.18)$$

$$\text{Setting } B = \frac{I}{K} \quad (3.19)$$

Equation (3.18) becomes:

$$\frac{dA}{dV} = \frac{B}{V} \Rightarrow \frac{dV}{dA} = \frac{V}{B} \quad (3.20)$$

Summarizing all the above derived equations, there are 5 main equations (3.3), (3.4), (3.17), (3.19) and (3.20).

Using equation (3.3) an expression for the voltage can be derived:

$$VN_p + IN_s R_s = AN_s N_p \Leftrightarrow$$

$$\text{Thus, } V = \frac{AN_s N_p - IN_s R_s}{N_p} \quad (3.21)$$

Equation (3.19) due to equations (3.4) and (3.17) becomes:

$$B = \frac{I}{K} = \frac{N_p I_{ph} - N_p I_o \left( \exp\left(\frac{A}{V_t}\right) - 1 \right) - \frac{A}{R_{sh}}}{\frac{N_p I_o \exp\left(\frac{A}{V_t}\right)}{V_t} + \frac{1}{R_{sh}}} =$$

$$\begin{aligned}
 & \frac{N_p R_{sh} I_{ph} - N_p R_{sh} I_o \left( \exp\left(\frac{A}{V_t}\right) - 1 \right) - A}{R_{sh}} \\
 = & \frac{N_p I_o R_{sh} \exp\left(\frac{A}{V_t}\right) + V_t}{V_t \cdot R_{sh}} \\
 & \frac{V_t (N_p R_{sh} I_{ph} - N_p R_{sh} I_o \left( \exp\left(\frac{A}{V_t}\right) - 1 \right) - A)}{N_p I_o R_{sh} \exp\left(\frac{A}{V_t}\right) + V_t} \tag{3.22}
 \end{aligned}$$

Working further, new formulas are derived. Equation (3.21) due to (3.4) becomes:

$$V = AN_s - N_s R_s I_{ph} + N_s R_s I_o \left( \exp\left(\frac{A}{V_t}\right) - 1 \right) + \frac{AN_s R_s}{N_p R_{sh}} \tag{3.23}$$

Analytical derivation of equation (3.23) is provided in Appendix A (A.1.1 a).

As stated in equation (3.20), taking the derivative of  $V$  ( $dV$ ) over  $dA$ , equation (3.23) becomes,

$$\frac{dV}{dA} = N_s + \frac{N_s R_s I_o \exp\left(\frac{A}{V_t}\right)}{V_t} + \frac{N_s R_s}{N_p R_{sh}} \tag{3.24}$$

Calculating the second term of equation (3.20), due to equation (3.23) and equation (3.22) it is:

$$\frac{V}{B} = \frac{\left( N_p I_o R_{sh} \exp\left(\frac{A}{V_t}\right) + V \right) \cdot \left( AN_s N_p R_{sh} - N_s R_s N_p R_{sh} I_{ph} + N_s R_s N_p R_{sh} I_o \left( \exp\left(\frac{A}{V_t}\right) - 1 \right) + AN_s R_s \right)}{N_p R_{sh} V_t \left( N_p R_{sh} I_{ph} - N_p R_{sh} I_o \left( \exp\left(\frac{A}{V_t}\right) - 1 \right) - A \right)} \tag{3.25}$$

Detail derivation of equation (3.25) is provided in Appendix A (A.1.1 b).

Both terms of equation (3.20) have been calculated. Equation (3.24) is equated with equation (3.25). Analytical equations (3.26) – (3.30) are provided in detail in Appendix

A (A.1.1 c). So, (3.30) is an equation with only unknown  $A$ , based on the five fitting parameters of the single diode equivalent electrical circuit.

Equation (3.30) contains exponential term, for our convenience we used Matlab software environment to solve this equation and determine the unknown parameter ( $A$ ).

$$\begin{aligned}
 & N_s N_p^2 R_{sh}^2 V_t I_{ph} - N_s N_p^2 R_{sh}^2 V_t I_o \exp\left(\frac{A}{V_t}\right) + N_s N_p^2 R_{sh}^2 V_t I_o - 2N_s N_p R_{sh} V_t A + 2N_s R_s N_p R_{sh} I_{ph} V_t \\
 & - 2N_s R_s N_p R_{sh} V_t I_o \exp\left(\frac{A}{V_t}\right) + 2N_s R_s V_t N_p R_{sh} I_o - 2N_s R_s V_t A + 2N_s R_s N_p^2 R_{sh}^2 I_o I_{ph} \exp\left(\frac{A}{V_t}\right) \\
 & - 2N_s R_s N_p^2 R_{sh}^2 I_o^2 \left(\exp\left(\frac{A}{V_t}\right)\right)^2 + 2N_s R_s N_p^2 R_{sh}^2 I_o^2 \exp\left(\frac{A}{V_t}\right) - 2N_s R_s N_p R_{sh} I_o A \exp\left(\frac{A}{V_t}\right) \\
 & - N_p^2 R_{sh}^2 N_s A I_o \exp\left(\frac{A}{V_t}\right) = 0
 \end{aligned} \tag{3.30}$$

The maximum current  $I$  is given by equation (3.4) and the maximum voltage  $V$  is given by equation (3.23). Evaluating equation (3.30) for a single solar cell,  $N_s=1$  and  $N_p=1$  it becomes:

$$\begin{aligned}
 & R_{sh}^2 V_t I_{ph} - R_{sh}^2 V_t I_o \exp\left(\frac{A}{V_t}\right) + R_{sh}^2 V_t I_o - 2R_{sh} V_t A + 2R_s R_{sh} I_{ph} V_t - 2R_s R_{sh} V_t I_o \exp\left(\frac{A}{V_t}\right) \\
 & + 2R_s V_t R_{sh} I_o - 2R_s V_t A + 2R_s R_{sh}^2 I_o I_{ph} \exp\left(\frac{A}{V_t}\right) - 2R_s R_{sh}^2 I_o^2 \left(\exp\left(\frac{A}{V_t}\right)\right)^2 \\
 & + 2R_s R_{sh}^2 I_o^2 \exp\left(\frac{A}{V_t}\right) - 2R_s R_{sh} I_o A \exp\left(\frac{A}{V_t}\right) - R_{sh}^2 A I_o \exp\left(\frac{A}{V_t}\right) = 0
 \end{aligned} \tag{3.31}$$

Equations giving maximum current and maximum voltage for a single solar cell become:

$$I(A) = I_{ph} - I_o \left( \exp\left(\frac{A}{V_t}\right) - 1 \right) - \frac{A}{R_{sh}} \tag{3.32}$$

$$V(A) = A - R_s I_{ph} + R_s I_o \left( \exp\left(\frac{A}{V_t}\right) - 1 \right) + \frac{A R_s}{R_{sh}} \tag{3.33}$$

Both maximum current and maximum voltage are expressed in terms of a new variable  $A$ , i.e.  $I_{mpp} = f(A)$  and  $V_{mpp} = f(A)$ . The maximum power is the product of the maximum voltage and maximum current.

### 3.4 Experimental Validation

The equations of the previous section were imported into the Matlab software environment in order to evaluate the accuracy of the model described. The equations are evaluated for different solar modules. Data provided by the manufacturers in standard test conditions (STC), for which irradiance is  $1000 \text{ W/m}^2$ , and temperature is  $25^\circ\text{C}$ , are referring in Table 3.1. Using the data of Table 3.1, Carrero et al. [140] estimated  $R_s$  and  $R_{sh}$  parameters. The results derived by Matlab software environment are compared with the data stated below (Table 3.1).

Table 3.1. Data from catalogues (STC) and estimated loss resistances (for  $n=1$ ).

Reproduced from [140].

Modules	No. cells	$V_{oc}$ (V)	$I_{sc}$ (A)	$V_{mpp}$ (V)	$I_{mpp}$ (A)	$P_{mpp}$ (W)	$R_s$ ( $\Omega$ )	$R_{sh}$ ( $\Omega$ )
AP 165	54	32.0	7.40	25.0	6.60	165	0.4676	61.8
ATERSA A 120	36	21.0	7.70	16.9	7.10	120	0.2030	91.2
ISOFOTONI-110	72	43.2	3.38	34.8	3.16	110	0.9608	916
BP 5170 S	72	44.2	5.00	36.0	4.72	170	0.5840	1965

To determine the current, voltage and power for the optimal operating point ( $I_{mpp}$ ,  $V_{mpp}$  and  $P_{mpp}$ ) corresponding to the maximum power point for STC, the known parameters are taken to be the *No. of cells*,  $V_{oc}$ ,  $I_{sc}$ ,  $R_s$  and  $R_{sh}$ . Two script files have been written, `findzeros.m` and `example1.m`. The source code, regarding the first module AP 165, can be seen in Appendix A (A.1.2). Similar is the source code for the other modules.

Executing the `findzeros.m` script file the maximum voltage, current and power are calculated. It has to be noted that the `findzeros.m` script file “calls” the `example1.m` script file, which initially determines the  $A$  variable (denoted  $x$  in the source code) and then the optimum operating point is specified according to the module applied.

Manufacturers’ data and experimental derived data by the proposed method are summarized in the Table 3.2. In order to evaluate the accuracy of the proposed method, the error for each module has been calculated in Table 3.2. The  $A$  variable is stated for each photovoltaic module.

Table 3.2. Summarize theoretical data provided by manufacturers and experimental data derived by the proposed method, along with errors for each photovoltaic module.

Modules	Manufacturers Data			Derived Data			Errors			Value
	$V_{mpp}$ (V)	$I_{mpp}$ (A)	$P_{mpp}$ (W)	$V_{mpp}$ (V)	$I_{mpp}$ (A)	$P_{mpp}$ (W)	$V_{mpp}$ (V)	$I_{mpp}$ (A)	$P_{mpp}$ (W)	A
AP 165	25.0	6.60	165	24.96	6.55	163.61	0.15%	0.72%	0.84%	0.519
ATERSA A 120	16.9	7.10	120	16.89	7.08	119.64	0.06%	0.22%	0.29%	0.509
ISOFOTONI-110	34.8	3.16	110	34.79	3.15	109.82	0.03%	0.12%	0.16%	0.525
BP 5170 S	36.0	4.72	170	35.99	4.71	169.86	0.01%	0.04%	0.08%	0.538

The percentage relative error is defined as following:

$$\text{Percentage Relative Error} = \frac{|theoretical - experimental|}{theoretical} \cdot 100\% \quad (3.34)$$

As it can be understood, the lower value of the percentage relative error means that the more accurate is the proposed computational algorithm based on the mathematical equations presented.

The deviation can be said that is almost negligible in all solar panels studied. The best case scenario shows a divergence in  $P_{mpp}$  of 0.08%, while the worst case 0.84%. The proposed equations can well be used to estimate the optimum operating point. It is accurate, reliable and easy to apply method for identifying the maximum operating point.

### 3.5 Resistor Sensitivity to MPP

The sensitivity of the equations derived to resistor variation is taken into account in this section. Proposed maximum power point method is examined for resistor deviation from its nominal value on series and shunt resistances up to 5%. Sensitivity tracking MPP is described in percentage relative error. All four modules have been studied. Results are demonstrated in Table 3.3 for changes in series resistance, while Table 3.4 illustrates changes in shunt resistance. Graphical representations of percentage relative error between deviation limits can be seen in Figure 3.2 and 3.3. Distinguishable are nominal values (Nom.), at “0% deviation resistance”.

Table 3.3. Percentage relative errors to MPP for series resistance variation from -5% to +5% of nominal value.

% Deviation Resistance	AP 165		ATERSA A 120		ISO FOTON I-110		BP 5170 S	
	Cell	% Error	Cell	% Error	Cell	% Error	Cell	% Error
-5% to + 5%	$R_s$ nom	MPP	$R_s$ nom	MPP	$R_s$ nom	MPP	$R_s$ nom	MPP
	8.659		5.638		13.344		8.111	
	mOhm		mOhm		mOhm		mOhm	
-5%	8.226	0.232	5.356	0.132	12.677	0.276	7.705	0.300
-4%	8.312	0.354	5.413	0.047	12.810	0.189	7.786	0.224
-3%	8.399	0.476	5.469	0.037	12.944	0.102	7.867	0.147
-2%	8.486	0.598	5.526	0.122	13.077	0.015	7.948	0.071
-1%	8.572	0.720	5.582	0.207	13.211	0.071	8.030	0.005
0%	8.659	0.842	5.638	0.292	13.344	0.158	8.111	0.081
1%	8.745	0.963	5.695	0.377	13.477	0.245	8.192	0.158
2%	8.832	1.085	5.751	0.462	13.611	0.332	8.273	0.234
3%	8.919	1.207	5.808	0.547	13.744	0.419	8.354	0.311
4%	9.005	1.328	5.864	0.632	13.878	0.506	8.435	0.387
5%	9.092	1.450	5.920	0.717	14.011	0.593	8.516	0.464

Table 3.4. Percentage relative errors to MPP for shunt resistance variation from -5% to +5% of nominal value.

% Deviation Resistance	AP 165		ATERSA A 120		ISO FOTON I-110		BP 5170 S	
	Cell	% Error	Cell	% Error	Cell	% Error	Cell	% Error
-5% to + 5%	$R_{sh}$ nom	MPP	$R_{sh}$ nom	MPP	$R_{sh}$ nom	MPP	$R_{sh}$ nom	MPP
	1.144		2.533		12.722		27.291	
	Ohm		Ohm		Ohm		Ohm	
-5%	1.087	1.138	2.406	0.420	12.086	0.217	25.927	0.101
-4%	1.098	1.076	2.432	0.393	12.213	0.205	26.200	0.097
-3%	1.110	1.016	2.457	0.367	12.340	0.193	26.472	0.093
-2%	1.121	0.956	2.482	0.342	12.467	0.181	26.745	0.089
-1%	1.133	0.898	2.508	0.317	12.595	0.170	27.018	0.085
0%	1.144	0.842	2.533	0.292	12.722	0.158	27.291	0.081
1%	1.155	0.786	2.558	0.268	12.849	0.147	27.564	0.078
2%	1.167	0.731	2.584	0.245	12.976	0.136	27.837	0.074
3%	1.178	0.678	2.609	0.222	13.103	0.126	28.110	0.071
4%	1.190	0.625	2.634	0.199	13.231	0.115	28.383	0.067
5%	1.201	0.574	2.660	0.177	13.358	0.105	28.656	0.064

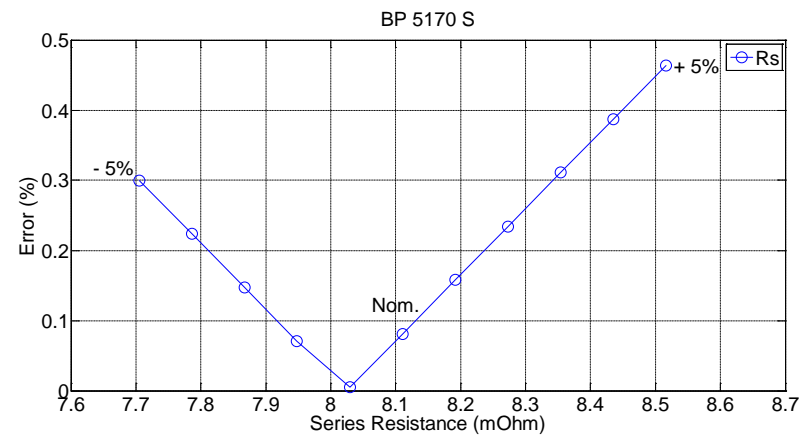
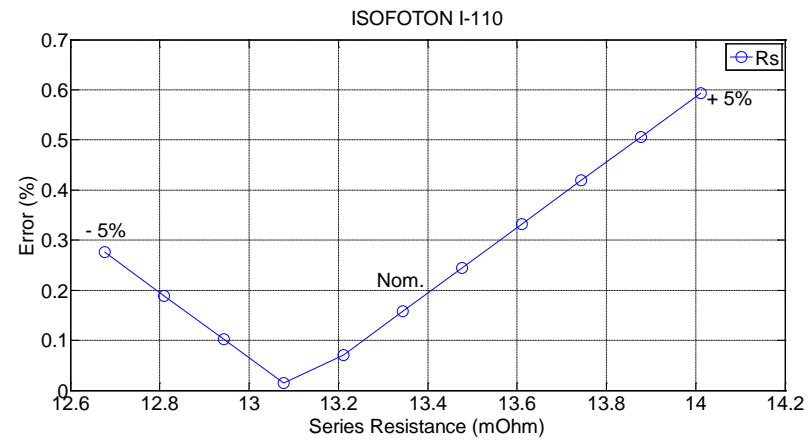
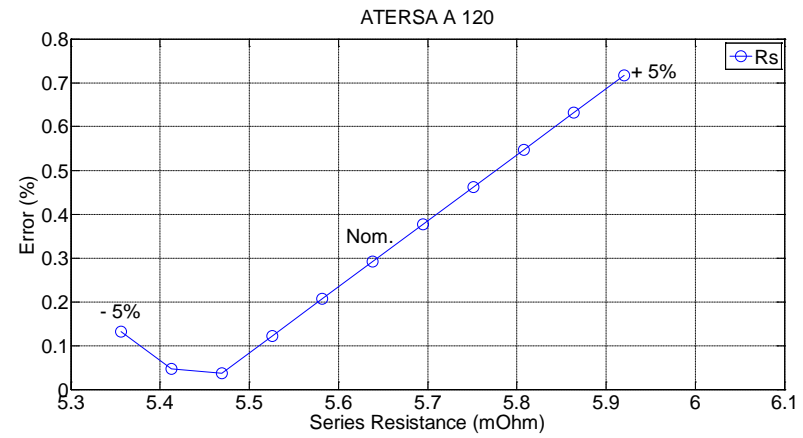
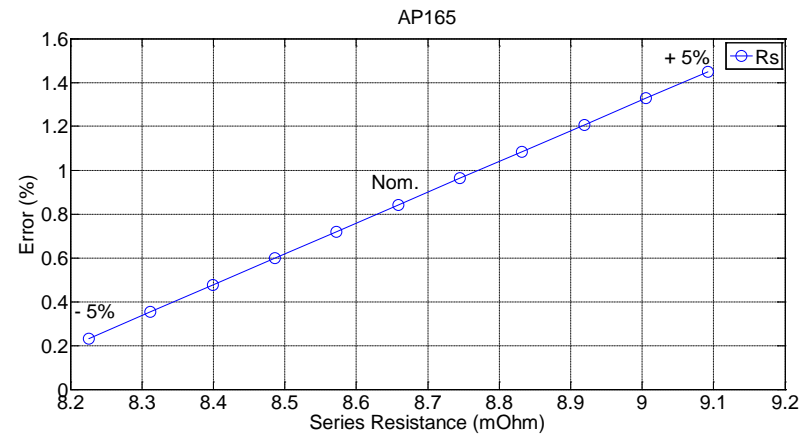


Figure 3.2. Percentage relative errors against series resistance deviation limits for all four modules.

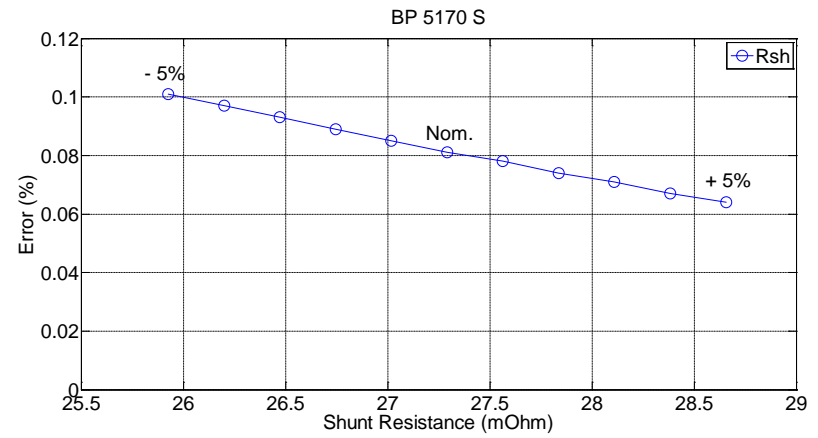
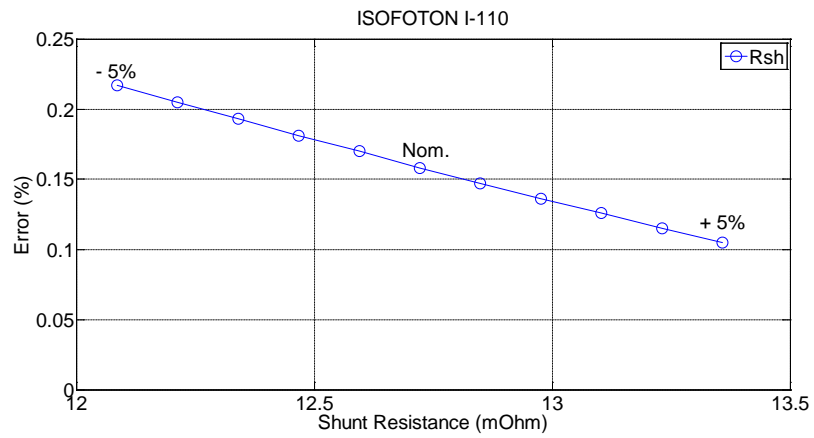
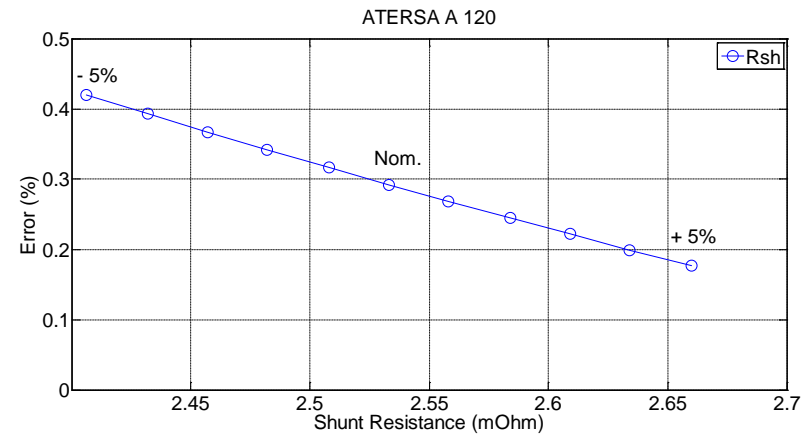
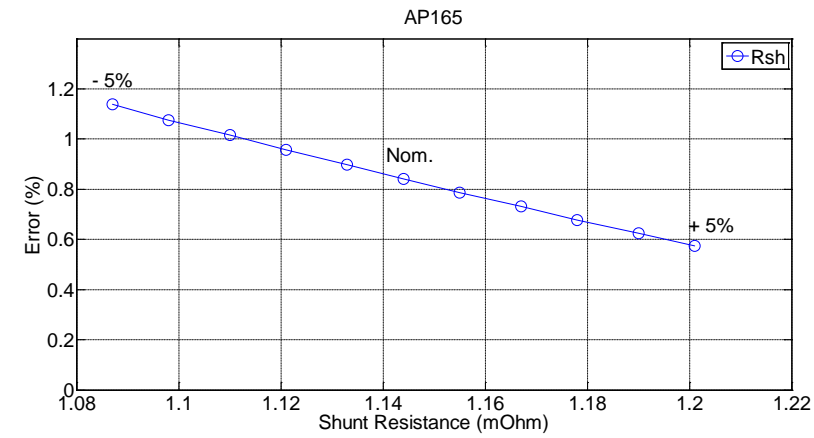


Figure 3.3. Percentage relative errors against shunt resistance deviation limits for all four modules.



In all cases considered module converge towards MPP when series resistance is decreased from its nominal value. In particular for each module the value of series resistance that approaches closer to MPP giving the smaller possible percentage error are summarized in Table 3.5.

Table 3.5. Percentage relative errors in respect to nominal value of series resistor.

AP 165		ATERSA A 120		ISO FOTON I-110		BP 5170 S	
Series Resistor	% Error to MPP	Series Resistor	% Error to MPP	Series Resistor	% Error to MPP	Series Resistor	% Error to MPP
Nominal Value A	0.842	Nominal Value A	0.292	Nominal Value A	0.158	Nominal Value A	0.081
Deviat.-5% Value A	0.232	Deviat.-3% Value A	0.037	Deviat.-2% Value A	0.015	Deviat.-1% Value A	0.005
	0.5190		0.5090		0.5253		0.5382
	0.5187		0.5089		0.5252		0.5381

On the other hand, in all cases considered, when shunt resistance increases to +5% of its nominal value, convergence improves towards MPP. Results are presented in Table 3.6.

Table 3.6. Percentage relative errors in respect to nominal value of shunt resistor.

AP 165		ATERSA A 120		ISO FOTON I-110		BP 5170 S	
Shunt Resistor	% Error to MPP	Shunt Resistor	% Error to MPP	Shunt Resistor	% Error to MPP	Shunt Resistor	% Error to MPP
Nominal Value A	0.842	Nominal Value A	0.292	Nominal Value A	0.158	Nominal Value A	0.081
Deviat.+5% Value A	0.574	Deviat.+5% Value A	0.177	Deviat.+5% Value A	0.105	Deviat.+5% Value A	0.064
	0.51904		0.50903		0.52530		0.538232
	0.51911		0.50906		0.52531		0.538236

Variation of series - shunt resistances and contribution towards better or worse cell performance has described in this section. Theoretically this can be explained because series resistance is zero. So, a decrease from its nominal value results in an improved percentage relative error. Similarly, shunt resistance is infinite, thus algorithm improves when parameter is increased from its nominal value. Although small percentage variation has observed in total, it is advantageous for practical usage to qualify sensitivity to error on cell parameters like resistances.

### 3.6 Sensitivity of parameters $I_o$ , $I_{ph}$ , $n$ to MPP

The impact of the remaining parameters ( $I_o$ ,  $I_{ph}$ ,  $n$ ) is evaluated in this section. The proposed maximum power point methodology is examined for deviation from its nominal value up to 5%. Sensitivity tracking MPP is described in percentage relative error for all four modules. Results are demonstrated in Table 3.7 for changes in saturation current ( $I_o$ ), while in Table 3.8 is presented changes in photocurrent ( $I_{ph}$ ). Ideality factor is ideal unity ( $n=1$ ); in real  $n$  is greater than unity ( $n>1$ ), typically varies from 1 to 2. Two cases are examined, variation of ideality factor up to +5% is presented in Table 3.9, as in all other parameters, but deviation less than unity are not considered since ideality factor is always greater than unity. Another case examined is the sensitivity to MPP as ideality factor varies in the whole range  $n \in [1, 2]$  and is demonstrated in Table 3.10. Graphical representations of percentage relative error between deviation limits for parameters studied can be seen in Figures 3.4, 3.5, 3.6 and 3.7. Nominal values (Nom.) is at “0% deviation”.

Table 3.7. Percentage relative errors to MPP for saturation current variation from -5% to +5% of nominal value.

%		AP 165		ATERSA A 120		ISO FOTON I-110		BP 5170 S	
Deviation		$I_o$		$I_o$		$I_o$		$I_o$	
		Cell	% Error	Cell	% Error	Cell	% Error	Cell	% Error
-5% to	$I_o$ nom	MPP		$I_o$ nom	MPP	$I_o$ nom	MPP	$I_o$ nom	MPP
+ 5%	6.544E-10			1.018E-09		2.375E-10		2.065E-10	
	A			A		A		A	
-5%	6.217E-10	0.581		9.677E-10	0.026	2.256E-10	0.103	1.962E-10	0.173
-4%	6.285E-10	0.633		9.779E-10	0.079	2.280E-10	0.051	1.982E-10	0.122
-3%	6.347E-10	0.685		9.881E-10	0.132	2.303E-10	0.001	2.003E-10	0.071
-2%	6.413E-10	0.737		9.982E-10	0.186	2.327E-10	0.053	2.024E-10	0.02
-1%	6.478E-10	0.789		1.008E-09	0.239	2.351E-10	0.106	2.044E-10	0.03
0%	6.544E-10	0.841		1.018E-09	0.292	2.375E-10	0.158	2.065E-10	0.081
1%	6.609E-10	0.894		1.028E-09	0.346	2.398E-10	0.211	2.086E-10	0.133
2%	6.675E-10	0.946		1.039E-09	0.399	2.422E-10	0.263	2.106E-10	0.184
3%	6.740E-10	0.998		1.049E-09	0.452	2.446E-10	0.316	2.127E-10	0.235
4%	6.806E-10	1.05		1.059E-09	0.505	2.470E-10	0.368	2.147E-10	0.286
5%	6.871E-10	1.102		1.069E-09	0.559	2.493E-10	0.421	2.168E-10	0.337

Table 3.8. Percentage relative errors to MPP for photocurrent variation from -5% to +5% of nominal value.

%		AP 165		ATERSA A 120		ISO FOTON I-110		BP 5170 S	
Deviation		$I_{ph}$		$I_{ph}$		$I_{ph}$		$I_{ph}$	
		Cell	% Error	Cell	% Error	Cell	% Error	Cell	% Error
-5% to	$I_{ph}$ nom	MPP		$I_{ph}$ nom	MPP	$I_{ph}$ nom	MPP	$I_{ph}$ nom	MPP
+ 5%	7.400 A			7.700 A		3.380 A		5 A	
-5%	7.030	5.506		7.315	4.996	3.211	4.793	4.75	4.732
-4%	7.104	4.568		7.392	4.052	3.244	3.863	4.8	3.799
-3%	7.178	3.632		7.469	3.109	3.278	2.934	4.85	2.867
-2%	7.252	2.699		7.546	2.169	3.312	2.007	4.9	1.937
-1%	7.326	1.769		7.623	1.23	3.346	1.082	4.95	1.008
0%	7.400	0.841		7.700	0.292	3.380	0.158	5	0.081
1%	7.474	0.082		7.777	0.642	3.413	0.762	5.05	0.843
2%	7.548	1.004		7.854	1.576	3.447	1.682	5.1	1.767
3%	7.622	1.924		7.931	2.508	3.481	2.600	5.15	2.690
4%	7.696	2.84		8.008	3.438	3.515	3.517	5.2	3.611
5%	7.770	3.754		8.085	4.367	3.549	4.431	5.25	4.530

Table 3.9. Percentage relative errors to MPP for ideality factor variation from 0% to +5% of nominal value.

Deviation		AP 165	ATERSA A 120	ISOFOTON I-110	BP 5170 S
<i>n</i>					
0% to	Cell	% Error	% Error	% Error	% Error
+ 5%	<i>n</i> nom 1	MPP	MPP	MPP	MPP
0%	1.0	0.842	0.292	0.158	0.081
1%	1.01	0.936	0.391	0.256	0.179
2%	1.02	1.030	0.488	0.354	0.275
3%	1.03	1.123	0.586	0.450	0.372
4%	1.04	1.216	0.682	0.547	0.467
5%	1.05	1.309	0.779	0.642	0.563

Table 3.10. Percentage relative errors to MPP for ideality factor variation from 1 to 2. Nominal value  $n=1$ .

Deviation		AP 165	ATERSA A 120	ISOFOTON I-110	BP 5170 S
<i>n</i>					
1 to 2	Cell	% Error	% Error	% Error	% Error
<i>n</i> nom 1		MPP	MPP	MPP	MPP
1.0		5.506	4.996	4.793	4.732
1.1		4.568	4.052	3.863	3.799
1.2		3.632	3.109	2.934	2.867
1.3		2.699	2.169	2.007	1.937
1.4		1.769	1.23	1.082	1.008
1.5		0.841	0.292	0.158	0.081
1.6		0.082	0.642	0.762	0.843
1.7		1.004	1.576	1.682	1.767
1.8		1.924	2.508	2.600	2.690
1.9		2.84	3.438	3.517	3.611
2.0		3.754	4.367	4.431	4.530

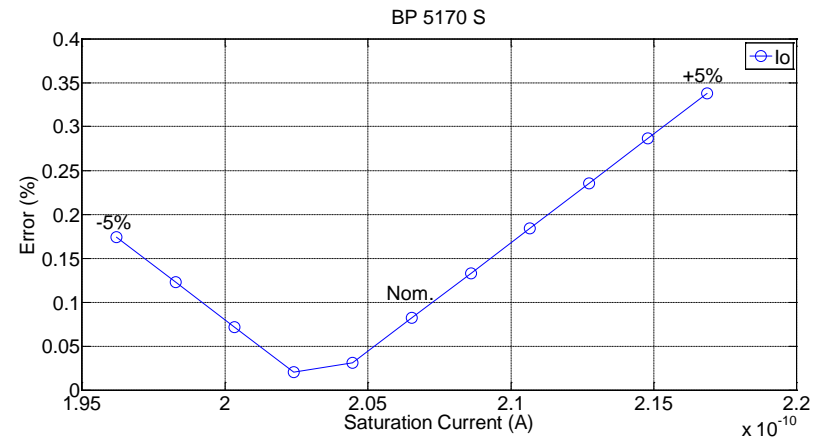
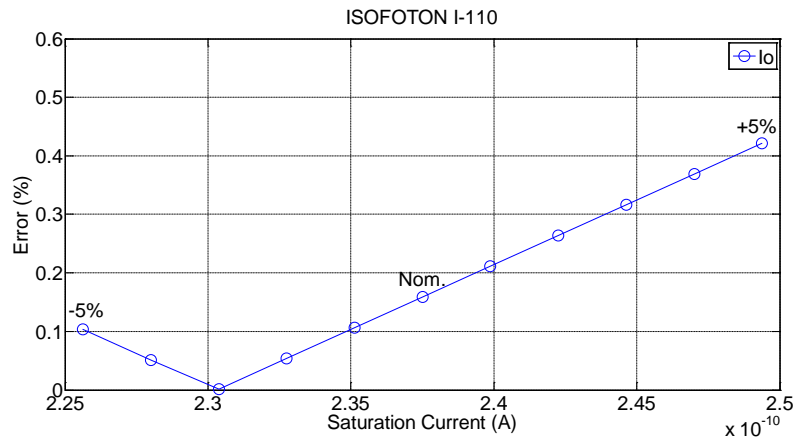
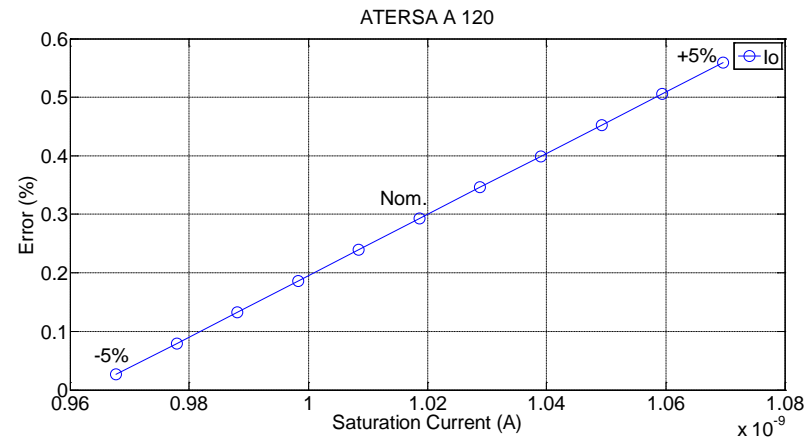
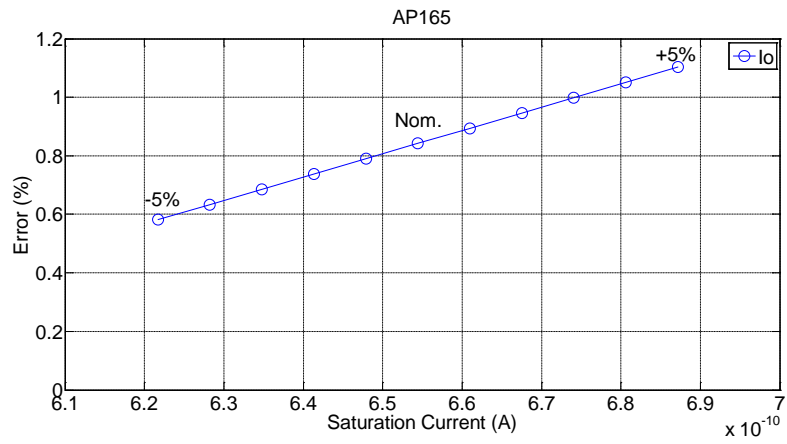


Figure 3.4. Percentage relative errors against saturation current deviation limits for all four modules.

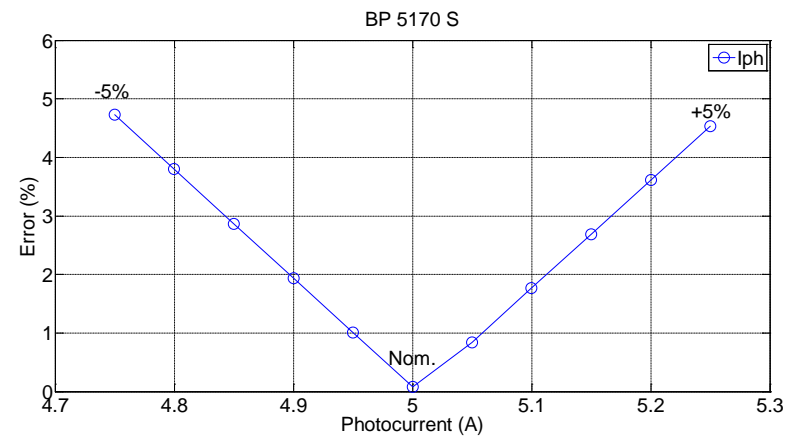
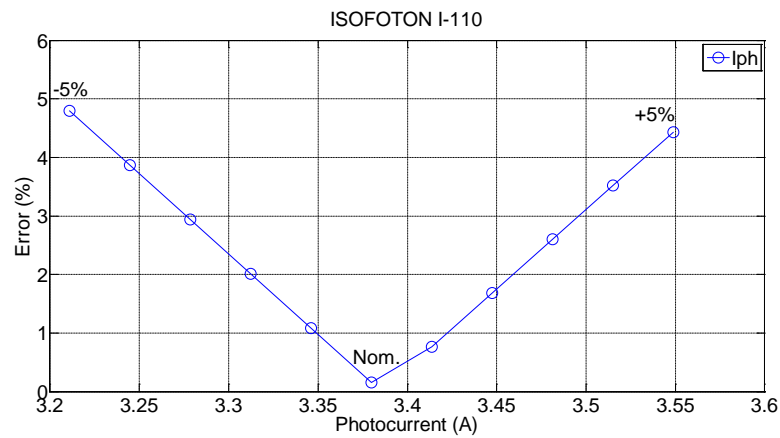
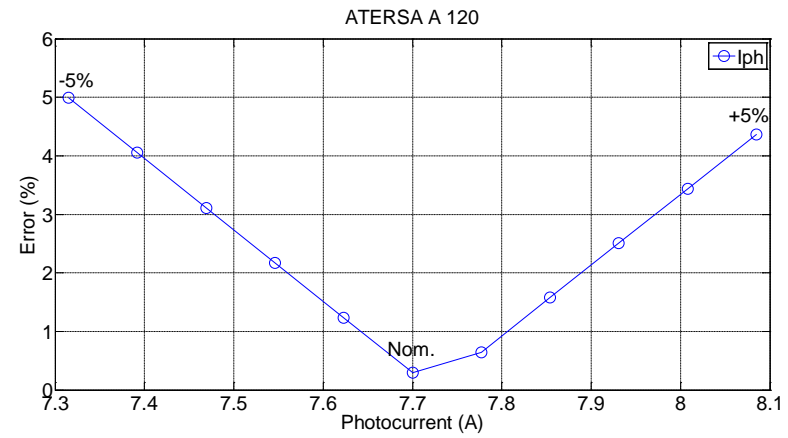
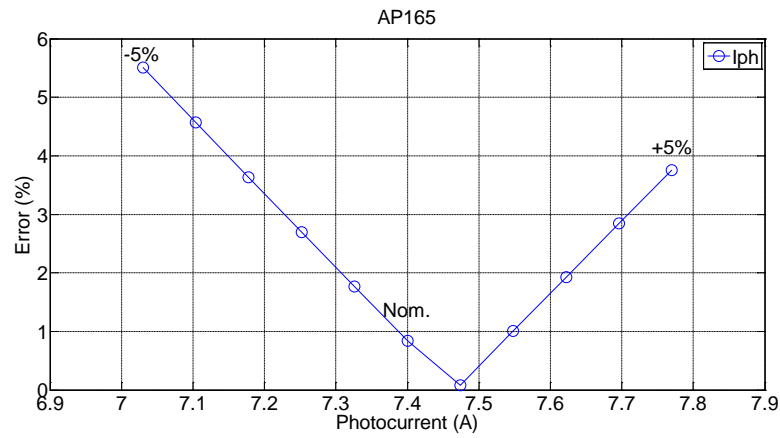


Figure 3.5. Percentage relative errors against photocurrent deviation limits for all four modules.

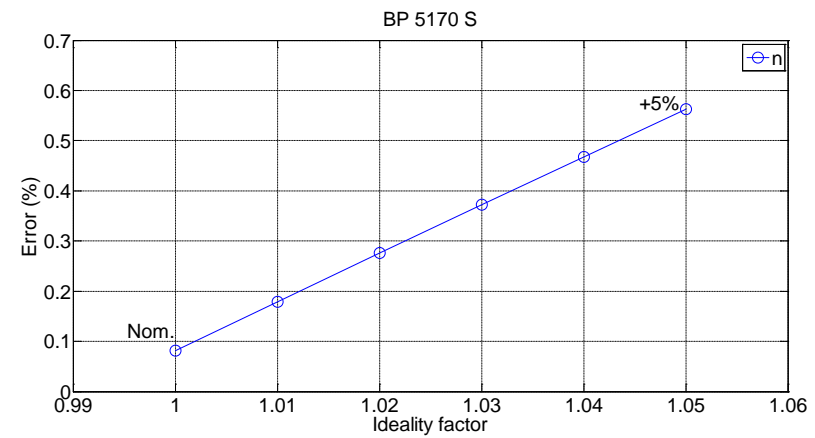
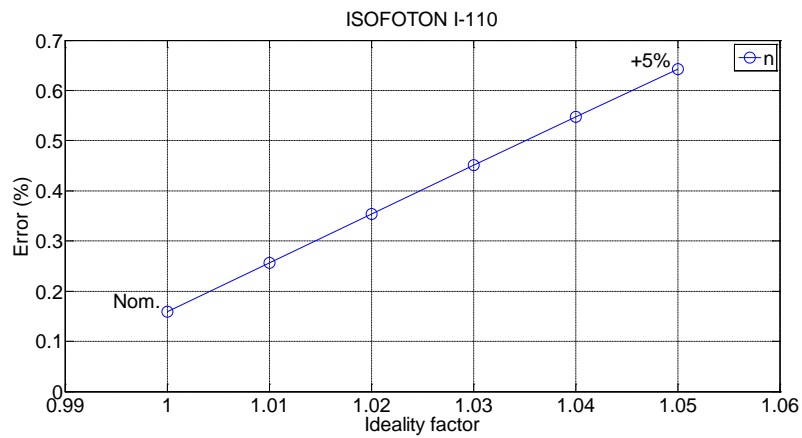
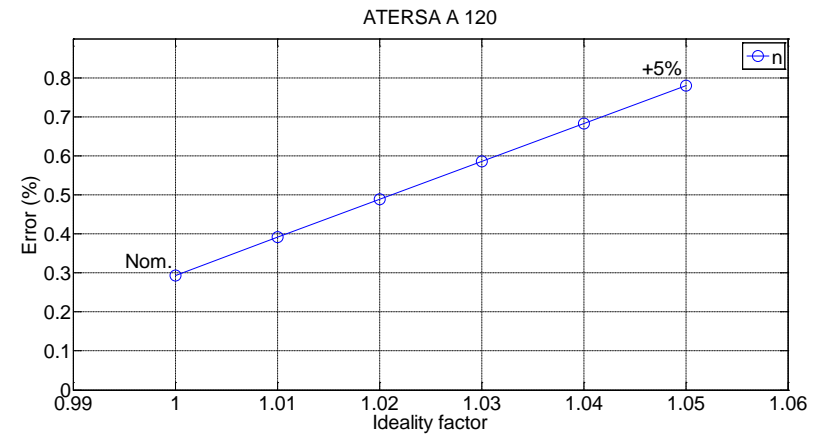
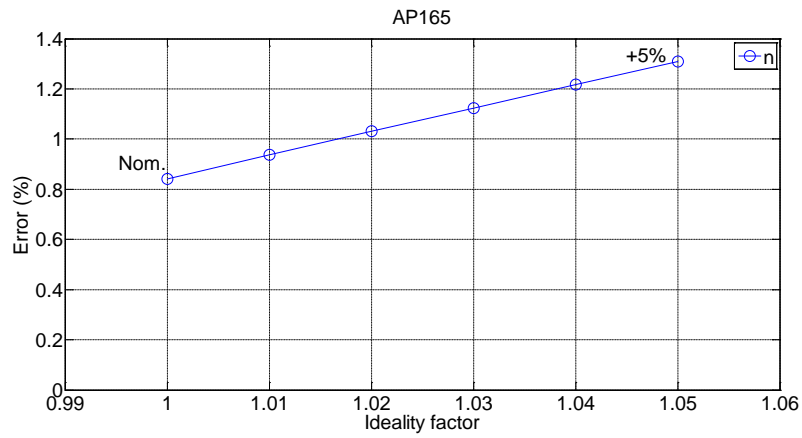


Figure 3.6. Percentage relative errors against ideality factor deviation limits for all four modules.

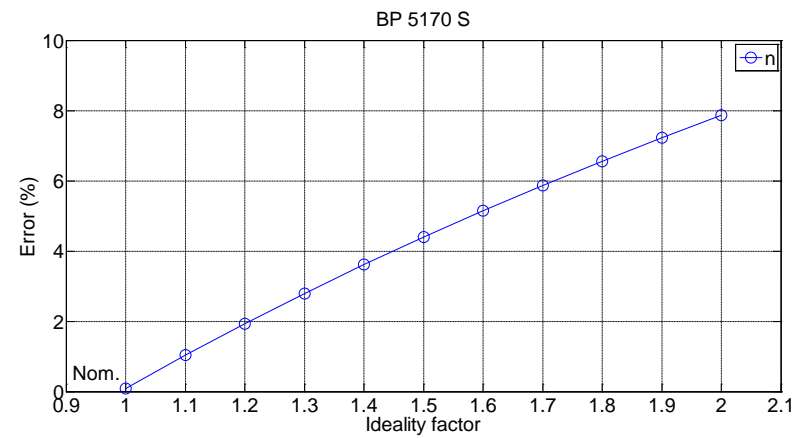
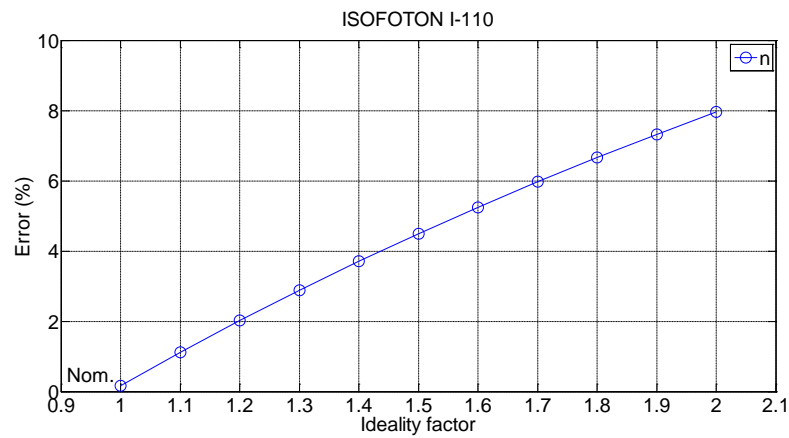
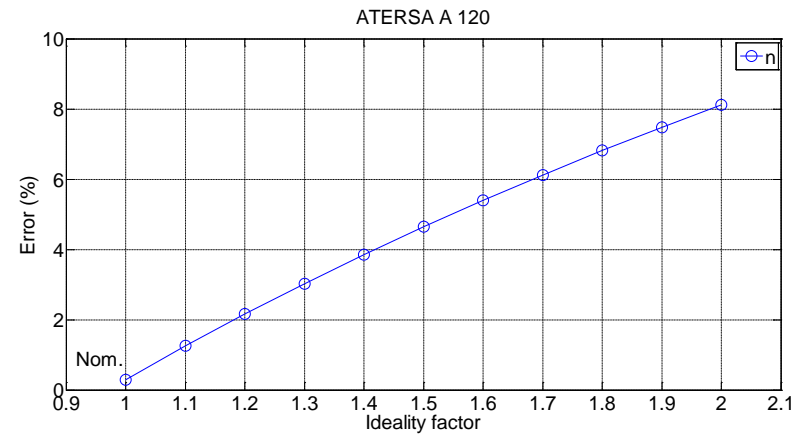
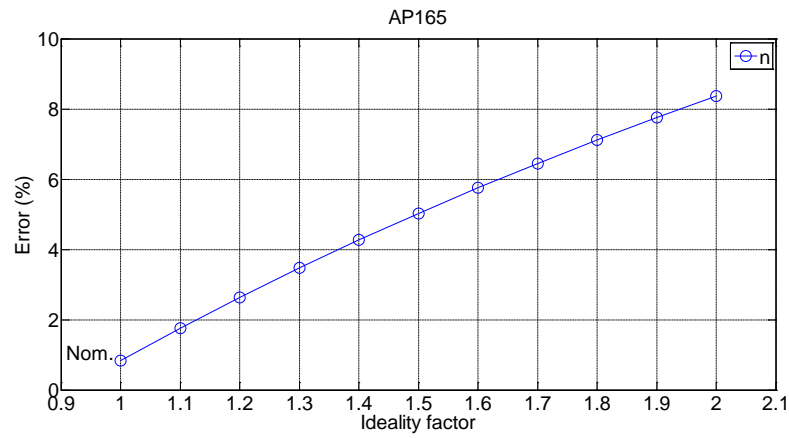


Figure 3.7. Percentage relative errors against ideality factor deviation limits for all four modules ( $n \in [1, 2]$ ).



Results suggest that as saturation current increases to +5% from its nominal value the highest percentage error is observed in all cases considered, while a decrease from its nominal value would produce a smaller error. Analytically, convergence towards MPP with the smallest possible error is noticed at -5% deviation for both AP 165 and ATERSA A 120 modules, while for ISOFOTON I-110 and BP 5170 S modules at -3% and -2% respectively.

Photocurrent at the nominal value has the smaller possible error in all cases examined, apart from AP 165 module where the smallest error is at +1% deviation, which is very close to the nominal value. A variation to higher or lower values from the nominal one will increase the percentage error which can reach up to 4.7%. This makes photocurrent the most important parameter among the others examined, since it has a big contribution towards predicting accurately the MPP. A small divergence would have a big impact affecting considerable MPP.

Ideality factor throughout all four solar modules studied indicates that an increase from its nominal value will correspond to an increase in percentage error. The closer to the nominal value the smaller the percentage error.

Concluding this section, sensitivity to error on cell parameters studied such as saturation current, photocurrent and ideality factor suggest that photocurrent influence on predicting accurately MPP has the higher impact effect, while the other two parameters have a smaller percentage error variation on predicting precisely the MPP. It has been analysed and graphically presented the sensitivity of all five fitting parameters. High degree of parameters extraction is required avoiding divergence to higher or lower extent.

### 3.7 Conclusion

The transcendental equation describing a solar cell I-V characteristic contains current on both sides in a function of the form,  $I = f(V, I)$ . In this work maximum current  $I_{mpp}$  and maximum voltage  $V_{mpp}$  are both expressed as a function of a new variable  $A$  i.e.  $I_{mpp} = f(A)$  and  $V_{mpp} = f(A)$ , a current-independent voltage expression is derived for the maximum operating point. Maximum power point is the product of maximum current and maximum voltage. The variable  $A$  is well defined mathematically.

Matlab software programming has been used along with data provided by manufacturers or data derived by formulas ( $R_s$  and  $R_{sh}$ ) to evaluate the accuracy of the method proposed. The impact of 5% deviation of all parameters ( $R_s$ ,  $R_{sh}$ ,  $I_o$ ,  $I_{ph}$ ,  $n$ ) has been examined and sensitivity determining MPP has been demonstrated calculating percentage error in all cases.

Concluding the above discussion, derivations are presented and an algorithm is proposed to identify the maximum operating point for a photovoltaic cell initial analysis indicates good performance of the approach. Data of real solar cells provided to test the convergence to the desired point of operation denote that the model can be an accurate tool for prediction purposes.

## 4 Modeling of Photovoltaic Cell Operation and Behavior Using and Improved $V_{BE}$ Multiplier

### 4.1 Introduction

Sets of I-V characteristic curves exist for a particular photovoltaic cell being operated in a range of illumination or temperature conditions. Many types of photovoltaic cell technologies are available and thus different characteristics can be obtained. Maximum power point tracking requirement is to extract maximum power over a wide range of light and temperature operational conditions.

SPICE circuit model can be used for simulation purposes, but they are not very suitable for evaluation and testing of DC/DC or DC/AC converters with or without MPPT. In order to accurately appraise photovoltaic systems practical laboratory methods are still required for testing and evaluation. For the purpose of this study we decided to design and built a flexible programmable cell emulator with characteristics matching an arbitrary photovoltaic cell at any practical chosen illumination and temperature.

To understand the electronic behavior of a solar cell, it is useful to create a model which is electrically equivalent, and is based on discrete electrical components whose behavior is well known [141]. The aim of this Chapter is to propose a simple circuit to model photovoltaic cell being operated over a wide range of illumination and temperature conditions allowing the rapid testing and evaluation of inverter and tracking systems. Developing an artificial solar cell would be beneficial to mimic solar cell operation in a controlled environment that it is not affected by external factors for indoor measurements in laboratories.

Two topologies will be proposed that can reliably model photovoltaic cell operation. An initial approach, “basic  $V_{BE}$  multiplier” has created limitation over operating temperature condition. In order to resolve this issue an “improved  $V_{BE}$  multiplier” circuit is proposed to model photovoltaic behavior over a wide range of operating conditions. Both circuits described have been built in order to study their operation.

## 4.2 Schematic overview of the experimental setup.

A schematic overview of the experimental set-up which all experimental measurements have performed is illustrated in Figure 4.1. The particular platform has been built and analysis provided in Chapter 5.

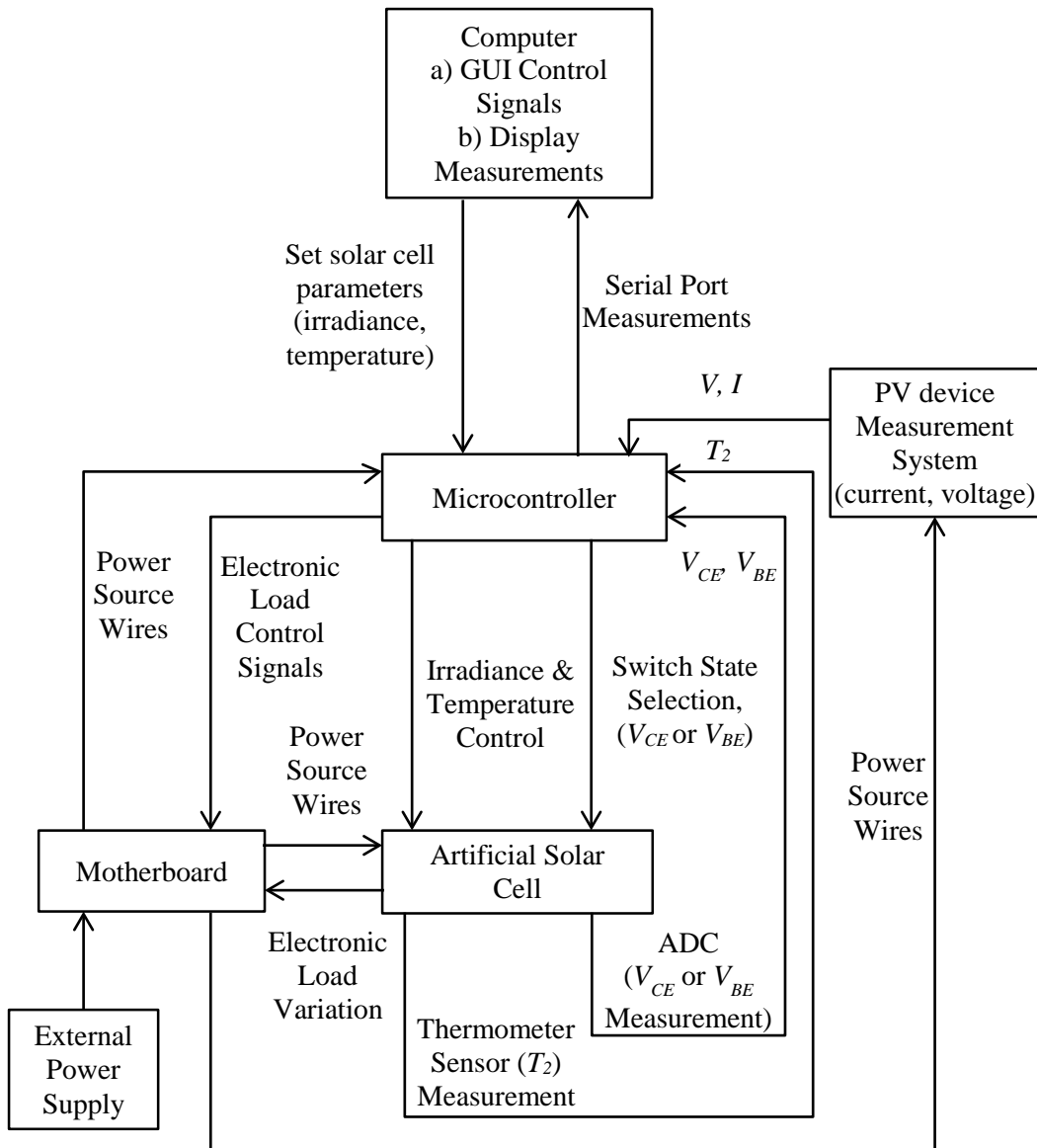


Figure 4.1. Schematic overview of the experimental set up.

This Chapter is focused in the “*Artificial Solar Cell*” board, which models photovoltaic cell operation. In this application two different transistor topologies are proposed.

The functionality of the system is direct interlinked to the “*Personal Computer*”. A suitable software sets solar cell parameters, irradiance and temperature experimental conditions. Measurements of voltage ( $V$ ) and current ( $I$ ) are obtained

Chapter 4. Modeling PV cell Operation, Behavior Using and Improved  $V_{BE}$  Multiplier by the “PV device Measurement System” board, are sent to the microcontroller and displayed in the Personal Computer.

The “Microcontroller” controls all necessary signals for the operation of the system. Across the artificial solar cell an electronic load has been placed which is controlled by the microcontroller and has been developed at the “Motherboard” board. The electronic load is based upon suitable operation of a MOSFET controlled by means of sweeping gate source voltage ( $V_{GS}$ ) [142]. As the load changes (controlling  $V_{GS}$ ) the operating current and voltage values on the IV characteristic curve are measured. A thermometer sensor measures temperature ( $T_2$ ) value of the transistor and routes it to the microcontroller that performs temperature compensation. A switch gives the ability to select voltage to be measured across the transistor terminals. Voltage across base emitter ( $V_{BE}$ ) or voltage across collector emitter ( $V_{CE}$ ) can be measured, with an analog to digital converter (ADC).

A thorough description of the platform is provided in Chapter 5. Each of the components illustrated in figure 4.1 has been implemented with electronic circuits that are analyzed in details. For such an application the digitally controlled solar emulator prototype can be programmed for a range of environmental conditions.

#### 4.2.1 Electronic load - Principle of operation

The basic circuit utilized to test PV modules using a MOSFET as an electronic load is shown in Figure 4.2.  $V_{GS}$  is the gate-source voltage,  $V_{DS}$  the drain-source voltage and  $I_D$  the drain current of the MOSFET.  $V_{PV}$  is the output voltage of the PV module,  $I_{PV}$  the output current,  $I_{sc}$  the short circuit current and  $V_{oc}$  the open circuit voltage.

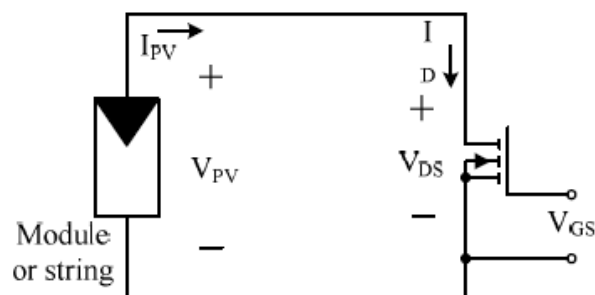


Figure 4.2. Basic test circuit for PV modules using a MOSFET as an electronic load. Reproduced from [142].

The characteristics of a MOSFET are shown in Figure 4.3 where each curve  $I_D$ - $V_{DS}$  (blue curves) was drawn for a given gate-source voltage ( $V_{GS}$ ). The  $I_{PV}$ - $V_{PV}$  characteristic of a PV module at standard test conditions (STC) is also shown in Figure 4.3 (red curve) [142]. In fact, the currents  $I_D$  and  $I_{PV}$  are the same.

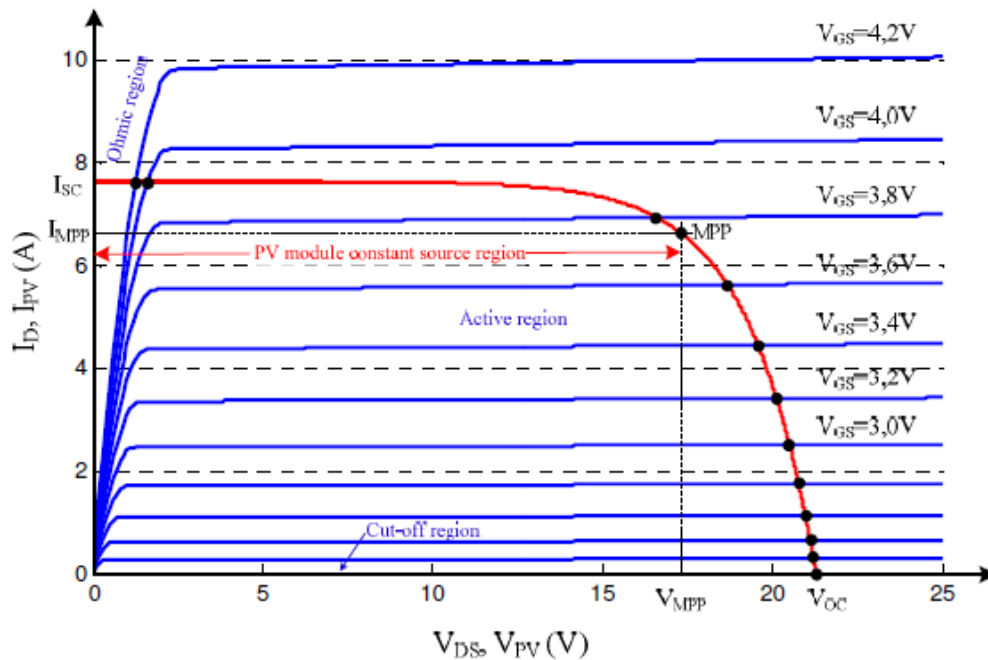


Figure 4.3. Characteristics of a PV module at STC and characteristics of a MOSFET. Reproduced from [142].

The operating point corresponds to the intersection of the PV module and MOSFET characteristics for a given voltage  $V_{GS}$ . By sweeping  $V_{GS}$  with a suitable signal the operating point of the MOSFET sweeps the  $I_{PV}$ - $V_{PV}$  characteristic between  $V_{oc}$  and  $I_{sc}$ . While  $V_{GS}$  is less than the threshold voltage  $V_{th}$ , the MOSFET will be OFF. When  $V_{GS}$  is increased above  $V_{th}$ , the device will operate in its active region where  $I_D$  rises approximately in a linear way with  $V_{GS}$ . [142]

The MOSFET should be driven by a low frequency scan signal with amplitude large enough to cover the complete range of PV panel characteristic [143]. A function generator could provide a sinusoidal or triangular signal of low frequency in the range of mHz and with amplitude between 0 V to 10 V.

According to the electronic load configuration adopted the MOSFET is driven ( $V_{GS}$ ) with a triangular waveform of amplitude 2.9V to 4V with small voltage increment (voltage step increment value  $760\mu\text{V}$ ), such as to obtain enough points to accurately describe the I-V curve and time duration of 87 seconds. Small

variation in  $V_{GS}$  can improve the I-V curve. As a result the visualization of the I-V characteristics can become more uniform and persistent.

In this section the theoretical principle has been described, while the electronic circuit built is demonstrated and discussed with further details in Chapter 5.

### 4.3 Analytical Model of a PV Cell

An equivalent circuit solar cell model, known as the “single diode model”, has been described in Chapter 2, (figure 2.7), while current – voltage relationship is given by equation (2.20).

A new circuit is proposed, (Figure 4.4), to mimic solar cell operation; having replaced the diode, a two terminal semiconductor device with a three terminal semiconductor device, such as a npn transistor with gain denoted by  $G$ . They are both pn junctions so it is worth studying its operational behavior that can give beneficial regulation of output voltage controlling the gain parameter ( $G$ ).

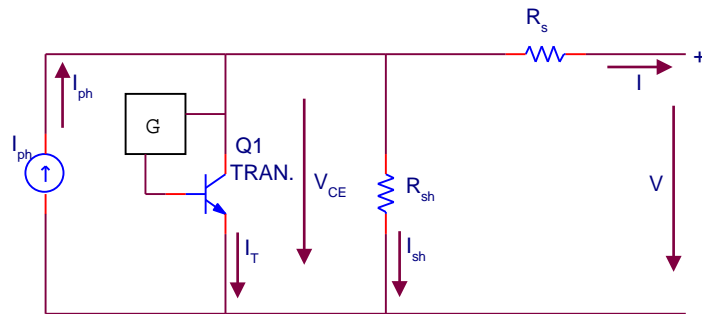


Figure 4.4. Proposed transistor equivalent circuit model.

In this work we demonstrate that by controlling  $G$  it is possible to make a diode with ideality factor  $n_1$ , saturation current  $I_{s1}$  and at a temperature  $T_1$  behave in similar manner as an arbitrary transistor with different ideality factor  $n_2$ , different saturation current  $I_{s2}$  and at a different temperature  $T_2$ . In this way the proposed transistor model can behave like a photovoltaic cell.

A theoretical analysis is performed below in order to derive a formula for gain value  $G$ , in terms of equations describing diode and transistor operation. In the analysis is considered the same current source ( $I_{ph}$ ), output voltage ( $V$ ), output current ( $I$ ), series resistance ( $R_s$  ideally zero) and shunt resistance ( $R_{sh}$  ideally

infinite). Thus, the circuits can be simplified and concentrate only on changing elements, diode and transistor with gain  $G$  value.

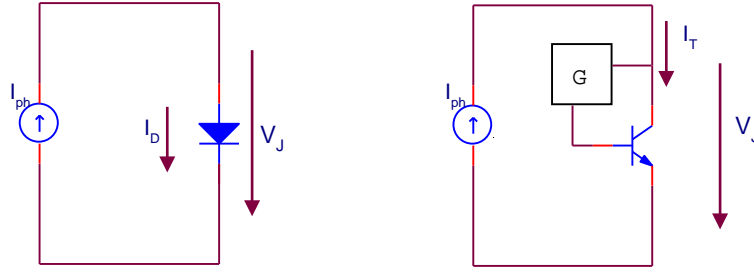


Figure 4.5. Current sources – diode and transistor with gain  $G$  circuits.

The current flowing through the diode  $I_D$  is given by the Shockley ideal diode equation:

$$I_D = I_{s1} \exp\left(\left(\frac{qV_J}{n_1kT_1}\right) - 1\right) \quad (4.1)$$

For, forward bias voltages the exponential term is very large, since the thermal voltage  $V_{T1}$  is very small in comparison. The subtracted “1” in the diode equation is then negligible and the forward diode current can be approximated by:

$$I_D \approx I_{s1} \exp\left(\frac{qV_J}{n_1kT_1}\right) \quad (4.2)$$

The current flowing through the transistor  $I_T$ , is the same as the current flowing through the diode  $I_D$ , since the same current source produces the same current. Current is related to the base emitter voltage by the Ebers-Moll relationship (sometimes labeled the Shockley equation), where:

$$I_T = I_{s2} \exp\left(\left(\frac{qV_{BE}}{n_2kT_2}\right) - 1\right) \quad (4.3)$$

Reverse saturation current is much smaller than the current supplied and is therefore negligible. Ignoring the reverse saturation current:

$$I_T \approx I_{s2} \exp\left(\frac{qV_{BE}}{n_2kT_2}\right) \quad (4.4)$$

For a given gain  $G$  it is:



$$V_{BE} = GV_{CE} \xrightarrow{V_{CE}=V_J} GV_J \quad (4.5)$$

Thus equation (4.4) due to equation (4.5) gives:

$$I_T \approx I_{s2} \exp\left(\frac{qGV_J}{n_2kT_2}\right) \quad (4.6)$$

Equating currents going through diode (equation 4.2) and transistor (equation 4.6) it is:

$$I_{s1} \exp\left(\frac{qV_J}{n_1kT_1}\right) = I_{s2} \exp\left(\frac{qGV_J}{n_2kT_2}\right)$$

$$\frac{I_{s1}}{I_{s2}} = \frac{\exp\left(\frac{qV_JG}{n_2kT_2}\right)}{\exp\left(\frac{qV_J}{n_1kT_1}\right)} = \exp\left(\frac{qV_JG}{n_2kT_2} - \frac{qV_J}{n_1kT_1}\right) = \exp\left(\frac{q}{k}\left(\frac{V_JG}{n_2T_2} - \frac{V_J}{n_1T_1}\right)\right) \quad (4.7)$$

Taking  $\ln$  in both sides:

$$\ln\left(\frac{I_{s1}}{I_{s2}}\right) = \frac{q}{k}\left(\frac{V_JG}{n_2T_2} - \frac{V_J}{n_1T_1}\right) = \frac{q}{k}\left(\frac{n_1T_1V_JG - n_2T_2V_J}{n_1T_1n_2T_2}\right) \Rightarrow \quad (4.8)$$

$$n_1T_1n_2T_2 \frac{k}{q} \ln\left(\frac{I_{s1}}{I_{s2}}\right) = n_1T_1V_JG - n_2T_2V_J \quad (4.9)$$

Solving for  $G$ , a formula for the gain is derived in terms of diode and transistor parameters:

$$G = \frac{n_1T_1n_2T_2 \frac{k}{q} \ln\left(\frac{I_{s1}}{I_{s2}}\right) + n_2T_2V_J}{n_1T_1V_J} \quad (4.10)$$

Thus an equation has been derived determining the gain  $G$  with a minimal set of parameters to achieve a representational model. This equation is going to be used for the proposed topologies that will be analysed in this Chapter.

Parameters that need to be varied to allow arbitrary junction and arbitrary temperature are  $I_{s1}$ ,  $n_1$ ,  $T_1$  referring to a simulated version of a solar cell (PC1D software) while  $I_{s2}$ ,  $n_2$ ,  $T_2$  referring to an artificial solar cell. Two methodologies

are described in this Chapter for extracting the above mentioned parameters one for each case.

#### 4.4 Basic $V_{BE}$ Multiplier

The basic  $V_{BE}$  multiplier is a well-known circuit. It is conventionally used to create a scaled copy of a bipolar transistor  $V_{BE}$  to generate bias voltages, most commonly in complementary class AB power output stages. As stated in [144] the bias circuit consists of a transistor  $Q_1$  with a resistor  $R_1$  connected between base and emitter and a resistor  $R_2$  connected between collector and base.

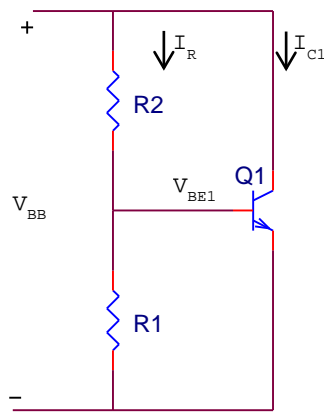


Figure 4.6.  $V_{BE}$  multiplier for biasing. Adapted from [144].

If the base current of  $Q_1$  is neglected, then  $R_1$  and  $R_2$  will carry the same current  $I_R$ , given by:

$$I_R = \frac{V_{BE1}}{R_1} \quad (4.11)$$

and the voltage  $V_{BB}$  across the bias network will be:

$$V_{BB} = I_R (R_1 + R_2) = V_{BE1} \left( 1 + \frac{R_2}{R_1} \right) \quad (4.12)$$

Thus, the circuit simply multiplies  $V_{BE1}$  by the factor  $(1 + R_2/R_1)$  and is known as the “ $V_{BE}$  multiplier” [144]. The multiplication factor is obviously under the designer’s control and can be used to establish the value of  $V_{BB}$  required.

Taking into consideration the biasing arrangement described above, a new photovoltaic cell model is proposed that employs the  $V_{BE}$  multiplier. The proposed topology can be seen in figure 4.7.

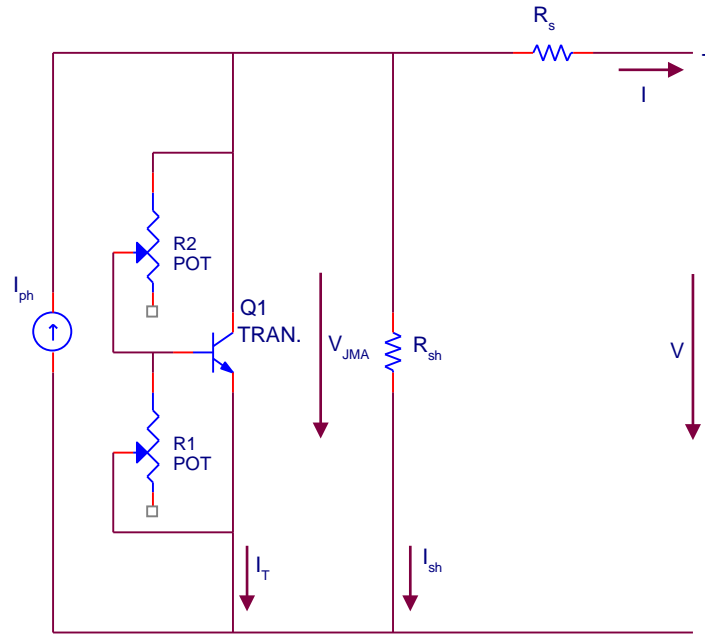


Figure 4.7. Proposed transistor model, biased with two potentiometers.

Adjusting the value of the potentiometers the voltage across the junction ( $V_{JMA}$ ) is regulated. In that means the output voltage  $V$  is controlled. The base emitter voltage ( $V_{BE}$ ) is given by the following formula:

$$V_{BE} = \frac{R1}{R1 + R2} \cdot V_{JMA} \quad (4.13)$$

or solving for  $V_{JMA}$  it is:

$$V_{JMA} = V_{BE} \left( \frac{R1 + R2}{R1} \right) = V_{BE} \left( 1 + \frac{R2}{R1} \right) \quad (4.14)$$

Comparing equation (4.5) with (4.13) the gain  $G$  is equal to:

$$G = \frac{R1}{R1 + R2} \quad (4.15)$$

The maximum gain of the circuit is 1, when  $R2=0$ . For higher values of  $R2$ , gain  $G$  drops to less than 1. Note that the circuit according to equation 4.14 is limited to the case where  $V_{JMA} \geq V_{BE}$ . The equality  $V_{JMA} = V_{BE}$  valid for  $R2 = 0$ , while for higher values of  $R2$  it is  $V_{JMA} > V_{BE}$ . So, if the reference device  $Q1$  is a conventional silicon transistor, then it is not possible to use this topology to represent a junction in a material with a smaller bandgap, or at a higher temperature than the  $Q1$ .

In most bias applications the choices for  $R1$  and  $R2$  are a compromise such that  $I_b$  is not a large fraction of the current through  $R2$ , but this also implies that there can be a significant resistive current path in parallel with the transistor, detracting from the ideal exponential behaviour. Experiments performed, indicate typical values for  $R2$  to be in the range of Ohms (0 – 10 Ohms) while  $R1$  has much higher value in kOhm range. A certain amount of current will go through resistor  $R2$  ( $I_{R2}$ ). Current  $I_{R2}$  is higher than the base current. Base current varies and depends on the beta ( $\beta$ ) of the transistor ( $I_b = I_c / \beta$ ). It has to be noted that if both resistors  $R1$  and  $R2$  are much higher (kOhm range) so that less current going through the resistor branch, the circuit operation does not behave like a solar cell. Also, if both resistances ( $R1$  and  $R2$ ) are small, the current flowing through the resistor branch is large, so the current flowing through transistor is small and circuit operation does not behave like a solar cell. So, resistor values have been selected such as to perform equivalent to a photovoltaic cell module.

Concluding, this topology remains a simple way to mimic solar cell behavior but it is not flexible enough to be used as a photovoltaic cell simulator due to the fact that  $G \leq 1$ . In all experiments presented circuit operation will be described in terms of the gain  $G$  value, since it is the overall effect of controlling the 2 resistor values.

#### 4.4.1 Parameter extraction from PC1D

As we have seen solar cell characteristic I/V curves can be obtained analytically (using well-known equations) or by use of an equivalent circuit model. A third way to obtain the I/V curve for a solar cell is by device simulation, generally by use of sophisticated semiconductor modelling packages such as PC1D. In this project we decided to use PC1D to obtain a consistent set of data for a device for a range of temperatures and insolation levels, we would then develop our solar cell emulator around this one data set.

A methodology is described in this section for extracting model parameters for the solar cell simulated in PC1D software. First, a silicon device has been chosen in PC1D selecting the “*pvcell.prm*” file. The default values were used, changing only the device area from the default value 100 cm<sup>2</sup> to 8 cm<sup>2</sup>, in order to study a smaller device area, constraining the current in mA region (up to 250 mA).

Theoretically, the series resistor has a small value, while the shunt resistor has a large value. In the device section of the simulation program values of internal series resistance was set to 0.5 Ohm, while the internal shunt elements was set to 0.00005 Siemens (20 kOhm). The diode ideality was set to 1. Also, intensity was constant  $0.1 \text{ W/cm}^2$  and spectrum AM 1.5. The default number of points (time steps) along the I – V curve is 16, with maximum available 200 points. The maximum available option was selected in order to have as many as possible data points along the I – V characteristic curve. When the simulation is concluded open circuit voltage and short circuit current are displayed in the results section.

The limitation of this circuit on the gain ( $G$ ), which can be 1 or less than 1, has a certain impact on the circuit operation, so for Gain value 0.99 (close to 1), a negative temperature of  $-20^\circ\text{C}$  was emulated in PC1D for silicon solar cell device. Parameters of PC1D program are summarized in Table 4.1.

Table 4.1. Parameters set and values obtained from PC1D software.

PC1D Parameters	Value
Insolation	1000 Watt/m <sup>2</sup>
Temperature	253 Kelvin ( $-20^\circ\text{C}$ )
Internal Series Resistance	0.5 Ohm
Internal Shunt Elements	0.00005 S (20 kOhm)
Diode ideality	1
Short Circuit Current	254.90 mA
Open Circuit Voltage	0.6905 V

In order to determine the remaining unknown parameters a curve fitting algorithm was utilized. A methodology for solving nonlinear least square (nonlinear data fitting) problem has been adopted, where the objective function is defined in terms of auxiliary functions  $\{f_i\}$ , where the index  $i$  indicates the particular data point.

$$\min_x f(x) = \sum_{i=1}^m f_i(x)^2 \quad (4.16)$$

The implementation of nonlinear least-square fit was performed in Matlab software environment. In the context of data fitting, the auxiliary functions  $\{f_i\}$  are not arbitrary nonlinear functions. They correspond to the residuals in a data fitting problem. Residual measures the vertical distance between the actual data point

and the data point according to the proposed model. If the error is zero, then the model fits the data with no error. In general terms it is:

$$[Observation] = [Model] + [Error] \quad (4.17)$$

The residual value is normalized and returned by the algorithm. Normalization means adjusting residual measured on different scales to a notionally common scale. The function describing photovoltaic cell behavior is given by equation (2.21). Thus, the function  $F$  whose sum of squares considered minimizing is:

$$Function, \quad F = I - \left( I_{ph} - I_o \left( \exp \left( \frac{V + IR_s}{V_t} \right) - 1 \right) - \frac{V + IR_s}{R_{sh}} \right) \quad (4.18)$$

The five fitting parameters are replaced as variables, and Function  $F$  becomes:

$$Function, \quad F = I - \left( x(1) - x(2) \left( \exp \left( \frac{V + Ix(3)}{\frac{x(4)kT}{q}} \right) - 1 \right) - \frac{V + Ix(3)}{x(5)} \right) \quad (4.19)$$

where,  $x(1)$  is the photocurrent  $I_{ph}$ ,  $x(2)$  is the saturation current  $I_o$ ,  $x(3)$  is the series resistance  $R_s$ ,  $x(4)$  is the ideality factor  $n$  and  $x(5)$  is the shunt resistance  $R_{sh}$ . Current and voltage data points provided by PC1D are denoted by  $I$  and  $V$  respectively.

The fitting algorithm has performed using “*LSQNONLIN*” routine in MATLAB to solve non-linear least squares problems in the form of:

$$[x, resnorm] = lsqnonlin (@ myfun, x0)$$

where,  $x$  are returned solution values,  $resnorm$  is the normalized residual,  $@myfun$  is the function whose sum of squares is minimized. Starts at point  $x0$  and finds a minimum  $x$  to the sum of squares of the function described in  $@myfun$ . Starting guess was set to the following values:

$$x0 = [x1 \ x2 \ x3 \ x4 \ x5] = [0.2547 \ 10e-15 \ 0.5 \ 1 \ 20000] \quad (4.20)$$

Invoking the optimizer “five model parameters” along with residual value obtained, are in table 4.2.

Table 4.2. Curve fitting algorithm calculated values.

Algorithm Parameters	Value
Photocurrent $I_{ph}$	254.28 mA
Saturation current $I_o$	$4.4997 \cdot 10^{-15}$ A
Ideality factor $n$	1
Series Resistance $R_s$	0.5007 Ohm
Shunt Resistance $R_{sh}$	20 kOhm
Normalized Residual $resnorm$	$3.76 \cdot 10^{-5}$

In the case examined the error is very small in the range of  $10^{-5}$ , indicating that the model fits the data almost perfectly. Below the two curves have been plotted for visualization purposes. The blue I-V curve refers to data obtained from PC1D, while the red curve shows the curve fitting algorithm.

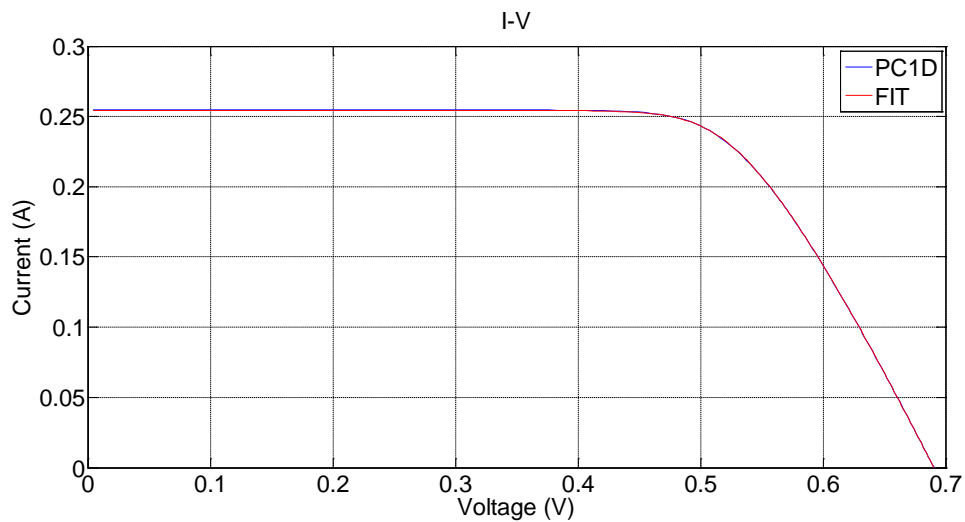


Figure 4.8. Current voltage characteristics, obtained from simulation and fitting algorithm.

As it can be seen in figure 4.8, there is good agreement between the two characteristics thereby verifying obtained values.

#### 4.4.2 Parameter extraction for the Transistor

A methodology for extracting the remaining 3 parameters for evaluating gain ( $G$ ) in equation 4.10 is described in this section in terms of the transistor utilized (BD243C). These parameters are saturation current  $I_{s2}$ , ideality factor  $n_2$  and temperature  $T_2$ .

The artificial solar cell was adjusted using the current source and  $G$  such as to perform in similar manner as the simulation condition described by PC1D

software. The I-V characteristic curves of the PC1D simulation (blue curve) and the proposed artificial solar cell circuit (red curve) are in accordance as it can be seen in Figure 4.9. The plots coincide with each other, with a small error denoted. A statistical indicator, RMS error value, for describing the error value between the two curves will be derived in the next section.

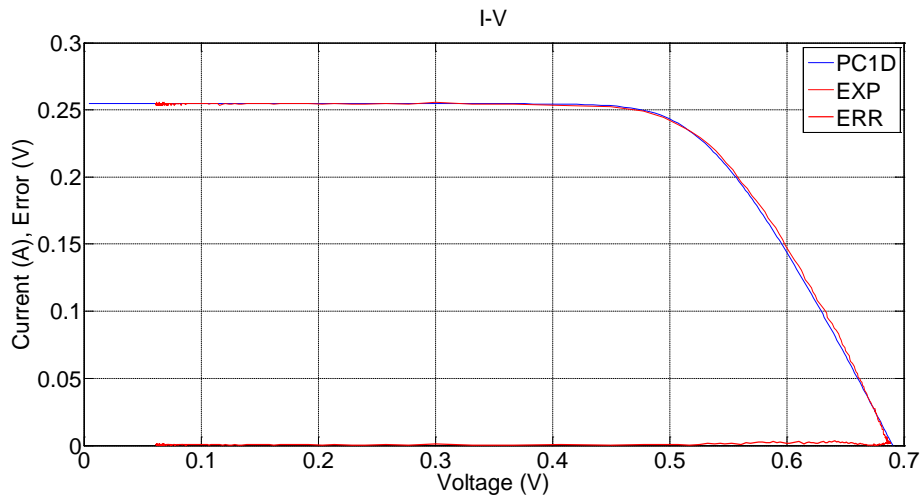


Figure 4.9. I-V characteristic curve plots for PC1D software simulation program, Artificial Solar Cell circuit proposed and Error.

As stated in [145] in order to extract the relevant parameters ( $I_{s2}$ ,  $n_2$ ,  $T_2$ ) a graph should be drawn of the current flowing through the transistor ( $I_T$ ) on a logarithmic scale against base emitter voltage ( $V_{BE}$ ). An exponential fit line was added to the graph, quoting the equation that best describes the data points. A statistical indicator  $R$  squared value describes the fit to the data, (1 is a perfect match) (figure 4.10).



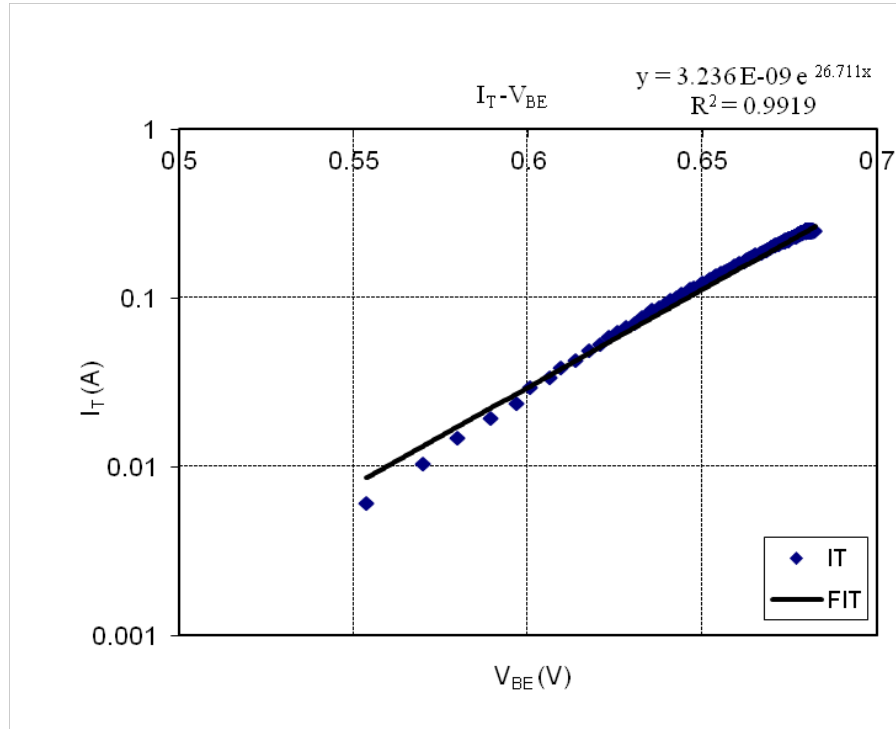


Figure 4.10. Plot of current flowing through the transistor in logarithmic scale against base emitter voltage.

The fit line equation and  $R$  squared “ $R^2$ ” values are:

$$y = 3.236 \cdot 10^{-9} \exp(26.711x), \quad R^2 = 0.9919 \quad (4.21)$$

Comparing the fit line equation (4.21) with equation (4.4), saturation current  $I_{s2}$  and thermal voltage  $V_{T2}$  can be extracted:

$$I_{s2} = 3.236 \cdot 10^{-9} \text{ A and } \frac{1}{V_{T2}} = 26.711 \Rightarrow V_{T2} = \frac{1}{26.711} \text{ (V)} \quad (4.22)$$

Knowing that the thermal voltage is given by the equation (2.22), replacing electronic charge and Boltzmann constants it is:

$$V_{T2} = \frac{1}{26.711} = \frac{n_2 k T_2}{q} \Rightarrow n_2 T_2 = \frac{q}{26.711 k} = 434.46 \text{ Kelvin} \quad (4.23)$$

Ideality factor and temperature of transistor have been extracted as a product. There is no need to compute each value separately, since on the formula derived for the  $G$  (equation 4.10) the term  $n_2 T_2$  is going to be substituted as a product. Also, in this section saturation current  $I_{s2}$  for the transistor has also been extracted.

Concluding it can be said that all necessary parameters for evaluating the gain ( $G$ ) (4.10), have been computed and the two methodologies utilized have been

Chapter 4. Modeling PV cell Operation, Behavior Using and Improved  $V_{BE}$  Multiplier analytically described, stating in each one the statistical indicators, *Residual* and *R squared* values.

#### 4.4.3 Error Calculation

In order to qualify the fit between current versus voltage characteristic curves in Figure 4.9, of theoretical and artificial proposed model, another statistical indicator has been calculated. Data analysis of the results has been performed computing the root mean square error (*RMSE*) which is a fundamental measure of accuracy, defined by the following relation:

$$RMSE = \left( \sum |e_i|^2 / N \right)^{\frac{1}{2}} \quad (4.24)$$

where,  $\Sigma$  is the sum,  $e_i$  is the error and  $N$  is the number of the data measurements.

The error is considered for current and voltage at the  $i^{th}$  point among  $N$  data that have been taken into account. Measurements close to open circuit and short circuit conditions should be avoided, since the shape of the curve changes to an extent that data analysis is less accurate, current and voltage are not well defined [146].

The *RMSE* was applied using the following formula:

$$RMSE = \left( \sum \left( (V_{theor} - V_{exp})^2 + (I_{theor} - I_{exp})^2 \right) / N \right)^{\frac{1}{2}} \quad (4.25)$$

where,  $V_{theor}$  and  $I_{theor}$  are the theoretically obtained values of voltage and current from PC1D respectively, while  $V_{exp}$  and  $I_{exp}$  are the experimentally obtained values of voltage and current from the proposed transistor artificial solar cell model respectively.

#### 4.4.4 Series Resistance Compensation

The series resistance selected in PC1D was 0.5 Ohm. Placing this value of resistor in the artificial solar cell circuit produces a divergence between I-V characteristic curves. A deviation of 0.05273 ( $\Omega^{-1}$ ) is noticeable in figure 4.11.

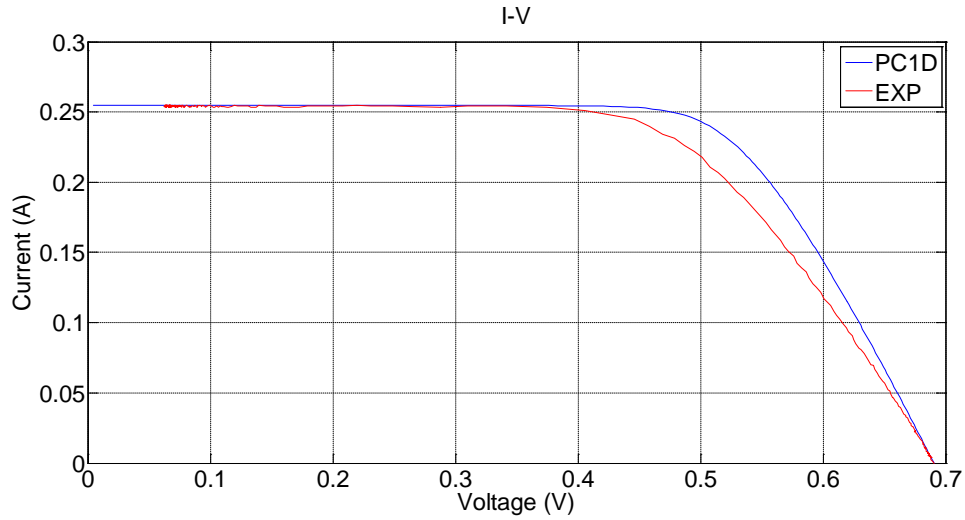


Figure 4.11. Deviation between I-V characteristic curves for standard series resistance.

A modification has applied to the circuit taking into account series resistance change. According to [140] a simple estimation of series resistance of a photovoltaic module is presented for low error modeling. Series resistance value is given by equation 4.26. A derivation of the formula and briefly description can be found in Appendix B.

$$R_s = \frac{1}{I_{mpp}} \left[ V_{oc} - V_{mpp} - nV_{th} \text{Ln} \frac{V_{mpp} + nV_{th} - I_{mpp} R_s}{nV_{th}} \right] \quad (4.26)$$

Since  $R_s$  is also within the logarithmic term, the solution cannot be achieved without resorting to an iterative procedure. It is possible to reach a good enough solution in two steps.

In the first step, the logarithmic term of equation (4.26) is approached by removing the numerator  $I_{mpp} R_s$  and  $nV_{th}$  and an initial  $R_{so}$  value is estimated:

$$R_{so} = \frac{1}{I_{mpp}} \left[ V_{oc} - V_{mpp} - nV_{th} \text{Ln} \frac{V_{mpp}}{nV_{th}} \right] \quad (4.27)$$

In the second step the  $R_{so}$  value of equation (4.27) is inserted into (4.26) to obtain a final  $R_{s1}$  value.

Evaluating the above formula with the values stated in Table 4.3 series resistance value was calculated.

Table 4.3. Data required for theoretical calculation of series resistance value.

Also, experimental resistor utilised along with percentage difference.

Data Parameters	
Temperature $T$	253 Kelvin
Maximum Voltage $V_{mpp}$	0.5068 V
Maximum Current $I_{mpp}$	0.2394 A
Open circuit voltage $V_{oc}$	0.6885 V
Series Resistance Theoretically calculated and Experimentally utilised	
Theoretical series resistance $R_s$	0.36 Ohm
Experimental series resistance $R_s$	0.37 Ohm
<i>Difference</i>	2.77 %

Theoretical series resistance value was computed to be  $R_s = 0.36$  Ohm. The value experimentally placed in the artificial solar cell in order to obtain the best possible match was  $R_s = 0.37$  Ohm, with a difference of 2.77% noticed compared to the theoretical estimated value. Percentage *difference* was calculated according to the following equation:

$$\text{Percentage Difference} = \frac{|\text{theoretical} - \text{experimental}|}{\text{theoretical}} \cdot 100\% \quad (4.28)$$

where, theoretical is the value calculated according to the formula provided, while experimental is the value of the series resistance placed in the proposed electronic circuit.

An important contribution to this difference comes from the resistor tolerance. There is a deviation between actual and conventional values due to resistor tolerances. The tolerance of a resistor is referred to the deviation from its nominal value resistance. The larger the resistor tolerance, the more it may vary, either up or down, from its nominal value. The smaller the resistor tolerance, the less it varies from its nominal value and, thus, the more stable it becomes. The most common way of specifying resistor tolerance is by percentage. Typical resistor

tolerances are 1 percent, 2 percent, 5 percent, 10 percent and 20 percent. The resistors utilized and actually placed in the proposed electronic circuit topology have a deviation from its nominal value up to  $\pm 5\%$  according to the manufacturer. This divergence can result in a difference between theoretically calculated and experimentally utilized resistor value.

Another reason is that the two I-V characteristic curves are not perfectly matched. Thus, any discrepancy in values of  $V_{oc}$ ,  $V_{mpp}$ ,  $I_{mpp}$  between theoretical indicated by PC1D and experimental attained increases the percentage difference. In addition the product parameter  $n_2T_2$  was extracted with a certain error stated in equation (4.21). Finally, the equation (4.26) itself contains an error of accuracy (0.5%) [140]. Summing all these factors can justify the difference of series resistance between the theoretically calculated and experimentally utilized value.

Concluding it can be said that applying correction to series resistance value results in a better fit between the I-V characteristic curves as indicated in Figure 4.9.

As it can be observed from equation (4.26) series resistance depends on parameters such as temperature ( $T$ ) included in the thermal voltage value, as well as open circuit voltage ( $V_{oc}$ ), maximum voltage ( $V_{mpp}$ ) and current ( $I_{mpp}$ ) which are greatly influenced by insolation and temperature conditions. These variations have to be considered in the artificial solar cell circuit in order the I-V characteristic curves to be in accordance.

#### 4.4.5 Experimental Results – Discussion

The basis of conducting an experiment has been set out. In this section the gain ( $G$ ) of the circuit is evaluated, with the data extracted in previous sections. All values used are summarized in Tables (4.4) and (4.5).

Table 4.4. Parameters related to PC1D simulation.

Simulation Parameters	
Ideality factor $n_I$	1
Saturation Current $I_{sI}$	$4.499 \cdot 10^{-15}$ A
Temperature $T_I$	253 Kelvin
Open Circuit Voltage $V_J$	0.6905 V

Table 4.5. Parameters related to Artificial Solar Cell proposed electronic circuit.

Artificial Solar Cell	
Ideality factor · Temperature $n_2T_2$	434.46 Kelvin
Saturation Current $I_{s2}$	$3.236 \cdot 10^{-9}$ A

Substituting values to equation (4.10) the gain  $G$  is computed:

$$G = \frac{n_1T_1n_2T_2 \frac{k}{q} \ln\left(\frac{I_{s1}}{I_{s2}}\right) + n_2T_2V_J}{n_1T_1V_J} = 0.986 \quad (4.29)$$

Experimental  $G$  measured value on the artificial solar cell is:

$$G = \frac{V_{BE}}{V_J} = \frac{0.6823}{0.6885} = 0.991 \quad (4.30)$$

The applicability has been tested to different temperature conditions. The same device (Si) with the same characteristics has been used in PC1D, varying only the temperature from  $-20^\circ\text{C}$  (253 Kelvin) to  $-40^\circ\text{C}$  (233 Kelvin) with a step of  $-10^\circ\text{C}$ . The gain of the artificial solar cell has been adjusted in order to match the output voltage according to PC1D. Parameters extracted from the simulation program ( $n_1T_1, I_{s1}, V_J$ ) along with the normalized residual “*Residual*” value, as well as parameters extracted for the artificial solar cell ( $n_2T_2, I_{s2}$ ) along with *R squared* “ $R^2$ ” value are summarized in Table 4.6 to 4.7 respectively. Series resistance compensation applied is shown in Table 4.8. Resistor biasing arrangements for all experiments performed is shown in Table 4.9.

Finally, graphical representation of all measurements obtained is illustrated below in Figures 4.12 and 4.13. Six parameters of series resistance, shunt resistance, saturation current, ideality factor time’s temperature, photocurrent and gain values are plotted against temperature conditions examined. The I-V characteristic curves for all cases considered are illustrated in Figure 4.14.

Table 4.6. Summarizing experimental setup values for experiment conducted, at 1000  $\text{W}/\text{m}^2$  irradiance and different temperature conditions.

Experimental Setup									
Temperature							G		
Insol.	T	$R_s$	$R_{sh}$	$I_o$	$nT$	$R^2$	$I_{ph}$	(Gain)	
$\text{W}/\text{m}^2$	(Kelv), ( $^{\circ}\text{C}$ )	(Ohm)	(kOhm)	(A)	(kelvin)		(mA)	Exper.	RMSE
	253 (-20)	0.37	20	3.24E-09	434.5	0.992	253.92	0.986	$1.36 \cdot 10^{-3}$
1000	243 (-30)	0.32	20	2.68E-09	430.1	0.992	253.79	0.957	$1.60 \cdot 10^{-3}$
	233 (-40)	0.27	20	1.74E-09	420.2	0.988	253.67	0.9304	$1.70 \cdot 10^{-3}$

Table 4.7. Summarizing theoretical setup values for experiment conducted, at 1000  $\text{W}/\text{m}^2$  irradiance and different temperature conditions.

Theoretical Setup									
Temperature							G		
Insol.	T	$R_s$	$R_{sh}$	$I_o$	$nT$	$R_{residual}$	$I_{ph}$	(Gain)	$V_J$
$\text{W}/\text{m}^2$	(Kelv), ( $^{\circ}\text{C}$ )	(Ohm)	(kOhm)	(A)	(kelvin)		(mA)	Theor.	(V)
	253 (-20)	0.5	20	4.50E-15	253	$3.76 \cdot 10^{-5}$	254.28	0.992	0.691
1000	243 (-30)	0.5	20	4.52E-16	243	$2.19 \cdot 10^{-5}$	254.17	0.959	0.711
	233 (-40)	0.5	20	3.76E-17	233	$3.10 \cdot 10^{-5}$	254.03	0.931	0.732

Table 4.8. Series resistance experimentally placed and theoretically calculated along with relevant data.

Series Resistance Compensation							
Temperature	Experim.	Theoretic.	Difference	$V_{i2}$	$V_{mpp2}$	$I_{mpp2}$	$V_{oc2}$
(Kelv), ( $^{\circ}\text{C}$ )	$R_s$ (Ohm)	$R_s$ (Ohm)	(%)	(Volt)	(V)	(A)	(V)
253 (-20)	0.37	0.36	2.77	0.0374	0.507	0.239	0.689
243 (-30)	0.32	0.34	5.88	0.0371	0.533	0.238	0.711
233 (-40)	0.27	0.30	10	0.0362	0.560	0.237	0.730

Table 4.9. Basic  $V_{BE}$  multiplier biasing arrangement for all cases considered.

Experimental Setup			
Insol.	Temperature	$R_2$	$R_1$
$\text{W}/\text{m}^2$	(Kelv), ( $^{\circ}\text{C}$ )	(Ohm)	(kOhm)
	253 (-20)	0	1
1000	243 (-30)	4.1	1
	233 (-40)	8.2	1

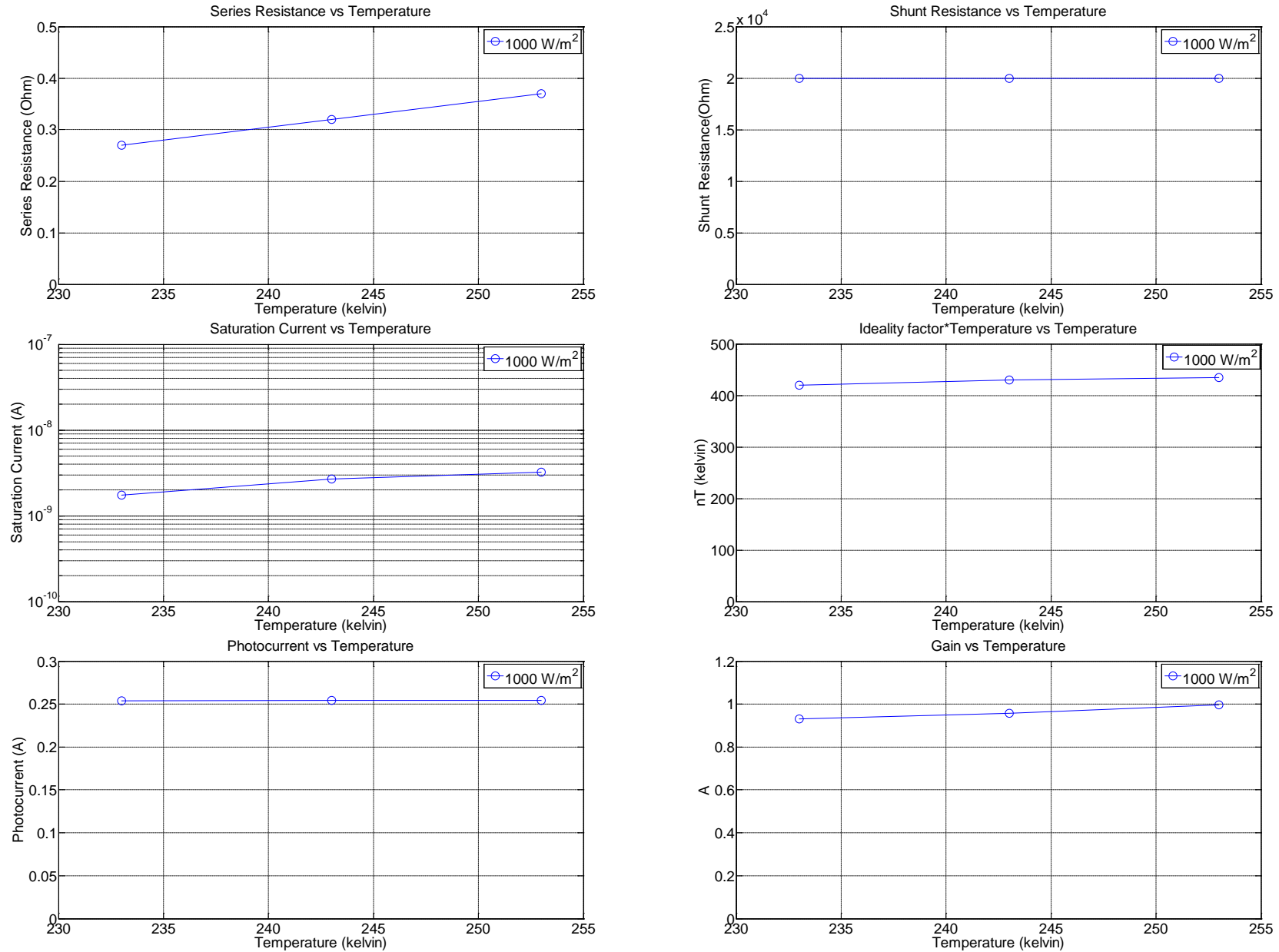


Figure 4.12. Experimental values versus Temperature for irradiance 1000 W/m<sup>2</sup>.



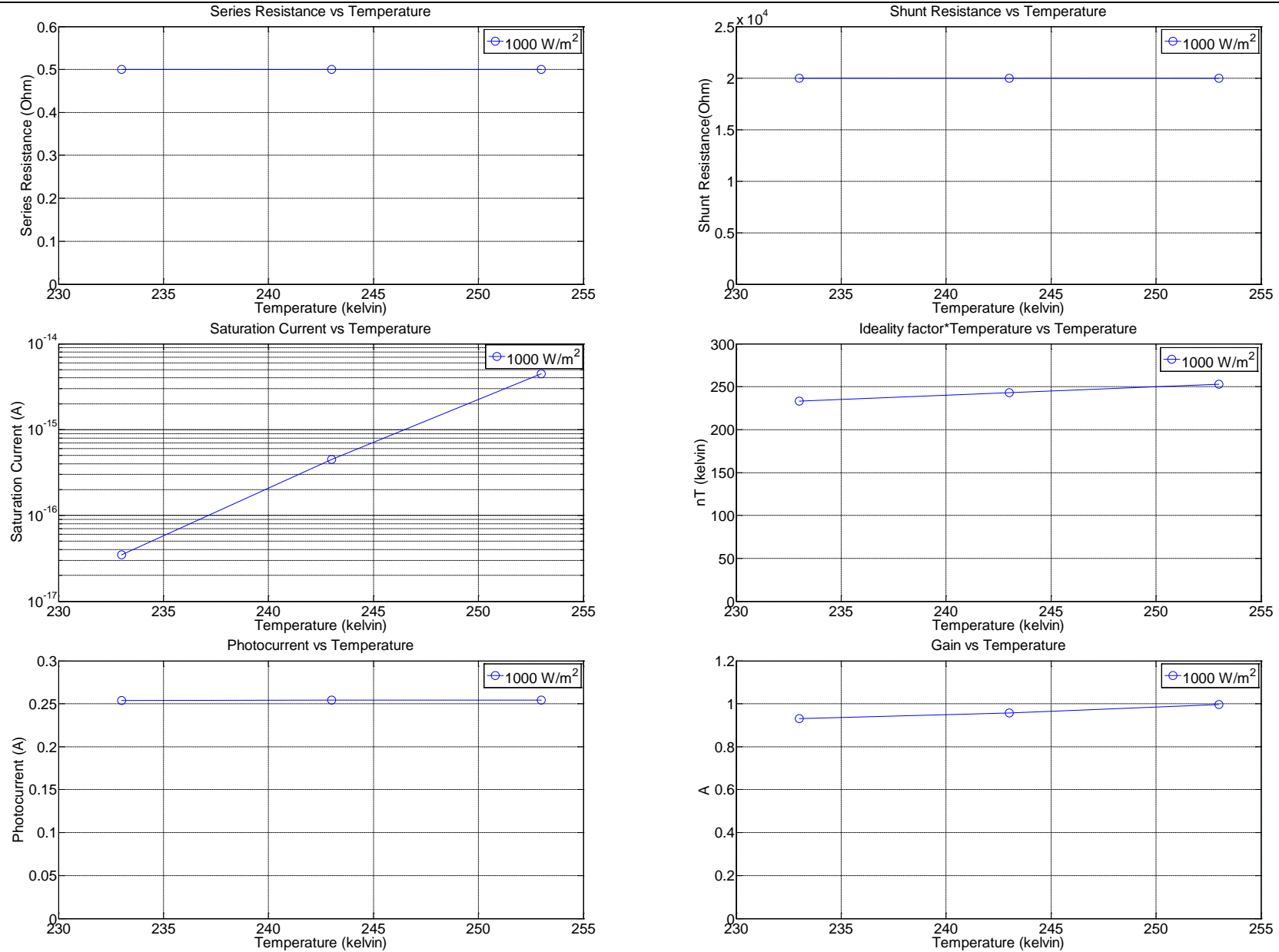


Figure 4.13. Theoretical values versus Temperature for irradiance  $1000 \text{ W/m}^2$ .

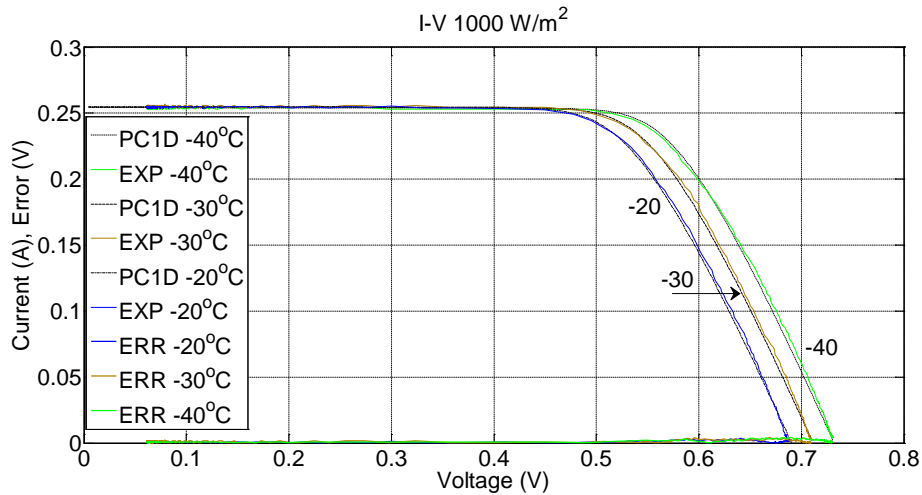


Figure 4.14. I-V characteristic curve plots for all cases considered.

Transistor extracted parameter “ $R_{squared}$ ” value in all cases considered is close to 1 (approximately 0.99) and the parameters extracted for the simulated version of the solar cell have small “ $Residual$ ” value ( $10^{-5}$ ). The small error in the data fitting problem suggests accurate parameter extraction.

The small  $RMSE$  value order of  $10^{-3}$  for best fit between I – V characteristic curves, illustrates that the proposed circuit topology analytically described is an accurate method for emulating artificially a solar cell. The Error versus Voltage plot at the bottom side for each case considered graphically illustrates the small discrepancy between characteristic curves, apart from the statistical indicator  $RMSE$ .

Summarizing all experiments performed, gain  $G$  values theoretical derived according to the formula 4.10 and experimentally measured, show numerical agreement at all cases considered. As gain decreases temperature decreases. According to formula (4.5) as gain decreases this results in an increase of open circuit voltage  $V_J$  for the same  $V_{BE}$  value. Increase of open circuit voltage  $V_J$  corresponds to temperature decrease for the particular solar cell as indicated in Figure 4.14.

There is a numerical agreement in values of shunt resistance and photocurrent for all cases considered. Shunt resistance is set to 20kOhm throughout all experiments. Photocurrent is almost constant with a small negligible variation in  $\mu A$  range. As temperature decreases photocurrent also slightly decreases.

Chapter 4. Modeling PV cell operation and Behaviour Using and Improved  $V_{BE}$  Multiplier

Series resistance compensation has applied to the artificial solar cell circuit such as to match I-V characteristic curves. Evaluating equation (4.26) which describes the series resistance, it is observed that as temperature decreases series resistance also decreases. In the simulation program series resistance value throughout all experiments conducted was kept constant (0.5 Ohm).

Saturation current values extracted experimentally are in the order of magnitude  $10^{-9}$  (A). Values extracted from the simulation program are in the range of  $10^{-15}$  to  $10^{-17}$  (A).

Ideality factor times temperature ( $nT$ ) values extracted experimentally are in the range of 435 to 420 (kelvin). On the other hand, parameters extracted from the simulation model are in the range of 253 to 233 (kelvin). In the theoretical approach for the ideal case considered ideality factor has theoretically unity value ( $n=1$ ). Thus, any increase in temperature will result in a proportional increase to the product of  $nT$ .

The  $nT$  differences of approximately 200K comparing the two cases presented. So, it is clear that saturation current changes in order to compensate for that difference such that the I-V characteristic curves to match. The saturation current for the transistor is on average seven orders of magnitude bigger than the saturation current of the simulated solar cell, in order to anticipate differences in the product  $nT$ .

Concluding on the “*Basic  $V_{BE}$  multiplier*” it is necessary to emphasize that this topology can sufficient emulate a solar cell and regulate output voltage but it is not flexible enough to be used as a reliable photovoltaic cell model to cover wide operational range. Working with the particular parameters stated in PC1D software program, minimum open circuit output voltage able to be emulated was 0.6905 V. This value corresponds to negative temperature of  $-20^{\circ}\text{C}$  in PC1D software program. Higher open circuit voltage values result to even more negative temperature conditions. It is clear that neither positive temperature nor smaller open circuit voltage conditions can be obtained with the conventional  $V_{BE}$  multiplier topology due to the limitation of the gain. So, a new “*improved  $V_{BE}$  multiplier*” will be proposed in the next section to cover a wide range of operational conditions.

## 4.5 Improved $V_{BE}$ Multiplier

Identifying the weaknesses of the “*basic  $V_{BE}$  multiplier*” modification of the electronic circuit was required to be able to emulate solar module in wider operational range. A new improved  $V_{BE}$  multiplier is now proposed.

The transistor circuit model for emulating a solar cell can be seen in Figure 4.4. Simplifying and concentrating only on the transistor element the block diagram is illustrated in figure 4.5. Omitting the current source, the ideal transistor with amplifier block circuit can be seen in Figure 4.15.

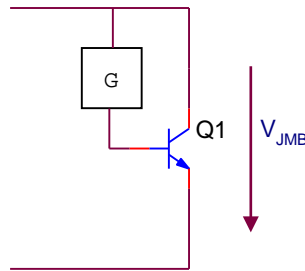


Figure 4.15. Ideal transistor with amplifier block diagram circuit.

According to equation (4.5)  $V_{JMB} = V_{BE} / G$ . For  $V_{JMB}$  to be less than  $V_{BE}$  we need  $G > 1$ , and for  $V_{JMB}$  to be larger than  $V_{BE}$ , we need  $G < 1$ . This implies large variation in the programmable gain. However, in reality, the range needed for  $G$  to allow modeling of most types of photovoltaic cell over realistic operating conditions is not very great and a simple circuit implementation is possible. Hence, the gain of the amplifier can be set to a well defined fixed value  $G_2$  greater than unity, and use a variable attenuator  $B$  at its input to realise an effective range of amplification  $G$ .

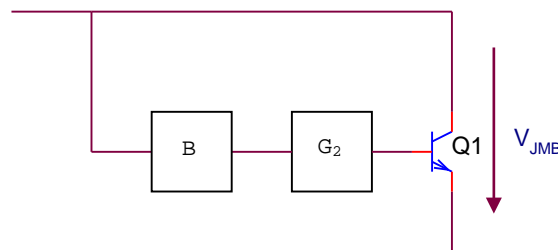


Figure 4.16. Circuit with amplifier  $G_2$  and attenuator  $B$ .

Amplification  $G_2$  can usefully be a small integer value of for example 2, allowing the modeling of junctions with effective forward voltages  $1/2$  of that of the

Chapter 4. Modeling PV cell operation and Behaviour Using and Improved  $V_{BE}$  Multiplier reference device  $QI$  when the attenuator factor  $B$  is unity. This can be described in terms of equations (4.31) and (4.32):

$$G = BG_2 \quad (4.31)$$

Evaluating equation (4.31) for  $B=1$  and  $G_2=2$ , will give a value of  $G=2$ . Replacing to formula (4.5) it is:

$$V_{JMB} = \frac{V_{BE}}{G} = \frac{V_{BE}}{2} \quad (4.32)$$

In this case if  $B$  is set to  $1/4$ , then the circuit will appear to have a forward voltage double that of  $QI$  at the same current.

A convenient practical implementation can be achieved using a simple non-inverting amplifier to realise  $G_2$ , with a simple potentiometer for the attenuator  $B$ .

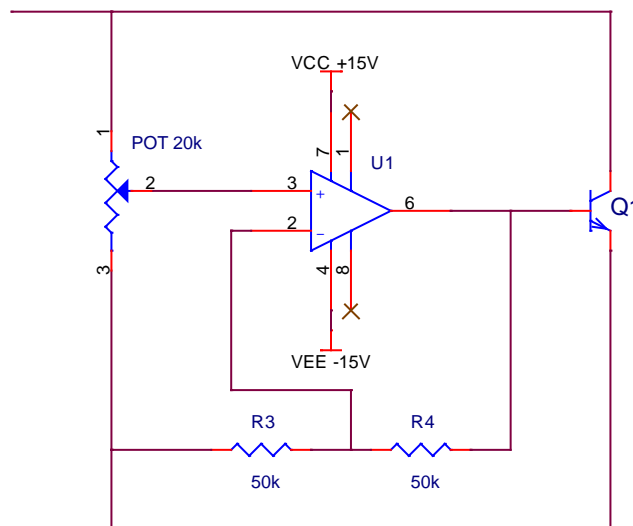


Figure 4.17. Circuit with non-inverting operational amplifier and resistive divider.

The advantage of this arrangement is that the base current for  $QI$  is now supplied by the operational amplifier, from its power supply and not from the input, hence beta variation has no impact on the ideality of the diode behaviour.

A further advantage arises from the use of the classical non-inverting operational amplifier topology in that its input resistance is very high, limited only by the specification of the particular operational amplifier used. As a consequence, it is possible to employ a potentiometer with a high absolute resistance, and hence make any parallel resistive current truly negligible, without having any impact on the accuracy of the attenuation factor. Enhancing this simple electronic circuit can

make it operate as a reliable artificial solar cell, as will be analysed in the next sections.

#### 4.5.1 Extracting PV Cell Parameters from PC1D

A similar experiment to that described in 4.4.1 was carried out, this time there was no longer any serious limitation to the temperature values used. The same silicon device was selected in PC1D and the device area was set to  $8 \text{ cm}^2$ , series resistance  $R_s$  to 0.5 Ohm and shunt resistance  $R_{sh}$  to 20kOhm (0.00005 Siemens). Ideality factor was set to 1, temperature to  $+40 \text{ }^\circ\text{C}$  (313 kelvin), intensity was constant  $0.1 \text{ W/cm}^2$  and spectrum to AM 1.5. Open circuit voltage and short circuit current are displayed in the results section when experiment was concluded. Parameters are summarized in Table 4.10.

Table 4.10. Parameters set and values obtained from PC1D software.

PC1D Parameters	Value
Insolation	1000 Watt/m <sup>2</sup>
Temperature	313 Kelvin (40 °C)
Internal Series Resistance	0.5 Ohm
Internal Shunt Elements	0.00005 S (20 kOhm)
Diode ideality	1
Short Circuit Current	255.83 mA
Open Circuit Voltage	0.5603 V

‘Five model parameters’ extraction was carried out (Table 4.11).

Table 4.11. Extracted values.

Algorithm Parameters	Value
Photocurrent $I_{ph}$	255.02 mA
Saturation current $I_o$	$2.4397 \cdot 10^{-10}$ (A)
Ideality factor $n$	1
Series Resistance $R_s$	0.501 Ohm
Shunt Resistance $R_{sh}$	19.999 kOhm
Normalized Residual $resnorm$	$4.33 \cdot 10^{-5}$

In the case examined the error is very small ( $10^{-5}$ ). The two I-V curves are plotted in Figure 4.18.

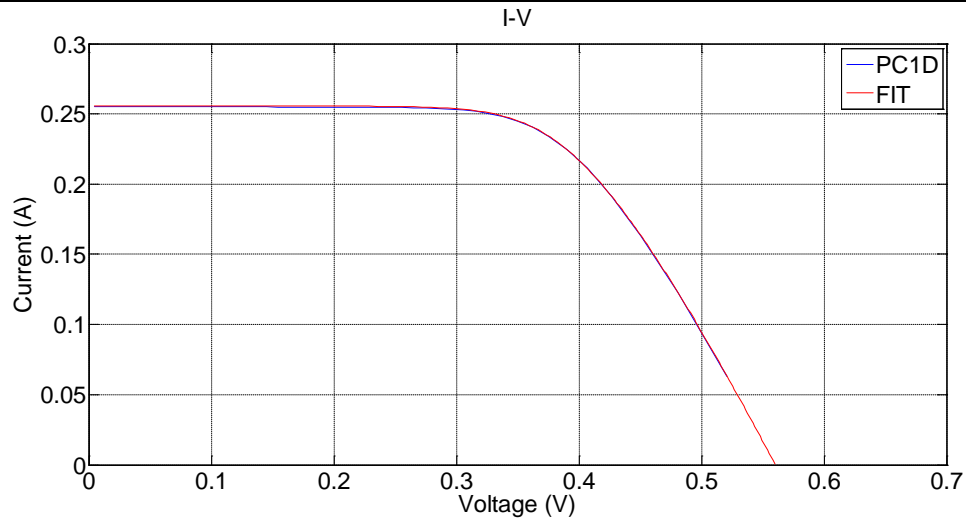


Figure 4.18. Current versus voltage characteristics, simulated version (PC1D) and fitting algorithm (FIT).

#### 4.5.2 Improved $V_{BE}$ Multiplier – Application to Modelling Photovoltaic Cell Behavior

Implementing the artificial solar cell with discrete components it will be clear that there may be some stability issues. For a fix load condition i.e. driving ( $V_{GS}$ ) the gate of the MOSFET on the electronic load with a particular voltage, in this example 0 Volt, the voltage across the output of the circuit was observed to oscillate. The voltage against time response can be seen in Figure (4.19). A large amplitude oscillation is observed at the region of open circuit voltage ( $V_{oc}$ ). Oscillations can occur primarily when operational amplifiers that are not properly compensated are used to drive capacitive loads. [147].

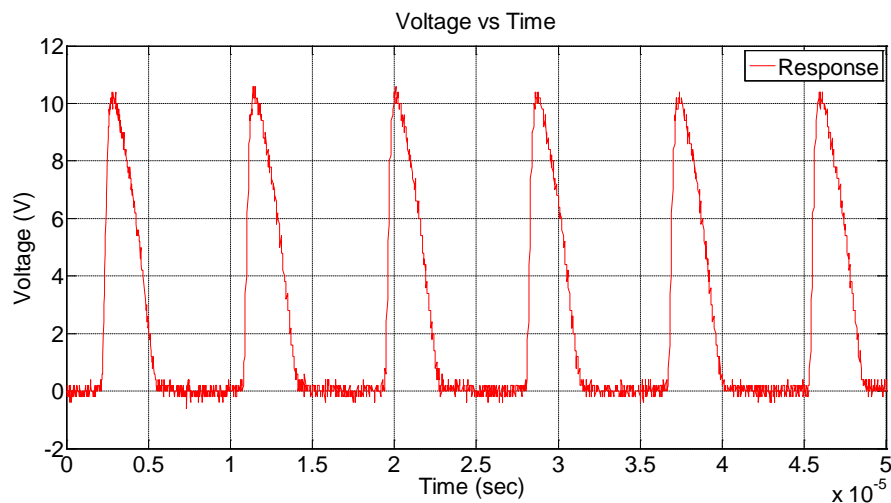


Figure 4.19. Oscillations observed in uncompensated circuit.

The ability of an operational amplifier to drive capacitive loads is affected by the internal architecture of the amplifier (i.e. output impedance  $R_o$ ) and the nature of the load impedance. To avoid sacrificing performance with light loads, most amplifiers are not heavily compensated internally for substantial capacitive loads, so external compensation techniques must be used to optimize those applications in which a large capacitive load at the output of the operational amplifier must be handled [148].

A commonly used compensation technique is the *in-loop* compensation. An isolation series resistor ( $R_{ISO}$ ) should be connected in series between the operational amplifier output and the capacitive load, to provide isolation and to avoid oscillations. A small-value capacitor ( $C_F$ ) is inserted in the feedback loop, between the operational amplifier output and the inverting input, providing a high frequency bypass around  $C_L$ , as shown in the Figure 4.20 [147, 148]. Together, these components allow capacitance loading while keeping the loop stable [147, 149].

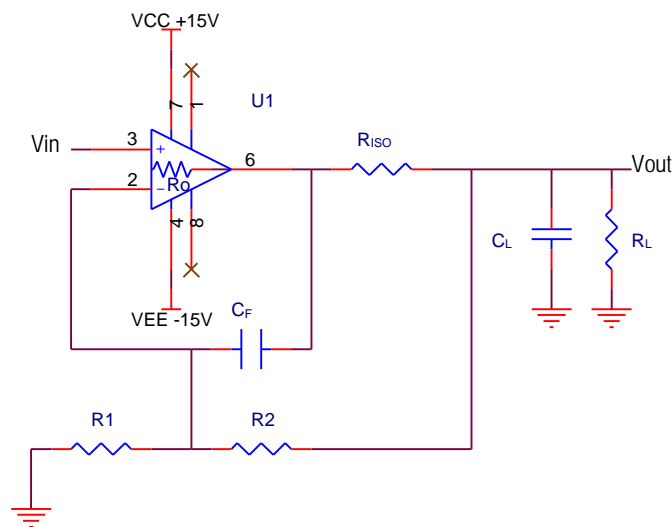


Figure 4.20. *In-loop compensation circuit.*

The basic, hybrid-pi model for the bipolar junction is shown in the figure 4.21. The three transistor terminals are emitter ( $E$ ), base ( $B$ ) and collector ( $C$ ). The base-emitter connection is through an input resistor  $r_\pi$ , and the base current causes a small-signal voltage drop across it,  $v_\pi$ . Voltage  $v_\pi$  induces a small-signal collector current via the voltage-controlled current source with current  $g_m v_\pi$ ,  $g_m$  is the transistor *transconductance*. The output resistance is denoted by  $r_o$ . [144].



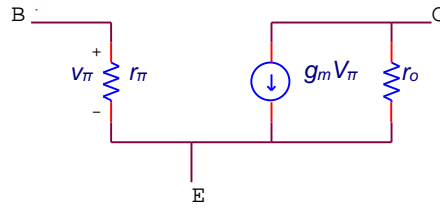


Figure 4.21. Simplified, low-frequency hybrid-pi bjt model. Adapted from [144].

As frequencies are increased transistor parasitic capacitances are modeled in Figure 4.22. Three parasitic elements are commonly added to the hybrid-pi model to make frequency predictions. One is the base-emitter capacitance  $C_{\pi}$ , which includes the base-emitter diffusion capacitance and the base-emitter junction capacitance. A second parasitic capacitance  $C_{\mu}$  connects the base to the collector; this capacitance represents the collector-base junction capacitance. The resistance  $r_x$  models the resistance of the silicon material of the base region between the base terminal B and a fictitious internal base terminal B'. The latter node represents the base side of the emitter-base junction. [144]

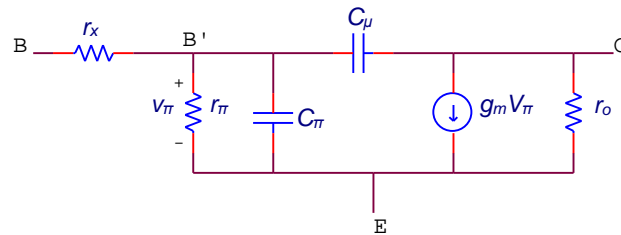


Figure 4.22. Bipolar hybrid-pi model with parasitic capacitances to model frequency dependence. Adapted from [144].

The ability of the operational amplifier is clear that is affected by the nature of the transistor, so compensation correction is required. Applying the *in-loop compensation* technique the proposed electronic circuit becomes as shown in Figure 4.23. The I-V characteristic curve is illustrated in Figure 4.24.

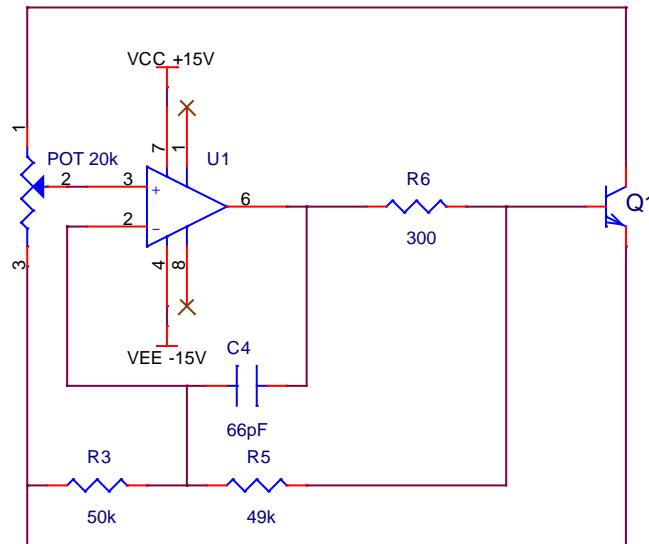


Figure 4.23. Applying the *in-loop compensation* technique to the proposed electronic circuit.

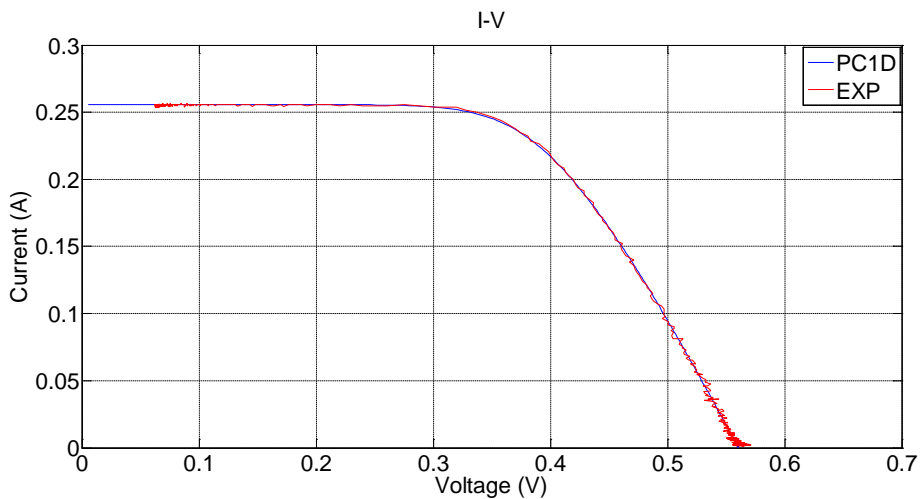


Figure 4.24. I-V characteristic curves observed in compensated circuit.

A substantial improvement can be observed to the instability issue arisen in the initial version of the electronic circuit proposed. The amplitude of the oscillation has decreased referring back to Figure 4.19. However, a small ripple is still present, particularly close to the open circuit voltage.

In order to manage this, a biasing arrangement in the transistor with two resistors is used, similar to the “*basic  $V_{BE}$  multiplier*”. The electronic circuit is illustrated in figure 4.25, obtaining the new “*improved  $V_{BE}$  multiplier*” topology. The I-V characteristic curves are demonstrated in Figure 4.26, along with the small error between the two curves.

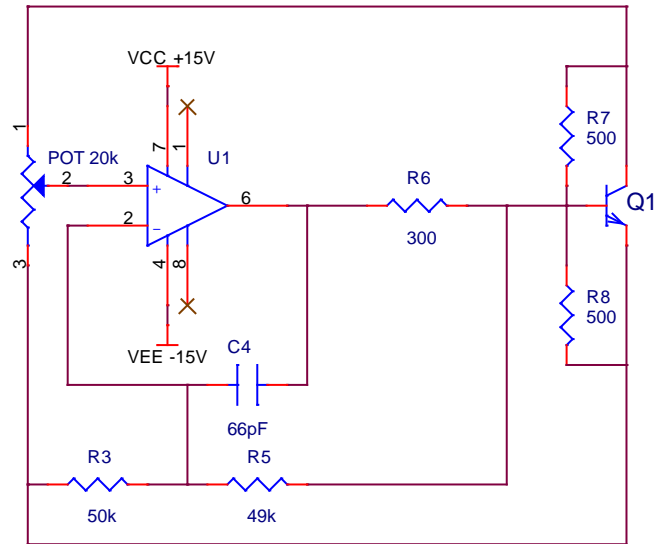


Figure 4.25. Circuit with non-inverting operational amplifier, resistive divider, in loop compensation and transistor biased. *Improved  $V_{BE}$  multiplier* topology.

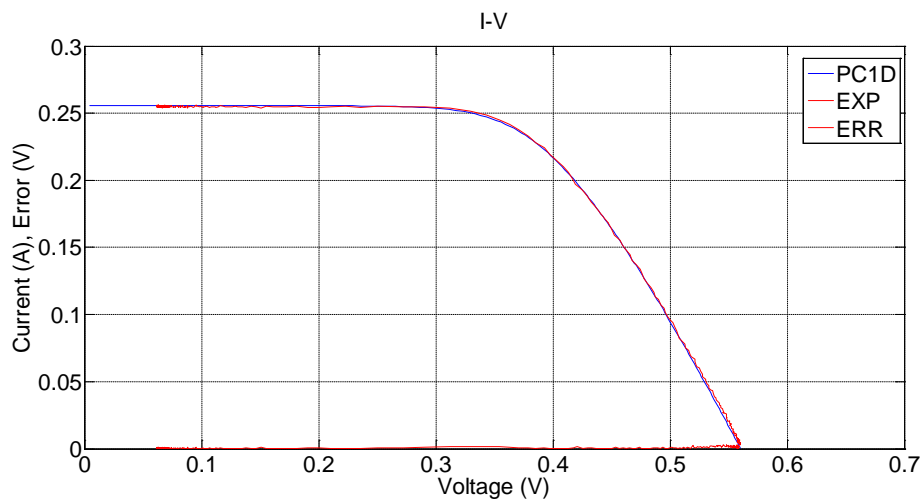


Figure 4.26. I-V characteristic curve related to *Improved  $V_{BE}$  multiplier* topology.

It is obvious that in the particular design, the *in-loop compensation* technique along with the biasing arrangement of the transistor attributes produces the expected I-V curve. Application to modeling photovoltaic cell operation and characteristics will be studied in the next sections using the *improved  $V_{BE}$  multiplier* circuit.

#### 4.5.3 Parameter Extraction for the Transistor

A similar methodology to the “*Basic  $V_{BE}$  multiplier*” (section 4.3.2) was followed for extracting the 3 relevant parameters for the transistor model the saturation current  $I_{s2}$ , ideality factor  $n_2$  and temperature  $T_2$  [145].

The artificial solar cell was adjusted to operate in similar manner to the proposed PC1D I-V characteristic curve illustrated in Figure 4.26. The voltage across the base emitter ( $V_{BE}$ ) as well as current flowing through the transistor ( $I_T$ ) was measured.  $I_T$  is plotted on a logarithmic scale against  $V_{BE}$  in figure 4.27, an exponential fit is also shown.

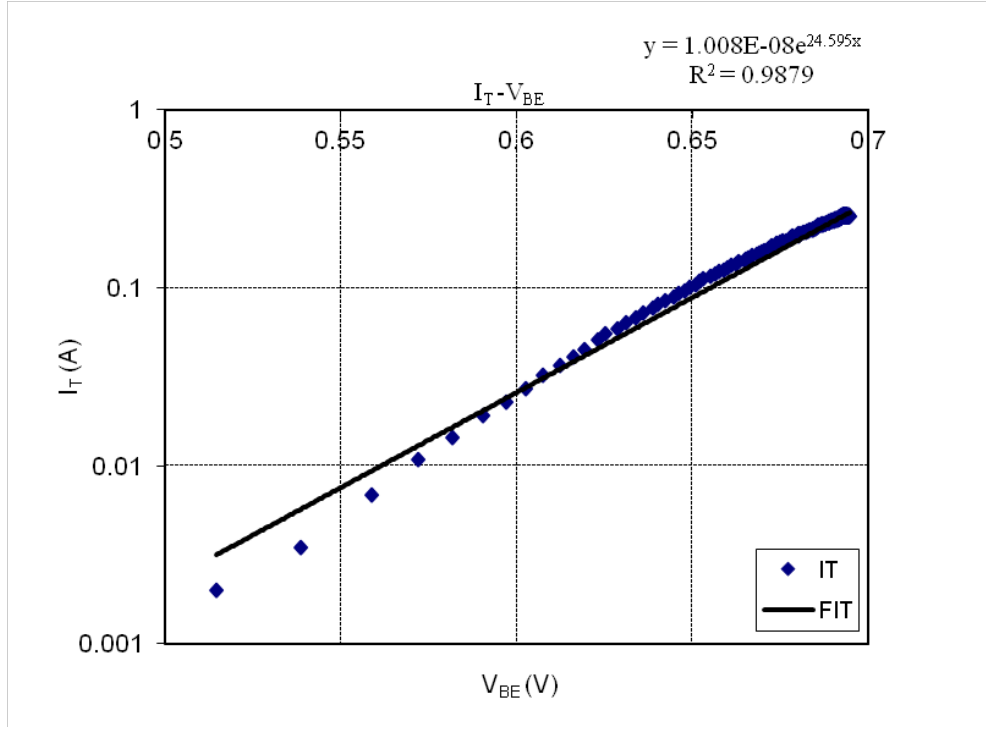


Figure 4.27. Plot of current flowing through the transistor in logarithmic scale against base emitter voltage.

Fit line equation and  $R$  squared values are:

$$y = 1.008E-08e^{24.595x}, R^2 = 0.9879 \quad (4.33)$$

Comparing the fit line equation (4.33) with equation (4.4), saturation current  $I_{s2}$  and thermal voltage  $V_{T2}$  can be extracted:

$$I_{s2} = 1.008e - 08 (A) \text{ and } \frac{1}{V_{T2}} = 24.595 \Rightarrow V_{T2} = \frac{1}{24.595} (V) \quad (4.34)$$

Knowing that the thermal voltage is given by the equation (2.22), replacing electronic charge and Boltzmann constants it is:

$$V_{T2} = \frac{1}{24.595} = \frac{n_2 k T_2}{q} \Rightarrow n_2 T_2 = \frac{q}{24.595 k} = 471.82 \text{ Kelvin} \quad (4.35)$$

Chapter 4. Modeling PV cell operation and Behaviour Using and Improved  $V_{BE}$  Multiplier  
 Summarizing, saturation current as well as the product of ideality factor time's temperature have been extracted in this section in terms of the transistor model. Parameters extracted for the simulation PC1D program in section 4.4.1 as well as parameters extracted for the artificial solar cell can be utilized to evaluate the gain ( $G$ ) described in equation (4.10).

#### 4.5.4 Series Resistance Compensation

As described in the case of the *Basic  $V_{BE}$  multiplier* section a simple estimation of series resistance is provided by the formulas (4.26 - 4.27). Series resistance values depend on parameters such as temperature ( $T$ ) which is included in the thermal voltage value, as well as open circuit voltage ( $V_{oc}$ ), voltage at maximum power point ( $V_{mpp}$ ) and current at maximum power point ( $I_{mpp}$ ) which are greatly influenced by insolation and temperature conditions. These factors have to be considered in the artificial solar cell.

Series resistance selected in PC1D software program was 0.5 Ohm. Placing this value of resistance in the artificial solar cell would result in a deviation of 0.0132 ( $\Omega^{-1}$ ) as illustrated in Figure 4.28.

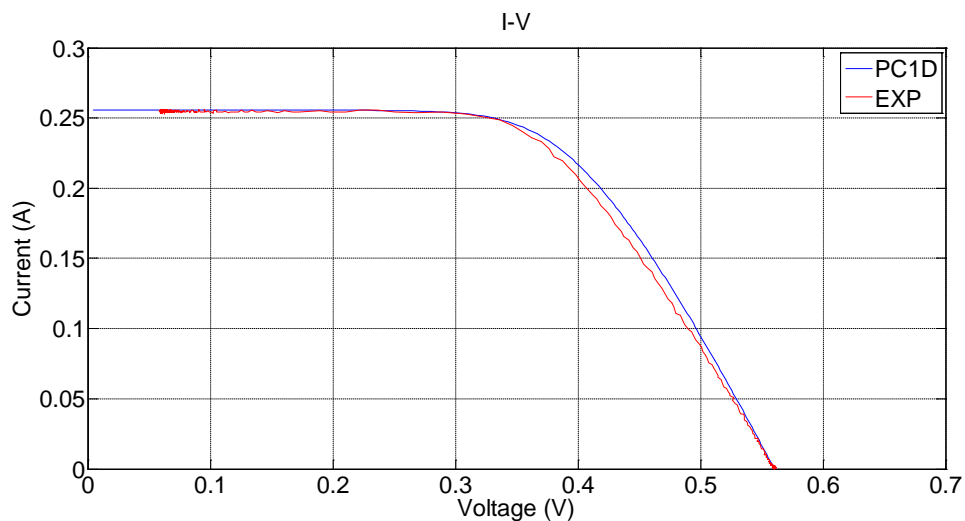


Figure 4.28. Series resistance uncompensated I-V characteristic curves.

Applying a suitable correction to series resistance value provides a better fit between I-V characteristic curves as shown in figure 4.26. Evaluating formulas (4.26 – 4.27) with the data provided in Table 4.12, series resistance value was calculated to be  $R_s = 0.41$  Ohm. The value experimentally placed in the artificial

Chapter 4. Modeling PV cell Operation, Behavior Using and Improved  $V_{BE}$  Multiplier solar cell such as the I-V characteristic curve to be in accordance was  $R_s = 0.42$  Ohm. A small *difference* of 2.43% is observed from the estimated value.

Table 4.12. Data required for theoretical calculation of series resistance value.

Also, experimental resistor utilised along with percentage difference.

Data Parameters	
Temperature $T$	313 Kelvin
Maximum Voltage $V_{mpp}$	0.3794 V
Maximum Current $I_{mpp}$	0.2329 A
Open circuit voltage $V_{oc}$	0.5603 V
Series Resistance Theoretically calculated and Experimentally utilised	
Theoretical series resistance $R_s$	0.41 Ohm
Experimental series resistance $R_s$	0.42 Ohm
<i>Difference</i>	2.43 %

It is clear that series resistance compensation is required in the artificial solar cell in order to attain match in the I-V characteristic curves.

#### 4.5.5 Temperature Compensation

In a practical application of this circuit it is clearly desirable to have a digital control of the attenuator factor so that the photovoltaic characteristics and its operating conditions may be set and altered as experiments demand. To this end, the analog potentiometer should be replaced with a digital potentiometer. This electronic configuration will be described in detail in Chapter 5, along with the microcontroller utilised for implementation of a programmable solar emulator.

In this section temperature compensation is considered and the methodology is analysed. To facilitate heat transfer from the transistor case to ambient a popular approach is to bolt the transistor to an extended metal surface. Such a metal surface then functions as a heat sink [144]. A temperature sensor is placed in the heat sink to provide temperature measurements.

Four I-V characteristic curves are shown in figure 4.29. The first experiment (EXP1) called “*cold start*” (red) was the characteristic taken immediately after the

Chapter 4. Modeling PV cell operation and Behaviour Using and Improved  $V_{BE}$  Multiplier system was switched on. The second experiment (EXP2) was carried out after 15 minutes of operation (green), this characteristic is observed a shift to higher voltage due to temperature increase of  $1.88^{\circ}\text{C}$ . The third experiment (EXP3) (brown) has compensation applied, bringing the curve back to the initial state. The error versus voltage for the three experiments is also plotted in Figure 4.30.

Compensation has performed according to formula (4.10) derived for the gain  $G$  value. The data parameters necessary for evaluation ( $I_{s1}$ ,  $n_1T_1$ ,  $I_{s2}$ ,  $n_2T_2$ ) have been computed, while digital temperature sensor measures temperature  $T_2$  and the data are sent to the microcontroller. Gain  $G$  value is updated and the microcontroller adjusts the digital potentiometer accordingly, succeeding theoretical and experimental I-V curves to match closely. In that means a good system response is obtained.

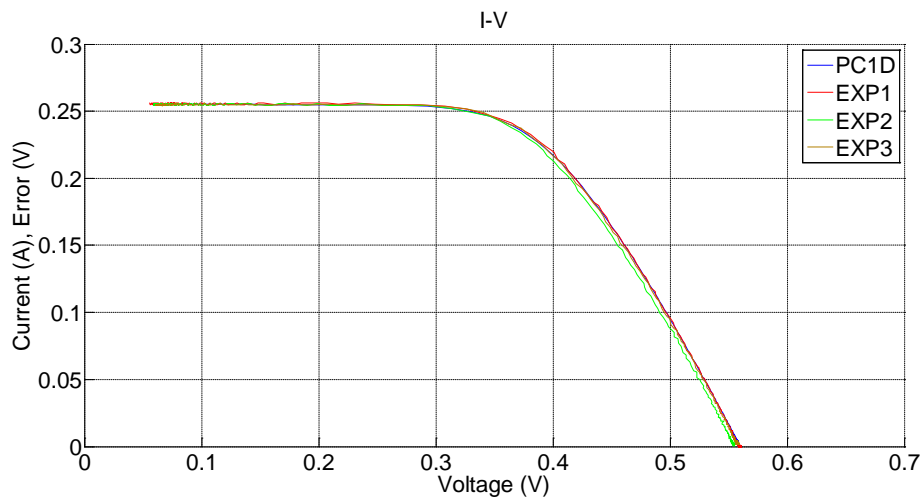


Figure 4.29. I-V characteristic curves for PC1D (blue line), EXP1 “cold start” (red), EXP2 (green) after 15 minutes of continuous operation, EXP3 (brown) after compensation technique is applied.

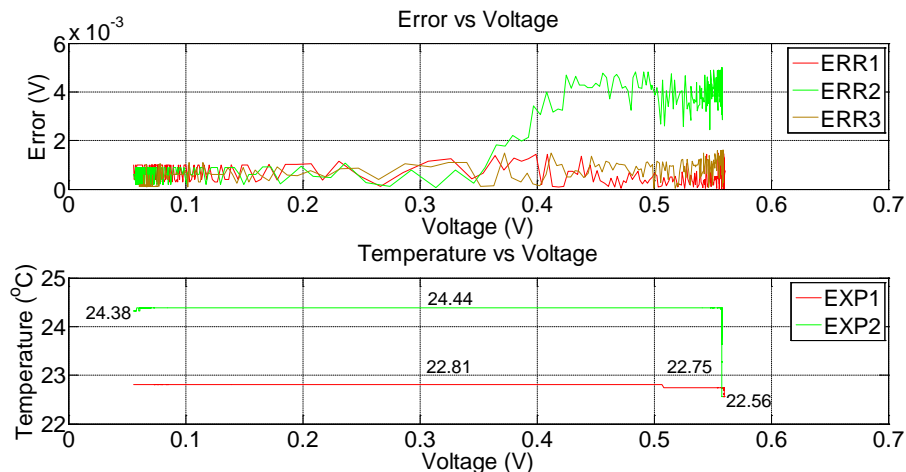


Figure 4.30. Error and temperature variation versus voltage for cases considered.

Describing figure 4.30, error and temperature variation versus voltage graphs, it seen that in the first case scenario (EXP1) the worse deviation between the theoretical and experimental I-V curve (ERR1) is 1.5 mV at the open circuit voltage, the difference drops to 1mV as experiment proceeds. Initially, ambient temperature was measured to be 22.56°C and increased to 22.75°C this a change of 0.19°C while measurements at the region close to open circuit voltage were taken. The main part of the I-V characteristic curve was extracted with an observed variation 0.06°C.

In the second case scenario (EXP2), the worse deviation (ERR2) shows an increase of 3.5mV and a deviation of 5 mV in total is observed close to the open circuit voltage, this also drops to 1mV as experiment proceeds. The temperature was initially measured 22.56°C and after 15 minutes of operation increased by 1.88°C to 24.44°C. The I-V characteristic curve was obtained at the same temperature (24.44°C) only towards to the end of the experiment there is a negligible temperature drop 0.06 °C.

In the third case (EXP3) with compensation applied, the worse deviation (ERR3) is 0.1mV more than the first case (red line) in total 1.6 mV, dropping to 1mV. The small divergence of 0.1mV when compensation is applied is due to the following reasons. Evaluation of gain  $G$  value has performed with parameters ( $I_{s1}$ ,  $n_1T_1$ ,  $I_{s2}$ ,  $n_2T_2$ ) that were extracted with a certain error as it has been analytically described. The temperature monitored is not at the junction of the transistor but at the heat sink and most changes in temperature are too small to be determined in these experiments. Summing all these factors, in the rather small temperature variations can be adequately compensated to improve the system response.

The compensation used is according to the formula (4.10).

$$G = \frac{n_1T_1n_2T_2 \frac{k}{q} \ln\left(\frac{I_{s1}}{I_{s2}}\right) + n_2T_2V_J}{n_1T_1V_J} = \frac{\left(n_1T_1n_2 \frac{k}{q} \ln\left(\frac{I_{s1}}{I_{s2}}\right) + n_2V_J\right)T_2}{n_1T_1V_J} = G_{comp}T_2 = 1.237 \quad (4.36)$$

$$\text{Where, } G_{comp} = \frac{\left(n_1T_1n_2 \frac{k}{q} \ln\left(\frac{I_{s1}}{I_{s2}}\right) + n_2V_J\right)}{n_1T_1V_J} \quad (4.37)$$



Chapter 4. Modeling PV cell operation and Behaviour Using and Improved  $V_{BE}$  Multiplier  $G$  (1.237) is used to set the digital potentiometer.  $G_{comp}$  is multiplied with the DS18B20 digital thermometer [150] sensor ( $T_2$ ) and is used for compensation purposes. Any change in  $T_2$  is considered and the  $G$  is updated. As temperature  $T_2$  increases to 24.44°C,  $G$  is such that is increased to 1.246 in the case examined.  $G$  is updated, compared to the original default value (1.237) and decreased accordingly (by 0.009) such as to always be constant at 1.237. The microcontroller adjusts the digital potentiometer to ensure a good system response.

Substituting the calculated values ( $I_{s1}$ ,  $n_1T_1$ ,  $I_{s2}$ ,  $n_2$ ,  $V_J$ )  $G_{comp}$  is 0.00418 K<sup>-1</sup>. If the  $G_{comp}$  value is set to 0.00422 K<sup>-1</sup> a perfect match to the ERR1 case is observed. This small deviation (of 0.94%) in  $G_{comp}$  value accounts for the error in extracted parameters ( $I_{s1}$ ,  $n_1T_1$ ,  $I_{s2}$ ,  $n_2$ ,  $V_J$ ) and provides an even better system response.

#### 4.5.6 Distribution of Data Points

The maximum available data points produced by PC1D are 200, while the experimental data points recorded are 1442 according to the electronic load configuration adopted. The MOSFET is driven ( $V_{GS}$ ) with a triangular waveform of amplitude 2.9V to 4V with, voltage step increment value 760μV and time duration 87 seconds. The theoretical principle has been introduced in section 4.2.1 and further described at implementation level in section 5.4.2. The distribution of data points can be seen in Figures 4.31 and 4.32.

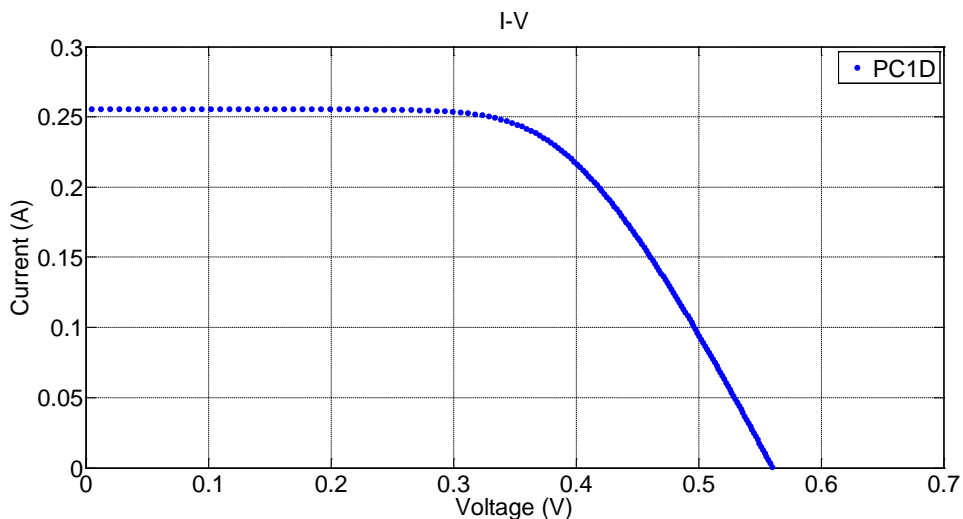


Figure 4.31. Distribution of simulation data points.

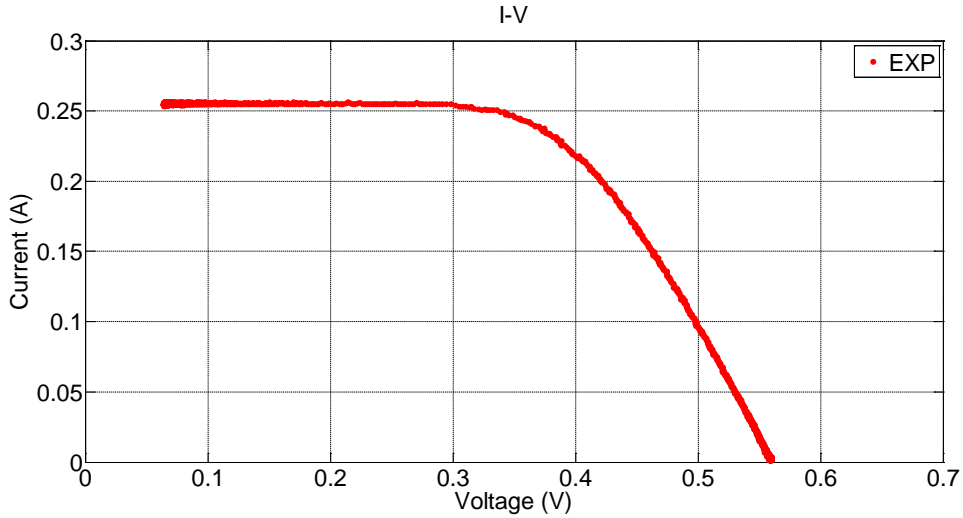


Figure 4.32. Distribution of experimental data points.

Higher resolution of data points is required on the simulated curve, particularly to increase the number of data points in the flat region, ( $V_{mpp}$  until  $I_{sc}$ ). In order to expand data, the fundamental I-V equation (2.20) is considered. The five fitting parameters describing the operation of the particular photovoltaic at the given conditions have been extracted and stated in Table 4.11. Thus, the function describing photovoltaic cell behavior is known and it can be evaluated for smaller step voltage changes in order to expand the theoretical data according to the I-V characteristic equation. In equation (2.20) the term  $V+IR_s$  is equated to a variable  $H$ . Thus, equation (2.20) becomes:

$$I = I_{ph} - I_o \left( \exp\left(\frac{qH}{nkT}\right) - 1 \right) - \frac{H}{R_{sh}} \quad (4.38)$$

where,

$$H = V + IR_s \quad (4.39)$$

The minimum and maximum values of  $H$  are when the cell is operated at short circuit and open circuit conditions respectively. They are defined by equations (4.40) and (4.41).

$$H_{\min} = V_{sc} + I_{sc}R_s \quad (4.40)$$

$$H_{\max} = V_{oc} + I_{oc}R_s \quad (4.41)$$

In order to increase the data points a small step increase of  $H$  from  $H_{min}$  to  $H_{max}$  was adopted, 0.05 mV (50  $\mu$ V) step increment, to ensure data are placed as close as possible to experimental data points to decrease the root mean square error ( $RMSE$ ) value. The voltage and current at any point is given by equations (4.42) and (4.43) accordingly.

$$V = H - IR_s = H - \left( \left( x(1) - x(2) \left( \exp \left( \frac{H}{\frac{x(4)kT}{q}} \right) - 1 \right) - \frac{H}{x(5)} \right) x(3) \right) \quad (4.42)$$

$$I = \frac{H - V}{x(3)} \quad (4.43)$$

where, solution  $x$  values are stated in Table 4.11.

Performing this procedure 8554 data points are obtained along the simulated I-V curve. The expanded distribution points can be seen in Figure 4.32.

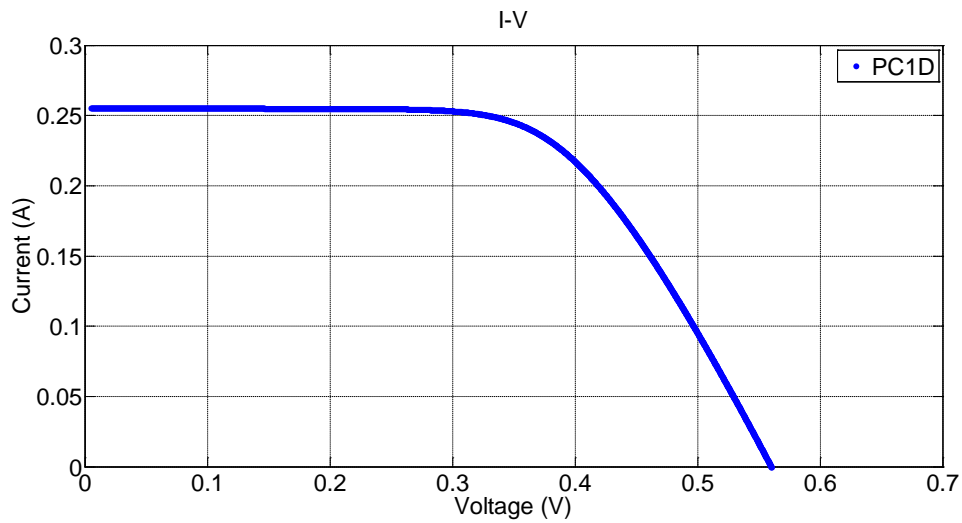


Figure 4.33. Distribution of expanded simulation data.

At this stage simulation data points are 8554, almost 6 times more than experimental data points. In order to compare them in the same meaningful way the data points have to be identical in size (both of them 1442).

Out of 8554 simulated data points only 1442 have to be selected, the one's situated as close as possible to the experimental data points, in order to have the smaller error.  $RMSE$  is taken into account considering current and voltage values at each point among the 1442 data.

Analytically, every theoretical point is compared to all available experimental points. The one that gives minimum error are stored to a new matrix, while the remaining points are discarded. In this manner, out of 8554 theoretical data points a new table is created that contains only 1442 data points that lie close to experimental values with minimum  $RMSE$ . In figure 4.34 is presented the new theoretical I-V curve.

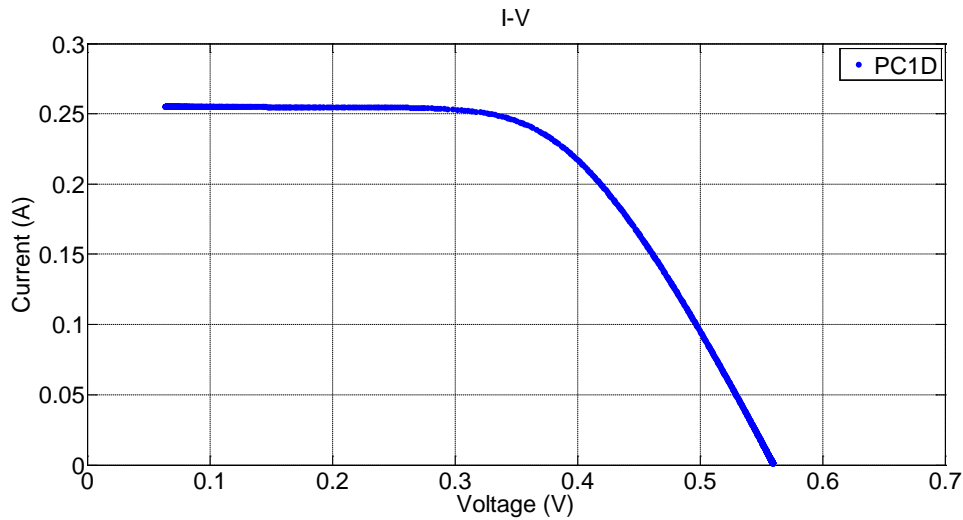


Figure 4.34. Final theoretical distribution data points.

Finally, in order to qualify the fit of experimentally measured data points against theoretically (simulated in PC1D) on the I-V characteristic curves a statistical indicator  $RMSE$  is calculated according to equation (4.24). Comparison is performed of current and voltage at the  $i^{th}$  point among  $N$  (1442) data points computing a normalized error value for the whole I-V curves. This value of  $RMSE$  is stated in every experiment conducted at different operating conditions of insolation and temperature.

#### 4.5.7 Discussion

The new “*improved  $V_{BE}$  multiplier*” circuit and its application to modeling photovoltaic cell behavior are discussed in this section. For the particular experiment described, values extracted for the simulation as well as from the artificial solar cell transistor model are presented in Tables 4.13 and 4.14.

Table 4.13. Parameters for simulated version of solar cell.

Simulation Parameters	
Ideality factor $n_1$	1
Saturation Current $I_{s1}$	$2.4397 \cdot 10^{-10}$ A
Temperature $T$	313 Kelvin
Open Circuit Voltage $V_J$	0.5603 V

Table 4.14. Parameters for artificial solar cell.

Artificial Solar Cell	
Ideality factor $\cdot$ Temperature $n_2T_2$	471.82 Kelvin
Saturation Current $I_{s2}$	$1.008 \cdot 10^{-8}$ A

Substituting values to equation (4.10) the gain  $G$  value is computed to be 1.237 (equation 4.36).

The experimental gain  $G$  value has been measured on the artificial solar cell:

$$G = \frac{V_{BE}}{V_J} = \frac{0.6943}{0.5603} = 1.239 \quad (4.44)$$

There is good numerical agreement with only a small divergence between the computed and experimentally measured gain, confirming the validity of modeling procedure.

Applicability has been tested to different temperature conditions varying the temperature from +60°C (333 kelvin) to -20°C (253 kelvin) in steps of 20°C. The gain ( $G$ ) of the artificial solar cell is adjusted to match the output voltage suggested by PC1D. Parameters extracted from the simulation program ( $n_1$ ,  $T_1$ ,  $I_{s1}$ ,  $V_J$ ) along with the normalized residual “*Residual*” value, as well as parameters extracted for the artificial solar cell ( $n_2T_2$ ,  $I_{s2}$ ) along with *R squared* “ $R^2$ ” value are summarized in Tables 4.15 and 4.16. Series resistance compensation applied (Table 4.17), along with percentage *difference* between experimental and theoretical calculated values.

Finally, graphical representation of all measurements obtained are illustrated in Figures 4.35 and 4.36. Series resistance, shunt resistance, saturation current, the product of ideality factor and temperature ( $nT$ ), photocurrent and gain values are

Chapter 4. Modeling PV cell Operation, Behavior Using and Improved  $V_{BE}$  Multiplier plotted against temperature conditions examined. The I-V characteristics for all cases are illustrated in Figure 4.37.

Table 4.15. Summary of values for experiment conducted at 1000 W/m<sup>2</sup> irradiance and different temperatures.

Experimental Setup									
Temperature						$G$			
Insol.	$T$	$R_s$	$R_{sh}$	$I_o$	$nT$	$R^2$	$I_{ph}$	(Gain)	
W/m <sup>2</sup>	(Kelv), (°C)	(Ohm)	(kOhm)	(A)	(kelvin)		(mA)	Exper.	RMSE
1000	253 (-20)	0.29	20	1.29E-08	486.1	0.973	254.08	1.020	$2.55 \cdot 10^{-3}$
	273 (0)	0.37	20	1.06E-08	471.7	0.987	254.22	1.070	$1.16 \cdot 10^{-3}$
	293 (20)	0.41	20	1.00E-08	470.3	0.99	254.41	1.145	$8.14 \cdot 10^{-4}$
	313 (40)	0.42	20	1.00E-08	471.8	0.988	254.60	1.239	$1.09 \cdot 10^{-3}$
	333 (60)	0.44	20	9.67E-09	460.6	0.986	254.82	1.316	$1.06 \cdot 10^{-3}$

Table 4.16. Summary of theoretical values for the experiment conducted at 1000 W/m<sup>2</sup> irradiance and different temperatures.

Theoretical Setup									
Temperature						$G$			
Insol.	$T$	$R_s$	$R_{sh}$	$I_o$	$nT$	$Residual$	$I_{ph}$	(Gain)	$V_J$
W/m <sup>2</sup>	(Kelv), (°C)	(Ohm)	(kOhm)	(A)	(kelvin)		(mA)	Theor.	(V)
1000	253 (-20)	0.5	20	4.47E-15	253	$7.97 \cdot 10^{-5}$	254.49	1.034	0.691
	273 (0)	0.5	20	2.79E-13	273	$5.57 \cdot 10^{-6}$	254.68	1.069	0.648
	293 (20)	0.5	20	1.02E-11	293	$7.69 \cdot 10^{-5}$	254.87	1.141	0.605
	313 (40)	0.5	20	2.44E-10	313	$4.33 \cdot 10^{-5}$	255.02	1.237	0.560
	333 (60)	0.5	20	4.08E-09	333	$9.08 \cdot 10^{-5}$	255.29	1.314	0.516

Table 4.17. Series resistance experimentally placed and theoretically calculated, along with relevant data.

Series Resistance Compensation							
Temperature T	Exper.	Theor.	Difference	$V_{i2}$	$V_{mpp2}$	$I_{mpp2}$	$V_{oc2}$
(Kelv), (°C)	$R_s$ (Ohm)	$R_s$ (Ohm)	(%)	(V)	(V)	(A)	(V)
253 (-20)	0.29	0.32	9.37	0.0419	0.511	0.236	0.691
273 (0)	0.37	0.34	8.82	0.0406	0.472	0.233	0.648
293 (20)	0.41	0.39	5.12	0.0405	0.422	0.234	0.605
313 (40)	0.42	0.41	2.43	0.0407	0.379	0.233	0.560
333 (60)	0.44	0.45	2.22	0.0397	0.333	0.234	0.516

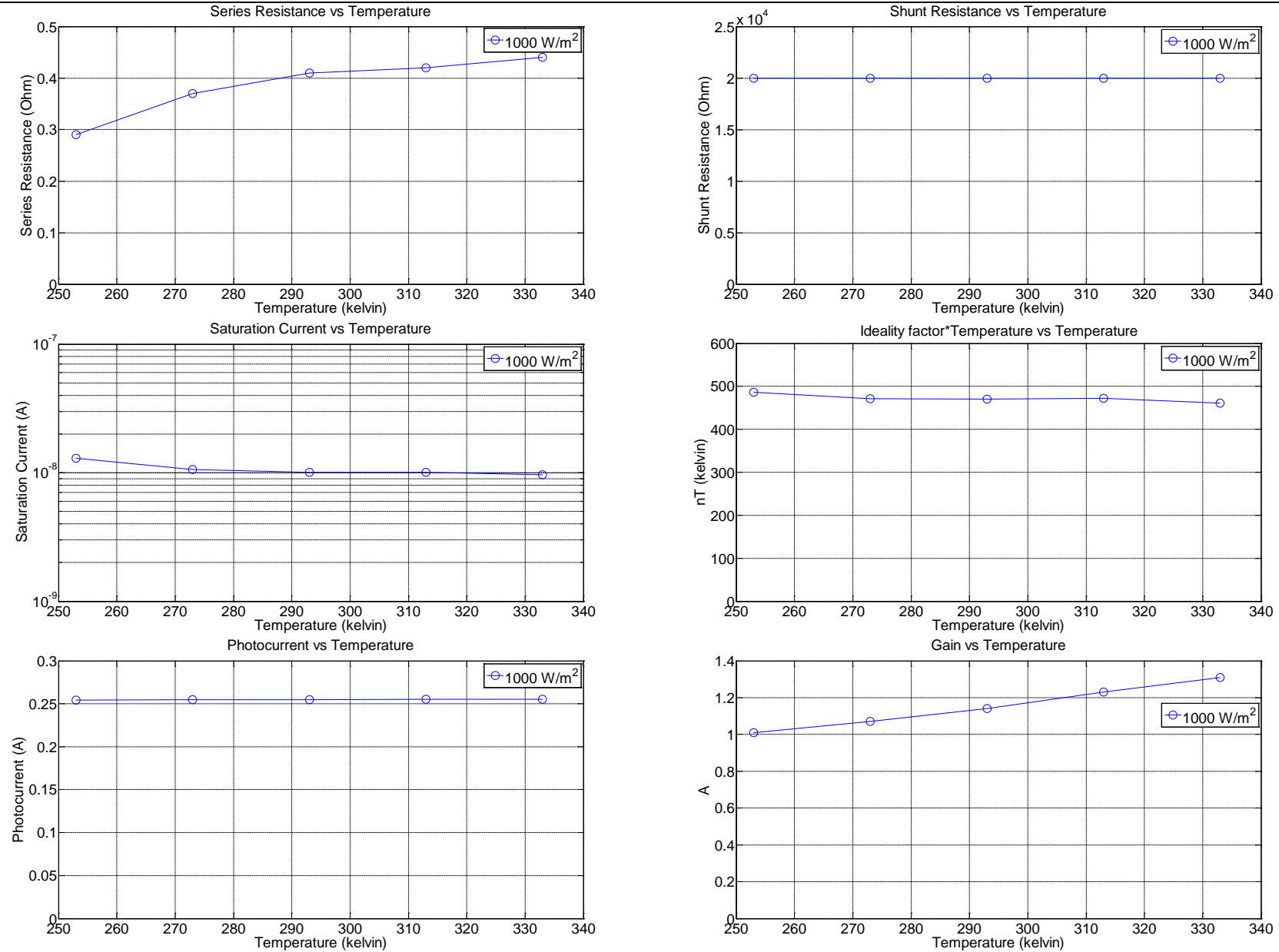


Figure 4.35. Experimental values versus Temperature for irradiance  $1000 \text{ W/m}^2$ .

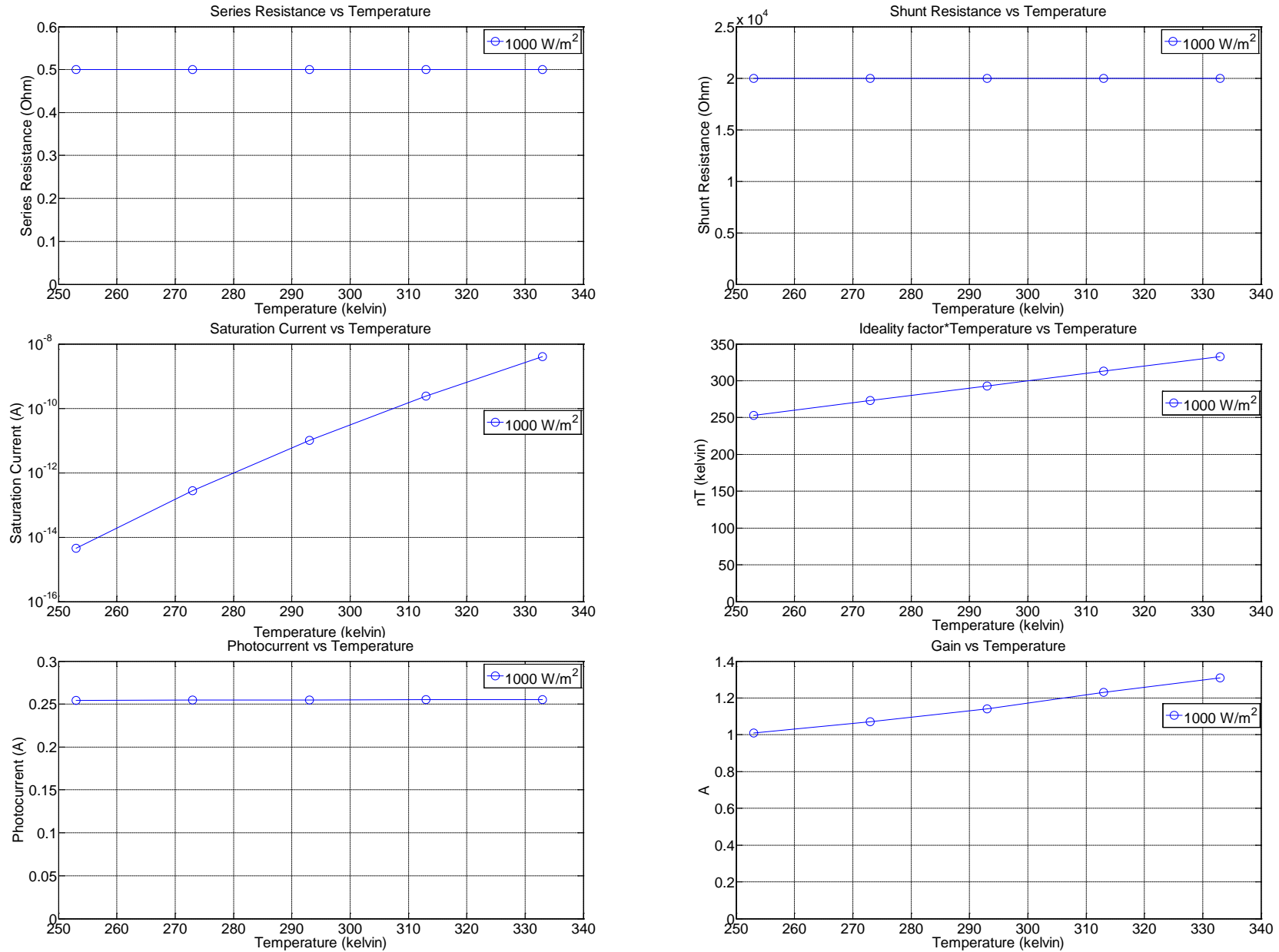


Figure 4.36. Theoretical values versus Temperature for irradiance 1000 W/m².



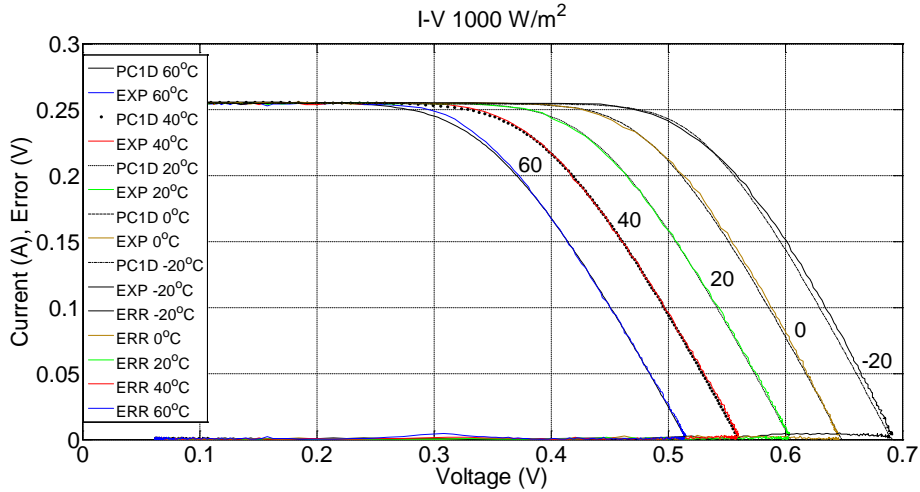


Figure 4.37. I-V characteristic for all cases considered.

The statistical indicator  $R$  squared value is for all transistor data parameters extracted ( $n_2T_2$ ,  $I_{s2}$ ) are close to the ideal of unity (approximately 0.98), suggesting accurate extraction and fitting of the data. Similarly, the five fitting parameters extracted from the PC1D software have small *residuals*, typically of the order of  $10^{-5}$  to  $10^{-6}$ , suggesting small error in the data fitting problem in each case.

Another statistical indicator, RMS error describes the discrepancy between the I-V characteristic plots. The small ( $10^{-3}$ ) along with the error versus voltage for each case indicate that the artificial solar cell provides a good mimic of the simulated cell.

In all experiments there is numerical agreement in all gain values ( $G$ ). A temperature increase is observed while increasing  $G$ . This can be explained considering equation (4.5), as  $G$  increases the open circuit voltage ( $V_J$ ) will decrease for the same base emitter voltage ( $V_{BE}$ ). In this way, a decrease of open circuit voltage as illustrated in Figure 4.37 corresponds to higher temperature conditions.

Numerical agreement is observed to values of shunt resistance as well as photocurrent. Shunt resistance is set to 20kOhm in all experiments. Photocurrent is almost constant (255 mA) in all cases examined with small negligible variation in the  $\mu$ A range. As temperature increases the photocurrent also increases.

Series resistance in the simulation program was kept constant (0.5 Ohm) in all experiments however, series resistance compensation was applied to the artificial solar cell. An increase in series resistance is observed as temperature increases.

Saturation current values extracted experimentally are in the order of magnitude  $10^{-8}$  (A). Values extracted from the simulation program are in the range of  $10^{-9}$  to  $10^{-15}$  (A).

The product of ideality factor and temperature ( $nT$ ) extracted from the transistor model are in the range of 486 to 460 (kelvin) whereas parameters extracted from the simulation model are in the range of 253 to 333 (kelvin). In the theoretical approach values of ( $nT$ ) depends only on temperature conditions, since for the ideal case considered ideality factor is theoretically unity ( $n=1$ ). Thus, any increase in temperature will result in a proportional increase to the product of  $nT$ , while it will be unaffected to irradiance changes.

The product of ideality factor and temperature ( $nT$ ) is different in all cases presented, comparing experimental and theoretical approach a difference of 200 (Kelvin) on average is noticed. So, saturation current does change in order to compensate that difference such as artificial solar cell operate in similar manner to the simulated model and the I-V characteristic curves to match. The saturation current of the transistor has a maximum difference seven orders of magnitude, while on average it is four orders of magnitude bigger than the saturation current of the simulated solar cell, in order to anticipate differences in the product of  $nT$ .

Concluding, the “Improved  $V_{BE}$  multiplier” is a new design that can be utilized as a reliable photovoltaic cell emulator to cover a wide range of operational conditions.

## 4.6 Conclusion

With carefully designed controls, both the ‘*basic*’ and the ‘*improved  $V_{BE}$  multiplier*’ topologies have been shown to operate just like solar cell. However, the ‘*improved  $V_{BE}$  multiplier*’ is clearly more flexible and able to operate across a wide range of operational conditions.

Simple electronic circuit topologies proposed herein can be expanded to represent different types of photovoltaic technologies being operated over a wide range of illumination and temperature conditions, allowing the rapid testing and evaluation of inverting and tracking systems. The electronic circuit(s) proposed may also be used in other systems as arbitrary junction diode replicas.

In a practical application of this circuit it is clearly desirable to have a digital control, so that the photovoltaic characteristics and its operating conditions may be set and altered as experiments demand. This scheme will be described in Chapter 5, along with all the necessary electronic components included for implementation of a programmable digitally controlled solar emulator.



## 5 Programmable Solar Cell Emulator

### 5.1 Introduction

Solar simulators are an integral part of any laboratory involved in photovoltaics. Typically these simulators can be based around software control of conventional and relatively expensive power supplies, or based around cells or modules contained within calibrated light sources (conventionally used to test the efficiency of cells under very specific or standardised conditions). Researchers or analysts wishing to assess photovoltaic systems (rather than cells) can use a photovoltaic cell in a solar simulator. Insolation can be varied using filters and temperature can be controlled using a temperature-stage. All in all this becomes a rather complex and expensive experimental apparatus and for many it will be more convenient to test photovoltaic systems and MPPT algorithms outdoors using real sunlight. While this has the benefit of being ‘real’ it has the disadvantage of being inconvenient and impossible to control or standardise. One of the main goals of this work is to explore the feasibility of an electronic ‘solar simulator’ or emulator that utilises relatively simple electronic equivalent circuits and does not require an expensive light-source or temperature stage and yet can mimic a range of cell types for a wide range of insolation and temperature conditions.

In this chapter, the ‘*improved  $V_{BE}$  multiplier*’ topology developed in chapter 4 is used as the ‘simple’ equivalent circuit and detailed descriptions of both the hardware and the software required for the computer-controlled emulator.

### 5.2 Aims – Experimental System

Different arrangements of different systems have implemented by researchers in order to reproduce realistic outdoor conditions indoors with adjustable insolation and temperature conditions. There is an opportunity of a new type of programmable emulation solar system based on a new proposed transistor circuit model analyzed in Chapter 4, along with necessary electronic components.

A major element of this Chapter is to describe design and develop a new simulator prototype that provides irradiance and temperature variability. A relative small to

medium system controlled in a lab environment able to carry out the same tasks. Provide fast and accurate I-V measurements to any given environmental condition.

The system is constructed from simple electronics components rather than a combination and functionality of several different types of costly equipment. Microcontroller is the heart of the system. It receives input signals, processes them and produces output signals. It is responsible for the operation of the whole Emulation Platform.

A schematic overview of the digitally controlled emulation solar system was illustrated in figure 4.1. Each component of the prototype platform is analysed thoroughly in this Chapter and is presented in figure 5.1.

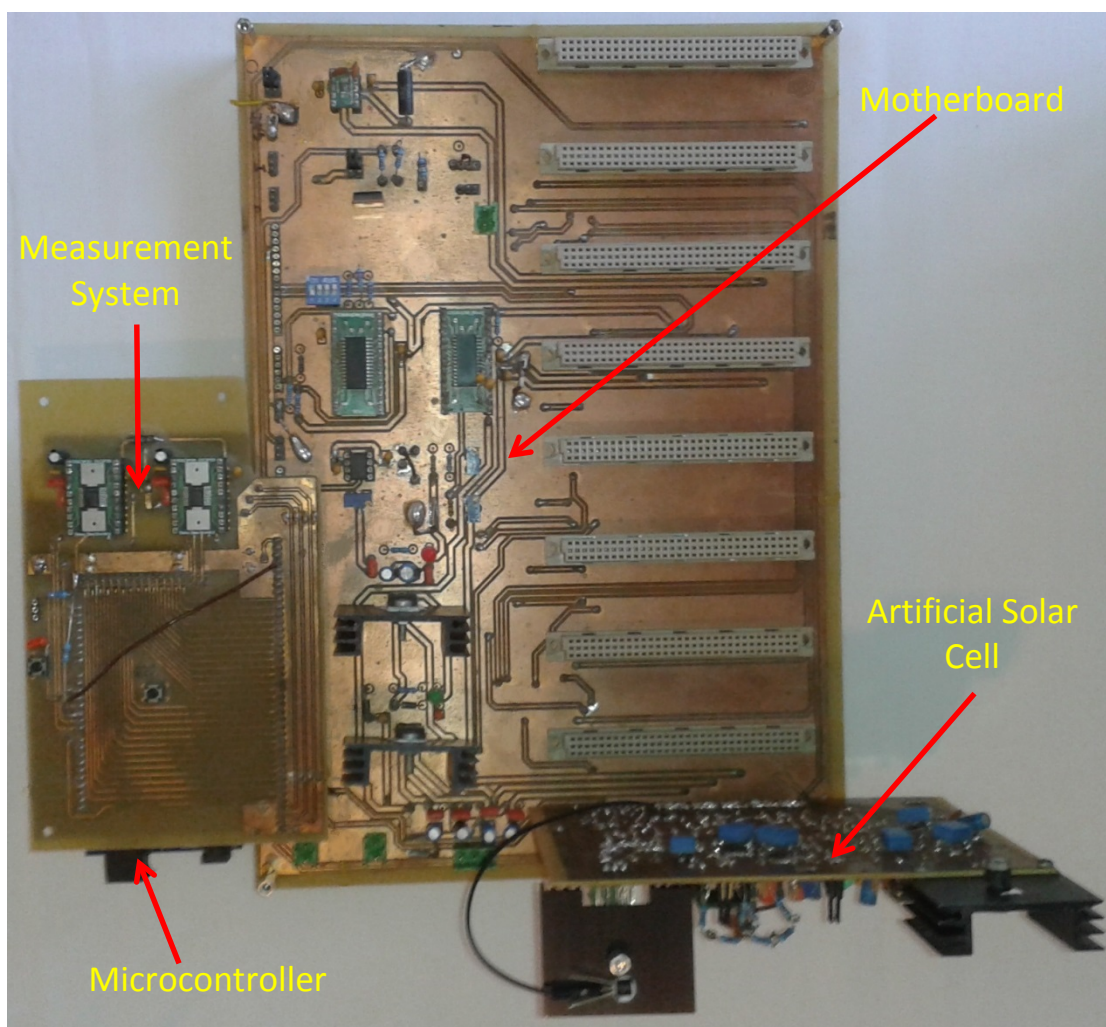


Figure 5.1. Prototype Digitally Controlled Emulation Solar System (“DiceSol”).

### 5.3 Design and construction of artificial solar cell board

Based on the design described in Chapter 4, necessary electronic components are added to digitize operation. A schematic overview and implementation of the artificial solar cell board are illustrated in figure 5.2 and 5.3 respectively.

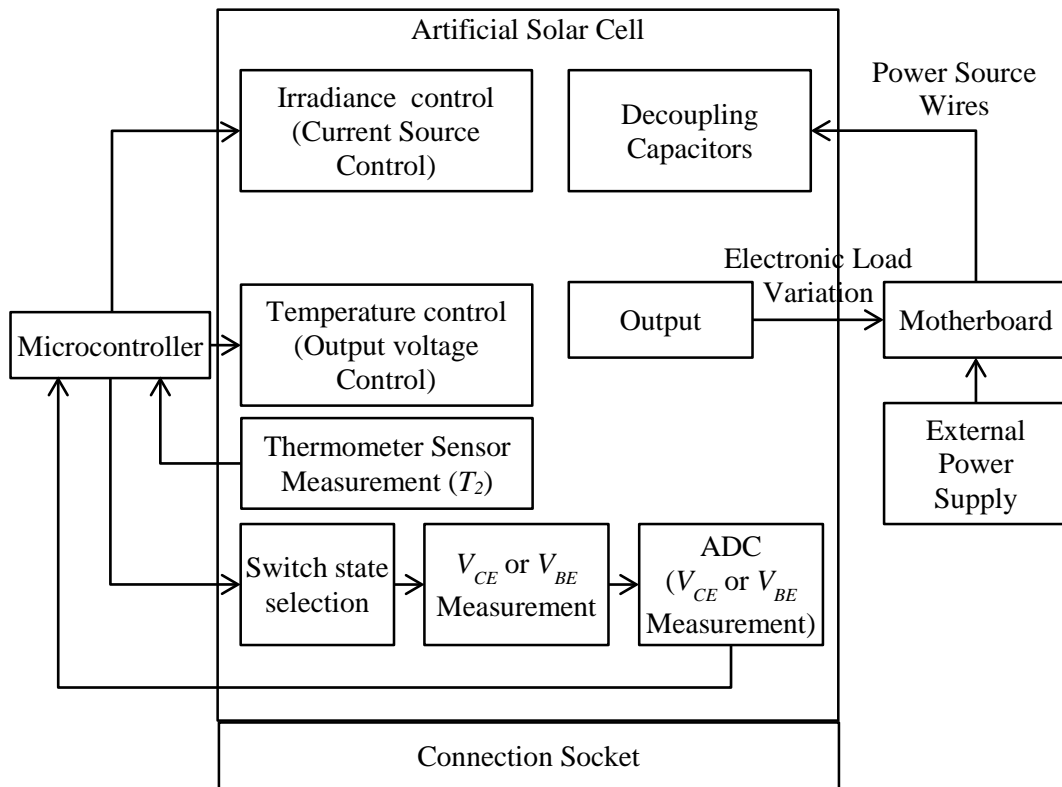


Figure 5.2. Schematic overview of artificial solar cell board.

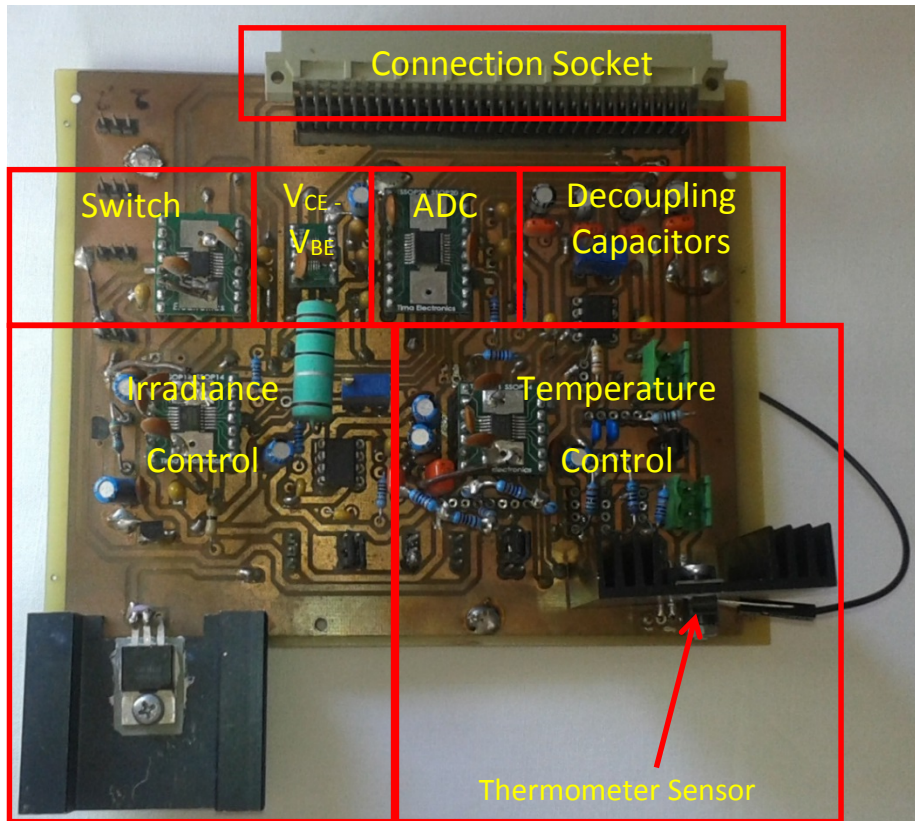


Figure 5.3. Artificial solar cell board.

### 5.3.1 Current Source

An accurate adjustable current source is utilized able to deliver a current up to 390mA. Experiments to insolation level up to  $1500 \text{ W/m}^2$  can be performed for the particular silicon device selected in PC1D covering a wide range of irradiance change. The circuit is based on the topology described in [151] and is illustrated in Figure 5.4.

A MOSFET sets each current with respect to the ‘setting resistor’ ( $R_{setting}$ ). A voltage is applied (12V) in order to drive the current. So, essentially it is the voltage difference across the setting resistor that sets the current flow through the artificial solar cell.

The current is set by the gate of the MOSFET (IRF9540N P-Channel MOSFET). The operational amplifier OP07 adjusts  $Q1$  gate voltage to force the voltage across the setting resistor to equal the voltage between  $V_{CC}$  and the potentiometer’s wiper.

The values of potentiometer  $R_{pot1}$  and resistor  $R4$  are selected in order to obtain an adjustable current source. The regulation of the current flow to the virtual solar



cell is accomplished by adjusting the potentiometer  $R_{pot1}$ . An ammeter can be used to measure output current of the current source, which flows to the artificial solar cell.

For a particular potentiometer value a current is flowing to the artificial solar cell which is related to insolation level according to values obtained from the simulation program (PC1D). So, the current source has been characterized and calibrated to insolation level.

$Q2$  acts as a constant current sink to minimize error in the reference voltage when the supply voltage varies. Decoupling capacitors  $C1$  and  $C2$  are used in the power supply of the operational amplifier OP07.

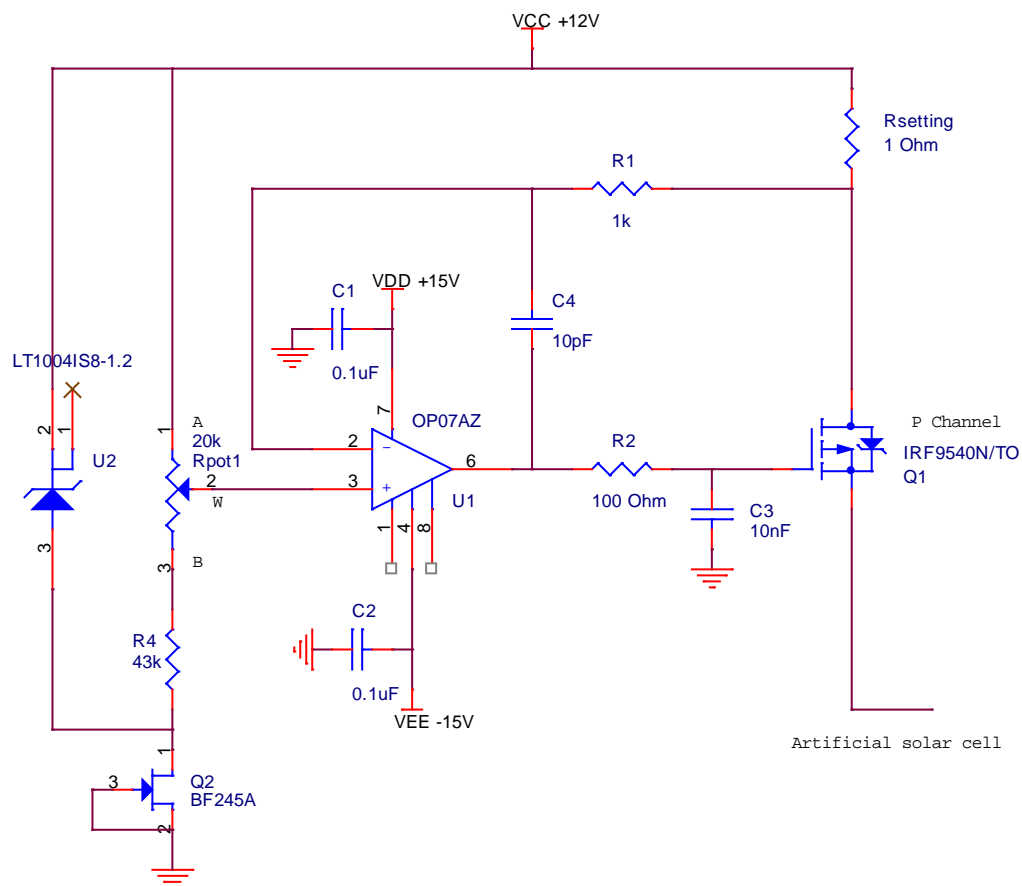


Figure 5.4. Current Source for control of the optically generated current. Adapted from [151].

### 5.3.2 Proposed Transistor Topology

The electronic circuit has been thoroughly described in Chapter 4 and can be seen in Figure 5.5. Signals  $c1$ ,  $b1$  and  $e1$  are collector, base and emitter voltages

respectively, driven to a digital switch. Thus, the user can select which voltage difference ( $V_{CE}$  or  $V_{BE}$ ) would like to measure, as it will be demonstrated in the next section.

The proposed circuit topology has been described in Chapter 4 in terms of Gain ( $G$ ). So, calibration of the potentiometer value  $R_{pot2}$  has performed relating it to gain  $G$ . By controlling potentiometer values  $R_{pot1}$  and  $R_{pot2}$ , the output current or voltage regulation can be accomplished.

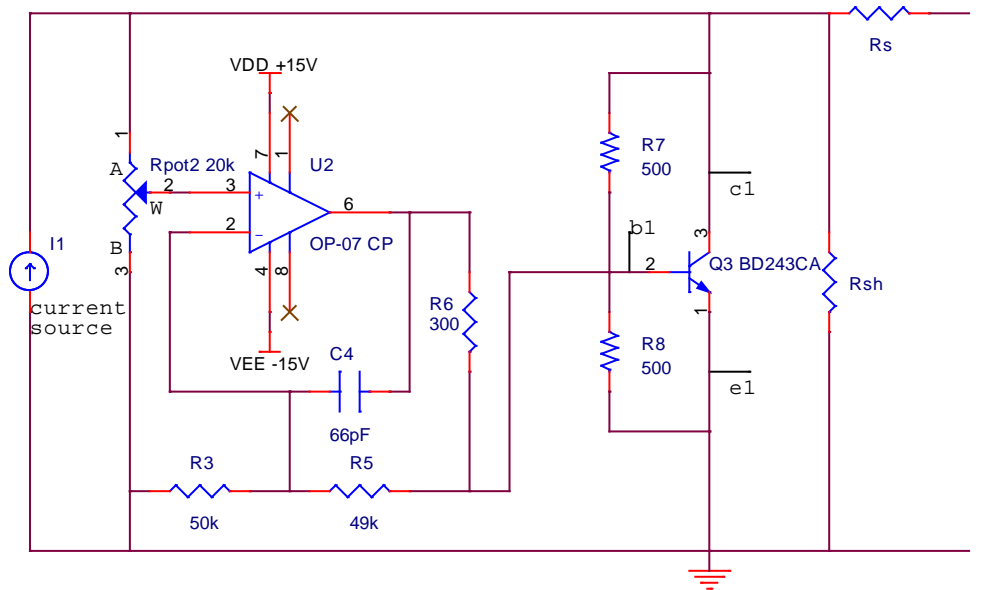


Figure 5.5. Proposed artificial solar cell topology.

### 5.3.3 Digital Potentiometer

To digitize system operation, analog potentiometers ( $R_{pot1}$  and  $R_{pot2}$ ) have been replaced with digital potentiometers (AD5292). The device wiper (W) is controllable through Serial Peripheral Interface Bus (SPI digital interface). Power supplies are decoupled with a capacitor and pull up resistors have placed to +5V.

Four logic signals are required for the SPI Bus to operate. The first one is the Serial Clock Input (*sclk*) which is configured by the microcontroller to begin a communication. The second one is the Master Output, Slave Input (*mosi*) for Serial Data Input. The third signal is the Master Input, Slave Output (*miso*) for read back mode. Finally, the Slave Select (*ss*) enables the chip selection. Master is the microcontroller and slave is the digital potentiometer.

The electronic circuit configuration, as described in the datasheet [152], is available in Figure 5.6.

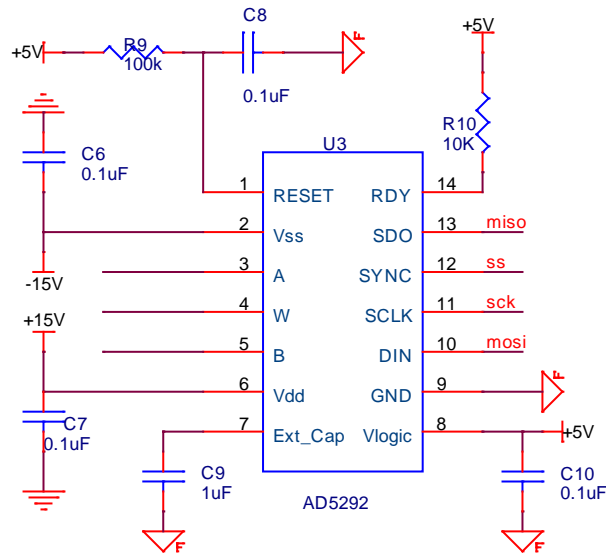


Figure 5.6. Digital potentiometer configuration. W wiper of potentiometer, moving from terminal A to terminal B. Adapted from [152].

### 5.3.4 Digital Switch

A digital switch device, contains two independent selectable switches. The purpose is to select signal voltages collector (*cI*) or base (*bI*) and emitter (*eI*). Schematic configuration of integrated circuit ADG1436 can be seen in figure 5.7 [153]. The *INx (svcbe)* is the logic control input, determining the on switches. The source terminal *SxA* or *SxB* can be selected according to the following truth table:

Table 5.1. Digital switch truth table. Adapted from [153].

<i>INX</i>	<i>SxA</i>	<i>SxB</i>
0	Off	On (base and emitter)
1	On (collector and emitter)	Off

Collector and emitter are selected when *S1A* and *S2A* are on while base and emitter are selected when *S1B* and *S2B* are on.

Effectively, collector or base voltage is selected on this stage through *D1* pin3 (signal *vcbI*). Emitter voltage is always driven to the next stage through *D2* pin11 (signal *eIout*), since *S2B* and *S2A* are shorted.

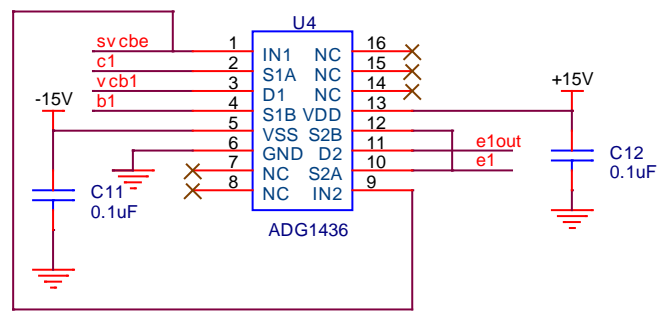


Figure 5.7. Digital Switch schematic configuration. Adapted from [153].

### 5.3.5 Difference Amplifier

A precision difference amplifier, with high accuracy dc performance with 0.08% maximum gain error, instrumentation amplifier is used (figure 5.8). The AD8271 is a low distortion, precision difference amplifier and the configuration of internal gain setting resistor has selected in order to provide unity gain [154]. There are two cases considered, selection of either differential voltage of collector emitter ( $V_{CE}$ ) or voltage of base emitter ( $V_{BE}$ ).

In the case that collector voltage is selected at pin 1, configuring the switch at previous stage accordingly and by having pin 10 always available as the emitter voltage, the differential voltage of  $V_{CE}$  can be measured by driving the signal to a measuring device such as an analog to digital converter.

The second case scenario is when at pin 1 base voltage is selected, configuring the switch at the previous stage and by having pin 10 available, the output voltage ( $v_{out1}$ ) of the instrumentational amplifier is going to be  $V_{BE}$ .

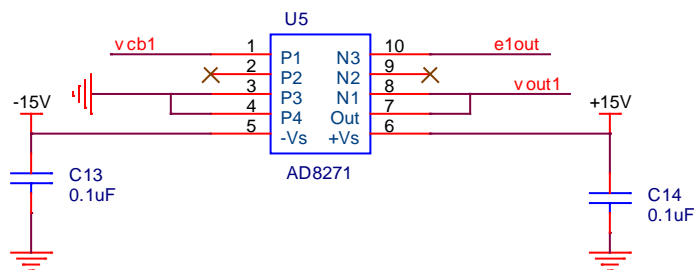


Figure 5.8. Instrumentation amplifier configured as a difference amplifier.

Adapted from [154].

### 5.3.6 Analog to Digital Converter (ADC)

An analog to digital converter (adc) is used to record voltage data ( $V_{CE}$  and  $V_{BE}$ ). The pin configuration of MAX1132 and typical application circuit, as described in [155], can be seen in figure 5.9. It is configured in mode of bipolar input ranges  $\pm 12V$ , so that positive and negative voltages can be measured. It is fully compatible with SPI interface.

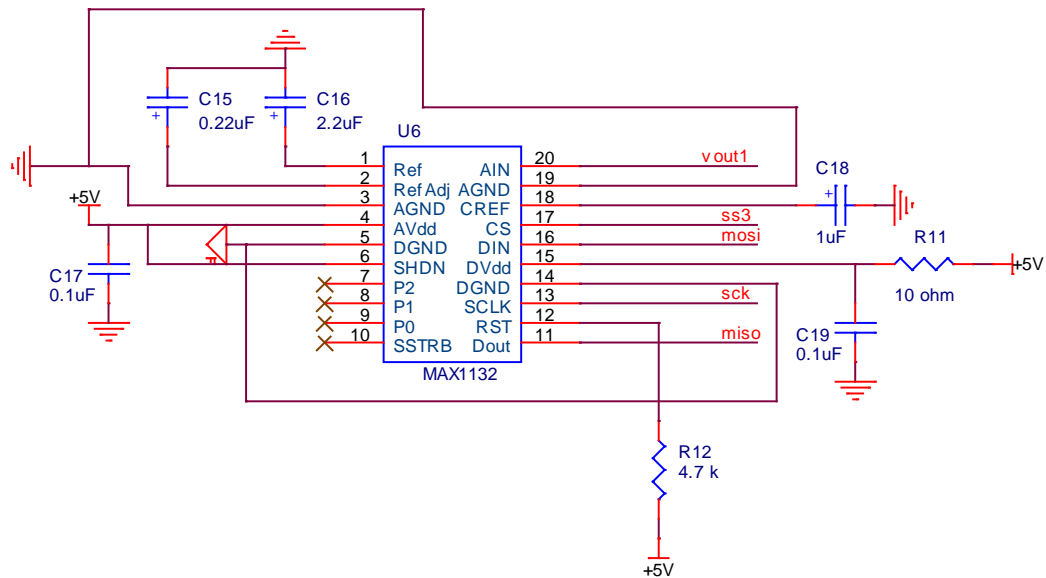


Figure 5.9. Analog to digital converter MAX1132 pin configuration and typical application circuit. Adapted from [155].

### 5.3.7 Temperature Sensor

The DS18B20 digital thermometer has been utilized for temperature measurements. This is necessary for temperature compensation in the transistor. Compensation is applied in order to improve system response.

A temperature sensor is placed in the transistor heat sink to monitor temperature changes at continuous mode operation of the *Emulation Solar System*. As described in Chapter 4 (“Temperature Compensation” section), the data is sent to the microcontroller, the new value of  $G$  is calculated and is compensated by adjusting the gain value of the amplifier accordingly.

The communication with the microprocessor occurs over a 1-wire bus that by definition requires only one data line (and ground). The circuit configuration is

shown in Figure 5.10. An external power supply of +5V is connected to the  $V_{DD}$  pin. The 1-wire bus requires an external pull up resistor of approximately 5kOhm.

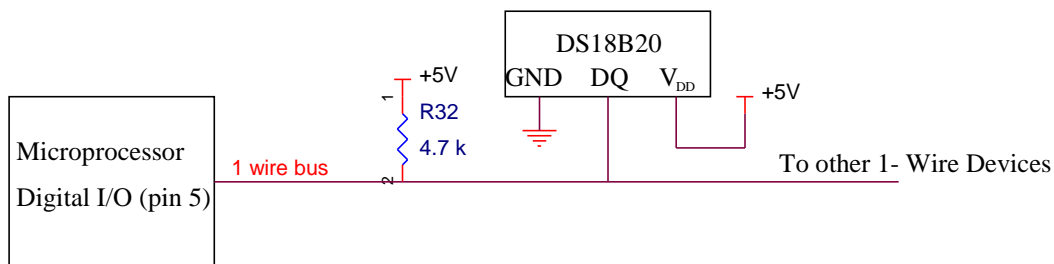


Figure 5.10. Digital thermometer configuration. Adapted from [150].

### 5.3.8 Connection Socket

A connection socket of the artificial solar cell to the motherboard is made using a 64-pin header (2 rows by 32 contacts) of 0.1" (2.54 mm) spacing. Figure 5.11 illustrates the complete pinout, with +15V, -15V, +12V and +5V power supply to the cell. The 0 Ohm resistor connects the analog ground to the digital ground at one point in the artificial solar cell board.

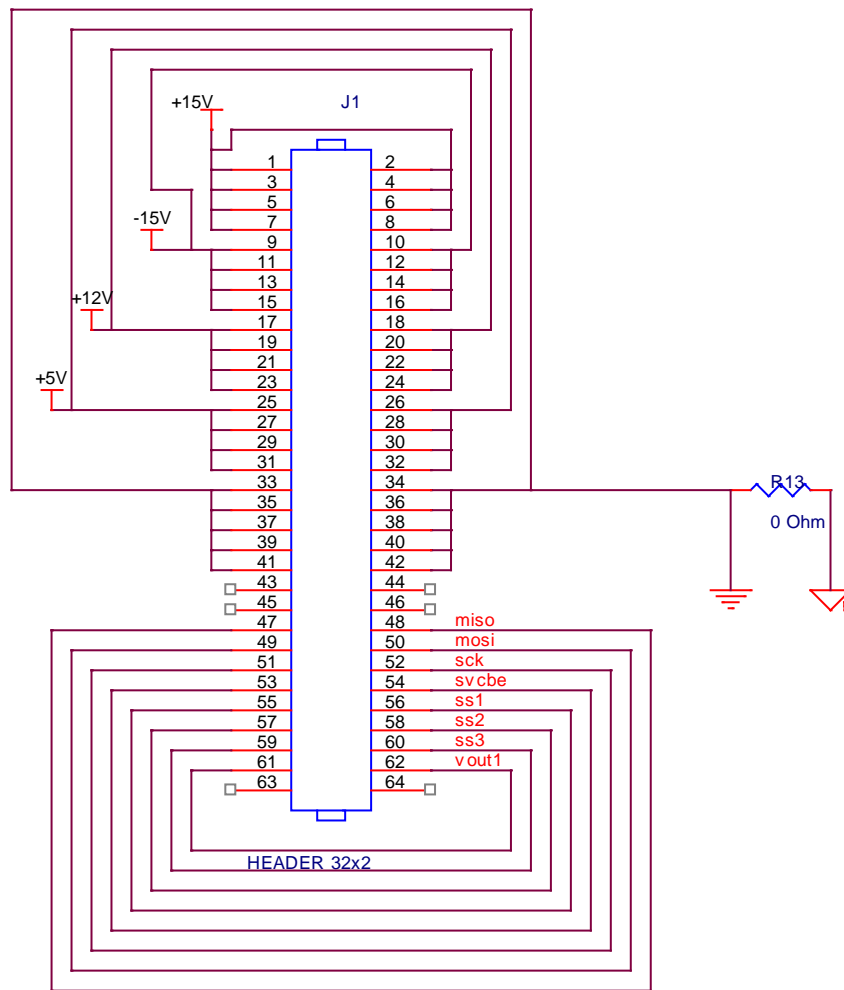


Figure 5.11. Pin Header layout.

Signals, *miso*, *mosi*, *sck* and *ss* are the four logic signals for the Serial Peripheral Interface Bus (SPI digital Interface). There are three devices, one digital potentiometer that controls current source, a second digital potentiometer that controls artificial solar cell output voltage and an analog to digital converter for measuring purposes. Chip selection is performed through signals *ss1*, *ss2* and *ss3* respectively. Signal *svcbe* controls the state of the digital switch. Signal *vout1* is the voltage ( $V_{CE}$  or  $V_{BE}$ ) measured by the analog to digital converter.

### 5.3.9 Decoupling Capacitors

One common kind of decoupling is to protect a powered circuit from signals in the power supply. To decouple a subcircuit from AC signals or voltage spikes on a power supply bypass capacitors are often used.

The 0.1 $\mu$ F is used to bypass high frequency noise and 10 $\mu$ F is to keep power source stable. [156, 157].

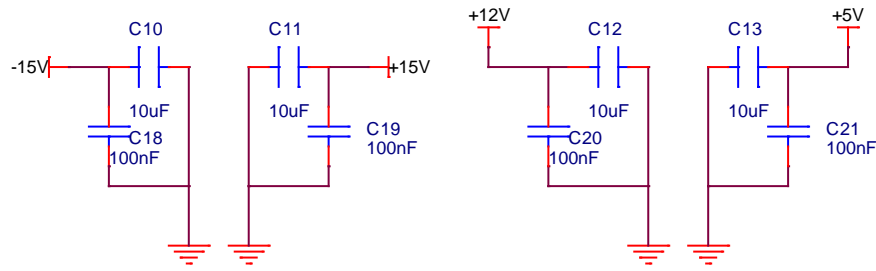


Figure 5.12. Decoupling Capacitors.

### 5.4 Motherboard Circuit Design

A second board has been designed named “motherboard” that comprises an electronic load, a digital to analog converter, an I-squared-C expander and voltage regulators. A schematic overview and implementation of the motherboard are illustrated in figure 5.13 and 5.14 respectively.

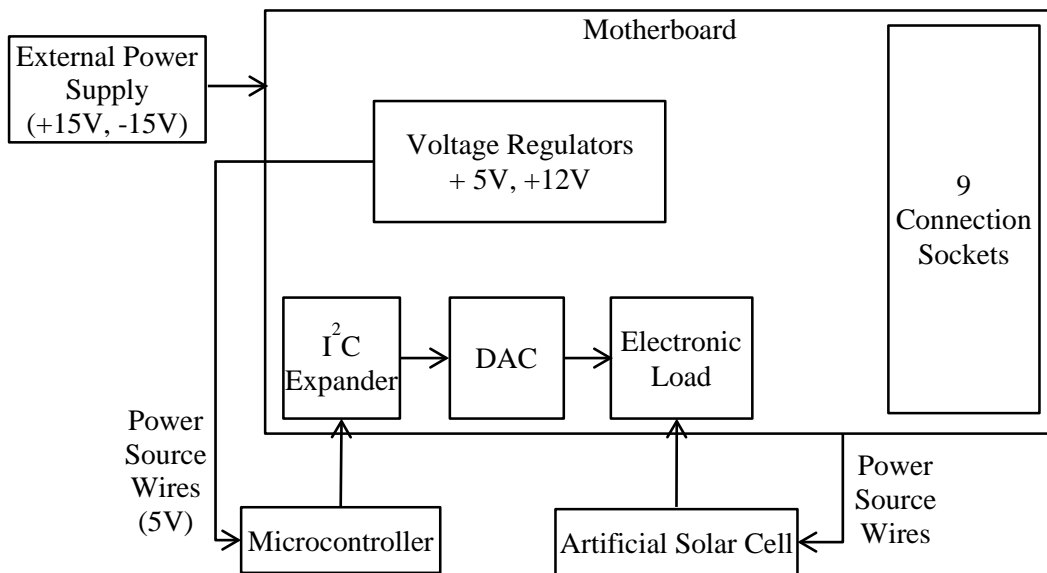


Figure 5.13. Schematic overview of motherboard.



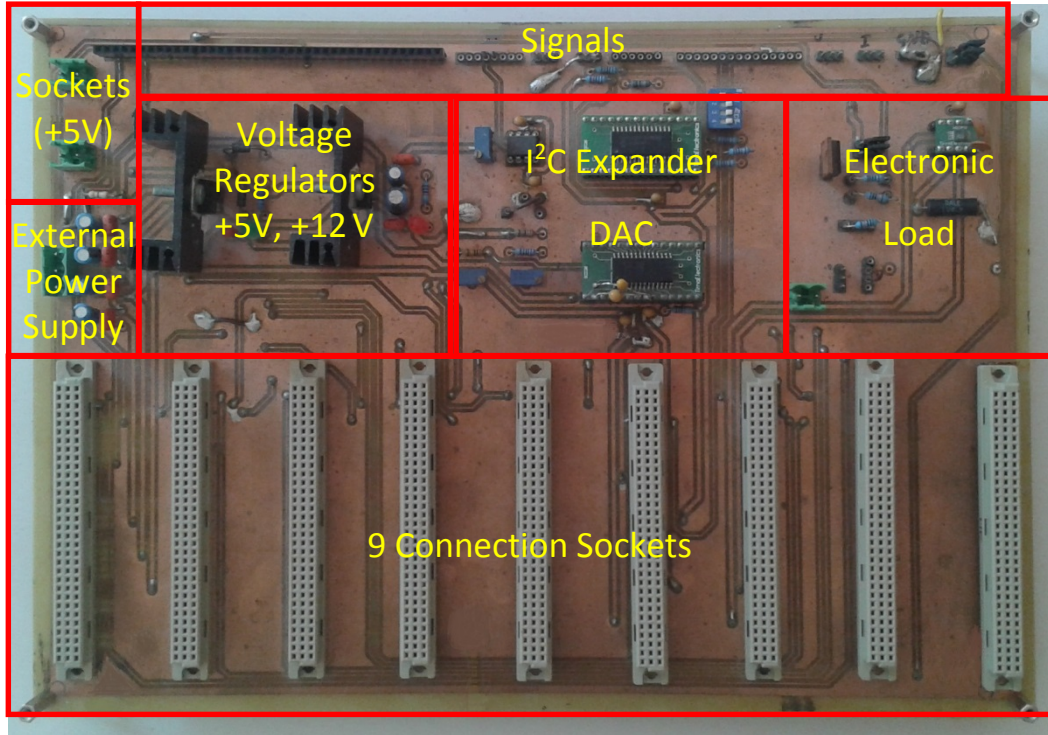


Figure 5.14. Motherboard.

#### 5.4.1 Electronic load circuit

The principle of operation has been described in Section (4.2.1). An electronic fast varying load based upon suitable operation of Metal Oxide Field Effect Transistors (MOSFETs) in its active region, controlled by means of sweeping gate source voltage, is built in order to trace the I-V characteristic.

The circuit operates as a load controlled by voltage. By sweeping  $V_{GS}$  in the appropriate range, the operating point of the MOSFET can be changed, which also drives the operating point of the PV panel to move along its I-V characteristic curve.

In Figure 5.15, a resistor of 100 Ohm ( $R14$ ) is used for protecting the gate of the MOSFET and the 100 kOhm ( $R15$ ) is a pull down resistor. The output current of the PV panel is sensed using a sense resistor ( $R_{sense} = 0.2$  Ohm) in conjunction with a precision gain operational amplifier LT1991 operating it in a topology of gain five [158]. Voltage is actually measured across the sense resistor, but since the value of the resistor is 0.2 Ohm and the gain of operational amplifier is 5 ( $0.2 \cdot 5=1$ ), voltage equals to current.

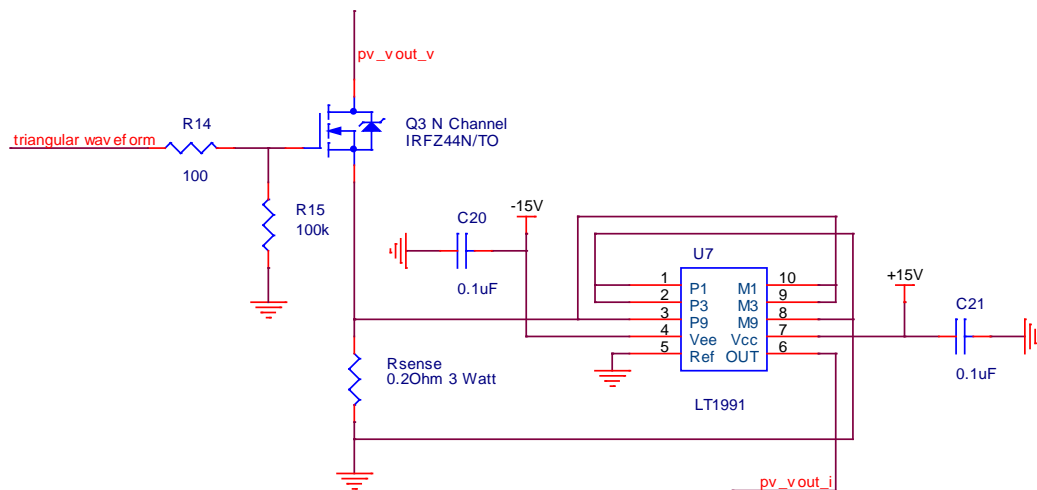


Figure 5.15. Electronic load configuration.

The I-V characteristic is monitored, measuring  $pv\_vout\_v$  and  $pv\_vout\_i$  signals, voltage and current respectively. The outputs Voltage and Current are fed to the inputs of the two measuring devices, analog to digital converters, to track the I-V characteristic of the PV module.

While  $V_{GS}$  is less than the threshold voltage  $V_{th}$ , the MOSFET will be OFF. When  $V_{GS}$  is increased above  $V_{th}$ , the device will operate in its active region where  $I_D$  rises approximately in a linear way with  $V_{GS}$ . [142]

The MOSFET should be driven by a low frequency scan signal with amplitude large enough to cover the complete range of PV panel characteristic [143]. A function generator could provide a sinusoidal or triangular signal (figure 5.15 triangular waveform) of low frequency and with amplitude between 0 V to 10 V. Voltage  $V_{GS}$  should vary slowly in order to increase the number of operating points captured in the flat region, ( $V_{mpp}$  until  $I_{sc}$ ) [143]. Small variation in  $V_{GS}$  can improve the trace of the I-V curve.

The value of  $V_{oc}$  is obtained by applying 0 V to the gate of the MOSFET, the MOSFET is OFF, it does not conduct and operates as open circuit. The value of  $I_{sc}$  is obtained by applying 10 V to the gate of the MOSFET (short circuit). The true value of  $I_{sc}$  is not exactly achieved since the PV module is not short circuited because of the sense resistance and the internal resistance of the MOSFET ( $R_{DS(on)}$ ).

### 5.4.2 Triangular Waveform

A digital to analog converter is employed to provide the triangular waveform instead of using a function generator. The DAC715 [159] is a digital to analog converter with output range from 0 to +10V, with amplitude large enough to cover the complete range of PV panel characteristic.

A ramp signal is actually produced by the DAC with voltage values between 2.9V and 4V. Lower amplitude voltage than 2.9V, will give repetitive measurements close to  $V_{oc}$  region, while higher amplitude values than 4V, will give repetitive measurements close to  $I_{sc}$  region. It was experimentally observed that this range is enough to cover the complete range of PV panel characteristic under examination concentrating to the most useful part of the I-V curve, eliminating repetitive measurements towards the two ends of the curve. The minimum step value of the DAC is  $152\mu\text{V}$  and in the particular implementation a step value of 5 ( $5 \cdot 152\mu\text{V} = 760\mu\text{V}$ ) was selected in order to obtain enough points to accurately describe the I-V curve as it was explained in “Distribution of Data points” (Section 4.5.6). The time duration of the triangular waveform is 87 seconds. Higher step values can result in biasing the results towards the two ends ( $V_{oc}$  and  $I_{sc}$ ). Small variation in  $V_{GS}$  can improve the trace of the I-V curve. As a result the visualization of the trace of the I-V characteristics can become more uniform and persistent. Power supply connections and data bits ( $D15$  to  $D0$ ) can be seen in figure 5.16.

Finally, an operational amplifier, voltage follower (buffer), has placed at the output of the DAC for driving the base of the MOSFET. Potentiometer  $R22$  connected between pins 1 and 8 of the OP07 is an optional offset nulling adjustable circuit.

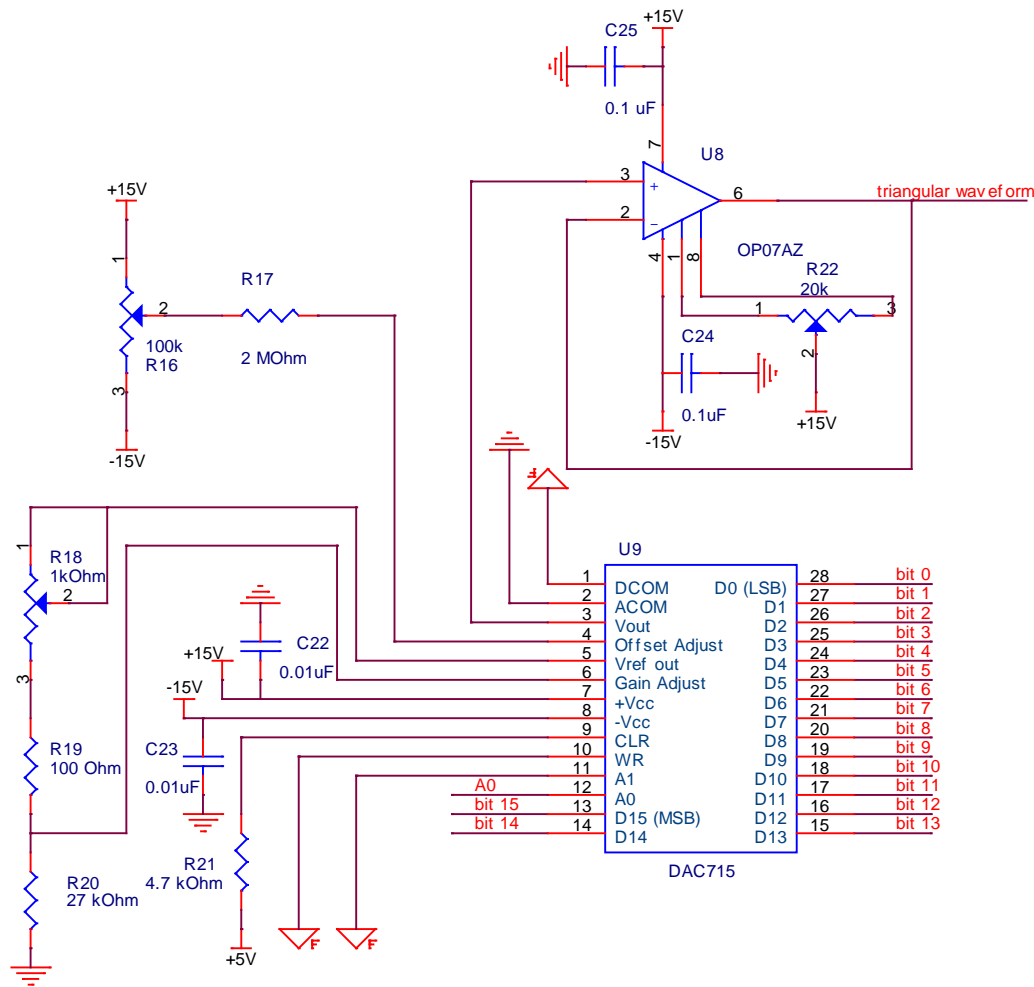


Figure 5.16. DAC provides triangular waveform. Adapted from [159].

Buffer for driving the MOSFET.

### 5.4.3 I/O I-squared-C Expander

Instead of using 16 general-purpose input/output (GPIO) pins of the microcontroller for operating the DAC, an I-squared-C (I<sup>2</sup>C) expander chip is used that requires only two bus lines, serial data line (SDA) and serial clock line (SCL).

The MCP23017 device is a 16 bit, general purpose I/O expansion for I<sup>2</sup>C bus application. The 16 bit I/O port functionality consists of two 8-bit ports (PORTA and PORTB) [160].

Hardware address pins (A0, A1, A2) are used to determine the device address. The configuration of the address is hardware made through dip switch, all connected to ground. The device connected to the bus is software addressable by a unique address. There are two interrupt pins, not used in this particular implementation.

Microcontroller is the master device, while there is only one slave device, the MCP23017 on the I<sup>2</sup>C bus.

Both SDA and SCL lines are “open drain” drivers. What this means is that the chip can drive its output low (0V), but it cannot drive it high (5V). For the line to be able to go high, pull up resistors required to 5V supply. Both bus lines remain high unless there is a communication by pulling the bus low. To initiate communication microcontroller pulls the SDA line low. It has the responsibility to drive the SCL line with clock pulses. [161]

The MCP23017 electronic connections can be seen in figure 5.17.

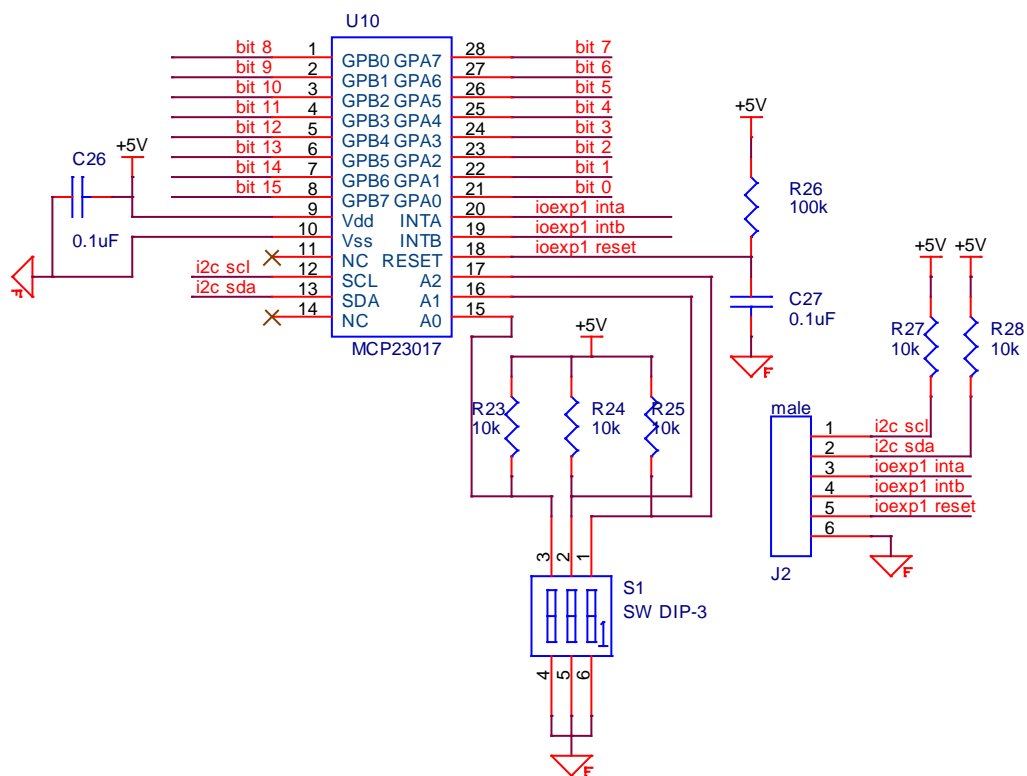


Figure 5.17. I-squared-C Expander configuration circuit. Adapted from [160].

#### 5.4.4 Voltage Regulators

A power supply provides + 15 Volt and -15 Volt. In order to operate devices two voltage regulators are required, to maintain a constant output voltage level.

A positive voltage regulator is utilized with output voltage +5V. A typical application circuit can be seen below in figure 5.18 [162]. It is recommended that regulator input is bypassed with a capacitor, if the regulator is located in a distance from the power supply. Although no output capacitor is needed for

stability, it does improve transient response. Diodes  $D1$  and  $D2$  are used for protection reasons.  $D1$  protects the regulator from output polarity reversals during startup and short circuit operation.  $D2$  is placed as a protection circuit to prevent reverse bias. A green LED with a resistor is used to indicate the user that the circuit is working properly.

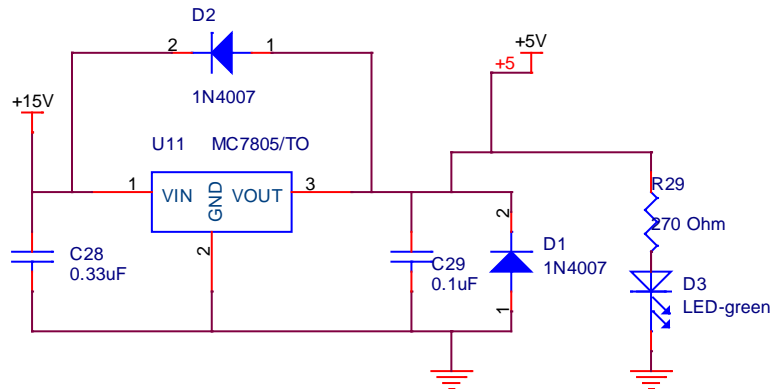


Figure 5.18. Voltage regulator at +5V. Adapted from [162].

A positive voltage regulator is utilized with output voltage +12V. Input capacitor is required in most regulator designs. The output capacitor 22µF is required for stability, capacitors 100nF (input and output) are used for decoupling. A typical application circuit [163] can be seen in figure 5.19. The LT1084 does not need any protection diodes. The internal diode between the input and the output ensures device safety. A red LED with a resistor is used to indicate the user that the circuit is working properly.

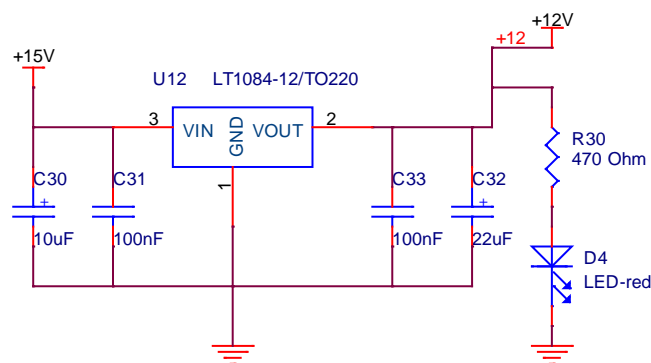


Figure 5.19. Voltage regulator at +12V. Adapted from [163].

#### 5.4.5 Other Components

The system was configured to allow up to 9 artificial solar cells to be fitted into the motherboard. It has to be stated that the system is fully expandable. The only

constrain for placing up to 9 artificial solar cells is the size of the electronic board utilized. Placing in the motherboard all necessary electronic components, the space left in the board was enough for up to 9 artificial solar cells.

There are three more headers used (figure 5.20). The first one contains all the signals required for the microcontroller. The second has the measuring parameters of output current and voltage. The third one is a power supply connector. Finally, the analog ground is connected to the digital ground at one point at the “motherboard” by a 0 Ohm resistor.

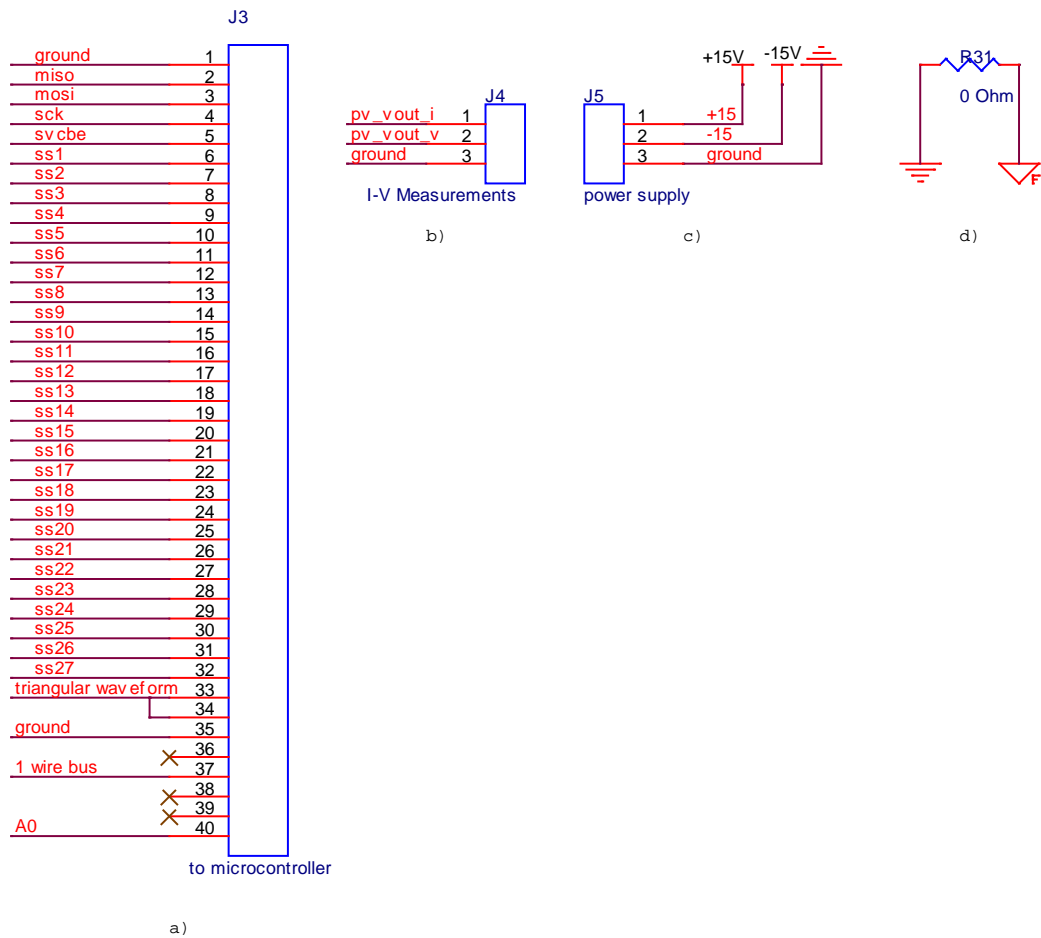


Figure 5.20. a) Signals to the microcontroller, b) Measuring current and voltage, c) power supply connector d) Digital to analog ground connection through 0 Ohm resistor.

## 5.5 Measurement System Recording Current – Voltage Data

A schematic overview and implementation of the measurement system board are illustrated in figure 5.21 and 5.22 respectively.

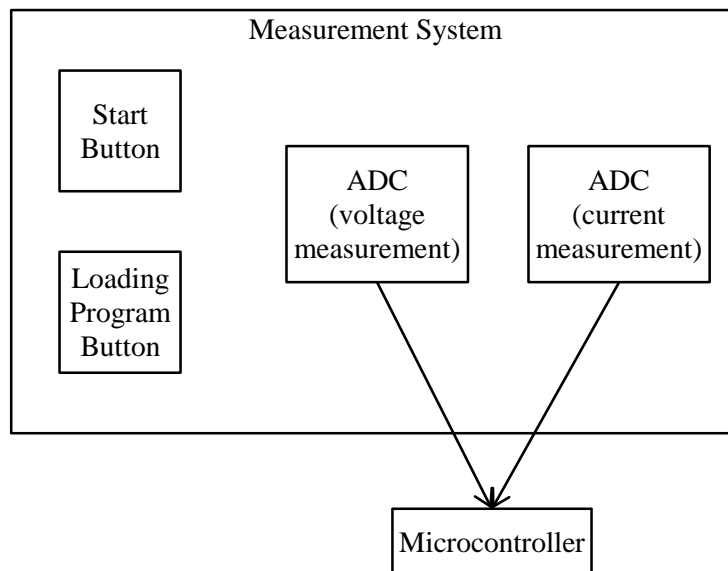


Figure 5.21. Schematic overview of the measurement system board.

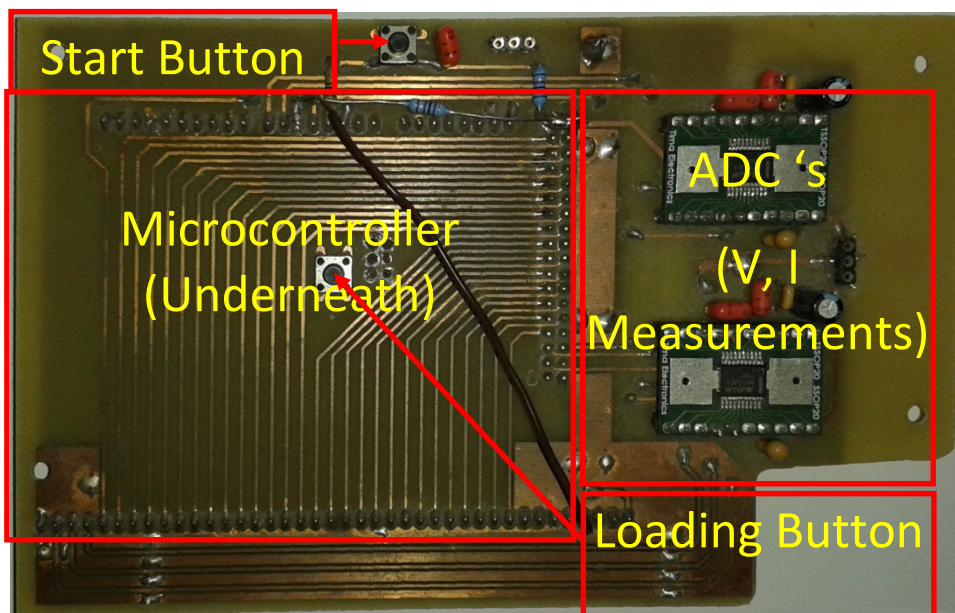


Figure 5.22. Measurement System board.

The third board was developed to allow measurements of output voltage and current of the artificial solar cell to be made. It contains two analog to digital converters for output voltage and current.

The board contains two buttons. The first one is the start button ( $S_2$ ) of the experiment. When it is pressed the experiment starts. The second one is the reset button ( $S_3$ ) of the microcontroller and it used when a software program is loaded to the microcontroller.

Male headers were placed so that the board can be placed on the top of the Arduino PCB microcontroller, which has female headers.



All electronic components, 2 ADC's, 2 buttons and male headers, along with the electronic connections of the board can be seen in figure 5.23. Analog to digital converters have the same electronic circuit configuration, as described previously.

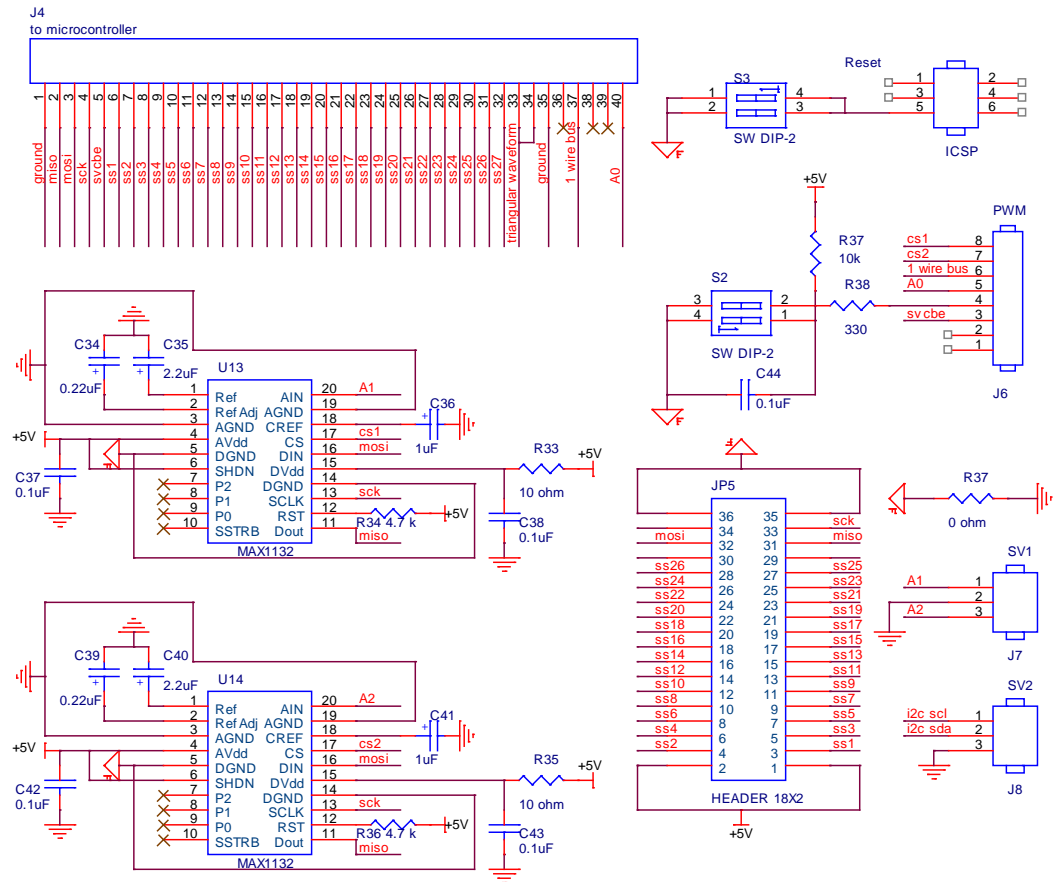


Figure 5.23. Measuring output voltage and current circuit design.

## 5.6 Graphical User Interface (GUI)

A graphical user interface (GUI) illustrated in figure 5.24 has been developed to allow a user to interact with electronic devices, such as digital potentiometers through graphical slider(s) and/or a text based interface, digital switches and connect/disconnect buttons.

Up to nine artificial solar cells can be placed in the motherboard. Each cell has two digital potentiometers, one for controlling the current source (irradiance) and a second one for controlling the output voltage (temperature). Thus, if all cells are placed, eighteen digital potentiometers have to be controlled.

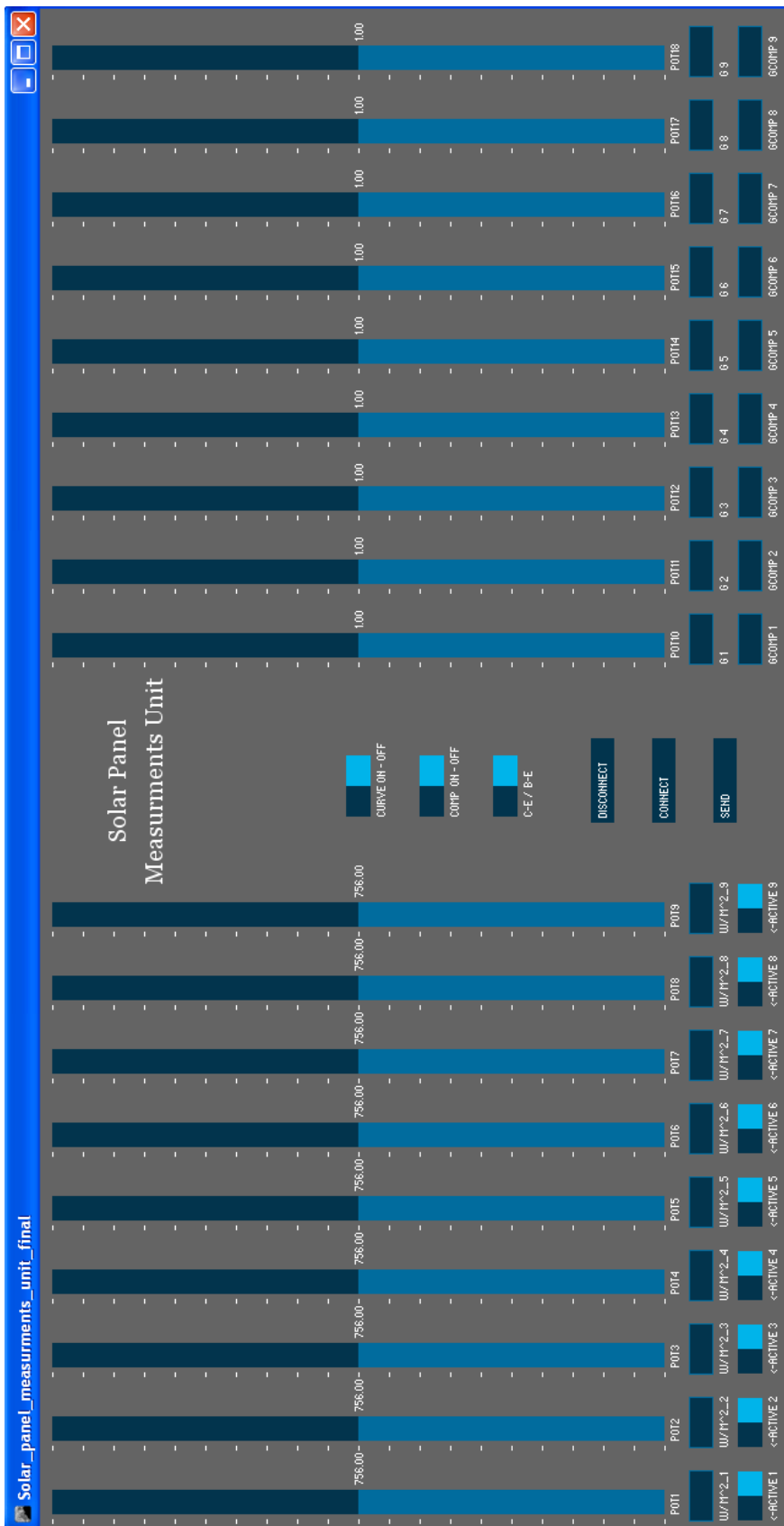


Figure 5.24. GUI Solar panel control unit.

Potentiometers *pot1* to *pot9* are associated to irradiance control. Minimum value is  $0 \text{ W/m}^2$  while maximum value is  $1500 \text{ W/m}^2$ . Potentiometers *pot10* to *pot18* are related to output voltage regulation, which is associated to temperature control as well. Minimum value of the gain is 0, while maximum value is almost 2.

An ease of use interaction with digital potentiometers, allowing the user to select a value, is achieved through graphical sliders. Alternatively, a value can be typed in the “value” box underneath the slider to obtain a specific value for the selected digital potentiometer.

The number of cells placed in the motherboard can be enabled using the graphical toggle switch button “*Active*” underneath the corresponding artificial solar cell. Placing for example one artificial solar cell at the first slot and making it active, with the graphical toggle switch on the left hand side, enables digital potentiometers *pot1* and *pot10*.

If the user would like to perform an experiment and acquire an I-V characteristic curve, the corresponding graphical toggle switch “*CURVE ON-OFF*” has to be enabled (*ON* – left hand side). The electronic load starts to change and the operating point will move along the I-V characteristic curve. The experiment starts when *SI* button is pressed, on the measurement system board. The purpose of “*CURVE OFF*” option is for setting only irradiance and output voltage of the artificial solar cell without acquiring an I-V curve. This is the case when the artificial solar cell is connected to a MPPT device which will be described in Chapter 6.

Temperature compensation is performed by enabling the graphical toggle switch “*COMP ON-OFF*” (*ON* – left hand side) and by filling the  $G_{comp}$  value ( $G_{comp}=G/T_2$ ). As temperature  $T_2$  increases, gain  $G$  value is updated and the microcontroller adjusts the digital potentiometer accordingly.

Among others, distinguishable is a graphical toggle switch button in the interface design for selecting measurements either of the collector emitter voltage (*C-E*) or base emitter voltage (*B-E*) across the transistor.

Finally, “*Connect*”, “*Disconnect*” and “*Send*” buttons are included in the software program. Having finished all the necessary adjustments of the digital potentiometers, enabling the appropriate artificial solar cells, setting I-V curve *ON*

or *OFF*, with or without compensation, and selecting  $V_{CE}$  or  $V_{BE}$  measurement, the user should press the send button for sending all the settings to the microcontroller. Then the “*Disconnect*” button has to be pressed in order to release the com port and enable the microcontroller to use the com port to display data at build-in serial monitor of arduino. When the experiment has completed and measurements have obtained, the user can press the “*Connect*” button in the GUI and proceed to any changes required to perform the next experiment.

## 5.7 Microcontroller Board

Arduino Mega 2560 (figure 5.25) is used as a microcontroller board based on the ATmega2560 processor, in order to control signals to the digital potentiometers, analog to digital converters, digital to analog converter, I-squared-C expander and digital switch, necessary for the operation of the Solar Emulator Platform.

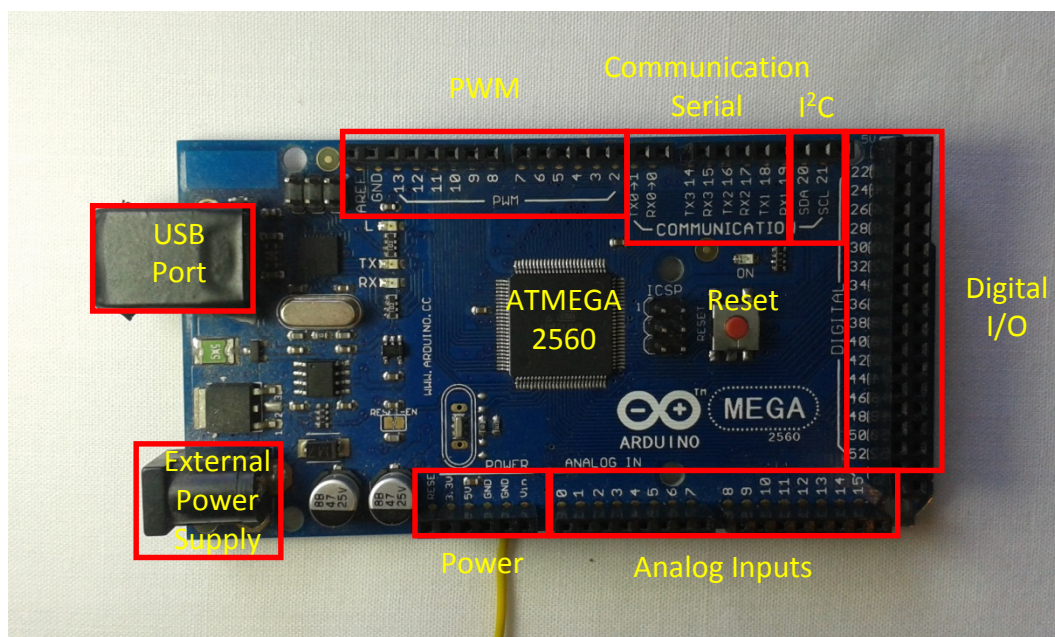


Figure 5.25. Microcontroller board.

It has 54 digital input/output pins, 16 analog inputs, a 16MHz crystal oscillator, a USB connection, a power jack and a reset button. Microcontroller fully documentation is available in [164]. Each of the 54 digital pins on the Arduino Mega can be used as an input or output, using *pinMode()*, *digitalWrite()*, and *digitalRead()* functions. There are built-in functions for SPI, I<sup>2</sup>C and 1-wire communication protocols.

Arduino built-in serial monitor is used to communicate with the computer via USB port. As an experiment is conducted, measurements of voltage, current, collector emitter voltage, base emitter voltage and temperature data are obtained and can be plotted graphically.

A flowchart of the process is provided in figure 5.26.

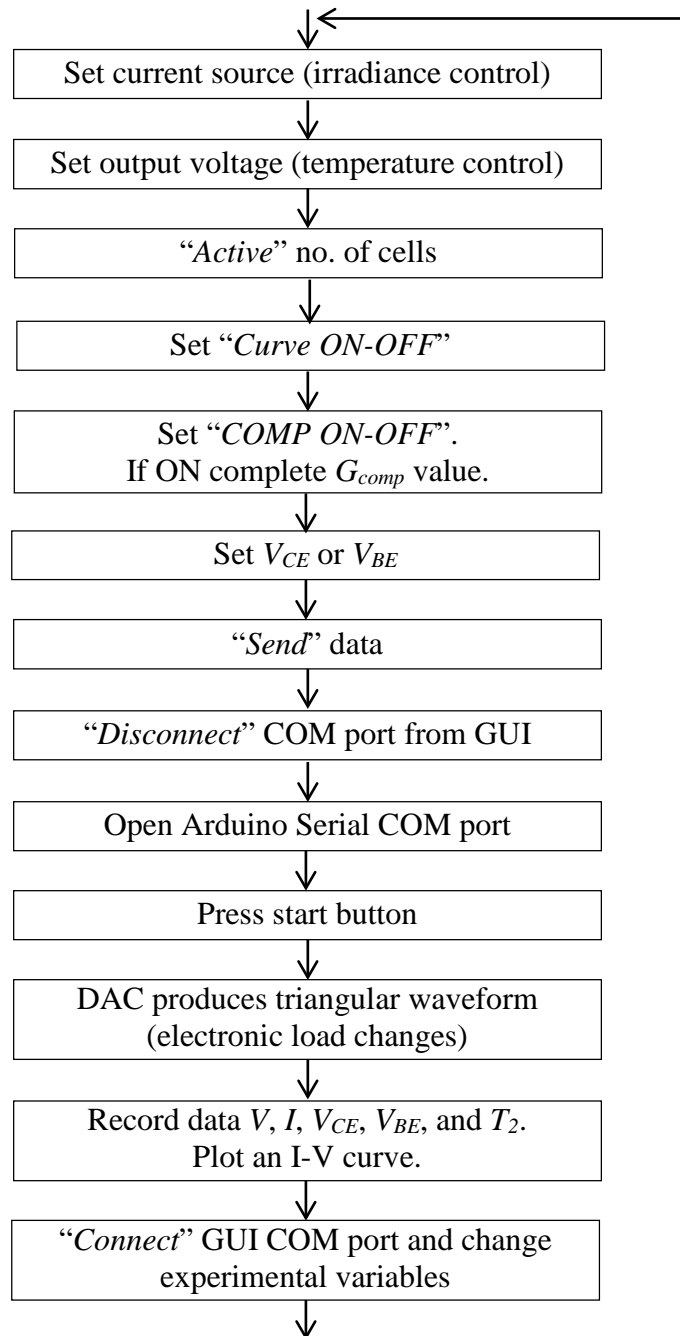


Figure 5.26. Flowchart of the process.

## 5.8 Experimental Results

As in chapter 4, a ‘silicon device’ was chosen in PC1D. The mostly default values were used however, device area was set to  $8 \text{ cm}^2$ , series resistance  $R_s = 0.5 \text{ Ohm}$ , shunt resistance  $R_{sh} = 20\text{kOhm}$  ( $0.00005 \text{ Siemens}$ ). The intensity was varied at  $0.08$ ,  $0.06$  and  $0.04 \text{ Watt/cm}^2$  and temperature was varied from  $+60 \text{ }^\circ\text{C}$  ( $333 \text{ kelvin}$ ) to  $-20^\circ\text{C}$  ( $253 \text{ kelvin}$ ) in steps of  $20 \text{ }^\circ\text{C}$ .

Gain ( $G$ ) for the artificial solar cell and current source were adjusted to match changes in temperature and irradiance, respectively. In order to test quality of fit between theoretical (PC1D) and experimentally (artificial solar cell) obtained I-V characteristic curves, a statistical value of root mean square error ( $RMSE$ ) was calculated.

Ideality factor and temperature were extracted from PC1D software, while saturation current was determined solving the non linear least square problem.

The product of ideality and temperature ( $nT$ ) and saturation current were extracted for the artificial solar cell. The methodology followed has described in Chapter 4.

Values of experimental study performed based on the transistor model are provided in Table 5.2 (Appendix C), while theoretical values based on PC1D software are presented in Table 5.3 (Appendix C).

Finally, all results are plotted in Figures 5.27 to 5.30. The I-V characteristic curves for all cases considered are illustrated in Figure 5.31.

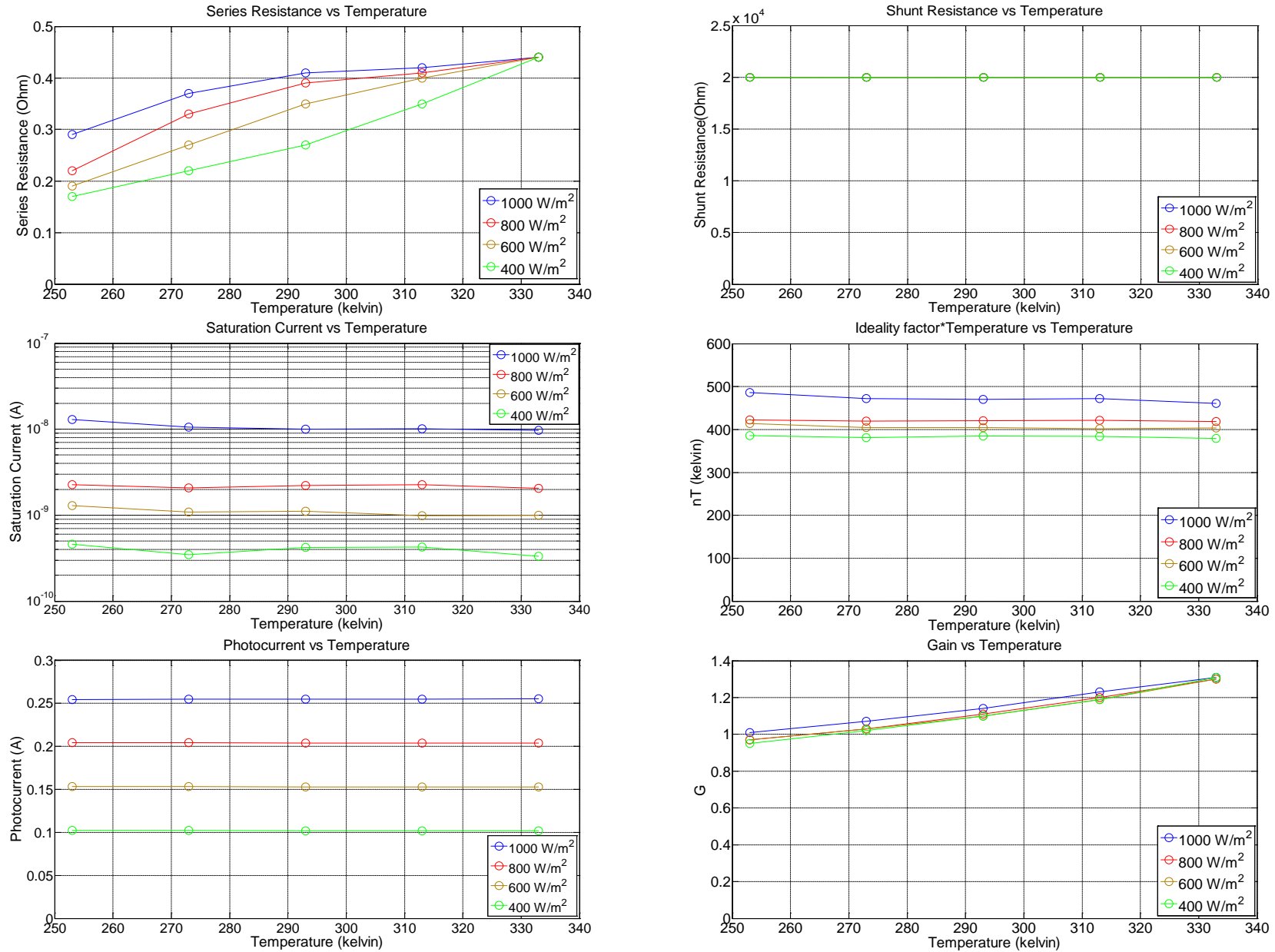


Figure 5.27. Experimental values versus temperature for different irradiances.

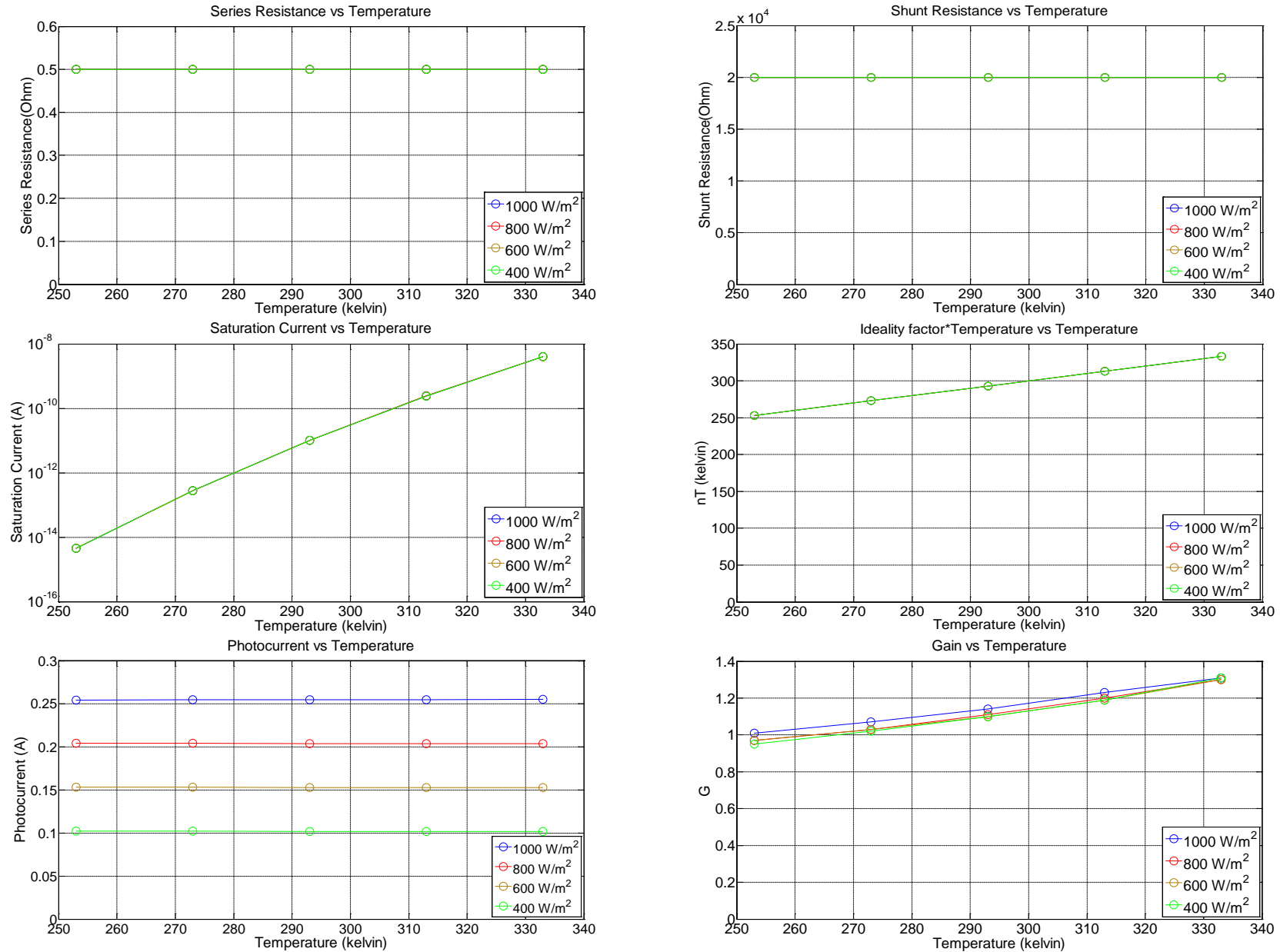


Figure 5.28. Theoretical values versus temperature for different irradiances.



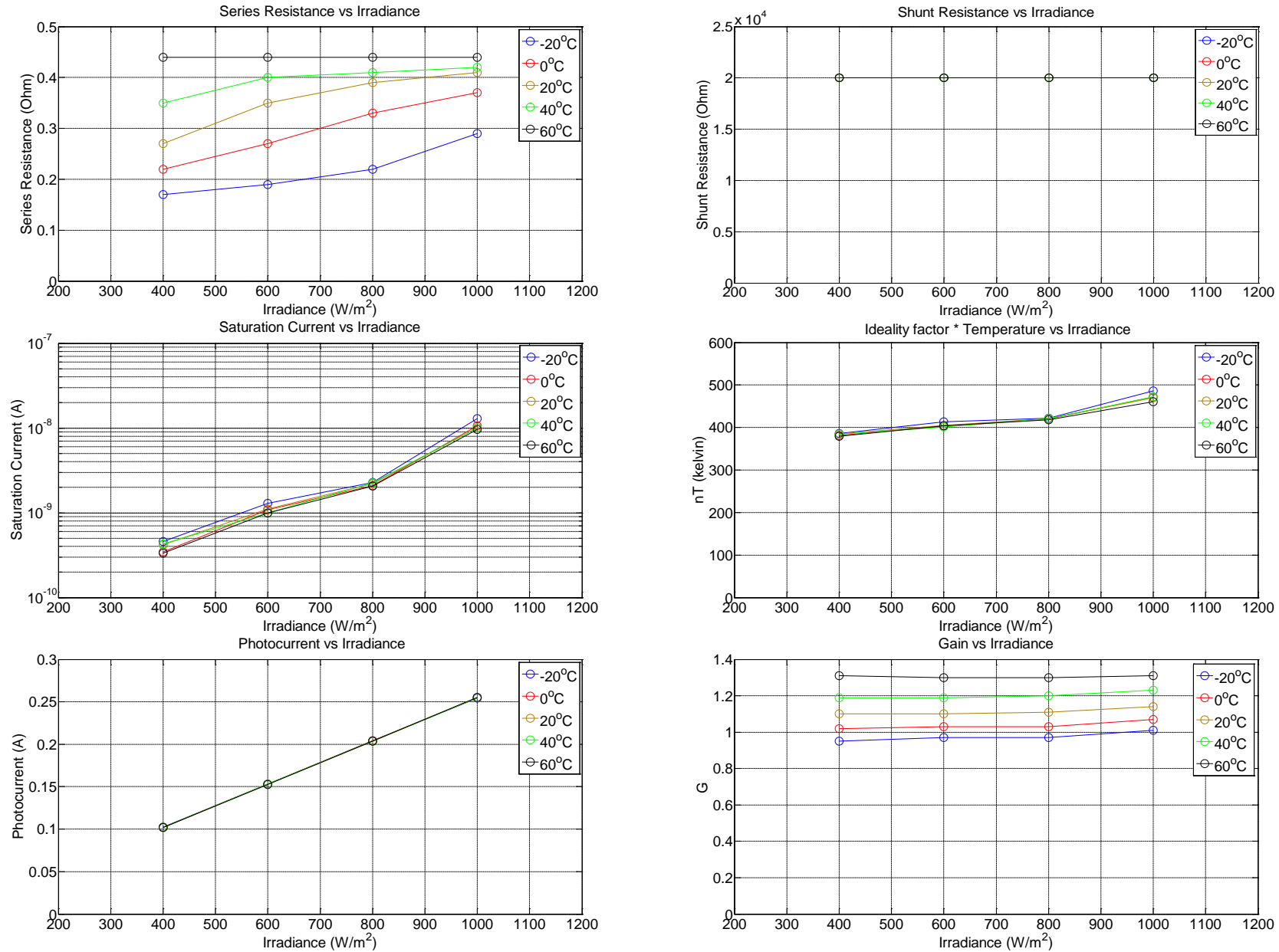


Figure 5.29. Experimental values versus irradiance for different temperatures.

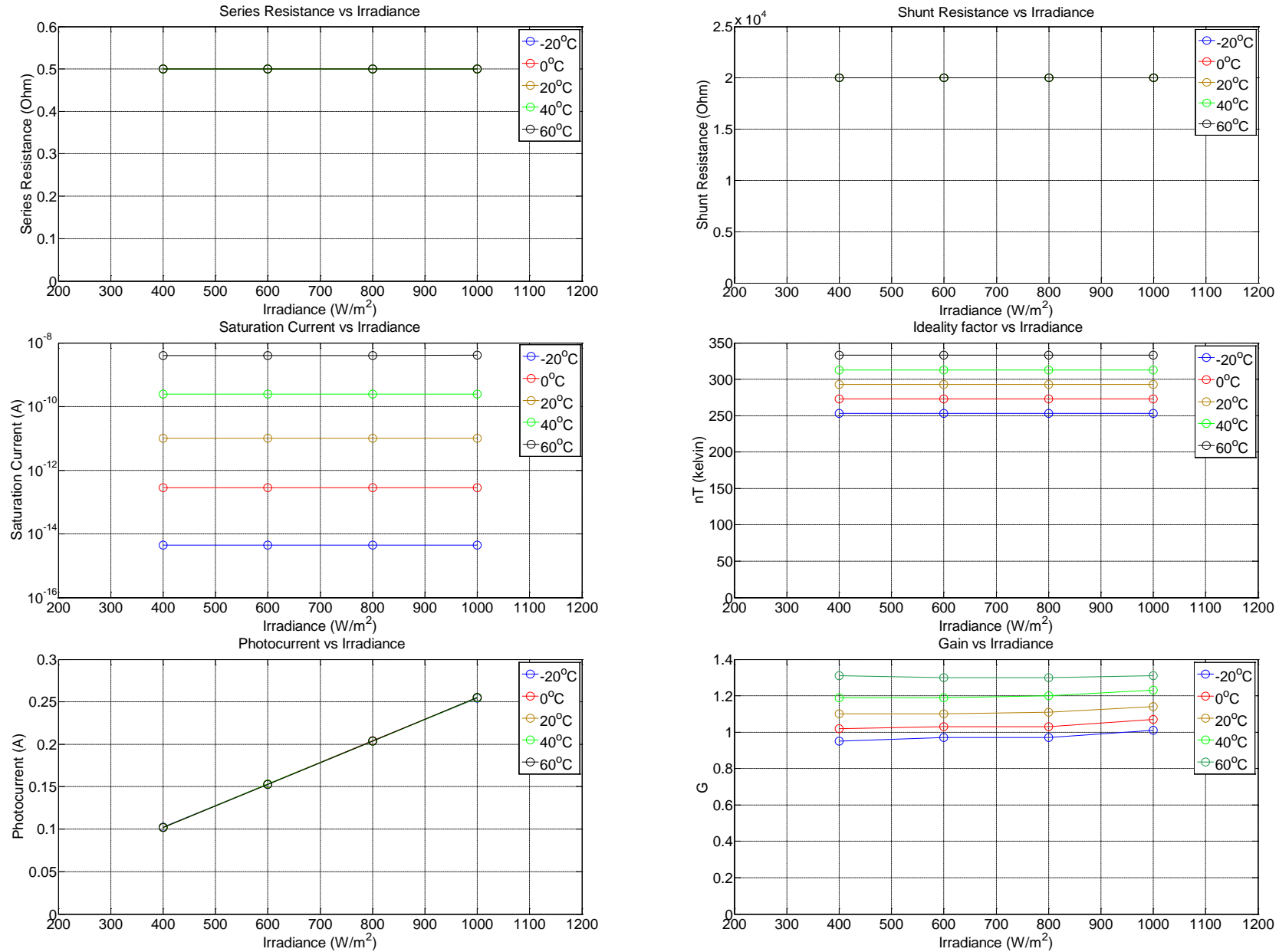


Figure 5.30. Theoretical values versus irradiance for different temperatures.

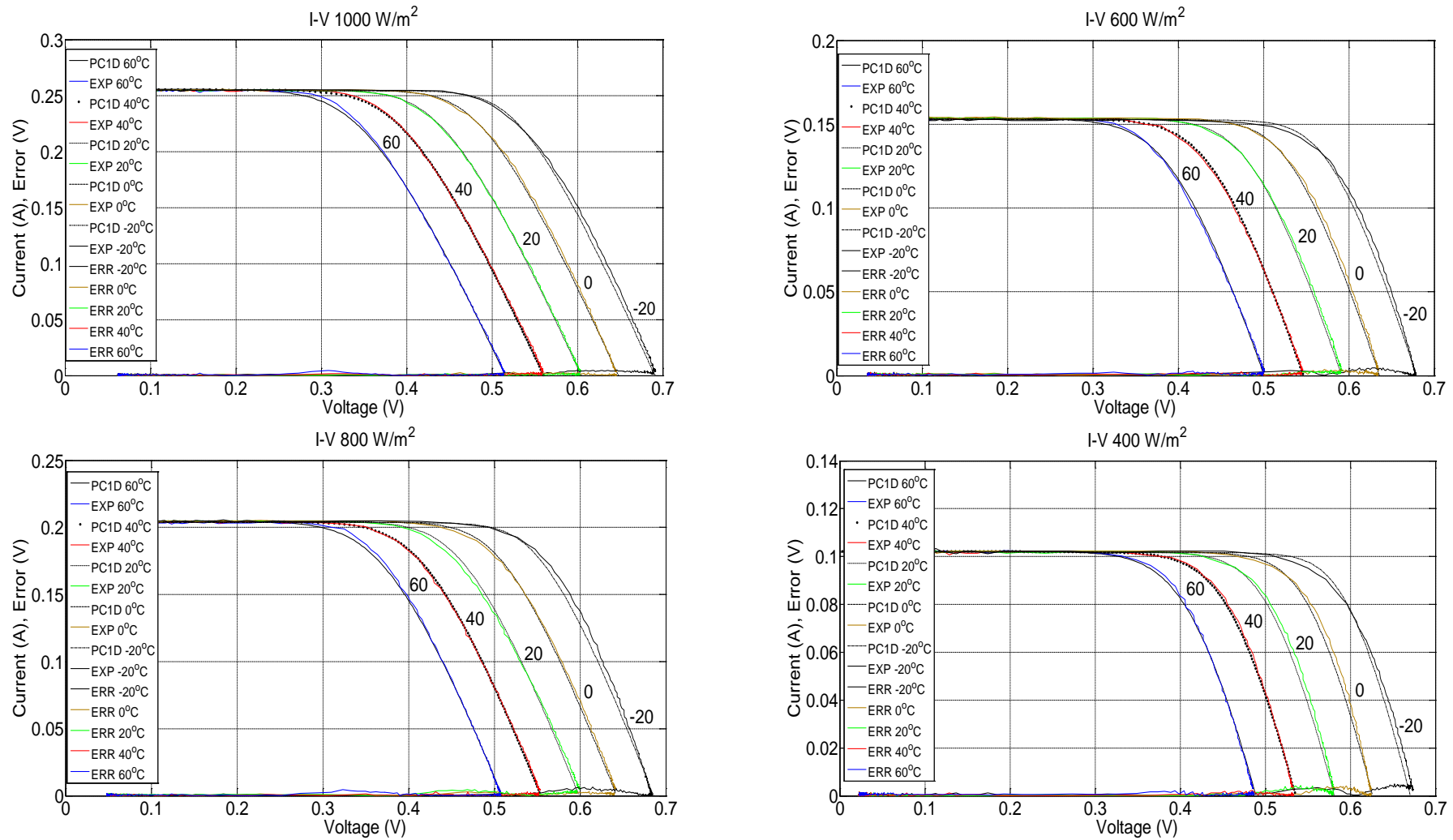


Figure 5.31. I-V characteristics for all cases considered.

The statistical indicator *R squared* value extracted for all data parameters ( $n_2T_2$ ,  $I_{s2}$ ) is close to 1 (approximately 0.98), indicating an accurate extraction along with a good fit to the data. The small *Residual* value ( $10^{-5}/10^{-6}$ ) suggests that the five fitting parameters from PC1D software have small error. The small RMS error values ( $10^{-3}$ ) suggest that the I-V characteristic curves between artificial solar cell and software simulation program are in good accordance.

Results demonstrate numerical agreement of gain values ( $G$ ), between experimentally measured and theoretically computed values according to equation derived in Chapter 4. Gain increases as temperature increases since the formula (4.10) derived is dependent on temperature, while gain value is almost constant to irradiance change with a small decrease as irradiance drops. Considering equation (4.5) ( $V_{BE}=GV_J$ ) as  $G$  increases open circuit voltage ( $V_J$ ) will decrease for the same base emitter voltage ( $V_{BE}$ ) value. The decrease of open circuit voltage as illustrated in figure 5.31 corresponds to higher temperature conditions.

There is a numerical agreement in values of shunt resistance and photocurrent as well. Shunt resistance is 20kOhm throughout all experiments. Photocurrent increases as irradiance increases by approximately 50 mA for every 200 W/m<sup>2</sup> increase in irradiance. Temperature increase has a smaller impact affect to photocurrent, less than 1mA for 80°C variation.

Series resistance values placed in the artificial solar cell, so that to match I-V characteristic curves as analyzed in Chapter 4 are stated in table 5.2 (Appendix C). It can be observed that as irradiance and temperature increases, series resistance increases as well, evaluating equation (4.26) which describes series resistance value. In the simulation program series resistance value throughout all experiments conducted was kept constant (0.5 Ohm).

Saturation current extracted experimentally is in the range of  $10^{-8}$  to  $10^{-10}$  (A). Values extracted from simulation program are in the order of magnitude  $10^{-9}$  to  $10^{-15}$  (A). In the graphical representation of the theoretical setup Saturation current versus Temperature values almost coincide and points are not distinguishable in the graph since values are similar.

The product  $nT$  values extracted experimentally are in the range of 380 to 480 (kelvin). On the other hand, parameters extracted from simulation program are in the range of 253 to 333 (kelvin). In the theoretical approach values ( $nT$ ) depends

on temperature condition only, since for ideal case considered ideality factor is theoretically unity ( $n=1$ ). Thus, an increase in temperature will increase proportionally the product  $nT$  according to temperature value, while it will be unaffected to irradiance changes.

The value of  $nT$  is found to be different in both cases presented, comparing experimental and theoretical approach on average 140 (Kelvin) difference is observed. Saturation current changes in order to compensate. The saturation current for the transistor is approximately five orders of magnitude bigger than the saturation current of the solar cell in PC1D, in order to anticipate differences in the product  $nT$ .

Performing non-linear interpolation in Matlab the figure 5.32 was obtained that gives estimation of intermediate values of  $G$  for different insolation and temperature conditions. An example is provided i.e. insolation  $X=700 \text{ W/m}^2$ , temperature  $Y=283 \text{ kelvin}$  ( $10^\circ\text{C}$ ),  $G$  is estimated to be  $Z=1.066$ . Conducting the same experiment  $G$  was measured to be 1.07, with 0.37% deviation from the estimated value.

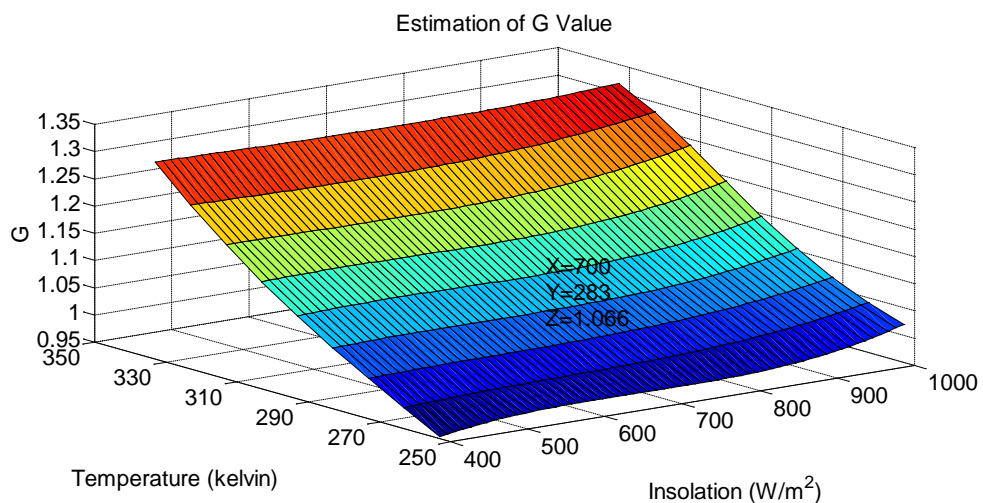


Figure 5.32. Non-linear interpolation for estimating  $G$  value.

## 5.9 Discussion

The functionality of the simulator, user event handling, control and measurement are direct interlink to the personal computer.

The cost of the system implemented herein apart of the cost of the personal computer is no more than £230. That includes one artificial solar cell,

motherboard, measurement system and microcontroller. A second artificial solar cell will increase the cost approximately by £40 and up to 9 artificial solar cells can be used. Solar emulator described in [124] is based on a precision BK9153 power supply with maximum output voltage 60V and maximum current 9A. The cost of this device is £1300 approximately. The cost of the LED based solar emulator system designed in [131] costs around £40k as estimated by the designer of the prototype, since it is based on functionality of several costly items of equipment. Finally, SunaPlayer [133] cost is about \$100 per unit if manufactured in large quantities of 10K or above. It supports medium range systems with output currents up to 1.89A and voltage up to 9.8V.

SunaPlayer is using a pair of bipolar junction transistors (BJT) connected in a common collector configuration. In the proposed platform a single transistor is proposed in a common emitter configuration. Another difference is that SunaPlayer takes IV curves as input and emulates a solar cell. For every  $V_{be}$  an error is calculated and a controller iteratively reduces the error. In that means it selects an appropriate IV curve, stored in a card reader, from solar panel traces collected either experimentally or from datasheets. Also, generating IV curves for solar cells is out of the scope of the SunaPlayer.

The proposed programmable digitally controlled emulation solar system is based on a new transistor circuit model able to imitate solar cell behavior. It can be considered as a medium scale system, designed for measurements of maximum voltage up to 12V, according to the analog to digital converter utilized and maximum current that can flow through the boards is up to 1.5A, by changing resistor R4 value of the proposed current source in Figure 5.4.

The maximum resolution value of the digital to analog converter utilized is 152  $\mu\text{V}$ . A step value of 5 ( $5 \cdot 152\mu\text{V} = 760 \mu\text{V}$ ) was adopted, obtaining 1442 measurements to characterize accurately the whole I-V characteristic curve. The step value can be altered in the software to obtain more or less points along the I-V curve.

The methodology of parameter extraction has been analytically presented using statistical indicators to quantify fitting values instead of using an existing database. Characteristic I-V curves were plotted for 20 experiments conducted

covering a wide range of irradiance and temperature conditions demonstrating applicability of the system.

The system implemented does not require a light source for illuminating the test device. The cost price includes the implementation price and maintenance. Finally, the emulator is modular, so that PV cells can be connected in series or in parallel to further simulate a whole PV array system or even another artificial solar cell with different characteristics.

## 5.10 Conclusion

A system has been developed to emulate solar cell behavior under changing environmental conditions. The system works as reliable and accurately as intended. Rigorous testing has been carried out to demonstrate feasibility of obtaining I-V characteristic curves at different environmental conditions. The analysis of the prototype simulator system has shown that it has the potential to deliver good quality PV characteristics defined by PC1D. In principle this could be a real solar cell and can be extended to any given range of insolation and temperature. Even though this study is focused on silicon solar cell this can be extended to any type of solar cell (Ge, GaAs, InP etc.).

Placing two or three artificial solar cells in series opens the possibility for the development of a novel measurement method that can fully mimic behavior of multi junction – tandem or triple junction – solar cells in a fully programmable automated mode. The system developed would be able to mimic a solar cell in a controllable environment that is not affected by external factors. This allows repeatable conditions, to test PV equipment overall performance.

Use of this equipment with a maximum power point tracking device is described in Chapter 6.





## 6 Maximum Power Point Tracking Implementation

### 6.1 Introduction

This Chapter links the theoretical mathematical derivation of maximum power point presented in Chapter 3 to implementation and experimental testing using artificial solar cells described in chapters 4 and 5.

The aim of this Chapter is to investigate a new MPPT algorithm that can operate in any PV system, small or large scale by implementation using artificial solar cell mimicking small-scale systems, (i.e. suitable for charging Li-ion batteries). The proposed algorithm should maintain tracking over wide variations of illumination levels and the proposed algorithm should converge to the MPP with good tracking effectiveness and dynamic response.

Experimental comparison to different MPPT techniques available in the literature, is provided.

### 6.2 Portable Devices Self Charging

A large demand for portable, on-demand energy comes from consumer electronic devices like mobile phones, laptops, tablets, netbooks, and portable music players as analyzed in Chapter 1. The need for standalone devices, designed to work for long periods without a power supply is rapidly increasing. Energy harvesting and storage is one of the challenges facing mobile devices makers.

Typically a mobile device needs to be periodically charged via the electrical network. An alternative approach is a scheme where the mobile device generates some of its own power, thus reducing or even eliminating the need for numerous charging cycles.

Solar power generation has already been used in some portable devices. One example is the XO-1 laptop which is targeted at school children in rural areas where access is limited [165].

A few years ago, several cell phone manufacturers tried putting solar cells on the back of phones like the Samsung Crest [166] and Sharp Hybrid [167].

It is clear that due to rapid expansion of mobile communication there is a lot of interest towards generating electricity from the sun. In this Chapter a case study is examined of MPPT operation in small scale systems suitable for charging Li – Ion batteries of mobile phones. Today, lithium batteries are widely used [165] in mobile electronic devices.

Although, a Li – Ion battery has not been used in this study, the process of charging a Li – Ion battery has been considered. This has set a condition regarding the minimum voltage that should be as part of the mobile device section. A standard one cell Li – Ion battery has nominal voltage 3.7 V. A battery of 1000 mAh with recommended charging current by the manufacturer to be usually 1/10 of the capacity, thus 100mA. The Li – Ion battery is equivalent to a  $37\Omega$  load resistor according to Ohm's law. The closer available resistor value used in the implementation is  $39\Omega$  (figure 6.5).

For the energy harvesting system it is important to understand the voltage of the energy storage device. A common one cell lithium-ion battery has an open circuit voltage range of 3.7V to 4.2V. The maximum voltage of the cell is 4.2V and the nominal (average) voltage is 3.7V.

In this work, output voltage was aimed to be above 3.7V in order to be able to charge the battery. It has not implemented any charging circuit. Integrated circuit, such as MCP 73832 [168] can be used to charge a Lithium ion battery with input voltage range to be 3.75V to 6V. Although some additional circuitry may be needed to prevent collapse of the voltage rail.

### 6.3 Experimental System

The experimental system illustrated in Figure 6.1 is constituted by four main elements, the artificial solar cells, the dc to dc converter, the microcontroller and a Personal Computer (PC).

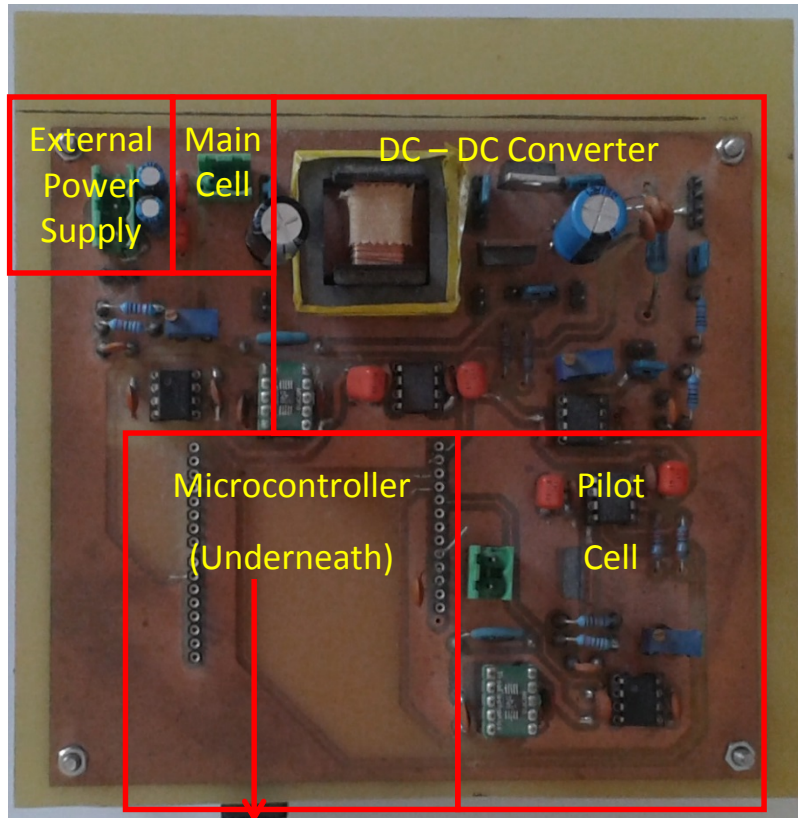


Figure 6.1. Experimental System.

Microcontrollers are popular for Maximum Power Point Tracking control over the last decade [87, 169, 76]. The main difference between the methods used is the proposed MPPT algorithm. The algorithm running in the microcontroller is based on the mathematical derivation proposed in Chapter 3 giving the advantage of working with an accurate mathematical model that can precisely predict the maximum power point, based on the 5 fitting parameters ( $I_{ph}$ ,  $I_o$ ,  $n$ ,  $R_s$ ,  $R_{sh}$ ).

System operation is analysed in Section 6.6. Apart from the microcontroller, which is described in section 6.7, a Personal Computer (PC) is utilized in this study running Matlab software program. The MPPT algorithm was developed and implemented in Matlab software environment. The algorithm has to determine A variable stated in equation (3.30). This equation contains exponential terms and Matlab software has been used for convenient purpose in order to solve this equation. The algorithm is based on the *fzero* command utilized in Matlab as a function file. The algorithm created by Van Wijngaarden Dekker, and others at the Mathematical Center in Amsterdam in the 1960s. It uses a combination of bisection, secant and inverse interpolation methods. The algorithm was first published by Dekker (1969) [170]. A description and analysis were given by Wilkinson [171]. The aim in this Chapter is not to implement the *fzero* algorithm,

but to examine the performance of the proposed methodology/technique. So, Matlab software program is a helpful/convenient tool in our study. Thus, there is an interaction between the microcontroller and a PC running Matlab software program.

Experimental testing is realized using artificial solar cells that is described in section 6.4. A pilot artificial solar cell is used for measuring open circuit voltage ( $V_{oc}$ ) and short circuit current ( $I_{sc}$ ), necessary to operate the algorithm. The microcontroller reads the data and transfers them through usb port to the PC. Matlab executes the algorithm, based on the mathematical derivation, finding the maximum power point and returns the optimum operating point to the microcontroller. Then the microcontroller will generate the PWM signal with the corresponding duty cycle. A second artificial solar cell at the input of a DC to DC converter is then driven to the desired maximum power point.

A switch mode DC-DC boost converter is utilized, that is described in section 6.5. Energy storage components such as inductor and capacitors control the energy flow from the solar module to the load continuously opening and closing a switch. Pulse Width Modulation drives the switch in such a manner to maximize artificial solar cell output power.

### 6.4 Pilot Artificial Solar Cell

In order to measure short circuit current ( $I_{sc}$ ) and open circuit voltage ( $V_{oc}$ ) instead of momentarily shutting down the power converter incurring to temporarily loss of power, a pilot cell is used to measure  $I_{sc}$  and  $V_{oc}$  as in [92]. In general, the pilot cell must be carefully chosen to closely represent the characteristics of the PV array. It can either be one cell on its own, or a cell of the PV array that is temporarily removed from the circuit. In this particular implementation the pilot solar cell is an independent artificial solar cell. Both pilot and test cells are built using electronic components and controls described in Chapter 4. The PV array comprises eight pilot cells connected in series.

#### 6.4.1 Pilot Artificial Solar Cell Electronic Circuit Configuration

The principle of operation for measuring  $V_{oc}$  and  $I_{sc}$  in the artificial pilot cell is illustrated in Figure 6.2.

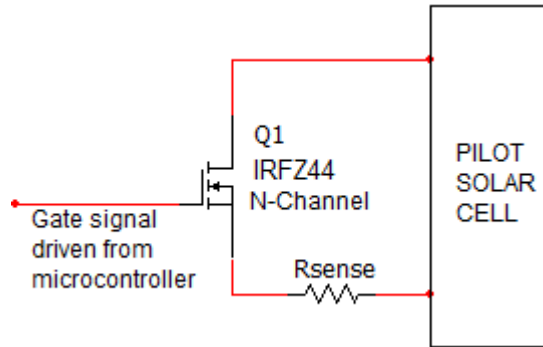


Figure 6.2. Basic Circuit for measuring  $I_{sc}$  and  $V_{oc}$ , using a MOSFET.

The basic circuit is utilized connecting the pilot artificial solar cell to a MOSFET (IRFZ44Z N-channel) which is used as a switch. The Gate signal is controlled by the microcontroller. When is low (0 Volt) the switch is open, thus the open circuit voltage of the pilot artificial solar cell is measured. When is high (5 Volt) the switch is closed, thus the short circuit current is obtained as a voltage drop across the sense resistor.

Analytically, the circuit consists of a sense resistor of 0.5 Ohm, in conjunction with a precision gain operational amplifier LT1991. A topology of gain 10 [158] is used enabling the microcontroller operating at 5V, to measure current up to 1 Amp.

A voltage divider (Figure 6.3) is used to measure the open circuit voltage. The maximum voltage that can be measured by the microcontroller is up to 5 Volt. By using a voltage divider ( $R_1 = R_2 = 10 \text{ k}\Omega$ ) the range increases to 10 Volt. A buffer is then placed and the signal is routed to the microcontroller.

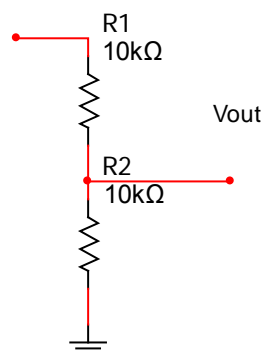


Figure 6.3. Voltage divider configuration.

For input voltage up to 10V, the output voltage will be 5V.

As the microcontroller might not have the drive capability to directly drive the gate of the MOSFET, MCP1407 buffer device is used to provide additional drive capability. Decoupling capacitors (1 $\mu$ F and 100nF) are recommended in the datasheet [172] and are placed close to the driver.

Electronic circuit connections are illustrated in Figure 6.4. The configuration is comprised of 3 main parts, the current sensing – measuring  $I_{sc}$ , open circuit voltage – measuring  $V_{oc}$  and driving the MOSFET. The pilot artificial solar cell is connected to J1 connector and an N-channel MOSFET (IRFZ44Z) is used as a switch.

Pins utilized on the microcontroller are, IO2, A1 and A2. The gate signal is controlled by the microcontroller IO2, a general purpose digital input/output pin2. Analog pin 1 (A1) and Analog pin 2 (A2) measure  $V_{oc}$  and  $I_{sc}$  respectively.

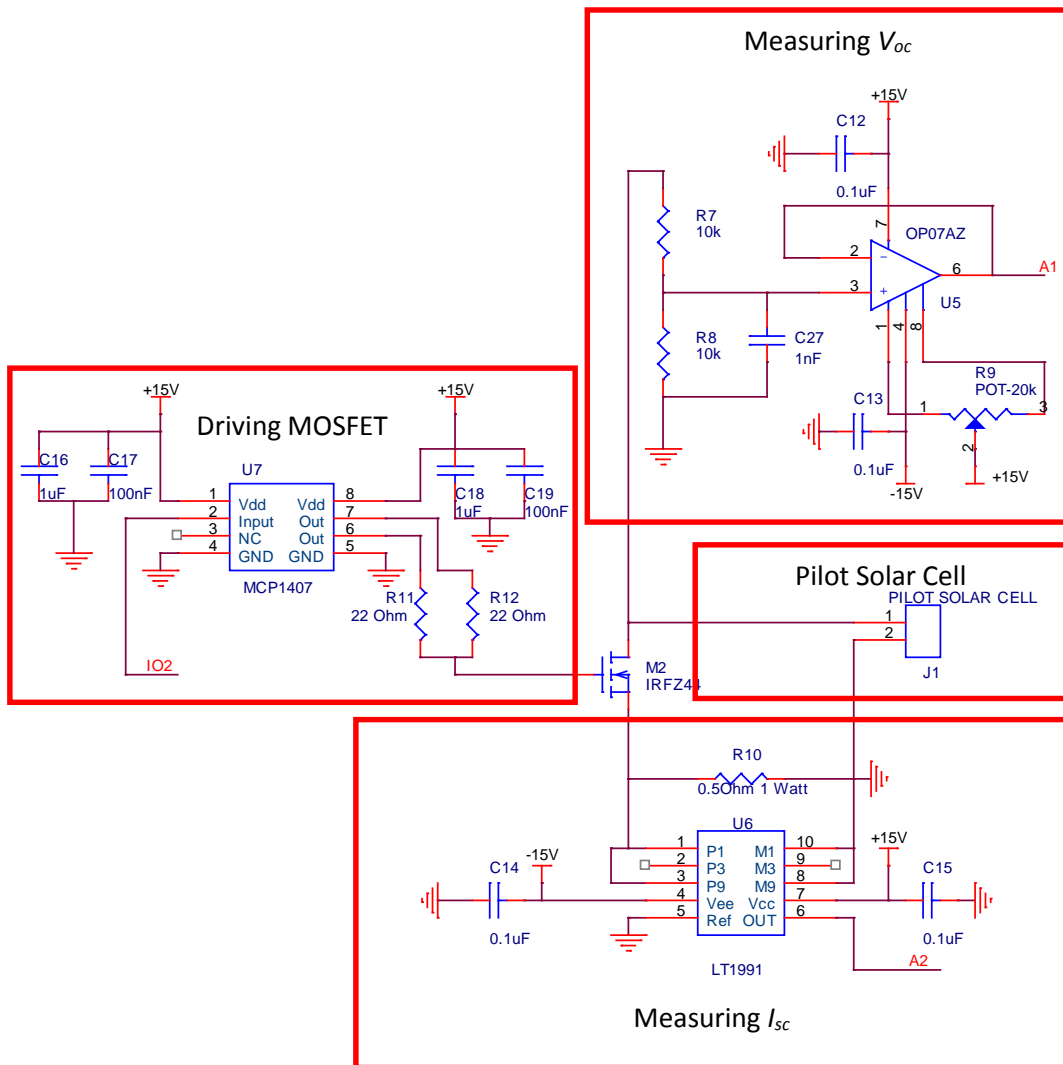


Figure 6.4. Pilot cell circuit configuration.

## 6.5 DC to DC Boost Converter

The switch-mode converter is the core of the entire supply. This allows energy at one potential to be drawn, stored as magnetic energy in an inductor, or in the electric field of the capacitor and then released at a different potential. This task is accomplished utilizing switch power techniques. Normally, the goal of a switch-mode power supply is to provide a constant output voltage or current. In power trackers, the goal is to provide a fixed input voltage and current, such that the array is held at the maximum power point, while allowing the output to match the battery voltage.

A switching converter consists of capacitors, an inductor, a diode and a switch. All these devices ideally do not consume power, which is the reason for the high efficiencies of switching converters. The switch is realized with a switched mode semiconductor device, an N-channel MOSFET. It is switched on and off by driving square wave signals at the gate. During the operation of the converter, the switch will be switched at constant frequency  $f_s$  3.91 kHz. A higher frequency would minimize inductance requirements and switching losses can be minimized by operating at relatively low switching frequencies.

Most experimental results reported in the literature are obtained using DC-DC converters working at some tens of kHz (up to 20 kHz). Spiazzi et al [173] have shown that PV panel reactive parasitic elements, like output shunt capacitance and series inductance can play a key role in determining the overall algorithm efficiency. At relative high switching frequency (300 kHz) the combined effect of the parasitic inductance and capacitance reduces the effectiveness of the MPPT algorithm to 73% from 96%, referring to Yan Hong Lim *et al* [106]. Trying to push the switching frequency toward hundreds of kHz there is a trade-off between efficiency and converter volume.

### 6.5.1 DC to DC Boost Converter Electronic Circuit Configuration

A circuit model is provided in Figure 6.5. The circuits used for measuring input and output voltage is similar to those described, at pilot solar cell for measuring  $V_{oc}$ . A voltage divider is used to increase the operational range from 0 to 10Volt, protecting the microcontroller from damage. A buffer is then placed and the input

voltage signal is routed to Analog pin 3 of the microcontroller, while the output voltage signal is routed to Analog pin 5 of the microcontroller.

The current flow through the PV Array, in the form of an artificial solar cell, placed at the input of the DC-DC converter is sensed using a sense resistor of 0.5 Ohm, in conjunction with a precision gain operational amplifier LT1991. It is a similar topology of gain 10, as described for the pilot artificial solar cell for sensing  $I_{sc}$  current, being able to measure current up to 1 Amp. The signal is driven to Analog pin 4 of the microcontroller.

A Pulse Width Modulation (PWM) signal is controlled by the microcontroller (digital I/O pin 9). As the microcontroller might not have the drive capability to directly drive the gate of the MOSFET, MCP1407 buffer device is used to provide additional drive capability. PWM frequency was adjusted by changing Timer1 TCCR1B register value, to obtain a switching frequency of 3.906 kHz. The optimum duty cycle is obtained by the algorithm executed in Matlab.



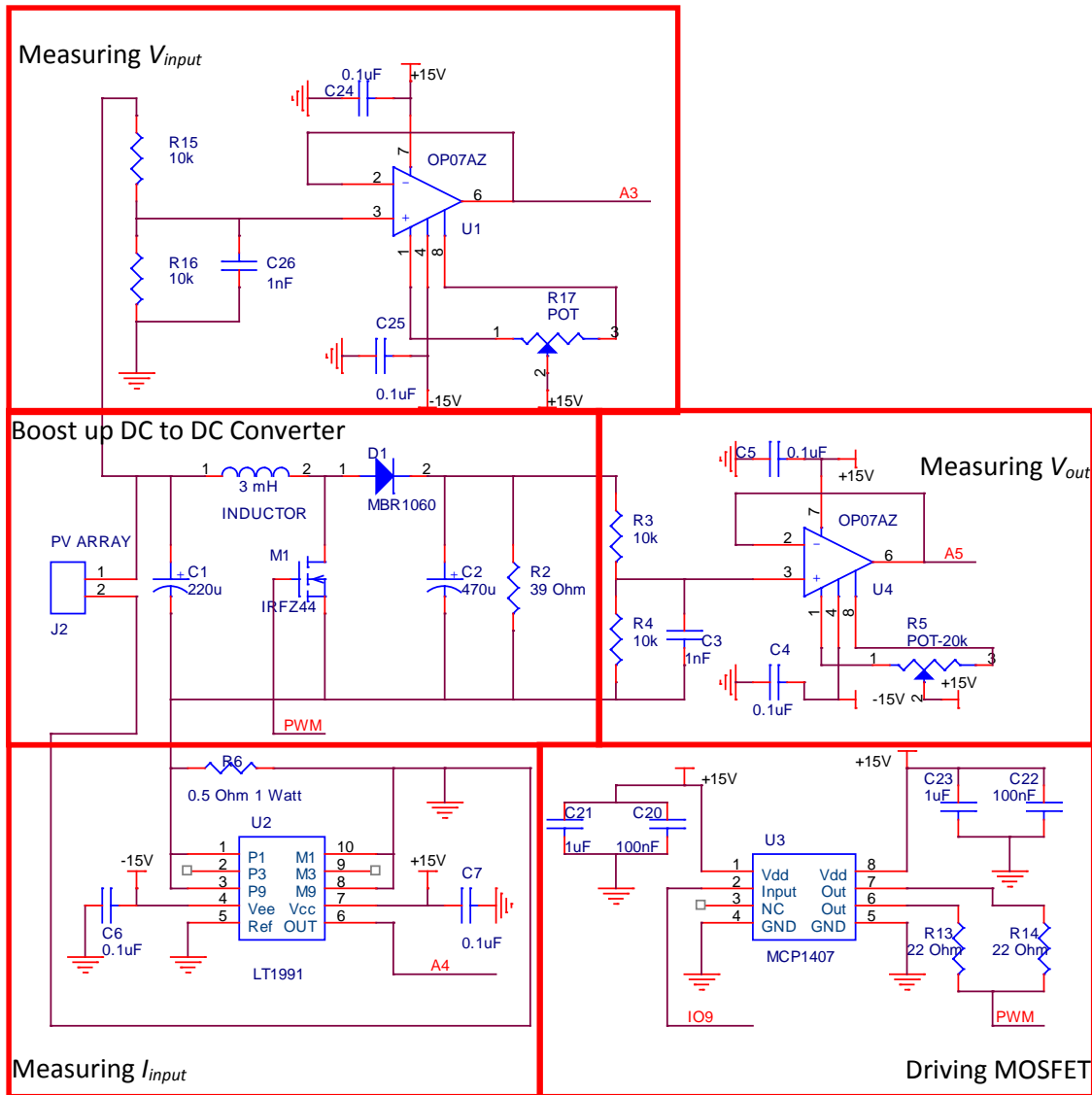


Figure 6.5. In detail circuit schematic.

## 6.6 System Operation

The system operation consists of 4 stages. During the first stage, numerical inputs of short circuit current ( $I_{sc}$ ) and open circuit voltage ( $V_{oc}$ ) are obtained by opening and closing a switch on the pilot cell. In the second stage, inputs are fed from the microcontroller to Matlab software program in order to compute the theoretical Maximum Power Point (MPP) according to the proposed algorithm. The third stage involves calculation of the error  $E$ , between the theoretical MPP and the actual operating point of the cell. A change in the duty cycle of the power converter is performed while calculating error  $E$ . When minimum error  $E$  has obtained the optimum duty cycle is found. Finally, this optimum duty cycle drives the power converter to operate at MPP. Controlling the duty ratio in this fashion

assures that the MPP will be continuously tracked, making the proposed method a true MPP tracker. As it will be demonstrated through experiments performed an accurate identify of MPP is determined.

Once the MPP is reached the operation of the PV array is maintained unless a change in irradiance or temperature is noted, in terms of  $I_{sc}$  and  $V_{oc}$  respectively. The algorithm computes the new MPP and the system is driven to the new MPP. Software code written in Matlab environment, along with comments is available in Appendix D.

## 6.7 Microcontroller

Arduino Mega has been utilized for controlling all necessary signals for the operation of the Solar Emulator Platform. Arduino uno is a second microcontroller employed, dedicated to the operation of the MPPT system developed.

The Arduino Uno is a microcontroller board based on the ATmega328. Most important features can be seen in Figure 6.6. It has 14 digital input/output pins (of which 6 can be used as PWM outputs), 6 analog inputs, a USB connection, a power jack and a reset button. [174]

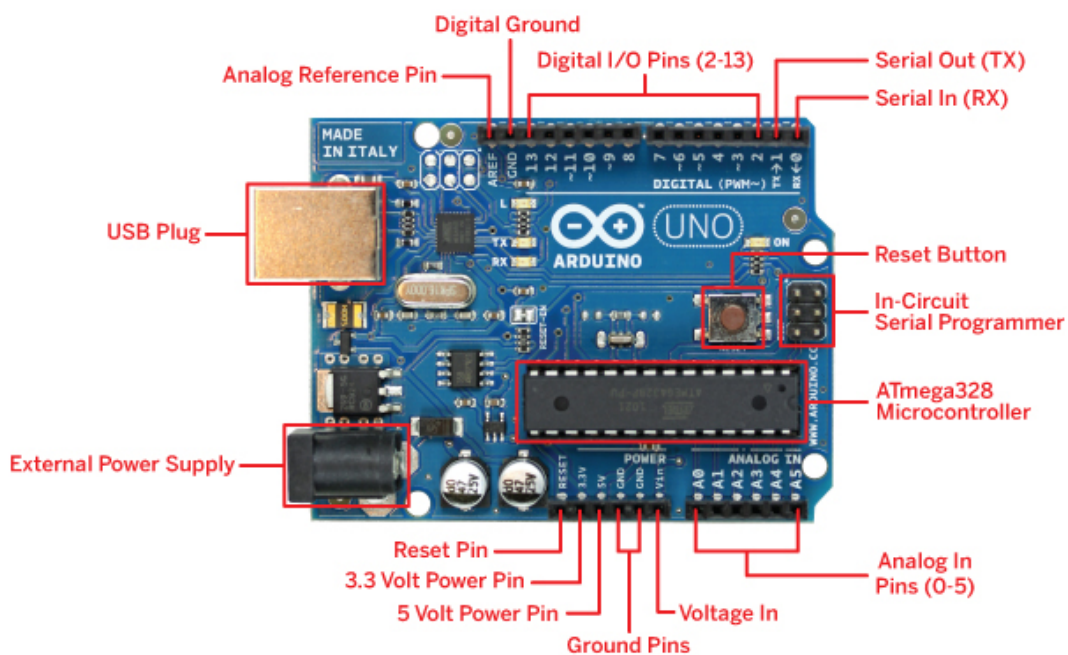


Figure 6.6. Arduino Uno microcontroller.

The microcontroller controls all the signals and more specific is used in the Pilot Cell circuit for measuring purposes of the open circuit voltage, short circuit current and driving the gate of the MOSFET. Also, in the DC–DC boost up converter circuit for measuring purposes of the input voltage, input current, output voltage and driving the gate of the MOSFET.

The Arduino Uno has a number of facilities for communicating with a computer and especially with Matlab software program. Open source code is provided by MathWorks (Giampiero Campa).

## 6.8 Evaluation, Experimental Results - Discussion

The artificial solar cells were based on parameters extracted from PC1D detailed in chapter 5. To evaluate the effectiveness of the method proposed 15 experiments were conducted. The response of the artificial solar cell tracking the MPP at different illumination levels and temperature are studied. Irradiance was altered from 0 to 1000 Watt/m<sup>2</sup>, 0 to 800 Watt/m<sup>2</sup> and 0 to 600 Watt/m<sup>2</sup> while temperature was varied from -20°C to +60°C in steps of 20°C.

Theoretical comparison is performed between data provided by PC1D software and data obtained executing the proposed mathematical algorithm analysed in Chapter 3. Also, experimental data of maximum power point (MPP exper.) are presented in Table 6.1 along with percentage convergence to experimental values ( $P_{max}$  exper.) obtained by the artificial solar cell. A small discrepancy between  $P_{max}$  theoretical values provided by PC1D software and  $P_{max}$  experimental ( $P_{max}$  exper.) given by artificial solar cell due to the small deviation of the two I-V characteristic curves as described in Chapter 4 and 5.

In order to evaluate the accuracy of the proposed method, the percentage relative error is defined as following:

$$\text{Percentage Relative Error} = \frac{\text{theoretical} - \text{experimental}}{\text{theoretical}} \cdot 100\% \quad (6.1)$$

The convergence is then calculated:

$$\text{Convergence} = 100\% - \text{Percentage Relative Error} \quad (6.2)$$

Deviation is calculated as percentage relative error. The higher the Convergence values the closer to the optimum operating point. An excellent performance is observed, with high tracking efficiency in terms of power convergence to the maximum power point. Deviation in percentage between the theoretical and experimental  $P_{max}$  is small in all cases studied.

Theoretically, an almost perfect match is observed between the Proposed Algorithm Methodology and PC1D simulator. The best case scenario convergence is 99.98% (600 W/m<sup>2</sup>, 60°C), while the worse 99.67% (800 W/m<sup>2</sup>, 60°C).

Running the proposed algorithm the maximum power point (MPP Exper.) reached, as well as convergence values are indicated in Table 6.1. Operation is shown to be close to experimental value of  $P_{max}$  throughout all experiments performed under changing atmospheric conditions, varying both irradiance and temperature. Output voltage varies from 3.75 to 5.63 Volt while duty cycle from 18.5% to 49.4%. The best case scenario convergence is 99.3% (1000 W/m<sup>2</sup>, 40°C), while the worse is 98.10% (1000 W/m<sup>2</sup>, 60°C).

Table 6.1. Experiments performed testing the proposed MPP methodology, varying insolation and temperature conditions.

Environmental Conditions		Theoretical			Experimental					
Insolat. (W/m <sup>2</sup> )	Temp (°C)	$P_{max}$	$P_{max}$		$P_{max}$	MPP (%)	Duty Cycle (%)	$V_{out}$ (Volt)		
		PC1D (Watt)	Proposed Algor. (Watt)	(%) Conv.	Exper. (Watt)					
1000	-20	0.9742	0.9717	99.74	0.977	0.28	0.9641	98.67	40.4	5.63
	0	0.8843	0.8859	99.82	0.883	0.14	0.8701	98.53	42.8	5.33
	20	0.7938	0.7956	99.77	0.8068	1.63	0.7992	99.05	43.5	5.05
	40	0.7035	0.7054	99.72	0.715	1.63	0.710	99.30	48.3	4.90
	60	0.6142	0.6161	99.69	0.6259	1.90	0.614	98.10	49.4	4.39
800	-20	0.8090	0.8105	99.81	0.8006	1.03	0.7882	98.45	28.6	5.28
	0	0.736	0.7376	99.78	0.7362	0.02	0.7294	99.07	32.1	5.02
	20	0.6623	0.6637	99.79	0.6681	0.08	0.658	98.48	35.7	4.76
	40	0.5885	0.59	99.76	0.600	1.95	0.595	99.16	41.6	4.46
	60	0.5152	0.5169	99.67	0.5253	1.96	0.5168	98.38	45.5	4.09
600	-20	0.6274	0.6285	99.83	0.6265	0.14	0.6171	98.50	18.5	4.67
	0	0.5717	0.5729	99.80	0.5703	0.24	0.5654	99.14	21.9	4.44
	20	0.5155	0.5168	99.76	0.518	0.48	0.5087	98.20	27.4	4.20
	40	0.4592	0.4601	99.80	0.465	1.26	0.460	98.93	25.9	3.99
	60	0.4031	0.4031	99.98	0.4112	1.99	0.405	98.49	33.3	3.75

Maximum power point against temperature for three different insolation levels studied and of maximum power point against insolation for five temperature values are plotted in figures 6.7 and 6.8.

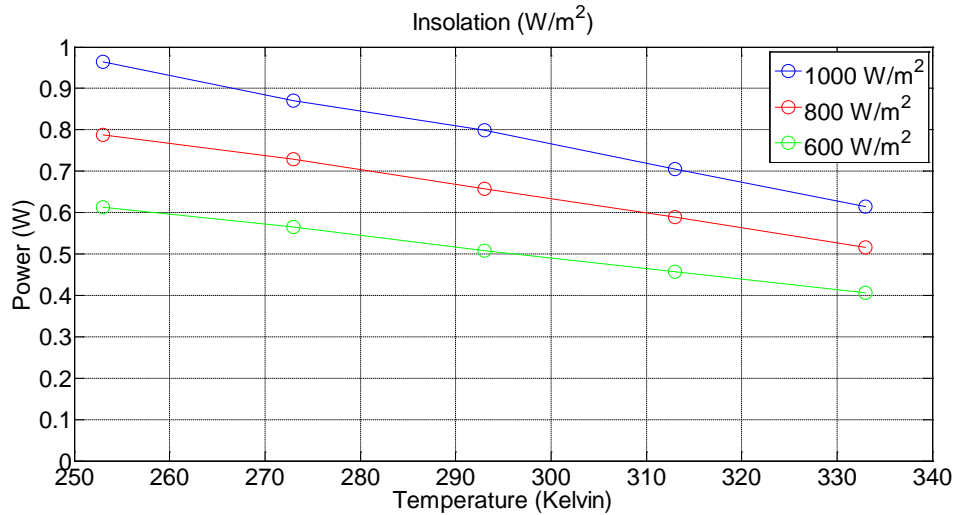


Figure 6.7. Maximum power point against temperature, for three insolation levels.

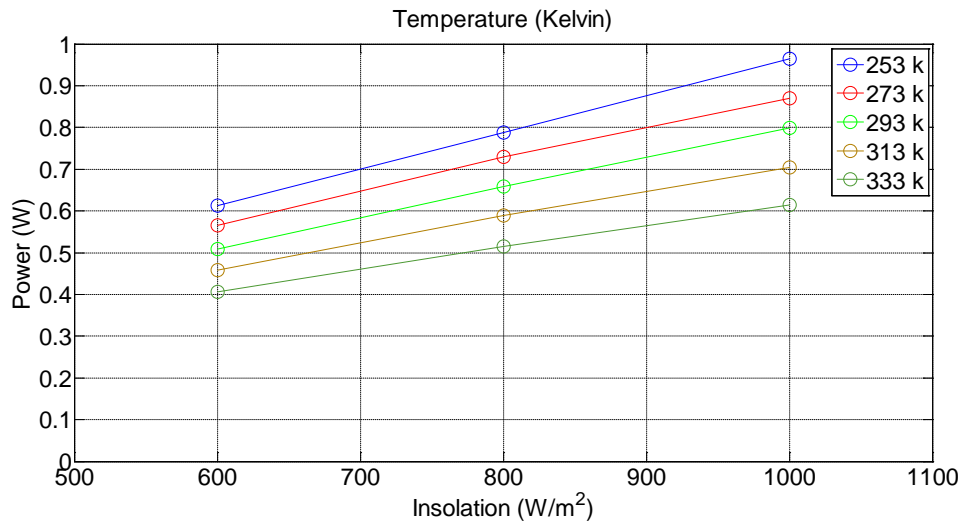


Figure 6.8. Maximum power point against insolation, for five temperature values.

Both diagrams illustrate that the higher the insolation level the higher the maximum power produced and it drops as temperature increases.

### 6.8.1 Comparison against FOCV and FSOC

The proposed method “Goose Waddle (GW)” developed and implemented is compared with fractional open-circuit voltage (FOCV) and fractional short-circuit current (FSOC) techniques. Efficiencies in operating at MPP for both FOCV and FSOC have been computed. The PV array technically never operates at MPP, but is approximated by equation (6.3) in fractional open-circuit voltage method and by equation (6.4) in fractional short-circuit current method. MPP is never

perfectly matched, but depending on the application of the PV system this can be sometimes adequately.

$$V_{mpp} \approx k1 \cdot V_{oc} \tag{6.3}$$

$$I_{mpp} \approx k2 \cdot I_{sc} \tag{6.4}$$

$k1$  and  $k2$  are constants of proportionality, and are between 0.70 to 0.80 and 0.9 to 0.98 respectively [99].

Since,  $k1$  and  $k2$  are dependent on the characteristics of the PV array being used [99, 66] they have computed beforehand by determining the ratio  $V_{mpp}/V_{oc}$  and  $I_{mpp}/I_{sc}$  for irradiance  $800 \text{ W/m}^2$  and temperature  $20^\circ\text{C}$ . The constants of proportionality were found  $k1 = 0.728$ ,  $k2 = 0.928$  and they were kept constant throughout all experiments for FOCV and FSCC techniques examined.

In order to realize an analysis of the performance of the three different MPPT techniques, they are experimentally compared taking into account three different irradiation diagrams (Figure 6.9). The first one, Case 1, is characterized by high irradiation levels of  $800\text{-}1000\text{-}800 \text{ W/m}^2$  with a time of 30 sec. The second one, Case 2, with medium-high-medium irradiation levels of  $600\text{-}1000\text{-}600 \text{ W/m}^2$  with a time of 30 sec. Finally, the third one, Case 3, with low-medium-low irradiation levels of  $400\text{-}600\text{-}400 \text{ W/m}^2$  with a time of 30 sec. The temperature in all cases is  $40^\circ\text{C}$ .

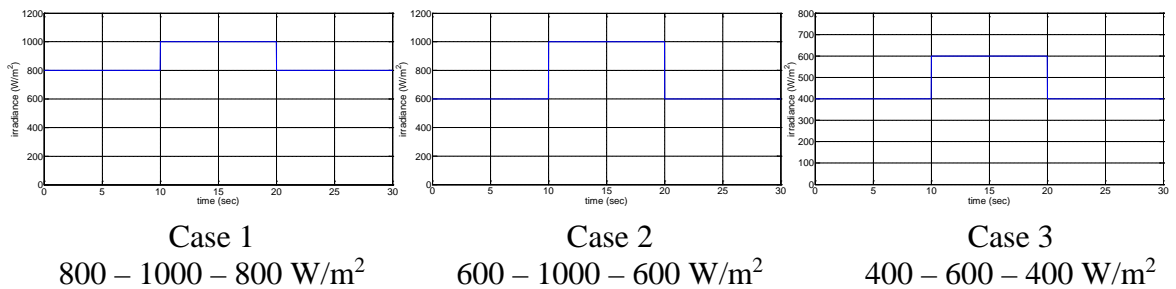
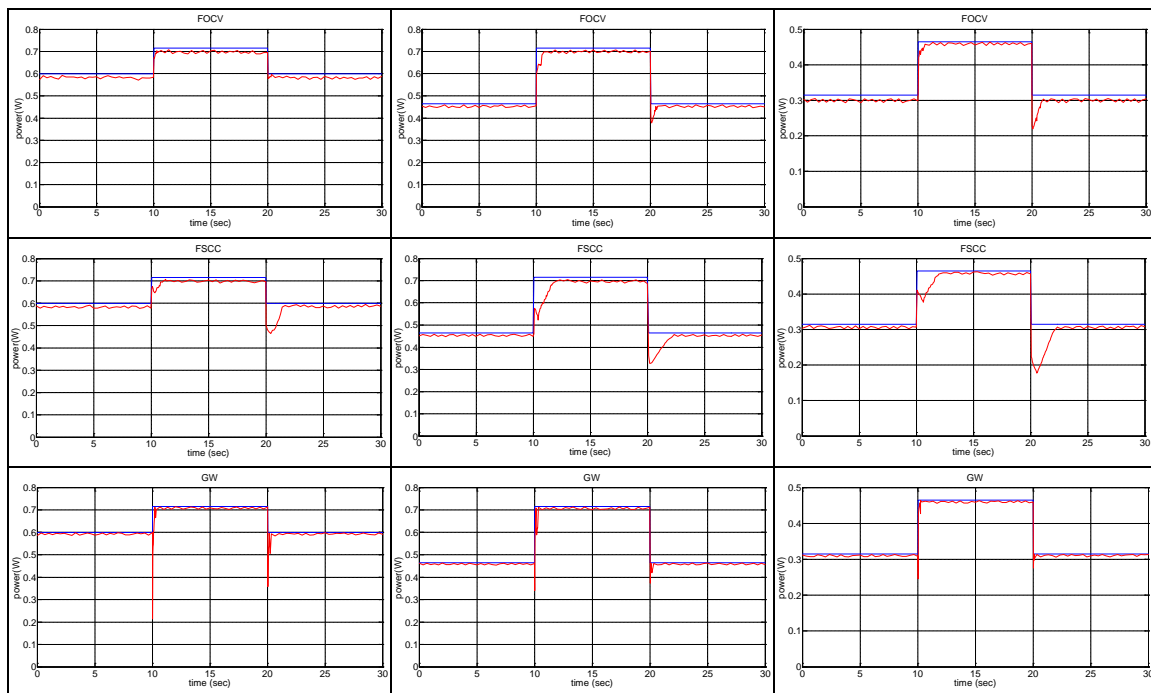


Figure 6.9. Irradiation diagrams of cases 1, 2 and 3.

Figure 6.10 shows the power generated (red line) from the artificial solar cell with the same converter configuration and different MPPT techniques, namely FOCV, FSCC and Proposed method (GW), in three cases under examination. The diagrams also show the ideal power (blue line), obtained using an ideal MPPT technique that it is equal to the maximum power that the artificial solar cell can

produce and it can be considered as a qualitative reference to compare tests results.



Case 1

Case 2

Case 3

800 – 1000 – 800 W/m<sup>2</sup>

600 – 1000 – 600 W/m<sup>2</sup>

400 – 600 – 400 W/m<sup>2</sup>

Figure 6.10. Power generated in all cases by different MPPT methods (red line) and ideal MPPT method (blue line).

The evaluation of the algorithms performance is based on the power measurement valuating the total energy produced during the same time.

Table 6.2. Energy generated as function of MPPT technique and irradiance input.

Insolation (W/m <sup>2</sup> )	Theoretical Energy (J)	FOCV (J)	FSCC (J)	GW (J)
800-1000-800	19.15	18.62	18.53	18.89
600-1000-600	16.45	15.97	15.73	16.21
400-600-400	10.95	10.53	10.46	10.79

Percentage efficiencies of the above experiments are summarized in the Table 6.3.



Table 6.3. Percentage efficiencies of FOCV, FSCC and GW.

Insolation (W/m <sup>2</sup> )	FOCV (%)	FSCC (%)	GW (%)
800-1000-800	97.24	96.76	98.65
600-1000-600	97.10	95.65	98.53
400-600-400	96.19	95.56	98.58

As is evident in table 6.3 the GW is superior to the other FOCV and FSCC. This can be explained by the fact that FOCV and FSCC are considering open circuit voltage or short circuit current, as an approximation to the MPP and they are not operating as true MPP tracking techniques. In that means, both algorithms loose a lot of valuable information - parameters of the I-V characteristic curve. On the other hand, the proposed algorithm is a true MPP tracker, considering the whole I-V characteristic curve with model parameters ( $I_{ph}$ ,  $I_o$ ,  $n$ ,  $R_s$ ,  $R_{sh}$ ,  $T$ ) improving the performance. Proposed algorithm indicates small divergence compared to theoretical values. At all cases considered convergence is higher than 98.53% and GW exhibits high performance independent of irradiation levels. On the contrary, FOCV and FSCC efficiency drops as insolation level decrease.

For different insolation values convergence time in seconds is presented in table 6.4 for all algorithms studied. Insolation in each of them is splinted in two transition cases.

Table 6.4. Time to reach steady state condition in each algorithm studied.

Insolation (W/m <sup>2</sup> )		FOCV (sec)	FSCC (sec)	GW (sec)
800-1000-800	800-1000	0.290	1.25	0.257
	1000-800	0.330	1.42	0.246
600-1000-600	600-1000	0.520	1.95	0.254
	1000-600	0.568	2.15	0.168
400-600-400	400-600	0.752	2.02	0.251
	600-400	0.810	2.23	0.160

The proposed algorithm overall requires less time to reach steady state. In terms of FOCV and FSCC, as irradiance level drops more time is required to reach steady state and converge at MPP. However, GW shows better transient response, even at low insolation level. Experiments presented above for the 3 techniques,

namely FOCV, FSCC and the proposed algorithm (GW) are characterized as F/M (fast to medium), M (medium) and F (fast) respectively according to table 6.4.

Similar, experiments have performed in [88, 90]. More specific, experiments presented in [90] refer to irradiation level 441 – 587 – 441 ( $\text{W/m}^2$ ). The solar simulator used in [90] is realized by using both incandescent and halogen lamps. Combining the lamps in the system examined the particular irradiation levels were obtained. In [88] simulation only in Matlab was performed to irradiation level 800 – 1000 – 800 ( $\text{W/m}^2$ ) and separately 600 – 1000 ( $\text{W/m}^2$ ), 1000 – 600 ( $\text{W/m}^2$ ). Numerical results are summarized in Table 6.5 below.

Table 6.5. Percentage efficiencies of FOCV and FSCC. Adapted from [88, 90].

Insolation ( $\text{W/m}^2$ )	FOCV (%)	FSCC (%)
800-1000-800	95.28	93.30
600-1000, 1000-600	95.03, 94.73	91.36, 90.28
441-587-441	93.5	91

In [88, 90] is stated that in both FOCV and FSCC techniques require an additional static switch, for measuring PV open circuit voltage and PV short circuit current respectively, providing low energy supply. This is mainly due to power annulment during electronic switching. The efficiency of FOCV and FSCC techniques have improved in this work by adding the open circuit and short circuit switch to a pilot cell instead of the complete PV system connected to the DC to DC converter. This conclusion can be drawn comparing efficiencies of Table 6.3 against Table 6.5.

Concerning FOCV and FSCC presented in [90], the voltage or current reference value is refreshed every 3 sec through the open voltage or short circuit current measurement. For this measurement it is necessary 10 msec without power generation distinguishable at the diagrams as power drop.

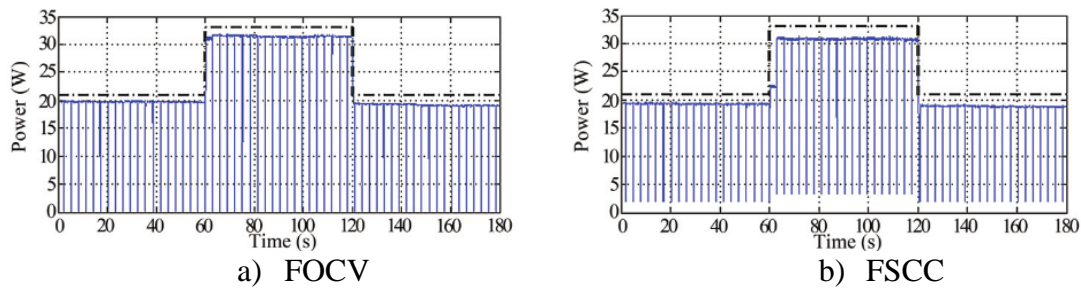


Figure 6.11. Power generated by the PV array by different MPPT methods (solid line) and ideal (dot-dashed line). a) FOCV and b) FSCC. Reproduced from [90].

In this work, as it can be seen in figure 6.10 there is no power annulment during electronic switching, since a pilot solar cell has been utilized. For both FOCV and FSCC duty cycle variation is 0.78%. The increment size determines how fast the MPP is tracked. The small duty cycle variation decreases the speed of the algorithm dynamic behavior and the system shows poor dynamic response, but it increases the precision in reaching MPP. Fast tracking can be achieved with bigger increments but the system might not operate exactly at the MPP and oscillate about it instead; so there is a trade-off.

On the other hand, GW starts with a large step 3.9% of duty cycle. A smaller step is adopted toward MPP. This indicates that the algorithm offers a fast tracking in the first stage and finer tuning in the second stage. In details the algorithm operation is described in section 6.8.1 (“Transient Response”).

To complete our analysis a discussion about the cost of the MPPT techniques is presented. A good cost comparison can be made by knowing whether the technique is analog or digital, whether it requires software and programming and the number of sensors. Analog implementation is generally cheaper than digital, which normally involves a microcontroller that needs to be programmed.

After these considerations, the cost of FOCV and FSCC are characterized as L (Low) and L/M (Low/Medium) respectively, since only one sensor is required and as they do not require a microcontroller they are easy and cheap to implement algorithms. It is easier to measure voltage than current and the current sensors are usually more expensive.

Finally the proposed algorithm requires two sensors (voltage and current), and a microcontroller. This increases the cost and for these reasons is characterized as M/H (Medium/High).

Table 6.6 proposes a classification based on the analysis performed in this section summarizing main features of MPPT algorithms studied.

Table 6.6. Main features of MPPT techniques presented.

MPPT Technique	PV array dependent	True MPPT	Convergence speed	Analog or digital	Sensed parameters	Cost	Average Efficiency %
FOCV	Yes	No	F/M	Both	Voltage	L	96.84
FSCC	Yes	No	M	Both	Current	L/M	96
GW	Yes	Yes	F	Digital	Voltage, Current	M/H	98.58

### 6.9 Oscilloscope Characteristic Waveforms

Waveforms obtained from the oscilloscope at various points of the DC to DC converter are presented in this section. The experiment studied is for Irradiance  $800 \text{ W/m}^2$  and Temperature  $40^\circ\text{C}$ .

The gate of the MOSFET is driven with 15V pk-pk square wave signal (figure 6.12). The duty cycle is 41.6% and the frequency is 3.91 kHz (period  $255\mu\text{s}$ ).

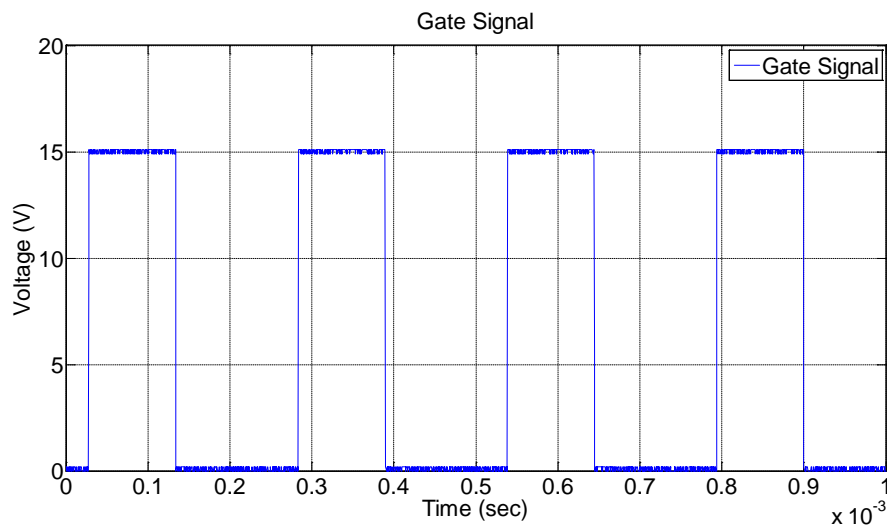


Figure 6.12. Square wave gate signal in the MOSFET of dc-dc converter.

The input voltage (figure 6.13) is 3.12 V. The output voltage is stable, having a value of 4.46 V (Figure 6.14).

Figure 6.13, shows the input voltage, the voltage across the coil which varies from  $V_{in}$  to  $V_{in} - V_{out}$  and the voltage across the drain to source of the MOSFET which varies from 0 to  $V_{out}$ .

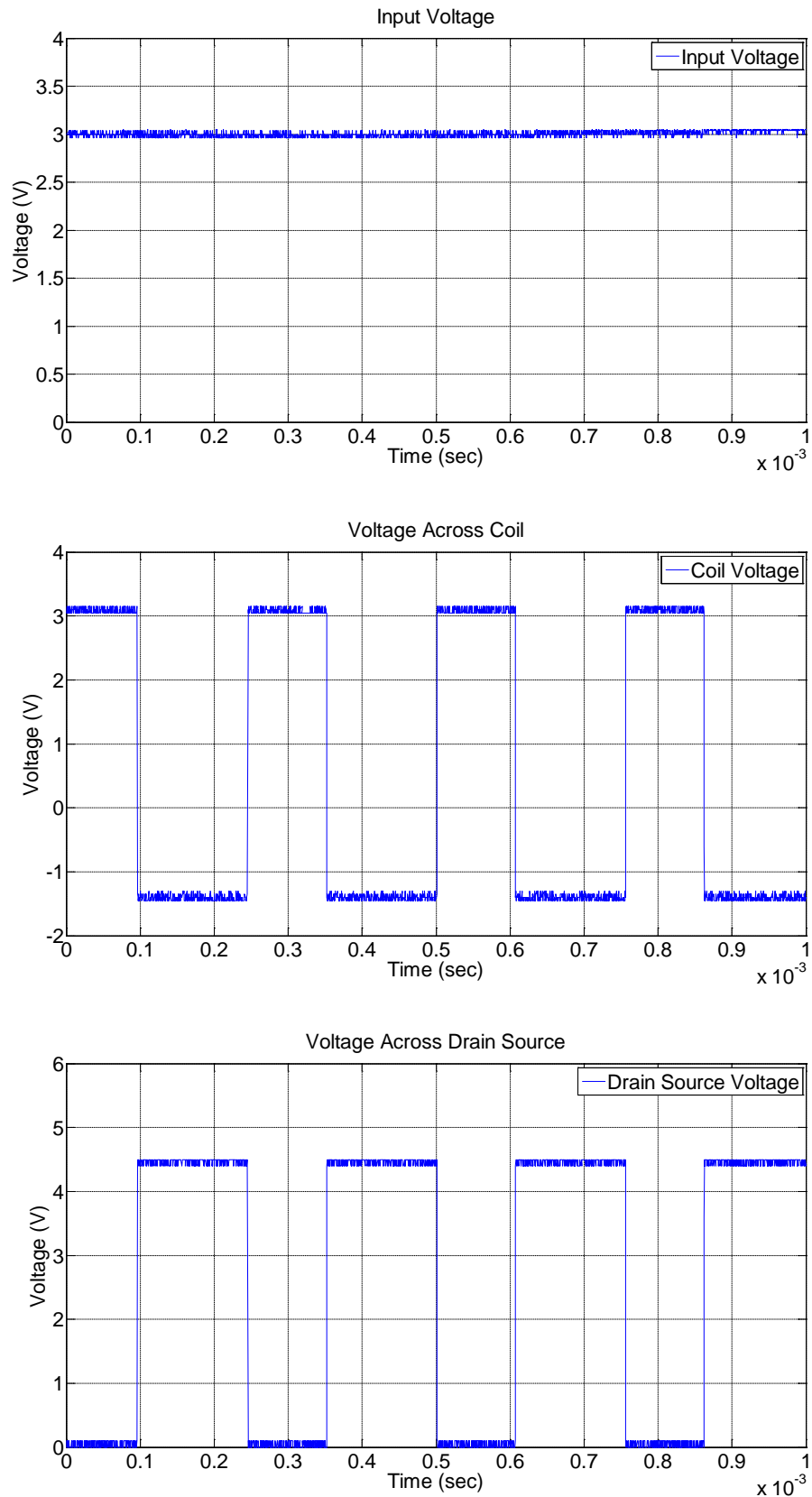


Figure 6.13. Input voltage, voltage across coil and voltage across drain source.

Figure 6.14, shows the voltage across the drain to source of the MOSFET which varies from 0 to  $V_{out}$ , the voltage across the diode which varies from 0 to  $-V_{out}$  and the output voltage.

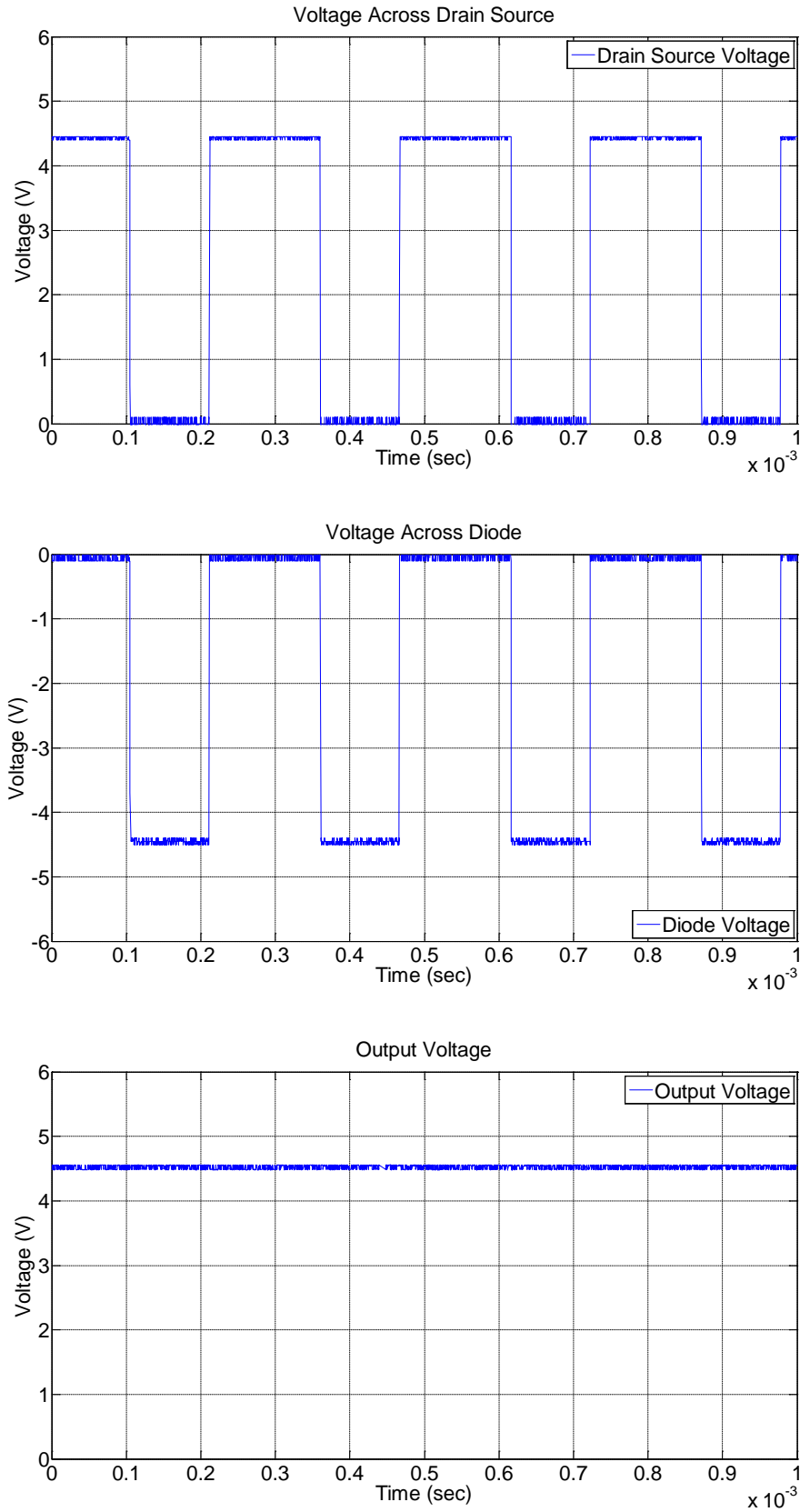


Figure 6.14. Drain-Source voltage, voltage across the diode and output voltage.

All waveforms captured are in accordance to theory presented in Chapter 2.

### 6.9.1 Transient Response

In this section transient response of the system is presented and MPPT algorithm proposed is analysed in more detail. Figure 6.15 illustrates a change of insolation from  $1000 \text{ W/m}^2$  to  $800 \text{ W/m}^2$  at  $40^\circ\text{C}$ . The characteristic input current is obtained across the sense resistor ( $0.5 \text{ Ohm}$ ), thus the current flowing through the circuit is doubled, when the steady state condition has reached. The input voltage is  $3.12 \text{ V}$ , while the power produced is the product of current time's voltage, and has half the magnitude.

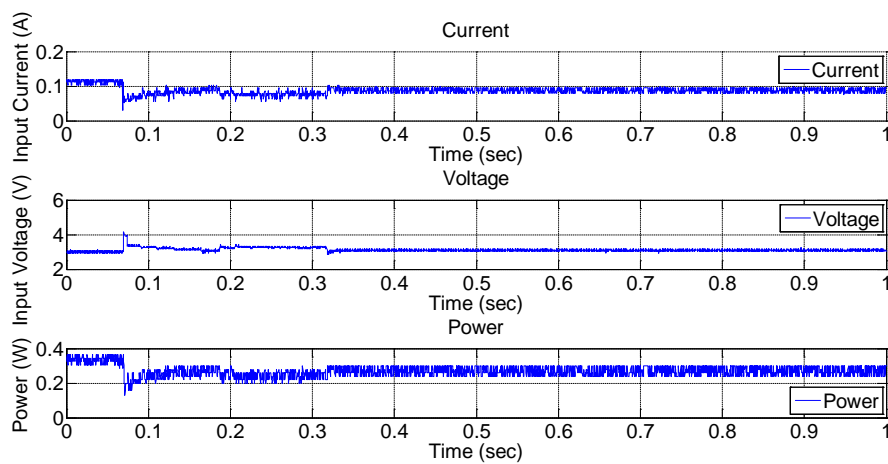


Figure 6.15. Transition from  $1000 \text{ W/m}^2$  to  $800 \text{ W/m}^2$  at  $40^\circ\text{C}$ . Time response 246.5 msec. Characteristics of input current, voltage and power produced.

The initial duty cycle is set to 7.8 % (20· minimum resolution, where minimum resolution is 0.39%). The duty cycle increases rapidly with a large step, 3.9%. Error ( $E$ ) is calculated between theoretical power at MPP according to the accurate proposed algorithm and actual power in the operating point of the cell. Also, the derivative of power is calculated, while derivative of power is greater or equal to zero, the operating point is to the left hand side of MPP in the P-V characteristic curve (Figure 6.16). When the derivative of power becomes negative, operation point has passed MPP and moved to the right hand side of the P – V characteristic curve.

Depending on the step value of the duty cycle, there might be a case where power at point B is greater than power at point A, although MPP has passed and operation point is at the right hand side of the MPP. The actual decrease in power

(derivative  $dP < 0$ ) will become apparent when operating point has reached point C. For this reason the duty cycle returns two values back in the algorithm making sure operating point is on the left hand side of the P-V characteristic curve. A smaller step of the duty cycle is now adopted, which is half of the above step. The error is calculated between optimum power value computed from the accurate mathematical model and actual power measured at the operating point. This procedure is repeated i.e. each time operation point passes to the right hand side it returns back to the left hand side by taken further half of the duty cycle value, calculating error ( $E$ ) during the whole procedure. When minimum error ( $E$ ) has obtained the optimum duty cycle value has reached. At the end, optimum duty cycle drives the gate of the MOSFET, such as input current and voltage operates the system at or near the MPP.

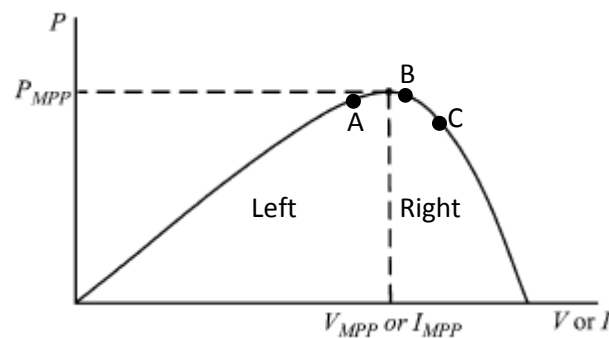


Figure 6.16. Characteristic PV array power curve.

In this way the algorithm offers fast tracking in the first stage calculating the derivative of power helping to identify where the operating point lies along the P-V characteristic curve. In the second stage finer tuning is succeeded calculating error between theoretical maximum power point according to the proposed algorithm and power at the actual operating point. The procedure described is based on the minimum error for finding the optimum duty cycle.

When minimum resolution in duty cycle step value (0.39%) is reached the algorithm “breaks” returning the value of minimum error along with the optimum duty cycle. It is not necessarily the optimum duty cycle when duty cycle step has its minimum resolution value, but when minimum error has computed during the procedure. A flow chart of the algorithm can be seen in figure 6.17.

A small value of permitted error is proposed (10 mV change in terms of  $V_{oc}$  and 1.5 mA change in terms of  $I_{sc}$ , instead of 0) to improve the sensitivity and eliminate the steady state error as in [86].



Using this methodology, the operating point of the PV array does not oscillate around MPP, as in P&O and Hill-Climbing algorithms, giving rise to wasting amount of the available energy, since the algorithm stops modifying the operating voltage (in terms of duty cycle) when the correct value has reached as the IncCond algorithm.

Also, oscillation is avoided compared to [106] where the technique followed is based on location of MPP at the point where  $dP/dV=0$ . It is stated in [106] that it is impossible to reach MPP exactly because if  $V=V_{mpp}$ , the switch in the DC to DC converter opens making  $V$  to increase but this subsequently leads to the switch closing making  $V$  to decrease. Thus, the voltage wanders around  $V_{mpp}$ .

Time response to converge at the MPP is 0.2465 seconds. The energy if the system was operating continuously for 0.2465 seconds at MPP would be  $W_{max} = 1.9908$  Joule. During the procedure for finding the MPP is produced  $W_{prod} = 1.6498$  Joule. Thus, there is a loss of  $W_{loss} = 0.3404$  joule (17.1% loss).

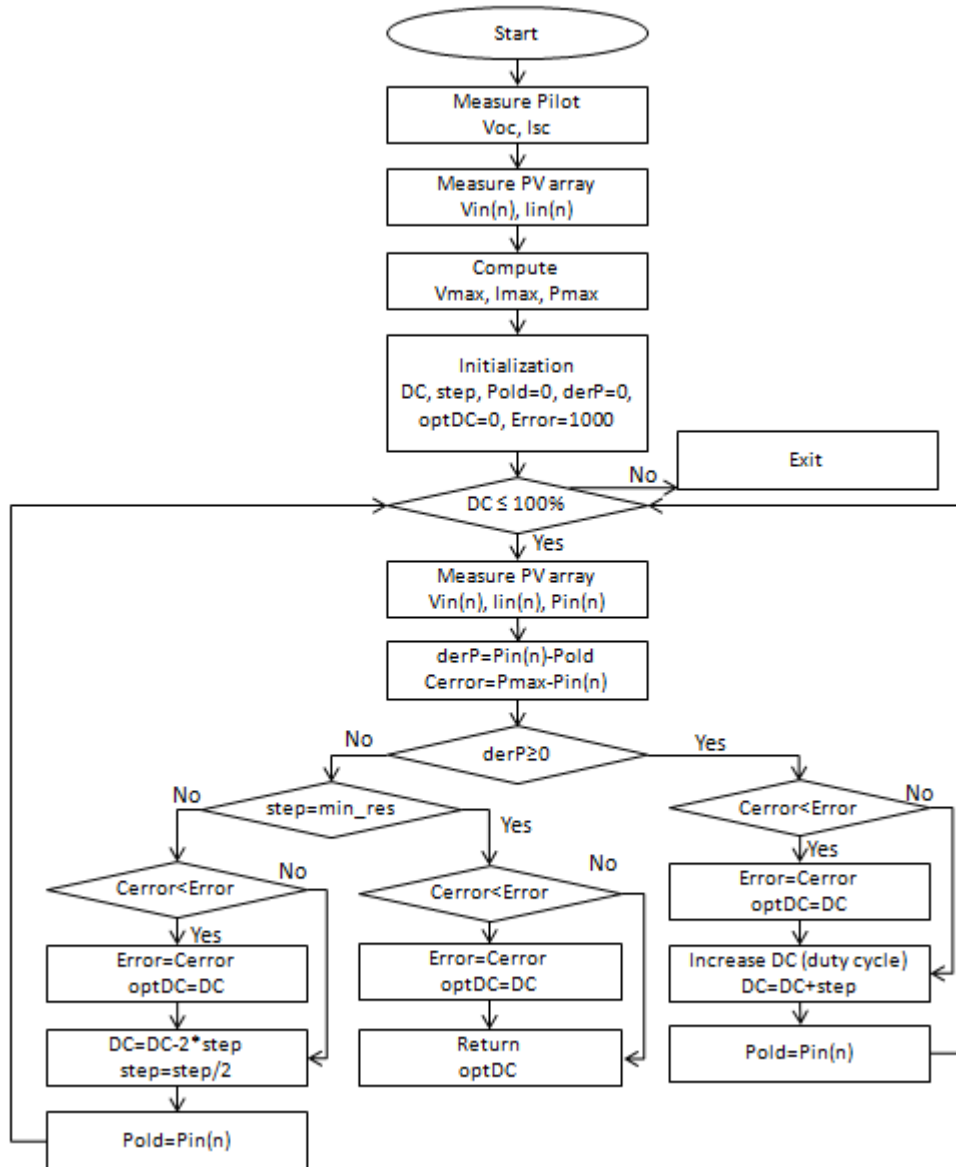


Figure 6.17. GW flow chart.

## 6.10 Estimating Inductance and Capacitance Values

Values of inductor and output capacitor are calculated below:

To find the value of *inductance* required, equation (2.56) is used, derived in Chapter 2. A good estimation for inductor ripple current [175, 176] is 20% to 40% of the input current (measured 186.8 mA). Considering the average value (30%) for inductor ripple, knowing that the operating frequency is 3.91 kHz (i.e.  $T_s=255.3 \cdot 10^{-6}$ sec), duty cycle 41.6% and input voltage 3.12V it is:

$$L = \frac{V_{in}DT_s}{2\Delta i_L} = 2.95mH \quad (6.5)$$

Inductor value of 3 mH was selected.

The *output capacitance* was calculated according to equation (2.60), derived in Chapter 2. Assuming that the output voltage ripple is 1% of its dc value measured 4.46 V, output current value of 0.1143 A (according to Ohm's law for 39 Ohm resistor) and for effective series resistance of the capacitor 0.1 Ohm, the capacitor value is:

$$C = \frac{I_o D T_s}{\Delta V_{out} - I_{in} ESR} = 468.33 \mu F \quad (6.6)$$

A capacitor value of 470  $\mu F$  was selected.

### 6.11 Calculating Converter Losses

Converter losses are calculated analytically, based on equations 2.61 through 2.75, described on section 2.9.3.7 "Power Losses and Efficiency of Boost Converter for Continuous Conduction Mode (CCM)".

*Conduction loss* of the MOSFET is given by equation (2.63), where  $r_{DS}$  is the MOSFET on-resistance ( $11.1 \cdot 10^{-3}$  Ohm) and  $I_{Srms}$  is the switch current rms value given by equation (2.62):

$$I_{S_{rms}} = \frac{I_o \sqrt{D}}{1-D} = 0.1262 \text{ A} \quad (6.7)$$

Thus,

$$P_{rDS} = r_{DS} I_{Srms}^2 = 0.176 \text{ mW} \quad (6.8)$$

*Switching loss* of the MOSFET is given by equation (2.64). Thus:

$$P_{sw} = f_s C_o V_o^2 = 0.01866 \text{ mW} \quad (6.9)$$

Where  $f_s$  is the switching frequency,  $C_o$  is the MOSFET output capacitance according to the datasheet ( $240 \cdot 10^{-12}$  F) and  $V_o$  is the output voltage.

Hence, the total *power dissipation* in the MOSFET is:

$$P_{FET} = P_{rDS} + P_{sw} = r_{DS} I_{Srms}^2 + f_s C_o V_o^2 = 0.1946 \text{ mW} \quad (6.10)$$

The overall *diode conduction loss* is given by equation (2.71), where, diode power loss due to  $R_F$  is  $P_{RF}$  and power loss associated with the forward bias voltage  $V_F$  of the diode is  $P_{VF}$ .

Diode current is given by equation (2.67), so for  $I_o = 0.1143$  A it is:

$$I_{Drms} = \frac{I_o}{\sqrt{1-D}} = 0.1495 \text{ A} \quad (6.11)$$

Forward bias voltage  $V_F$  of the diode MBR1060 is 0.3V according to the datasheet [177] for a current of 0.1143 A and resistor  $R_F$  is 25mOhm [178].

Thus, the overall *diode conduction loss* is,

$$P_D = R_F I_{Drms}^2 + V_F I_o = 34.84 \text{ mW} \quad (6.12)$$

The *inductor loss* is given by equation (2.74), where:

$$I_{Lrms} = I_I = 0.1868 \text{ A} \quad (6.13)$$

and the *inductor resistance* is:

$$r_L = 0.5 \text{ Ohm} \quad (6.14)$$

Thus,

$$P_{rL} = r_L I_{Lrms}^2 = 17.44 \text{ mW} \quad (6.15)$$

Power loss at the *current sensing resistor*:

$$P_{RES} = I_I^2 R_{sense} \quad (6.16)$$

where *sense resistor* value is:

$$R_{sense} = 0.5 \text{ Ohm} \quad (6.17)$$

Thus:

$$P_{RES} = I_I^2 R = 17.44 \text{ mW} \quad (6.18)$$

Summing up all the above and power losses in the boost up converter:

$$P_{LS} = P_{FET} + P_D + P_{rL} + P_{RES} = 69.91 \text{ mW} \quad (6.19)$$

Yielding the *converter efficiency* according to equation (2.83):

$$n = \frac{P_{in} - P_{loss}}{P_{in}} = 88\% \quad (6.20)$$

## 6.12 More Efficient MPPT Platform

This section focuses on consumption power required for the system to operate and discusses how to make more efficient energy usage. In this study use of an algorithm to achieve the highest power output of a photovoltaic panel as the input power source to the DC to DC converter has been explored. How the power consumed by the system could be reduced, but in the same time achieving correct performance of the system has also been considered.

In essence, the proposed method is based on a principle of mathematical computation. The mathematical equation contains exponential terms that has to be solved for determining the unknown variable. For this reason, Matlab software program was utilized running on a PC, powered by AC wall power. Average power consumed by a single laptop is about 35W [15]. Arduino board is a simple and ease way to interactive communicate with Matlab software through open source code. So, Matlab build in math functions give the ability to execute the required mathematical computations. The power consumption of Arduino Uno is approximately 250 mW.

A small solar cell device was considered in this particular work. PV power produced was approximately 310 mW in the high irradiation level scenario. It is clear that AC wall power required for the laptop as well as power required for the microcontroller to operate is much more than the produced power from the small sized artificially simulated solar cell.

The study presented in this Chapter has focused on proposing an efficient algorithm rather than an efficient platform. It is an experimental approach for research purpose. This is very much an experimental proof of concept lab prototype circuit, not an engineered product design. Technology implemented on a small device at experimental/research stage can have a huge impact as it is then implemented on a large scale.

In the production stage PC and Matlab will be replaced by a microcontroller unit (MCU) for computing and determining variable  $A$ . This could be done developing  $f_{zero}$  algorithm. An Algol 60 version (short for ALGOritmic Language 1960) with some improvements is given in [179]. A Fortran version, upon which  $f_{zero}$  is based, is in [180].

In the particular application a reasonable number for a computer program of 36 function evaluation are required to convergence as it has been computed in Matlab.

The  $f_{zero}$  algorithm and in extension the Matlab software program were utilized for convenience. The target was not to implement  $f_{zero}$  file function. The main objective was to study and proof that in the implementation level the proposed algorithm has high performance as theoretically proved in Chapter 3.

In a related concept, both cost and use of energy are important factors to control and be aware of in a MPPT system. Alternative options of control are available. A MCU PIC18F4620 [181] can be adopted. The integrated PWM module, ADC module and idle operation mode can make the design more flexible and practical.

The benefit of choosing a MCU (the particular family or any similar processor) is the relative low cost € compared to Arduino Uno board which cost about €25. The PC would not be any more necessary for mathematical calculation reducing further the cost and in the same time making the MPPT system portable. Aside from the cost of the processor and the PC, consumption power is reduced. Current consumption of the Microchip microcontroller is typical 2.5 mA according to [181] at 5 V, thus typical power consumption is 12.5mW. Also, I/O pin loading have an impact on the current consumption. This is the worse case scenario, since in the idle mode typical current consumption is 1.1 mA, thus power consumption is 5.5mW (at 5V voltage supply). The PIC needs to be active when there is a change in irradiance (in terms of  $I_{sc}$ ) or temperature (in terms of  $V_{oc}$ ) condition.

Concluding this section, it is clear that a cheaper processor could be used to achieve similar performance and conserve energy in terms of using a lower power consumption microcontroller and eliminating the use of the PC.

### 6.13 Conclusion

A novel technique for efficiently maximizing the output power of an artificial solar panel supplying a load under varying illumination conditions has been presented. It shows good tracking performance and in all cases better than two MPPT techniques (FOCV, FSCC). The algorithm has been tested in small scale systems for charging a Li-ion battery. Although testing has performed for a small scale systems, applicability of the proposed algorithm can be extended to larger scale systems without constraint.

The GW is basing its accuracy on a mathematical tool without prior knowledge of the  $V_{mpp}$  or  $I_{mpp}$ . Maximum power point has predicted with precision while the computation method is reliable showing excellent tracking performance with good dynamic response. It does depend on the PV array requiring knowledge of 5 fitting parameters. Requires a microcontroller than has to be programmed. So, it is a more expensive approach compared to cheaper analog version of MPP. Using this approach efficiency is improved significantly, and it operates as a true MPP.

In this Chapter has demonstrated that not only a MPPT algorithm can be tested but a system is built that allows in principle MPPT algorithms to be tested against each other. Also, the system can be used as a laboratory way of testing and assessing small algorithms of variety of cell technologies.





## 7 Conclusions and Future Works

### 7.1 Conclusions

For practical purposes the power delivered by a photovoltaic system always should be the highest it can be. This being the case, the most interesting operating point along the I-V curve is the maximum power point, in this regard five fitting parameters that support the basic single diode equivalent circuit is very appropriate for characterizing photovoltaic operation.

A new simple, elegant and low level calculation procedure for estimating the MPP of photovoltaic modules is presented. It requires digital computation and panel characteristic parameters ( $I_{ph}$ ,  $I_o$ ,  $n$ ,  $R_s$ ,  $R_{sh}$ ). In other available MPP approaches, such as P&O and IncCond, computation needs to be carried out but they are not dependent on the panel characteristics. In FOCV and FSCC methodologies the constant of proportionality has to be computed beforehand and for this reason they are dependent on the specific PV array. The MPP is never perfectly matched and both methodologies (FOCV and FSCC) are an approximation method.

Functionalization of the proposed technique has been studied on four different real photovoltaic modules by data provided from manufacturers or other researchers. Results indicate an efficient algorithm that provides reliable estimation of the MPP. The best case scenario has shown a divergence in  $P_{mpp}$  of 0.08% while the worst 0.84%. In all cases analysed in this study the results showed a negligible error, demonstrating the validity of the present approach. The proposed algorithm can be an accurate tool for prediction purposes of MPP.

The new method is examined for sensitivity, up to  $\pm 5\%$  deviation from its nominal values of the five fitting parameters ( $R_s$ ,  $R_{sh}$ ,  $n$ ,  $I_o$ ,  $I_{ph}$ ). The photocurrent ( $I_{ph}$ ) has the higher impact effect giving an error up to 5% from its nominal value, while other four fitting parameters give an error less than 1.5% on all four modules studied. This is apparent since the shape of the I-V curve changes greatly with variation of  $I_{ph}$ , which is highly dependent on solar radiation. That makes significant the accurate extraction of five fitting parameters that can minimize deviation from the MPP.

Two topologies, a basic and improved  $V_{BE}$  multiplier have been proposed in this work that can reliably model solar cell operation. However, the improved  $V_{BE}$  multiplier version is more flexible, to model photovoltaic cell being operated over a wide range of illumination and temperature conditions. Rigorous testing has been carried out to demonstrate the feasibility of obtaining I-V characteristic curves at different environmental conditions.

The applicability of the above circuit topology was demonstrated by utilizing a few more simple electronic circuit components in order to implement a digitally programmable solar emulator system. The analysis of the prototype emulator system “*DiceSol*” has shown that it has the potential to deliver good quality PV device measurements defined by simulation program PC1D with small *RMSE* ( $10^{-3}$ ). In principle this could be a real solar cell and can be extended to any given range of insolation and temperature. Even though this study is focused on crystalline silicon solar cell this can be extended to any type of solar cell (InP, GaAs etc.). The circuit may also be used in other systems as an arbitrary junction diode replica.

The flexibility in measurement conditions make the system a useful tool to do research in the laboratory more practically. This system that wholly depends upon controllable conditions of irradiance and temperature is very convenient for performing repeatable tests on photovoltaic inverters and maximum power point tracking devices in environmental conditions near to real time. At the same time, such a system can be programmed to work automatically and unattended for evaluation and testing DC/DC or DC/AC converters with or without MPPT. The cost of the system implemented herein is one the smallest among similar emulator solar systems presented, with no maintenance required.

Maintenance is referring to replacement of light bulb (due to limited lamp lifetime) or homogeneity adjustments of light output in solar simulators based on artificial light sources. Properties of the light bulbs are changing with age in both intensity and spectral distribution [127, 128]. In LED’s based simulators an unavoidable disadvantage is the degradation of LED’s throughout their lifetime [126]. Thus, it is necessary to check specifications and perform homogeneity adjustments (uniformity of light output over illumination area) increasing in this means operational/maintenance cost of solar simulator consisting of light sources.

Sunaplayer selects an appropriate IV curve, stored in a card reader, from solar panel traces collected either experimentally or from datasheets. Generating IV curves for solar cells is out of the scope of the SunaPlayer. On the contrast “*DiceSol*” can generate an IV characteristic curve upon suitable control of insolation or temperature conditions, in terms of  $I_{sc}$  or  $V_{oc}$ , without requiring a storage device.

In this thesis, the concept of the mathematical expressions for voltage, current and power at optimum operating point was successfully applied to a well-known DC–DC boost converter configuration. Tracking effectiveness was thoroughly studied, indicating good convergence to MPP under varying atmospheric conditions. Based on the parameters used, tracking effectiveness showed good static and dynamic performance. At all cases considered (low, medium or high irradiation levels) convergence was higher than 98.53%. Reacquisition of tracking was achieved rapidly; convergence time on average is 220 msec.

A comparison is performed against fractional open circuit voltage and fractional short circuit current highlighting the differences. Experimental results show the performance of the proposed method to be better than the two improved MPPT techniques (FOCV, FSCC). On average efficiency of FOCV and FSCC are 96.84% and 96% respectively. Also, it has been observed that as irradiance drops, more time is required to reach steady state. In cases of FOCV and FSCC, about 0.8 sec and 2.23 sec is required respectively to converge at MPP. Goose Waddle method shows better overall system response even to low irradiance level. The best case scenario is 0.160 sec while the worse 0.257 sec, indicating superiority of the proposed algorithm in both dynamic system response and performance.

FOCV and FSCC control methods technically never operate at MPP. They are not true MPPT techniques compared to the proposed method. Depending on the PV system application this can sometimes be adequate. Easy and cheap implementation might be more important, making FOCV and FSSC viable.

On the other hand, the proposed control method can find applicability on systems where the cost and complexity of the MPP tracker are not as important as its performance and reliability. Analog implementation is generally cheaper than digital, which involves a microcontroller that needs to be programmed. The

proposed implementation possesses great potential for photovoltaic applications where accuracy and a true MPP tracker are required.

Although, the proposed algorithm was tested with small scale systems it can find applicability to larger scale systems without any constraints. Finally, the MPPT system along with the artificial solar cells developed within this work have a great potential for assessing and testing other MPPT algorithms. Comparison of different MPPT algorithms can be performed and can be applied on a variety of cell technologies.

The combination of a prototype system which emulates accurately the solar cell behavior – operation along with the development of a MPPT platform able to operate with different MPPT algorithms available in the literature are two helpful tools for any laboratory involved in photovoltaics and can assist on a variety of photovoltaic applications.

## 7.2 Future Work

This work has been a contribution towards the development of a new accurate tool for predicting a single point in the I-V characteristic curve, that is the maximum power point. Current and voltage at the maximum power point were both expressed in terms of a new  $A$  variable i.e.  $I_{mpp}=f(A)$  and  $V_{mpp}=f(A)$ . The  $A$  variable was well defined in mathematical means and has been quoted for all four different photovoltaic modules that were examined. It is worth studying whether variation of the  $A$  value could describe the whole I-V characteristic curve and define the range, lower and upper limit, of the  $A$  value. In this way apart from the single MPP value the whole I-V curve can be described with the help of the  $A$ .

The programmable digitally controlled emulator solar system designed and constructed throughout this work is a rich platform from which to launch a number of investigative avenues. Along with the MPPT system opens the possibility to a whole range of research areas in photovoltaic devices. Test operation of multi-junction (tandem or triple junction) solar cells and assess MPPT algorithms on multi-junction cells are two main aspects.

One of the most promising devices for efficiently converting sunlight into electricity is the multi-junction solar cell. Multi-junction solar cells consist of series stacked  $pn$  junction layers. The subcells are stacked on top of one another

so that sunlight first strikes the highest bandgap subcell, which is tuned to light with the shortest wavelengths or highest energies. The longer wavelengths pass through the first subcell and strike the lower bandgap subcells. This means that a broader range of wavelengths are absorbed due to extended solar spectrum coverage, improving the cell's sunlight to electrical energy conversion efficiency.

Since, the multi-junction solar cell is a configuration of series connected solar cells, output voltage is attained by addition of the subcell voltages, while current is clamped by the subcell that produces the lowest current in the cell [182, 183, 184]. Experiments performed to tandem and triple junction solar cell topologies indicate promising results. Connecting them together in series, the overall result obtained is in accordance to the above described principle. However, sufficient device modeling of multi-junction solar cells or data provided by other researchers in this field are required in order to feed accurate information to each of the artificial solar cell, examine the overall response and come to save conclusions.

The next step would be to connect them to the MPPT system test platform and assess the performance of the proposed algorithm at multi-junction solar cells. Similarly, FOCV and FSCC or any other available MPPT algorithm can be studied and determine efficiency response.



## Appendix A

### A.1 Mathematical Derivation – Matlab scripts

#### A.1.1 Mathematical Derivation

Mathematical equations are derived in details in this section.

a) Equation (3.21) due to (3.4) becomes:

$$V = \frac{AN_s N_p - N_s R_s \left( N_p I_{ph} - N_p I_o \left( \exp\left(\frac{A}{V_t}\right) - 1 \right) - \frac{A}{R_{sh}} \right)}{N_p} \Rightarrow$$

$$V = \frac{AN_s N_p - N_s R_s N_p I_{ph} + N_s R_s N_p I_o \left( \exp\left(\frac{A}{V_t}\right) - 1 \right) + \frac{AN_s R_s}{R_{sh}}}{N_p} \Rightarrow$$

$$V = AN_s - N_s R_s I_{ph} + N_s R_s I_o \left( \exp\left(\frac{A}{V_t}\right) - 1 \right) + \frac{AN_s R_s}{N_p R_{sh}} \quad (3.23)$$

b) Calculating the second term of equation (3.20), due to equation (3.23) and equation (3.22) it is:

$$\frac{V}{B} = \frac{AN_s N_p R_{sh} - N_s R_s N_p R_{sh} I_{ph} + N_s R_s N_p R_{sh} I_o \left( \exp\left(\frac{A}{V_t}\right) - 1 \right) + AN_s R_s}{N_p R_{sh}} =$$

$$\frac{V_t \left( N_p R_{sh} I_{ph} - N_p R_{sh} I_o \left( \exp\left(\frac{A}{V_t}\right) - 1 \right) - A \right)}{N_p I_o R_{sh} \exp\left(\frac{A}{V_t}\right) + V_t}$$

$$\frac{\left( N_p I_o R_{sh} \exp\left(\frac{A}{V_t}\right) + V_t \right) \cdot \left( AN_s N_p R_{sh} - N_s R_s N_p R_{sh} I_{ph} + N_s R_s N_p R_{sh} I_o \left( \exp\left(\frac{A}{V_t}\right) - 1 \right) + AN_s R_s \right)}{N_p R_{sh} V_t \left( N_p R_{sh} I_{ph} - N_p R_{sh} I_o \left( \exp\left(\frac{A}{V_t}\right) - 1 \right) - A \right)} \quad (3.25)$$

c) Both terms of equation (3.20) has been calculated. Equation (3.24) is equated with equation (3.25). Thus, equation (3.20) becomes:

$$\frac{dV}{dA} = \frac{V}{B} \Leftrightarrow$$

$$N_s + \frac{N_s R_s I_o \exp\left(\frac{A}{V_t}\right)}{V_t} + \frac{N_s R_s}{N_p R_{sh}} = \frac{\left(N_p I_o R_{sh} \exp\left(\frac{A}{V_t}\right) + V_t\right) \cdot \left(AN_s N_p R_{sh} - N_s R_s N_p R_{sh} I_{ph} + N_s R_s N_p R_{sh} I_o \left(\exp\left(\frac{A}{V_t}\right) - 1\right) + AN_s R_s\right)}{N_p R_{sh} V_t \cdot \left(N_p R_{sh} I_{ph} - N_p R_{sh} I_o \cdot \left(\exp\left(\frac{A}{V_t}\right) - 1\right) - A\right)} \Leftrightarrow$$

$$\frac{N_s N_p R_{sh} V_t + N_s R_s V_t + N_s R_s N_p R_{sh} I_o \exp\left(\frac{A}{V_t}\right)}{N_p R_{sh} V_t} = \frac{\left(N_p I_o R_{sh} \exp\left(\frac{A}{V_t}\right) + V_t\right) \cdot \left(AN_s N_p R_{sh} - N_s R_s N_p R_{sh} I_{ph} + N_s R_s N_p R_{sh} I_o \left(\exp\left(\frac{A}{V_t}\right) - 1\right) + AN_s R_s\right)}{N_p R_{sh} V_t \cdot \left(N_p R_{sh} I_{ph} - N_p R_{sh} I_o \left(\exp\left(\frac{A}{V_t}\right) - 1\right) - A\right)} \Leftrightarrow$$

$$\left(N_s N_p R_{sh} V_t + N_s R_s V_t + N_s R_s N_p R_{sh} I_o \exp\left(\frac{A}{V_t}\right)\right) \cdot \left(N_p R_{sh} I_{ph} - N_p R_{sh} I_o \left(\exp\left(\frac{A}{V_t}\right) - 1\right) - A\right) =$$

$$\left(N_p I_o R_{sh} \exp\left(\frac{A}{V_t}\right) + V_t\right) \cdot \left(AN_s N_p R_{sh} - N_s R_s N_p R_{sh} I_{ph} + N_s R_s N_p R_{sh} I_o \left(\exp\left(\frac{A}{V_t}\right) - 1\right) + AN_s R_s\right) \quad (3.26)$$



Let's work at first side of equation (3.26):

$$\begin{aligned}
 & \left( N_s N_p R_{sh} V_t + N_s R_s V_t + N_s R_s N_p R_{sh} I_o \exp\left(\frac{A}{V_t}\right) \right) \cdot \left( N_p R_{sh} I_{ph} - N_p R_{sh} I_o \left( \exp\left(\frac{A}{V_t}\right) - 1 \right) - A \right) = \\
 & \left( N_s N_p R_{sh} V_t N_p R_{sh} I_{ph} - N_s N_p R_{sh} V_t N_p R_{sh} I_o \exp\left(\frac{A}{V_t}\right) + N_s N_p R_{sh} V_t N_p R_{sh} I_o - N_s N_p R_{sh} V_t A + N_s R_s V_t N_p R_{sh} I_{ph} - N_s R_s V_t N_p R_{sh} I_o \exp\left(\frac{A}{V_t}\right) \right. \\
 & + N_s R_s V_t N_p R_{sh} I_o - N_s R_s V_t A + N_s R_s N_s R_{sh} I_o \exp\left(\frac{A}{V_t}\right) N_p R_{sh} I_{ph} - N_s R_s N_p R_{sh} I_o \exp\left(\frac{A}{V_t}\right) N_p R_{sh} I_o \exp\left(\frac{A}{V_t}\right) + N_s R_s N_p R_{sh} I_o \exp\left(\frac{A}{V_t}\right) N_p R_{sh} I_o \\
 & \left. - N_s R_s N_p R_{sh} I_o \exp\left(\frac{A}{V_t}\right) A \right) = \\
 & \left( N_s N_p^2 R_{sh}^2 V_t I_{ph} - N_s N_p^2 R_{sh}^2 V_t I_o \exp\left(\frac{A}{V_t}\right) + N_s N_p^2 R_{sh}^2 V_t I_o - N_s N_p R_{sh} V_t A + N_s R_s V_t N_p R_{sh} I_{ph} - N_s R_s V_t N_p R_{sh} I_o \exp\left(\frac{A}{V_t}\right) + N_s R_s V_t N_p R_{sh} I_o - N_s R_s V_t A \right. \\
 & \left. + N_s R_s N_p^2 R_{sh}^2 I_o I_{ph} \exp\left(\frac{A}{V_t}\right) - N_s R_s N_p^2 R_{sh}^2 I_o^2 \left( \exp\left(\frac{A}{V_t}\right) \right)^2 + N_s R_s N_p^2 R_{sh}^2 I_o^2 \exp\left(\frac{A}{V_t}\right) - N_s R_s N_p R_{sh} I_o \exp\left(\frac{A}{V_t}\right) A \right) \tag{3.27}
 \end{aligned}$$

Similar the second side of equation (3.26) becomes:

$$\begin{aligned}
 & \left( N_p I_o R_{sh} \exp\left(\frac{A}{V_t}\right) + V_t \right) \cdot \left( AN_s N_p R_{sh} - N_s R_s N_p R_{sh} I_{ph} + N_s R_s N_p R_{sh} I_o \left( \exp\left(\frac{A}{V_t}\right) - 1 \right) + AN_s R_s \right) = \\
 & N_p^2 R_{sh}^2 \cdot N_s A I_o \exp\left(\frac{A}{V_t}\right) - N_p I_o R_{sh} \exp\left(\frac{A}{V_t}\right) N_s R_s N_p R_{sh} I_{ph} + N_p I_o R_{sh} \exp\left(\frac{A}{V_t}\right) N_s R_s N_p R_{sh} I_o \exp\left(\frac{A}{V_t}\right) - N_p I_o R_{sh} \exp\left(\frac{A}{V_t}\right) N_s R_s N_p R_{sh} I_o \\
 & + N_p I_o R_{sh} \exp\left(\frac{A}{V_t}\right) AN_s R_s + AN_s N_p R_{sh} V_t - N_s R_s N_p R_{sh} I_{ph} V_t + N_s R_s N_p R_{sh} I_o V_t \exp\left(\frac{A}{V_t}\right) - N_s R_s N_p R_{sh} I_o V_t + AN_s R_s V_t = \\
 & N_p^2 R_{sh}^2 N_s A I_o \exp\left(\frac{A}{V_t}\right) - N_s R_s N_p^2 R_{sh}^2 I_o I_{ph} \exp\left(\frac{A}{V_t}\right) + N_s R_s N_p^2 R_{sh}^2 I_o^2 \left( \exp\left(\frac{A}{V_t}\right) \right)^2 - N_s R_s N_p^2 R_{sh}^2 I_o^2 \exp\left(\frac{A}{V_t}\right) + N_s R_s N_p R_{sh} I_o A \exp\left(\frac{A}{V_t}\right) \\
 & + AN_s N_p R_{sh} V_t - N_s R_s N_p R_{sh} I_{ph} V_t + N_s R_s N_p R_{sh} I_o V_t \exp\left(\frac{A}{V_t}\right) - N_s R_s N_p R_{sh} I_o V_t + AN_s R_s V_t \tag{3.28}
 \end{aligned}$$

Equating both terms of equation (3.26), i.e. equation (3.27) with (3.28) it is:

$$N_s N_p^2 R_{sh}^2 V_t I_{ph} - N_s N_p^2 R_{sh}^2 V_t I_o \exp\left(\frac{A}{V_t}\right) + N_s N_p^2 R_{sh}^2 V_t I_o - N_s N_p R_{sh} V_t A + N_s R_s N_p R_{sh} V_t I_{ph} - N_s R_s N_p R_{sh} V_t I_o \exp\left(\frac{A}{V_t}\right) + N_s R_s V_t N_p R_{sh} I_o - N_s R_s V_t A$$

$$\begin{aligned}
 & + N_s R_s N_p^2 R_{sh}^2 I_o I_{ph} \exp\left(\frac{A}{V_t}\right) - N_s R_s N_p^2 \cdot R_{sh}^2 \cdot I_o^2 \left(\exp\left(\frac{A}{V_t}\right)\right)^2 + N_s R_s N_p^2 R_{sh}^2 I_o^2 \exp\left(\frac{A}{V_t}\right) - N_s R_s N_p R_{sh} I_o \exp\left(\frac{A}{V_t}\right) A = \\
 & N_p^2 R_{sh}^2 N_s A I_o \exp\left(\frac{A}{V_t}\right) - N_s R_s N_p^2 R_{sh}^2 I_o I_{ph} \exp\left(\frac{A}{V_t}\right) + N_s R_s N_p^2 R_{sh}^2 I_o^2 \left(\exp\left(\frac{A}{V_t}\right)\right)^2 - N_s R_s N_p^2 R_{sh}^2 I_o^2 \exp\left(\frac{A}{V_t}\right) + N_s R_s N_p R_{sh} I_o A \exp\left(\frac{A}{V_t}\right) + A N_s N_p R_{sh} V_t \\
 & - N_s R_s N_p R_{sh} I_{ph} V_t + N_s R_s N_p R_{sh} I_o V_t \exp\left(\frac{A}{V_t}\right) - N_s R_s N_p R_{sh} I_o V_t + A N_s R_s V_t \Leftrightarrow
 \end{aligned} \tag{3.29}$$

Gathering terms of equation (3.29) it becomes:

$$\begin{aligned}
 & N_s N_p^2 R_{sh}^2 V_t I_{ph} - N_s N_p^2 R_{sh}^2 V_t I_o \exp\left(\frac{A}{V_t}\right) + N_s N_p^2 R_{sh}^2 V_t I_o - 2 N_s N_p R_{sh} V_t A + 2 N_s R_s N_p R_{sh} I_{ph} V_t - 2 N_s R_s N_p R_{sh} V_t I_o \exp\left(\frac{A}{V_t}\right) + 2 N_s R_s V_t N_p R_{sh} I_o \\
 & - 2 N_s R_s V_t A + 2 N_s R_s N_p^2 R_{sh}^2 I_o I_{ph} \exp\left(\frac{A}{V_t}\right) - 2 N_s R_s N_p^2 R_{sh}^2 I_o^2 \left(\exp\left(\frac{A}{V_t}\right)\right)^2 + 2 N_s R_s N_p^2 R_{sh}^2 I_o^2 \exp\left(\frac{A}{V_t}\right) - 2 N_s R_s N_p R_{sh} I_o A \exp\left(\frac{A}{V_t}\right) \\
 & - N_p^2 R_{sh}^2 N_s A I_o \exp\left(\frac{A}{V_t}\right) = 0
 \end{aligned} \tag{3.30}$$

### A.1.2 Matlab scripts

Two script files, written in Matlab software for module AP 165 can be seen in this section:

a) findzeros.m script file:

```
x=fzero(@(x) example1(x), 1)
```

```
Ns=54; % No. of cells in series
```

```
Np=1; % No. of cells in parallel
```

```
Iph=7.4/Np;
```

```
Voc=32;
```

```
n=1; % for STC
```

```
T=273+25; % for STC
```

```
k=1.380658e-23;
```

```
q = 1.602177e-19;
```

```
Rsh=Np*61.8/Ns;
```

```
Rs=Np*0.4676/Ns;
```

```
Vt=n*k*T/q;
```

```
Io=(Np*Iph-(Voc/(Rsh*Ns)))/(Np*(exp(Voc/(Ns*Vt))-1));
```

```
V=x*Ns-Ns*Rs*Iph+Np*Rs*Io*(exp(x/Vt)-1)+((x*Ns*Rs)/(Np*Rsh))
```

```
% Maximum voltage
```

```
I=Np*Iph-Np*Io*(exp(x/Vt)-1)-x/Rsh % Maximum current
```

```
P=V.*I % Maximum power
```

b) example1.m script file:

```
function f=example1(x)
```

```
Ns=54; % No. of cells in series
```

```
Np=1; % No. of cells in parallel
```

```
Iph=7.4/Np;
```

```
Voc=32;
```

```
n=1; % for STC
```

```
T=273+25; % for STC
```

```
k=1.380658e-23;
```

```
q = 1.602177e-19;
```

```
Rsh=Np*61.8/Ns;
```

```
Rs=Np*0.4676/Ns;
```

```
Vt=n*k*T/q;
```

```
Io=(Np*Iph-(Voc/(Rsh*Ns)))/(Np*(exp(Voc/(Ns*Vt))-1));
```

```
f=Ns*Np^2*Rsh^2*Vt*Iph-
```

```
Ns*Np^2*Rsh^2*Vt*Io*exp(x/Vt)+Ns*Np^2*Rsh^2*Vt*Io
```

```
2*Ns*Np*Rsh*Vt*x+2*Ns*Rs*Np*Rsh*Iph*Vt-
```

```
2*Ns*Rs*Np*Rsh*Vt*Io*exp(x/Vt)+2*Ns*Rs*Vt*Np*Rsh*Io-
```

```
2*Ns*Rs*Vt*x+2*Ns*Rs*Np^2*Rsh^2*Io*Iph*exp(x/Vt)-
```

```
2*Ns*Rs*Np^2*Rsh^2*Io^2*exp(x/Vt)^2+2*Ns*Rs*Np^2*Rsh^2*Io^2*exp(x/V
```

```
t)-2*Ns*Rs*Np*Rsh*Io*x*exp(x/Vt)-Np^2*Rsh^2*Ns*x*Io*exp(x/Vt)
```



## Appendix B

### B. Series Resistance Modelling

In this section an equation derived in [140] for determining series resistance of a photovoltaic module is presented. The equation that describes the single diode model behavior is given by the equation (2.20). By applying the short circuit conditions ( $I=I_{sc}$  and  $V=0$ ) to equation (2.20), photocurrent  $I_{ph}$  can be obtained as:

$$I_{ph} = \frac{I_{sc}(R_s + R_{sh})}{R_{sh}} + I_o \left( \exp \frac{I_{sc} R_s}{nV_{th}} - 1 \right) \quad (\text{B.1})$$

Most times  $I_{ph}$  is simplified by:

$$I_{ph} \approx \frac{I_{sc}(R_s + R_{sh})}{R_{sh}} \quad (\text{B.2})$$

Similarly, applying open circuit conditions ( $I=0$  and  $V=V_{oc}$ ) lead to an equation for saturation current  $I_o$ .

$$I_{ph} = I_o \left( \exp \frac{V_{oc}}{nV_{th}} - 1 \right) + \frac{V_{oc}}{R_{sh}} \quad (\text{B.3})$$

Substituting equation (B.1) in (B.3) and after some approximations:

$$I_o \approx \frac{I_{sc}(R_s + R_{sh}) - V_{oc}}{R_{sh}} \cdot \exp \left( - \frac{V_{oc}}{nV_{th}} \right) \quad (\text{B.4})$$

In the above equations it should be noted that  $V_{th}$  is given by:

$$V_{th} = \frac{kT}{q} \quad (\text{B.5})$$

At the maximum power point the following condition is met:

$$\frac{\partial P}{\partial V} = \frac{\partial}{\partial V}(VI) = I + V \frac{\partial I}{\partial V} = 0 \Rightarrow \frac{\partial I}{\partial V} = -\frac{I}{V} \quad (\text{B.6})$$

On the other hand, on deriving  $I$  with respect to  $V$  in the equation (2.20), it is obtained:

$$\frac{\partial I}{\partial V} = -\frac{1}{V} \left[ \frac{I_o (V - IR_s)}{nV_{th}} \cdot \exp\left(\frac{V + IR_s}{nV_{th}}\right) - \frac{V - IR_s}{R_{sh}} \right] \quad (\text{B.7})$$

Comparing equations (B.6) and (B.7) gives:

$$I_{mpp} = \frac{I_o (V_{mpp} - I_{mpp} R_s)}{nV_{th}} \cdot \exp\left(\frac{V_{mpp} + I_{mpp} R_s}{nV_{th}}\right) + \frac{V_{mpp} - I_{mpp} R_s}{R_{sh}} \quad (\text{B.8})$$

Nevertheless, due to the presence of  $I_o$  and the exponential term the current form of the equation (B.8) is not the most appropriate to assess the effect of loss resistance.

Through equations (2.20) and (B.2) and after some slight approximation:

$$I_o \approx \left[ \frac{(I_{sc} - I_{mpp})(R_s + R_{sh}) - V_{mpp}}{R_{sh}} \right] \cdot \exp\left(-\frac{V_{mpp} + I_{mpp} R_s}{nV_{th}}\right) \quad (\text{B.9})$$

By now substituting (B.9) in (B.8) and reordering it is obtained:

$$I_{mpp} \approx \left[ \frac{V_{mpp} - R_s I_{mpp}}{nV_{th}} \right] \cdot \left[ \frac{(I_{sc} - I_{mpp})(R_s + R_{sh})}{R_{sh}} - \frac{V_{mpp} - nV_{th}}{R_{sh}} \right] \quad (\text{B.10})$$

Bearing in mind that  $R_s \ll R_{sh}$  it is possible to simplify again (B.10) to adopt an even more explicit form.

$$I_{mpp} \approx \left[ \frac{V_{mpp} - R_s I_{mpp}}{nV_{th}} \right] \left[ I_{sc} - I_{mpp} - \frac{V_{mpp} - nV_{th}}{R_{sh}} \right] \quad (\text{B.11})$$

Since equation (B.11) does not contain any transcendental terms it is much more adequate than (B.8) for a qualitative analysis.

Similar to the way that  $I_{mp}$  has been approached, it will now be studied  $V_{mp}$ . Equating equations (2.20) in (B.8) and rearranging:

$$I_{ph} - \frac{2V_{mpp}}{R_{sh}} = I_o \left[ \frac{V_{mpp} + nV_{th} - I_{mpp} R_s}{nV_{th}} \cdot \exp\left(\frac{V_{mpp} + I_{mpp} R_s}{nV_{th}}\right) - 1 \right] \quad (\text{B.12})$$

Substituting  $I_{ph}$  and  $I_o$  in (B.12) through (B.1) and (B.4) and reordering again leads to:



$$[B] = [A] \exp\left(\frac{V_{mpp} + I_{mpp} R_s - V_{oc}}{nV_{th}}\right) \quad (B.13)$$

Equation (B.13) has been simplified by performing the substitutions:

$$A = \frac{V_{mpp} + nV_{th} - I_{mpp} R_s}{nV_{th}} \quad (B.14)$$

$$B = \frac{I_{sc}(R_s + R_{sh}) - 2V_{mpp}}{I_{sc}(R_s + R_{sh}) - V_{oc}} \quad (B.15)$$

Finally, taking logarithms in (B.13) it is obtained:

$$V_{mpp} = V_{oc} - I_{mpp} R_s - nV_{th} [\ln(A) - \ln(B)] \quad (B.16)$$

If  $R_{sh}$  is high enough to consider that  $\ln(B) \approx 0$ , equation (B.16) can be simplified and set out as:

$$V_{mpp} = V_{oc} - I_{mpp} R_s - nV_{th} \ln\left(\frac{V_{mpp} + nV_{th} - I_{mpp} R_s}{nV_{th}}\right) \quad (B.17)$$

With the help of equation (B.17) given the values of  $V_{mpp}$ ,  $I_{mpp}$  and  $V_{oc}$ , the corresponding value of  $R_s$  can be obtained that will allow the I-V curve of the model to pass through those points. The resulting equation is:

$$R_s = \frac{1}{I_{mpp}} \left[ V_{oc} - V_{mpp} - nV_{th} \ln \frac{V_{mpp} + nV_{th} - I_{mpp} R_s}{nV_{th}} \right] \quad (B.18)$$

Since  $R_s$  is also within the logarithmic term, the solution cannot be achieved without resorting to an iterative procedure. It is possible to reach a good enough solution in two steps:

In the first step, the logarithmic term of equation (B.18) is approached by removing the numerator  $I_{mpp} R_s$  and  $nV_{th}$  and an initial  $R_{so}$  value is estimated:

$$R_{so} = \frac{1}{I_{mpp}} \left[ V_{oc} - V_{mpp} - nV_{th} \ln \frac{V_{mpp}}{nV_{th}} \right] \quad (B.19)$$

In the second step the  $R_{so}$  value of equation (B.19) is inserted into (B.18) to obtain a final  $R_{s1}$  value.

If it is wished to improve the result the process can be repeated several times. It is enough to again insert the value obtained in second step into the equation (B.18). In most cases, from the second iteration ( $R_{s2}$ ) differences start to become irrelevant.

## Appendix C

**Table 5.2 Summarizing experimental values at different irradiances and temperatures.**

Experimental Setup										
Insol.	Temperature		$R_s$ (Ohm)	$R_{sh}$ (kOhm)	$I_o$ (A)	$nT$ (kelvin)	$R^2$	$G$		
	$T$ (Kelv), (°C)							$I_{ph}$ (mA)	(Gain) Exper.	$RMSE$
1000	253 (-20)		0.29	20	1.29E-08	486.1	0.973	254.08	1.020	$2.55 \cdot 10^{-3}$
	273 (0)		0.37	20	1.06E-08	471.7	0.987	254.22	1.070	$1.16 \cdot 10^{-3}$
	293 (20)		0.41	20	1.00E-08	470.3	0.990	254.41	1.145	$8.14 \cdot 10^{-4}$
	313 (40)		0.42	20	1.00E-08	471.8	0.988	254.60	1.239	$1.09 \cdot 10^{-3}$
	333 (60)		0.44	20	9.67E-09	460.6	0.986	254.82	1.316	$1.06 \cdot 10^{-3}$
800	253 (-20)		0.22	20	2.27E-09	422.0	0.975	203.28	0.976	$2.9 \cdot 10^{-3}$
	273 (0)		0.33	20	2.09E-09	419.8	0.984	203.35	1.037	$1.79 \cdot 10^{-3}$
	293 (20)		0.39	20	2.21E-09	420.7	0.985	203.48	1.108	$2.58 \cdot 10^{-3}$
	313 (40)		0.42	20	2.26E-09	421.2	0.987	203.56	1.201	$1.25 \cdot 10^{-3}$
	333 (60)		0.44	20	2.06E-09	418.6	0.985	203.63	1.306	$1.14 \cdot 10^{-3}$
600	253 (-20)		0.19	20	1.29E-09	413.7	0.975	152.28	0.975	$2.58 \cdot 10^{-3}$
	273 (0)		0.27	20	1.09E-09	404.3	0.981	152.41	1.029	$2.06 \cdot 10^{-3}$
	293 (20)		0.35	20	1.11E-09	404.8	0.986	152.52	1.106	$1.96 \cdot 10^{-3}$
	313 (40)		0.42	20	9.91E-10	401.6	0.983	152.62	1.195	$1.06 \cdot 10^{-3}$
	333 (60)		0.44	20	9.97E-10	403.5	0.986	152.68	1.307	$1.24 \cdot 10^{-3}$
400	253 (-20)		0.18	20	4.60E-10	386.2	0.973	101.31	0.954	$2.53 \cdot 10^{-3}$
	273 (0)		0.22	20	3.46E-10	381.0	0.986	101.45	1.025	$2.33 \cdot 10^{-3}$
	293 (20)		0.27	20	4.20E-10	385.1	0.988	101.60	1.103	$2.56 \cdot 10^{-3}$
	313 (40)		0.35	20	4.27E-10	384.0	0.988	101.70	1.197	$0.88 \cdot 10^{-3}$
	333 (60)		0.44	20	3.34E-10	379.2	0.986	101.82	1.312	$0.97 \cdot 10^{-3}$

**Table 5.3 Summarizing theoretical values for different irradiances and temperatures.**

Theoretical Setup									
Insol. W/m <sup>2</sup>	Temperature		$R_s$ (Ohm)	$R_{sh}$ (kOhm)	$I_o$ (A)	$nT$ (kelvin)	$I_{ph}$ (mA)	$G$	
	$T$ (Kelv), (°C)	$Residual$						(Gain) Theor.	$V_j$ (V)
1000	253 (-20)	0.5	20	4.48E-15	253	$7.97 \cdot 10^{-5}$	254.49	1.034	0.691
	273 (0)	0.5	20	2.79E-13	273	$5.57 \cdot 10^{-6}$	254.68	1.069	0.648
	293 (20)	0.5	20	1.02E-11	293	$7.69 \cdot 10^{-5}$	254.87	1.141	0.605
	313 (40)	0.5	20	2.44E-10	313	$4.33 \cdot 10^{-5}$	255.02	1.237	0.560
	333 (60)	0.5	20	4.08E-09	333	$9.08 \cdot 10^{-5}$	255.29	1.314	0.516
800	253 (-20)	0.5	20	4.48E-15	253	$0.53 \cdot 10^{-5}$	203.76	0.971	0.686
	273 (0)	0.5	20	2.80E-13	273	$2.25 \cdot 10^{-5}$	203.81	1.035	0.643
	293 (20)	0.5	20	1.03E-11	293	$2.47 \cdot 10^{-5}$	203.91	1.110	0.599
	313 (40)	0.5	20	2.45E-10	313	$5.19 \cdot 10^{-5}$	204.1	1.208	0.554
	333 (60)	0.5	20	4.01E-09	333	$0.16 \cdot 10^{-5}$	204.3	1.306	0.509
600	253 (-20)	0.5	20	4.48E-15	253	$0.21 \cdot 10^{-5}$	152.76	0.975	0.679
	273 (0)	0.5	20	2.81E-13	273	$2.14 \cdot 10^{-5}$	152.89	1.032	0.636
	293 (20)	0.5	20	1.03E-11	293	$1 \cdot 10^{-5}$	153.02	1.105	0.592
	313 (40)	0.5	20	2.44E-10	313	$1.08 \cdot 10^{-5}$	153.11	1.194	0.547
	333 (60)	0.5	20	4.03E-09	333	$1.21 \cdot 10^{-5}$	153.19	1.308	0.501
400	253 (-20)	0.5	20	4.48E-15	253	$1.46 \cdot 10^{-6}$	101.75	0.953	0.671
	273 (0)	0.5	20	2.80E-13	273	$2.48 \cdot 10^{-6}$	101.88	1.022	0.626
	293 (20)	0.5	20	1.03E-11	293	$4.70 \cdot 10^{-6}$	102.00	1.102	0.581
	313 (40)	0.5	20	2.45E-10	313	$9.76 \cdot 10^{-6}$	102.12	1.192	0.536
	333 (60)	0.5	20	4.03E-09	333	$4.95 \cdot 10^{-6}$	102.30	1.305	0.489

## Appendix D

### D. MPP Software Code in Matlab

#### findzeros.m script file

```
delete(instrfind({'Port'},{'COM16'}))
install_arduino()

global a;
global b;
global c;
clear c;
clear a;
clear b;

c = arduino('COM16');

double Vpilot=0; % voltage pilot cell
double Ipilot=0; % current pilot cell
A1=0;
A2=0;

% It must return at this point. Continues loop
% Start Pilot Cell measurement of Voc and Isc
startpoint = true;
while startpoint == true
c.pinMode(2,'output'); % pin 2 arduino output
c.digitalWrite(2,0); % low – 0 Volt at pin2, for volt measurement
Vpilot = c.analogRead(1); % read A1 pin arduino
Vpilot = 8*2*((5*Vpilot)/1024); % measurement of Voc
c.digitalWrite(2,1); % low – 5 Volt at pin2, for current measurement
Ipilot = c.analogRead(2); % read A2 pin arduino
Ipilot = (Ipilot/1024); % measurement of Isc
if (abs(A1-Vpilot)>0.010 || abs(A2-Ipilot)>0.0015)
A1=Vpilot;
```

## Appendix D

---

A2=I<sub>pilot</sub>;

fid=fopen('data.txt','wb');

fprintf(fid,'%5.3f %5.4f \r\n',V<sub>pilot</sub>,I<sub>pilot</sub>);

fclose(fid);

% End Pilot Cell measurement of Voc and Isc

% Start Cell measurement of V<sub>input</sub>, I<sub>input</sub> and V<sub>out</sub>.

V<sub>input</sub> = c.analogRead(3);

V<sub>input</sub> = 2\*((5\*V<sub>input</sub>)/1024);

I<sub>input</sub> = c.analogRead(4);

I<sub>input</sub> = (I<sub>input</sub>/1024);

V<sub>out</sub> = c.analogRead(5);

V<sub>out</sub> = 2\*((5\*V<sub>out</sub>)/1024);

% End Cell measurement of V and I

% findzeros.m script file:

x=fzero(@(x) example1(x),1);

N<sub>s</sub>=8; % No. of cells in series

N<sub>p</sub>=1; % No. of cells in parallel

I<sub>ph</sub>=I<sub>pilot</sub>/N<sub>p</sub>;

V<sub>oc</sub>=V<sub>pilot</sub>;

n=1; % for STC

T=273+40;

k=1.380658e-23;

q = 1.602177e-19;

R<sub>p</sub>=N<sub>p</sub>\*20000/N<sub>s</sub>;

R<sub>s</sub>=N<sub>p</sub>\*4/N<sub>s</sub>;

V<sub>t</sub>=n\*k\*T/q;

I<sub>o</sub>=(N<sub>p</sub>\*I<sub>ph</sub>-(V<sub>oc</sub>/(R<sub>p</sub>\*N<sub>s</sub>)))/(N<sub>p</sub>\*(exp(V<sub>oc</sub>/(N<sub>s</sub>\*V<sub>t</sub>))-1));

V<sub>max</sub>=x\*N<sub>s</sub>-N<sub>s</sub>\*R<sub>s</sub>\*I<sub>ph</sub>+N<sub>s</sub>\*R<sub>s</sub>\*I<sub>o</sub>\*(exp(x/V<sub>t</sub>)-

1)+((x\*N<sub>s</sub>\*R<sub>s</sub>)/(N<sub>p</sub>\*R<sub>p</sub>)); %Maximum voltage

---

```
Imax=Np*Iph-Np*Io*(exp(x/Vt)-1)-x/Rp; % Maximum current
```

```
Pmax=Vmax.*Imax; % Maximum power
```

```
% End of findzeros.m script file:
```

```
Pproduced = 0;
```

```
pwm_opt=0;
```

```
counter=0;
```

```
i=20;
```

```
di=10;
```

```
Pold=0;
```

```
derivP=0;
```

```
Error=1000;
```

```
tic
```

```
while(i<256)
```

```
    c.analogWrite(9,i);
```

```
    Iinput = c.analogRead(4);
```

```
    Iinput = (Iinput/1024);
```

```
    Vinput = c.analogRead(3);
```

```
    Vinput = 2*((5*Vinput)/1024);
```

```
    Pinput = Iinput * Vinput;
```

```
    derivP=Pinput-Pold;
```

```
    if Pinput<=P
```

```
        Cerror=abs(P-Pinput);
```

```
        counter = counter + 1;
```

```
        if derivP>=0
```

```
            i=i+di;
```

```
            if abs(Cerror)<Error
```

```
                Error=abs(Cerror);
```

```
                pwm_opt=i;
```

```
            end
```

```
            Pproduced = Pproduced + Pinput;
```

```
            Pold=Pinput;
```

```
        else
```

```
            if di==1
```

```
        break;
    else
        i=i-2*di;
        di=floor(di/2);
        if di==0
            di=1;
        end
        if abs(Cerror)<Error
            Error=abs(Cerror);
            pwm_opt=i;
        end
        Pproduced = Pproduced + Pinput

        Pold=Pinput;
    end
end
end
end

time=toc;
Wlost=(counter*P-Pproduced)*time; %units Joule
c.analogWrite(9,pwm_opt); %drive gate of MOSFET with optimum duty cycle

c.digitalWrite(2,0) % low – 0 Volt at pin2, for volt measurement
Vpilot = c.analogRead(1); % read A1 pin arduino
Vpilot = 8*2*((5*Vpilot)/1024); % measurement of Voc (pilot cell).
c.digitalWrite(2,1); % high – 5 Volt at pin2, for current measurement
Ipilot = c.analogRead(2); % read A2 pin arduino
Ipilot = (Ipilot/1024); % measurement of Isc (pilot cell)

Iinput = c.analogRead(4); % read A4 pin arduino
Iinput = (Iinput/1024) % measurement of Iinput (main cell)

Vinput = c.analogRead(3); % read A3 pin arduino
Vinput = 2*((5*Vinput)/1024); % measurement of Vinput (main cell).
```



---

```

Pininput = Iinput * Vininput; % computing Pininput (main cell)

Vout = c.analogRead(5); % read A5 pin arduino
Vout = 2*(5*Vout/1024); % measurement of Vout (main cell).

CerrorI=abs(Imax-Iinput) % error between (Imax) and (Iinput)
Ipilot % print Ipilot
Iinput % print Iinput
Imax % print Imax
per_I=((CerrorI)/Imax)*100 % percentage error
Iconverge=100- per_I % Iconverge

CerrorV=abs(Vmax-Vinput) % error between (Vmax) and (Vinput).
Vpilot % print Vpilot
Vinput % print Vinput
Vmax % print Vmax
per_V=((CerrorV)/Vmax)*100 % percentage error
Vconverge=100- per_V % Vconverge

CerrorP=abs(Pmax-Pininput); % error between (Pmax)and main (Pininput).
Pininput % print Pininput
Wlost % print lost Energy
Wmax=counter*P*time % print max Energy
Wprod=Pproduced*time % print produced Energy
Pmax % print Pmax
per_P= ((CerrorP)/Pmax)*100% percentage error.
Pconverge=100- per_P % Pconverge
Vout % print Vout (main cell)
pwm_opt % print optimum duty cycle
time % time taken for MPPT

end
end
delete (instrfind({'Port'},{'COM16'}))

```

**example1.m script file**

```

function f=example1(x)

fid=fopen('data.txt','r'); % opens file data.txt
A=fscanf(fid,'%f'); % read Vpilot, Ipilot
Ns=8; % No. of cells in series
Np=1; % No. of cells in parallel
Iph=A(2)/Np; % Photocurrent pilot cell
Voc=A(1); % Open circuit voltage pilot cell
n=1; % ideality factor for STC
T=273+40;
k=1.380658e-23; % Boltzmann constant
q = 1.602177e-19; % electron charge
Rp=Np*20000/Ns; % parallel resistor
Rs=Np*4/Ns; % series resistor
Vt=n*k*T/q; % thermal voltage
Io=(Np*Iph-(Voc/(Rp*Ns)))/(Np*(exp(Voc/(Ns*Vt))-1)); % saturation current

f=Np*Np^2*Rp^2*Vt*Iph-
Ns*Np^2*Rp^2*Vt*Io*exp(x/Vt)+Ns*Np^2*Rp^2*Vt*Io -
2*Ns*Np*Rp*Vt*x+2*Ns*Rs*Np*Rp*Iph*Vt-
2*Ns*Rs*Np*Rp*Vt*Io*exp(x/Vt)+ 2*Ns*Rs*Vt*Np*Rp*Io-
2*Ns*Rs*Vt*x+2*Ns*Rs*Np^2*Rp^2*Io*Iph*exp(x/Vt)-
2*Ns*Rs*Np^2*Rp^2*Io^2*exp(x/Vt)^2+2*Ns*Rs*Np^2*Rp^2*Io^2*exp(x/Vt)
-2*Ns*Rs*Np*Rp*Io*x*exp(x/Vt)-Np^2*Rp^2*Ns*x*Io*exp(x/Vt); % returning
a number x, which is used for computing Vmax and Imax

```

## 8 Bibliography

[1] Girma Zawdie and Abdelkader Djeflat, “Technology and Transition. The Maghreb at the Crossroads”, Frank Cass and Company Limited, London, 1996, ISBN: 9780714647456.

[2] Vukica Janković, Helena Mitwallyová, “The potential of the usage of renewable energy in the Czech Republic”, *International Journal of Social Sciences* Vol. III, No. 4, pp 39-48, 2014.

[3] R.S. Dhillon, George von Wuehlisch, “Mitigation of global warming through renewable biomass”, *Biomass and Bioenergy*, Vol. 48, pp 75–89, January 2013.

[4] Hansen J, Sato M, Kharecha P, Beerling D, Berner R, Masson-Delmotte V, et al., “Target Atmospheric CO<sub>2</sub>: Where Should Sumanity Aim?”, *The Open Atmospheric Science Journal*, Vol. 2, pp 217–231, October 2008.

[5] Bill Sweet, “Global CO<sub>2</sub> concentration reaches 400 Parts per Million”, *IEEE Spectrum*, May 2013.

[6] R. Saidur, E.A. Abdelaziz, A. Demirbas, M.S. Hossain, S. Mekhilef, “A review on biomass as a fuel for boilers”, *Renewable and Sustainable Energy Reviews*, Vol. 15, Issue 5, pp 2262–2289, June 2011.

[7] F.R. Pazheri, M.F. Othman, N.H. Malik, “A review on global renewable electricity scenario”, *Renewable and Sustainable Energy Reviews*, Vol. 31, pp 835–845, March 2014.

[8] V.V. Tyagi, Nurul A.A. Rahim, N.A. Rahim, Jeyraj A./L. Selvaraj, “Progress in solar PV technology: Research and achievement”, *Renewable and Sustainable Energy Reviews*, Vol. 20, pp 443–461, April 2013.

[9] Solar Power Europe, “Global Market Outlook for Solar Power 2015-2019”, Belgium, 2015, ISBN: 9789082228410.

[10] Gaetan Masson, Sinead Orlandi, Manoel Rekinge, “Global Market Outlook for Photovoltaic 2014-2018”, European Photovoltaic Industry Association, Sweden, 2014, ISBN: 9789082228403.

- [11] Jenny Nelson, Ajay Gambhir and Ned Ekins-Daukes, “Solar power for CO<sub>2</sub> mitigation”, Grantham Institute for Climate Change, Imperial College London, Briefing paper No. 11, January 2014.
- [12] Martin Junginger, Wilfried van Sark, André Faaij, “Technological Learning in the Energy Sector: Lessons for Policy, Industry and Science”, Edward Elgar Publishing Ltd, UK, August 2010, ISBN: 9781848448346.
- [13] European Photovoltaic Industry Association, “Global Market Outlook for Photovoltaic 2013-2017”, Belgium, 2013.
- [14] David Feldman, Galen Barbose, Robert Margolis, Ryan Wiser, Naim Darghouth and Alan Goodrich, “Photovoltaic (PV) Pricing Trends: Historical, Recent and Near-Term Projections”, Sunshot U.S. Department of Energy, November 2012.
- [15] Pavel Somavat and Vinod Namboodiri, “Energy Consumption of Personal Computing Including Portable Communication Devices”, Journal of Green Engineering, River Publishers, pp 447–475, July 2011.
- [16] Jonathan Koomey, “Energy use and the information economy”, The Physics of Sustainable Energy III, University of California, Berkeley, March 2014.
- [17] Ericsson, “Ericsson Mobility Report”, Revision A, June 2015, Sweden.
- [18] IDC Worldwide, “Forecast for global shipments of tablets, laptops and desktop PCs from 2010 to 2019 (in million units)”, March 2015.
- [19] European Commission DG TREN, “Personal Computers (desktops and laptops) and Computer Monitors”, IVF Industrial Research and Development Corporation, August 2007, Sweden.
- [20] Electric Power Research Institute, “iPad Electricity Consumption in Relation to Other Energy Consuming Devices - Executive Summary”, 2012, USA.
- [21] Central Intelligence Agency, “The World Factbook”, Annual Report, 20 November 2015, USA.
- [22] K.H. Hussein, I.Muta, T. Hoshino, and M. Osakada. “Maximum photovoltaic power tracking: an algorithm for rapidly changing atmospheric conditions”, IEE

---

Proceedings-Generation, Transmission and Distribution, Vol. 142, No. 1, pp 59-64,1995.

[23] Arturo Morales-Acevedo, “Solar Cells – Research and Application Perspectives”, InTech, Croatia, 2013, ISBN: 9789535110033.

[24] E. Becquerel, “On electron effects under the influence of solar radiation”, Comptes Rendus de l Academie Sciences Paris, Vol. 9, pp. 561-567, 1839.

[25] Anthony P. French, Edwin F. Taylor, “An introduction to Quantum Physics, The M.I.T. Introductory Physics Series”, Stanley Thornes Ltd, UK, 1998, ISBN: 9780393091069.

[26] Lewis M. Fraas, Larry D. Partain, “Solar Cells and Their Applications”, Second Edition, John Wiley & Sons, USA, 2010, ISBN: 9780470446331.

[27] Keith Leaver, “Microelectronic Devices”, Longman Scientific & Technical, UK, 1989, ISBN: 0582014948.

[28] Augustin McEvoy, Luis Castaner and Tom Markvart, “Solar Cells: Materials, Manufacture and Operation”, Second Edition, Academic Press, 2012, ISBN: 9780123869647.

[29] Simon M. Sze, Kwok K. Ng, “Physics of Semiconductor Devices”, Third Edition, John Wiley & Sons, USA, 2007, ISBN: 9780471143239.

[30] Darren M Bagnall, ELEC1205, Class Lecture, Topic: “Solid State Devices”, School of Electronics and Computer Science, University of Southampton, Southampton, UK, 2013.

[31] Chenming Calvin Hu, “Modern Semiconductor Devices for Integrated Circuits”, Prentice Hall, USA, 2010, ISBN: 9780136085256.

[32] Antonio Luque and Steven Hegedus, “Handbook of Photovoltaic Science and Engineering”, Second Edition, John Wiley & Sons, UK, 2011, ISBN: 9780470721698.

[33] Miro Zeman, ET3034LR, Class Lecture, Topic: “Solar Cells”, School of Aerospace Engineering, Delft University of Technology, Holland, 2003.

- [34] Adolf Goetzberger A, Joachim Knobloch., Bernhard Voss, “Crystalline Silicon Solar Cells”, John Wiley and Sons, Chichester, 1998, ISBN: 9780471971443.
- [35] Jenny Nelson, “The Physics of Solar Cells”, Imperial College Press, UK, 2003, ISBN: 9781860943409.
- [36] Martin Green, “Solar Cells, Operating Principles, Technology, and System Applications”, Prentice Hall series in solid state, Physical Electronics, USA, 1982, ISBN: 9780138222703.
- [37] William Schokley and Hans J. Queissar “Detailed Balance Limit of Efficiency of  $p$ - $n$  Junction Solar Cells”, Journal of Applied Physics, Vol. 32, No. 3, pp 510-519, March 1961.
- [38] Louise C. Hirst and Nicholas J. Ekins-Daukes, “Fundamental losses in solar cells”, Progress in Photovoltaics: Research and Applications, Vol. 19, pp 286-293, August 2010.
- [39] M. A. Green, K. Emery, Y. Hishikawa, W. Warta, and E. D. Dunlop, “Solar cell efficiency tables (Version 45)”, Progress in Photovoltaics, Vol. 23, Issue 1, pp 1-9, January 2015.
- [40] Olindo Isabella, Klaus Jager, Amo Smets, Rene Van Swaij, Miro Zeman, “Solar Energy, Fundamentals, Technology, and Systems”, UIT Cambridge, UK, 2016, ISBN: 9781906860325.
- [41] Augustin McEvoy, Tom Markvart, Luis Castaner, “Practical Handbook of Photovoltaics, Fundamentals and Applications”, Second Edition, Academic Press, UK, 2012, ISBN: 9780123859341.
- [42] Andrew Poon, “Advanced Photonics Technologies”, Lecture notes ELEC509, Hong Kong University of Science and Technology, Spring 2011.
- [43] John A. Duffie, William A. Beckman, “Solar Engineering of Thermal Processes”, Fourth Edition. John Wiley & Sons Inc., New Jersey, 2013, ISBN: 9780470873663.
- [44] Julian F. Randall, “Designing Indoor Solar Products, Photovoltaic Technologies for AES”, John Wiley & Sons, UK, 2005, ISBN: 9780470016619.

- [45] Stephen Beedy, Neil White, “Energy Harvesting for Autonomous Systems”, Artech House Series, Smart Materials, Structures and Systems, USA, 2010, ISBN: 9781596937185.
- [46] Nahla Mohamed Abd Alrahim Shannan, Nor Zaihar Yahaya, and Balbir Singh, “Single-Diode Model and Two-Diode Model of PV Modules: A Comparison”, IEEE International Conference on Control System, Computing and Engineering, pp 210-214, November 2013.
- [47] Kashif Ishaque, Zainal Salam, Hamed Taheri, “Simple, fast and accurate two-diode model for photovoltaic modules”, Solar Energy Materials and Solar Cells, Vol. 95, Issue 2, pp 586–594, February 2011.
- [48] P. Rodrigues, J. R. Camacho and F. B. Matos, “The application of Trust Region Method to estimate the parameters of photovoltaic modules through the use of single and double exponential models”, International Conference on Renewable Energies and Power Quality (ICREPPQ’11), Vol. 1, No.9, pp 524-529, April 2011.
- [49] Tomas Markvart, “Solar Electricity”, John Wiley & Sons, Second Edition, 2000, ISBN: 9780471988533.
- [50] Hannes Knopf “Analysis, Simulation and evaluation of maximum power point tracking (mppt) methods for a solar powered vehicle”, Master of Science Thesis in Electrical and Computer Engineering, Portland State University, 1999.
- [51] David Wolpert, Paul Ampadu, “Managing Temperature Effects in Nanoscale Adaptive Systems”, Springer, USA, 2012, ISBN: 9781461407478.
- [52] Lúcio Almeida Hecktheuer, “Análise de Associações de Módulos Fotovoltaicos”, Tese de Doutorado, Universidade Federal do Rio Grande do Sul, Porto Alegre, Brasil, June 2001.
- [53] Paul A. Basore and Donald A. Clugston, “PC1D Help Index”, Version 5.9, University of New South Wales, 2008.
- [54] Paul A. Basore, “Numerical Modeling of Textured Silicon Solar Cells Using PC-1D”, IEEE Transactions on Electron Devices, Vol. 37, No. 2, pp 337-343, February 1990.

- [55] Richtek Technology Corporation, “4.5A Step-Up DC/DC Converter”, DS8509A-00 datasheet, Taiwan, November 2013.
- [56] Texas Instrument, “Simple Switcher 1A Step - Down Voltage Regulator”, LM1575/LM2575/LM2575HV datasheet, USA, May 1999 [Revised April 2013].
- [57] Jaycar Electronics, “DC-DC Converters: A Primer”, Reference Datasheet DCDCCONV, Jaycar Electronics, Australia, 2001.
- [58] Texas Instrument, “Switching Regulator Fundamentals”, Application Report SNVA559A, Texas Instrument, USA, September 2012 – Revised September 2016.
- [59] Ned Mohan, Tore M. Undeland and William P. Robbins, “Power Electronics, Converters, Applications and Design”, John Wiley & Sons, Third Edition, USA, 2003, ISBN: 9780471226932.
- [60] Marian K. Kazimierczuk, “Pulse-width Modulated DC–DC, Power Converters”, John Wiley and Sons, Second Edition, 2015, ISBN: 9781119009542.
- [61] Charles R. Sullivan and Matthew J. Powers, “A high-efficiency maximum power point tracker for photovoltaic arrays in a solar-powered race vehicle”, 24<sup>th</sup> Annual IEEE Power Electronics Specialists Conference (PESC '93), pp 574–580, July 1993.
- [62] P. D. Van den Heever, S. Oberholzer, and J. H. R. Enslin, “High-efficient solar panel/wind turbine converter with maximal power control”, 3<sup>rd</sup> European Conference Power Electronics and Applications (EPE '89), Vol. 2, pp 663–668, October 1989.
- [63] Andreas F. Boehringer, “Self-adapting dc converter for solar spacecraft power supply”, IEEE Transactions on Aerospace Electronic Systems, Vol. AES-4, Issue. 1, pp 102–111, January 1968.
- [64] J. J. Schoeman and J. D. van Wyk, “A simplified maximal power controller for terrestrial photovoltaic panel arrays”, 13<sup>th</sup> Annual IEEE Power Electronics Specialists Conference (PESC '82), pp 361-367, June 1982.



- [65] S. Yuvarajan and Shanguang Xu, "Photo-voltaic power converter with a simple maximum-power-point-tracker", Proceedings of International Symposium on Circuits and Systems, Vol. 3, pp 399-402, 2003.
- [66] Trishan Eswam and Patrick L. Chapman, "Comparison of photovoltaic array maximum power point tracking techniques", IEEE Transactions on Energy Conversion, Vol. 22, No. 2, pp 439-449, June 2007.
- [67] V. Salas, E. Olias, A. Barrado, and A. Lazaro, "Review of maximum power point tracking algorithms for standalone photovoltaic systems", Solar Energy Materials and Solar Cells, Vol. 90, Issue. 11, pp 1555-1578, July 2006.
- [68] Abu Tariq, M.S. Jamil, "Development of analog maximum power point tracker for photovoltaic panel", International Conference on Power Electronic Drive Systems (PEDS 2005), pp 251-255, November – December 2005.
- [69] Weidong Xiao, William G. Dunford, "A Modified Adaptive Hill Climbing MPPT Method for Photovoltaic Power Systems", 35<sup>th</sup> Annual IEEE Power Electronics Specialists Conference (PESC 2004), pp 1957-1963, June 2004.
- [70] Chih-Chiang Hua and Jong Rong Lin, "Fully digital control of distributed photovoltaic power systems," IEEE International Symposium Industrial Electronics (ISIE 2001), pp 1–6, June 2001.
- [71] Nicola Femia, Giovanni Petrone, Giovanni Spagnuolo, and Massimo Vitelli, "Optimization of perturb and observe maximum power point tracking method", IEEE Transactions on Power Electronics, Vol. 20, No. 4, pp 963–973, July 2005.
- [72] Sachin Jain and Vivek Agarwal, "A new algorithm for rapid tracking of approximate maximum power point in photovoltaic systems", IEEE Power Electronics Letters, Vol. 2, No. 1, pp 16–19, March 2004.
- [73] J. D. van Wyk and J. H. R. Enslin, "A study of wind power converter with microprocessor based power control utilizing an over synchronous electronic scherbius cascade", Proceedings IEEE International Power Electronic Conference (IPEC '83), Vol. 1, pp 766-777, 1983.
- [74] W. J. A. Teuling, J. C. Marpinard, A. Capel, and D. O'Sullivan, "A New Maximum Power Point Tracking System", 24<sup>th</sup> Annual IEEE Power Electronics Specialists Conference (PESC '93), pp 833-838, July 1993.

- [75] Yomgho Kim, Hyunmin Jo, and Deokjung Kim, "A new peak power tracker for cost effective photovoltaic power system", 31<sup>st</sup> Intersociety Energy Conversion Engineering Conference (IECEC 96), Vol. 3, pp 1673-1678, September 1996.
- [76] Eftichios Koutroulis, Kostas Kalaitzakis, and Nicholaw C. Voulgaris, "Development of a microcontroller-based, photovoltaic maximum power point tracking control system", IEEE Transactions on Power Electronics, Vol. 16, No. 1, pp 46-54, January 2001.
- [77] Mao-Lin Chiang, Chih-Chiang Hua, and Jong-Rong Lin, "Direct Power Control for distributed PV Power System", Power Conversion Conference (PCC 2002), Vol. 1, pp 311-315, February 2002.
- [78] Chihchiang Hua and Jong Rong Lin, "DSP-based Controller Application in Battery Storage of Photovoltaic System", 22<sup>nd</sup> International Conference Industrial Electronics, Control and Instrumentaion (IEEE IECON 1996), Vol. 3, pp 1705-1710, August 1996.
- [79] O. Wasynczuk, "Dynamic behavior of a class of photovoltaic power systems", IEEE Transaction on Power Apparatus Systems, Vol. PAS-102, No. 9, pp 3031-3037, September 1983.
- [80] E. N. Costogue and S. Lindena, "Comparison of candidate solar array maximum power utilization approaches", 11<sup>th</sup> Intersociety Energy Conversion Engineering Conference (IECEC 76), Vol. 2, pp 1449-1456, September 1976.
- [81] Angelo Brambilla, Marcello Gambarara, Antonio Garutti, and Fabrizio Ronchi, "New approach to photovoltaic arrays maximum power point tracking", 30<sup>th</sup> Annual IEEE Power Electronics Specialists Conference (PESC '99), pp 632-637, July 1999.
- [82] Yeong-Chau Kuo, Tsorng-Juu Liang, and Jiann-Fuh Chen, "Novel maximum-power-point tracking controller for photovoltaic energy conversion system", IEEE Transactions on Industrial Electronics, Vol. 48, No. 3, pp 594-601, June 2001.

- [83] G. J. Yu, Y. S. Jung, J. Y. Choi, I. Choy, J. H. Song, and G. S. Kim, "A novel two-mode MPPT control algorithm based on comparative study of existing algorithms", *Solar Energy*, Vol. 76, Issue 4, pp 455-463, April 2004.
- [84] Wenkai Wu, N. Pongratananukul, Weihong Qiu, K. Rustom, T. Kasparis, and I. Batarseh, "DSP-based multiple peak power tracking for expandable power system", 18<sup>th</sup> Annual IEEE Applied Power Electronics Conference and Exposition (APEC '03), Vol. 1, pp 525-530, February 2003.
- [85] Awang Jusoh, Tole Sutikno, Tan Kar Guan, Saad Mekhilef, "A Review on Favourable Maximum Power Point Tracking Systems in Solar Energy Application" *TELKOMNIKA*, Vol.12, No.1, pp 6-22, March 2014.
- [86] Divya Teja Reddy Challa, I. Raghavendar, "Implementation of Incremental Conductance MPPT with Direct Control Method Using Cuk Converter", *International Journal of Modern Engineering Research (IJMER)*, Vol. 2, Issue 6, pp 4491-4496, November-December 2012.
- [87] Mihnea Rosu-Hamzescu, Sergiu Oprea, "Practical Guide to Implementing Solar Panel MPPT Algorithms", *Microchip*, Application Report AN1521, pp 1-16, November 2013.
- [88] Roberto Faranda, Sonia Leva, "Energy comparison of MPPT techniques for PV Systems", *WSEAS Transactions on Power Systems*, Vol. 3, Issue 6, pp 446-455, June 2008.
- [89] P. C. M. de Carvalho, R. S. T. Pontes, D. S. Oliveira, D. B. Riffel, R. G. V. de Oliveira, and S. B. Mesquita, "Control method of a photovoltaic powered reverse osmosis plant without batteries based on maximum power point tracking", *Transmission and Distribution Conference and Exposition: Latin America (IEEE/PES 2004)*, pp 137-142, November 2004.
- [90] A. Dolara, R. Faranda, S. Leva, "Energy Comparison of Seven MPPT Techniques for PV Systems", *Journal Electromagnetic Analysis & Applications*, Vol. 1, No. 3, pp 152-162, September 2009.
- [91] Eduardo Moreira Vicente, Robson Luiz Moreno and Enio Roberto Ribeiro, "MPPT Technique Based on Current and Temperature Measurement",

International Journal of Photoenergy, Hindawi Publishing Corporation, Vol. 2015, Article ID 242745, pp 1-9, February 2015.

[92] G. W. Hart, H. M. Branz, and C. H. Cox III, "Experimental tests of open loop maximum-power-point tracking techniques for photovoltaic arrays," *Solar Cells*, Vol. 13, Issue 2, pp 185–195, December 1984.

[93] Matthew Buresch, "Photovoltaic Energy Systems: Design and Installation", McGraw Hill, New York, 1983, ISBN: 9780070089525.

[94] Dean J. Patterson, "Electrical system design for a solar powered vehicle", 21<sup>st</sup> Annual IEEE Power Electronics Specialists Conference (PESC '90), pp 618-622, July 1990.

[95] Mohammad A. S. Masoum, Hooman Dehbonei and Ewald F. Fuchs, "Theoretical and experimental analyses of photovoltaic systems with voltage and current based maximum power-point tracking", *IEEE Transactions on Energy Conversion*, Vol. 17, No. 4, pp 514-522, December 2002.

[96] Hyeong Ju Noh, Dong-Yun Lee and Dong-Seok Hyun, "An improved MPPT converter with current compensation method for small scaled PV-applications", 28<sup>th</sup> Annual IEEE Conference of the Industrial Electronics Society (IECON 02), pp 1113-1118, November 2002.

[97] Kimiyoshi Kobayashi, Hirofumi Matsuo, and Yutaka Sekine, "A novel optimum operating point tracker of the solar cell power supply system", 35<sup>th</sup> Annual IEEE Power Electronics Specialists Conference (PESC 2004), pp 2147-2151, June 2004.

[98] Bernad Bekker and H. J. Beukes, "Finding an optimal PV panel maximum power point tracking method", 7<sup>th</sup> AFRICON IEEE Conference in Africa, pp 1125-1129, September 2004.

[99] Dave Freeman, "Introduction to Photovoltaic Systems Maximum Power Point Tracking", Texas Instruments, Application Report SLVA446, pp 1-7, November 2010.

[100] Davide Brunelli, Luca Benini, Clemens Moser, Lothar Thiele, "An Efficient Solar Energy Harvester for Wireless Sensor Nodes", *Design, Automation and Test in Europe (DATE '08)*, pp 104-109, March 2008.

- [101] S. M. Ferdous, Mahir Asif Mohammad, Farhan Nasrullah, Ahmed Mortuza Saleque, and A.Z.M.Shahriar Muttalib, "Design and Simulation of an Open Voltage Algorithm based Maximum Power Point Tracker for Battery Charging PV System", 7<sup>th</sup> International Conference on Electrical and Computer Engineering (ICECE 2012), pp 908-911, December 2012.
- [102] Noguchi Toshihiko, Shigenori Togashi, and Ryo Nakamoto, "Short-current pulse based adaptive maximum-power-point tracking for photovoltaic power generation system", Proceedings 2000 IEEE International Symposium on Industrial Electronics (ISIE' 2000), Vol. 1, pp 157-162, December 2000.
- [103] Nobuyoshi Mutoh, Takatoshi Matuo, Kazuhito Okada and Masahiro Sakai, "Prediction-Data-Based Maximum-Power-Point-Tracking Method for Photovoltaic Power Generation Systems", 33<sup>rd</sup> Annual IEEE Power Electronics Specialists Conference (PESC 2002), Vol. 3, pp 1489-1494, June 2002.
- [104] Ying Tung Hsiao, China-Hong Chen, "Maximum Power Tracking for Photovoltaic Power System", 37<sup>th</sup> IAS Annual Meeting, IEEE Industry Applications Conference, Vol. 2, pp 1035-1040, February 2002.
- [105] Trisham Eswam, Jonathan W. Kimball, Philip T. Krein, Patrick L. Chapman and Pallab Midya, "Dynamic Maximum Power Point Tracking of Photovoltaic Arrays Using Ripple Correlation Control", IEEE Transactions on Power Electronics, Vol. 21, No. 5, 1282-1291, September 2006.
- [106] Yan Hong Lim and David C. Hamill, "Synthesis, simulation and experimental verification of a maximum power point tracker from nonlinear dynamics", 32<sup>nd</sup> Annual IEEE Power Electronics Specialists Conference (PESC 2001), Vol. 1, pp 199-204, June 2001.
- [107] Saleh Elkelani Babaa, Matthew Armstrong, Volker Pickert, "Overview of Maximum Power Point Tracking Control Methods for PV Systems", Journal of Power and Energy Engineering, Vol. 2, pp 59-72, 2014.
- [108] Moacyr Aureliano Gomes de Brito, Luigi Galotto, Jr., Leonardo Poltronieri Sampaio, Guilherme de Azevedo e Melo, and Carlos Alberto Canesin, "Evaluation of the Main MPPT Techniques for Photovoltaic Applications", IEEE Transactions on Industrial Electronics, Vol. 60, Issue 3, pp 1156-1167, March 2013.

- [109] Roberto F. Coelho, Filipe M. Concer, Denizar C. Martins, “A MPPT Approach Based on Temperature Measurements Applied in PV Systems”, 9<sup>th</sup> IEEE/IAS International Conference on Industry Applications (INDUSCON 2010), pp 1-6, December 2010.
- [110] Pallavee Bhatnagar, R.K. Nema, “Maximum power point tracking control techniques: State-of-the-art in photovoltaic applications”, *Renewable and Sustainable Energy Reviews*, Vol. 23, pp 224-241, July 2013.
- [111] S. Malathy, R. Ramaprabha, “Maximum Power Point Tracking Based on Look up Table Approach”, *Advanced Materials Research* Vol. 768, pp 124-130, September 2013.
- [112] J. S. Christy Mano Raj and A. Ebenezer Jeyakumar, “A two stage successive estimation based maximum power point tracking technique for photovoltaic modules”, *Solar Energy*, Vol 103, pp 43–61, May 2014.
- [113] Masoum Mohammad A. S. and Dehbonei Hooman, “Design, construction and testing of a voltage-based maximum power point tracker (VMPPT) for small satellite power supply”, 13<sup>th</sup> Annual AIAA/USU Conference on Small Satellite, pp 1–12, August 1999.
- [114] Fathi A O Aashoor, “Maximum power point tracking techniques for photovoltaic water pumping system”, PhD Thesis, Department of Electronic and Electrical Engineering, University of Bath, May 2015.
- [115] D. P. Hohm and M. E. Ropp, “Comparative study of maximum power point tracking algorithms”, *Progress in Photovoltaics: Research and Applications*, Vol. 11, Issue 1, pp 47-62, January 2003.
- [116] L. Piegari and R. Rizzo, “Adaptive perturb and observe algorithm for photovoltaic maximum power point tracking”, *IET Renewable Power Generation*, Vol. 4, Issue 4, pp 317-328, February 2010.
- [117] Cristinel Dorofte, Uffe Borup, Frede Blaabjerg, “A combined two-method MPPT control scheme for grid-connected photovoltaic systems”, 2005 European Conference on Power Electronics and Applications, pp P1-P10, September 2005.

- [118] A. Yafaoui, B. Wu and R. Cheung, "Implementation of maximum power point tracking algorithm for residential photovoltaic systems", 2<sup>nd</sup> Canadian solar buildings conference Calgary, pp 1-6, June 2007.
- [119] Salas, V., Olias, E., Barrado, A. and Lazaro, A., "Review of the Maximum Power Point Tracking Algorithms for Stand-Alone Photovoltaic Systems", *Solar Energy Materials and Solar Cells*, Vol. 90, Issue 11, pp 1555-1578, July 2006.
- [120] Ali Reza Reisi, Mohammad Hassan Moradi, Shahriar Jamasb, "Classification and comparison of maximum power point tracking techniques for photovoltaic system: A review", *Renewable and Sustainable Energy Reviews*, Vol. 19, pp 433-443, March 2013.
- [121] Liu, C., Wu, B. and Cheung, R., "Advanced Algorithm for MPPT Control of Photovoltaic Systems", *Canadian Solar Buildings Conference*, pp 20-24, August 2004.
- [122] Ali Nasr Allah Ali, Mohamed H. Saied, Mohamed Z. Mostafa, Talaat M. Abdel- Moneim, "A Survey of Maximum PPT techniques of PV Systems", *Energytech, IEEE*, pp 299-316, May 2012.
- [123] Hardik P. Desai, and H. K. Patel, "Maximum Power Point Algorithm in PV Generation: An Overview," *Power Electronics and Drive Systems (PEDS '07)*, 7th International Conference, pp 624 – 630, November 2007.
- [124] Joseph Durago, "Photovoltaic Emulator Adaptable to Irradiance, Temperature and Panel-Specific I-V Curves", MSc Thesis, California Polytechnic State University, San Luis Obispo, June 2011.
- [125] Francisco M. González-Longatt, "Model of Photovoltaic Module in Matlab", 2DO Congreso Iberoamericano de Estudiantes de Ingenieria Electrica, Electronica Y Computacion (II CIBELEC), Vol. 2005, pp 1-5, December 2005.
- [126] Sun Ho Jang, Moo Whan Shin, "Fabrication and thermal optimization of LED solar cell simulator", *Current Applied Physics*, Vol. 10, Issue 3, pp S537–S539, May 2010.
- [127] Richard J. Matson, Keith A. Emery and Richard E. Bird, "Terrestrial solar spectra, solar simulation and solar cell short-circuit current calibration: A review", *Solar Cells*, Vol. 11, Issue 2, pp 105-145, March 1984.

- [128] Keith Emery, Daryl Myers and Steve Rummel, “Solar simulation-problems and solutions”, 20<sup>th</sup> IEEE Photovoltaic Specialists Conference, Vol. 2, pp 1087–1091, February 1988.
- [129] Shogo Kohraku, Kosuke Kurokawa, “A fundamental experiment for discrete – wavelength LED solar simulator”, Solar Energy Materials and Solar Cells, Vol. 90, Issues 18-19, pp 3364-3370, November 2006.
- [130] Martin Bliss, Thomas Richard Betts, Ralph Gottschalg, “An LED-based photovoltaic measurement system with variable spectrum and flash speed”, Solar Energy Materials & Solar Cells, Vol. 93, Issues 6-7, pp 825–830, June 2009.
- [131] Martin Bliss, “Measurement system for fast power and energy rating of photovoltaic devices”, PhD Thesis, Loughborough University, February 2011.
- [132] Md Khairi Amali Hj Husli “PV Device Characterisation: Temperature Control System Software Development and Test”, Loughborough University, September 2009.
- [133] Stanislav Bobovych, Nilanjan Banerjee, Ryan Robucci, James P. Parkerson, Jackson Schmandt, and Chintan Patel, “SunPlayer: high-accuracy emulation of solar cells”, 14<sup>th</sup> International Conference on Information Processing in Sensor Networks (IPSN’15), pp 59-70, April 2015.
- [134] Anand Savanth, Alex Weddell, James Myers, David Flynn, Bashir-Al-Hashimi, “Photovoltaic Cells for Micro-Scale Wireless Sensor Nodes: Measurement and Modeling to Assist System Design”, 3<sup>rd</sup> International Workshop on Energy Harvesting & Energy Neutral Sensing Systems (ACM ENSsys 2015), pp 15-20, November 2015.
- [135] Denso Sera, Tamas Kerekes, Remus Teodorescu and Frede Blaabjerg, “Improved MPPT algorithms for rapidly changing environmental conditions”, Proceedings of 12<sup>th</sup> International Conference on Power Electronics and Motion Control, pp 1614-1619, August 2006.
- [136] Denso Sera, Tamas Kerekes, Remus Teodorescu and Frede Blaabjerg, “Improved MPPT algorithms for rapidly changing environmental conditions”, Proceedings of IEEE International Symposium on Industrial Electronics, Vol. 2, pp 1420-1425, July 2006.



- 
- [137] Tat Luat Nguyen and Kay-Soon Low, "A global maximum power point tracking scheme employing DIRECT search algorithm for photovoltaic systems", *IEEE Transactions on Industrial Electronics*, Vol. 57, No. 10, pp 3456-3467, October, 2010.
- [138] Anwar Sohail, Harry Efstathiadis and Salahuddin Qazi, "Handbook of Research on Solar Energy Systems and Technologies", IGI Global, USA, 2012, ISBN: 9781466619968.
- [139] Il-Song Kim and Myung-Joong Youn, "Single-loop maximum power point tracker with fast settling time", *Annual Conference of the IEEE Industrial Electronics Society*, Vol. 30, pp 862-866, Korea, November 2004.
- [140] C. Carrero, J. Rodriguez, D. Ramirez, C. Platero, "Simple estimation of PV modules loss resistances for low error modeling", *Renewable Energy* Vol. 35, Issue 5, pp 1103-1108, May 2010.
- [141] Eduardo Lorenzo, "Solar Electricity: Engineering of Photovoltaic Systems", Progensa, 1994, ISBN: 9788486505554.
- [142] Vicente Leite and Faustino Chenlo, "An improved Electronic Circuit for Tracing the I-V Characteristics of Photovoltaic Modules and Strings", *International Conference on Renewable Energies and Power Quality*, Vol. 1, No. 8, pp 1224-1228, April 2010.
- [143] Yingying Kuai, S. Yuvarajan, "An electronic load for testing photovoltaic panels", *Journal of Power Sources*, Vol. 154, Issue 1, pp 308-313, March 2006.
- [144] Adel S Sedra, Kenneth C Smith, "Microelectronic Circuits", 6th Edition, Oxford University Press, 2010, ISBN 9780195323030.
- [145] Peter Wilson, ELEC 2216 Class Lecture, Topic: "Advanced Electronic Systems", School of Electronics and Computer Science, Southampton University, Southampton, UK, December 2014.
- [146] Chegaar M, Ouennoughi Z, Guechi F., "Extracting dc parameters of solar cell under illumination", *Vacuum*, Vol. 75, Issue 4, pp 367 – 372, August 2004.

- [147] Maithil Pachchigar, “Compensation techniques for driving large-capacitance loads with high speed amplifiers”, Applications Engineer, National Semiconductor Corporation, pp 1-4, February 2008.
- [148] Soufiane Bendaoud, Giampaolo Marino, “Practical Techniques to Avoid Instability Due to Capacitive Loading”, Analog Devices, Analog Dialogue, Vol. 38, No. 2, pp 9- 14, June 2004.
- [149] Jerald G. Graeme, “Applications of operational Amplifiers, Third Generation Techniques”, The Burr – Brown Electronic Series, Mc Graw Hill Book Company, 1973, ISBN 0070238901.
- [150] Maxim, “DS18B20 Programmable Resolution 1- Wire Digital Thermometer”, DS18B20 datasheet, 2008, Revision 042208.
- [151] Tim Regan, “Current Sense Circuit Collection. Making Sense of current”, Linear Technology, Application Note 105, 72-76, December 2005.
- [152] Analog Devices, “256-/1024-Position, Digital Potentiometers with Maximum  $\pm 1\%$  R-Tolerance Error and 20-TP Memory”, AD5292 datasheet, 2009-2010, Revision D.
- [153] Analog Devices, “1.5  $\Omega$  On Resistance,  $\pm 15\text{V}/12\text{V}/\pm 5\text{V}$ , iCOMS, Dual SPDT Switch, ADG1436 datasheet, 2008 – 2009, Revision A.
- [154] Analog Devices, “Programmable Gain, Precision Difference Amplifier”, AD8271 datasheet, 2009.
- [155] Maxim Integrated, “16 – BIT ADC, 200 ksps, 5V Single Supply with Reference”, MAX1132 datasheet, Aug. 2001.
- [156] Samsung, “Board Guide for Noise Immunity”, Samsung Electronics, System LSI Division, Korea, 2008.
- [157] Analog Devices, “Decoupling Techniques”, MT-101 Tutorial, March 2009.
- [158] Linear Technology, “Precision, 100 $\mu\text{A}$  Gain Selectable Amplifier”, LT1991 datasheet, USA 2006, Revision H.
- [159] Burr – Brown, “16-BIT DIGITAL – TO – ANALOG CONVERTER with 16-Bit Bus Interface”, DAC715 datasheet, USA July 1997.

- 
- [160] Microchip, “16-Bit I/O Expander with Serial Interface” MCP23017 datasheet, 2007.
- [161] Philips Semiconductor, Application Note AN10216-01 - I<sup>2</sup>C Manual, March 24, 2003.
- [162] ON Semiconductor, “MC7800, MC7800A, NCV7805, 1.0 A Positive Voltage Regulators”, MC7805CT datasheet, July 2004 – Rev. 13.
- [163] Linear Technology, “LT1083/LT1084/LT1085, 7.5A, 5A, 3A Low Dropout Positive Adjustable Regulators”, LT1084 datasheet, USA 1994.
- [164] Atmel, “ATmega 640/V – 1280/V – 1281/V – 2560/V – 2561/V.”, ATmega2560 datasheet, Revision 2549Q – AVR-02/2014, USA, 2014.
- [165] Arokia Nathan, Arman Ahnood, Matthew T. Cole, Sungsik Lee, Yuji Suzuki, Pritesh Hiralal, Francesco Bonaccorso, Tawfique Hasan, Luis Garcia-Gancedo, Andriy Dyadyusha, Samiul Haque, Piers Andrew, Stephan Hofmann, James Moultrie, Daping Chu, Andrew J. Flewitt, Andrea C. Ferrari, Michael J. Kelly, John Robertson, Gehan A. J. Amaratunga, and William I. Milne “Flexible Electronics: The Next Ubiquitous Platform”, Proceedings of the IEEE, Vol. 100, pp 1486-1517, May 2012.
- [166] Samsung Electronics, “GSM Mobile Phone: GT-E1107”, Mobile User Manual, 2009.
- [167] Sharp Electronics Corporation, “Solar Hybrid SH6230C”, a Solar-Powered Mobile Phone, 2010.
- [168] Microchip, “Miniature Single-Cell, Fully Integrated Li-Ion, Li-Polymer Charge Management Controllers”, MCP73831/2 datasheet, Revision G, USA, 2014.
- [169] A. Harish, M.V.D. Prasad, “Microcontroller Based Photovoltaic MPPT Charge Controller”, International Journal of Engineering Trends and Technology (IJETT), Vol. 4, Issue 4, pp 1018- 1021, April 2013.
- [170] David Kahaner, Cleve Moler and Stephen Nash, “Numerical Methods and Software”, Prentice-Hall, New Jersey, USA, 1989, ISBN: 9780136272588.

- [171] J. H. Wilkinson, “Two algorithms based on successive linear interpolation”, Technical Report STAN-CS-67-60, Computer Science Department, Stanford University, School of Humanities and Sciences, Technical Report No. CS60, California, USA, pp 1-13, April 1967.
- [172] Microchip, “6A High-Speed Power MOSFET Drivers”, MCP1406/07 Datasheet, December 2006, Revision A.
- [173] G. Spiazzi, S. Buso, P. Mattavelli “Analysis of MPPT algorithm for photovoltaic panel based on ripple correlation techniques in presence of parasitic components”, Power Electronics Conference, COBEP’09, Brazilian, IEEE, pp 88-95, December 2009.
- [174] Atmel, “8 bit AVR Microcontroller”, ATmega328P datasheet, Revision 8161D – AVR-10/09.
- [175] Brigitte Hauke, “Basic Calculation of a Boost Converter’s Power Stage”, Texas Instruments, Application Report SLVA372A, November 2009 – Revised April 2010.
- [176] Abhimanyu Singh Udawat, “Designing A Step-Up DC-To-DC Boost Converter”, Explore Labs Limited, Rajasthan, India, April 2015.
- [177] ON Semiconductor, “MBR1035 – MBR1060 Schottky Rectifiers”, MBR1060 datasheet, Revision 1.2.1, USA, October 2013.
- [178] Marian K. Kazimierczuk and Agasthya Ayachit, “Laboratory Manual for Pulse-Width Modulated DC-DC Power Converters”, Wiley & Sons, UK, 2016. ISBN: 9781119052760.
- [179] Richard P. Brent, “Algorithms for Minimization Without Derivatives”, Prentice-Hall, New Jersey, USA, 1973, ISBN: 978-0130223357.
- [180] Forsythe, G. E., M. A. Malcolm and C. B. Moler, “Computer Methods for Mathematical Computations”, Prentice-Hall, New Jersey, USA, 1977, ISBN: 9780131653320.
- [181] Microchip, “28/40/44 Pin, Enhanced Flash Microcontrollers with 10-BIT A/D and nanoWatt Technology”, PIC18F2525/2620/4525/4620 Datasheet, USA, 2008.

[182] R. R. Potter, J. R. Sites and S. Wagner, “Current – voltage response of tandem junction solar cells”, *Journal of Applied Physics*, Vol. 53, No. 7, pp 5269-5272, July 1982.

[183] Shin-ichiro Sato, Haruki Miyamoto, Mitsuru Imaizumi, Kazunori Shimazaki, Chiharu Morioka, Katsuyasu Kawano, Takeshi Ohshima, “Degradation modeling of InGaP/GaAs/Ge triple – junction solar cells irradiated with various – energy protons”, *Solar Energy Materials & Solar Cells* Vol. 93, Issues 6-7, pp 768 – 773, June 2009.

[184] Asaf Ben Or and Joseph Appelbaum, “Estimation of multi-junction solar cell parameters”, *Progress in Photovoltaics: Research and applications*, Vol. 21, Issue 4, pp 713- 723, February 2012.